COMPRESSIBILITY, VARIABLE DENSITY, AND CURVATURE EFFECTS ON TURBULENT SHEAR LAYERS

By
Kristen V. Matsuno and Sanjiva Lele

Prepared with support from
the National Science Foundation Graduate Research Fellowship, and
the NASA Ames Research Center

Report No. TF-190

Flow Physics and Computational Engineering Group
Department of Mechanical Engineering
Stanford University
Stanford, CA 94305

December 2022

Some Compressibility, Variable Density, And Curvature Effects On Turbulent Shear Layers

By

Kristen V. Matsuno and Sanjiva Lele

Prepared with support from
the National Science Foundation Graduate Research Fellowship, and
the NASA Ames Research Center

Report No. TF-190

Flow Physics and Computational Engineering Group
Department of Mechanical Engineering
Stanford University
Stanford, CA 94305

December 2022

Abstract

Turbulent mixing layers occur between two streams of fluids with different kinematic and/or thermodynamic properties, and are fundamental flow features which influence the dynamics of a wide variety of applications, ranging from the mixing efficiency of fuel injection in internal combustion to vehicle loads in external aerodynamics. Two motivating applications behind this research include the study of high-speed jets in cross-flow and supersonic retro-propulsion, which occurs as aerospace vehicles use jet plumes to decelerate during entry, descent, and landing. Both these applications are highly influenced by hot jet plumes under highly compressible conditions which exhibit significant streamwise curvature. Simulating the entire flow field associated with such applications is extremely computationally expensive; capturing all important flow features at full resolution is exorbitant for the purposes of engineering design. Thus, grasping the full behavior of turbulent mixing layers in a representative parameter space enables the development of models which can reliably and accurately predict the complex flow fields present in these engineering applications. This work enriches the present understanding of mixing in turbulent shear layers via the systematic inclusion of compressibility, variable density, and streamwise curvature effects.

The spreading, or growth rate, of turbulent shear layers is known to decrease with increasing compressibility. In Chapter 2, turbulent shear layers without differences in freestream density and without streamwise curvature are investigated at six levels of increasing compressibility (convective Mach numbers ranging from 0.2 to 2.0). Dilatational velocities and pressure-dilatation magnitudes show little contribution to shear layer growth rates, even under highly compressible conditions. A new turbulent length and velocity scale is introduced and shown to scale key turbulent quantities.

Inclusion of freestream density variations are also known to decreasing mixing layer growth rates. Chapter 3 focuses on turbulent shear layers with and without freestream density differences at three representative compressibility levels, again without streamwise curvature. Convective Mach numbers of 0.2, 0.8 and 2.0 and freestream density ratios of 1 and 7 are investigated. Trends with increasing compressibility and the importance of mixing layer asymmetry are identified–shear layer centerlines and turbulent stresses in variable density shear layers are biased towards the less-dense

freestream, which reduces the turbulent mixing of the mean momentum profile and corresponding growth rates.

Chapter 4 presents data and observations for shear layers which include streamwise curvature effects. A database of mixing layers at two convective Mach numbers (0.2 and 0.8), three density ratios (1/7, 1 and 7), and weak and strong curvature levels is presented. The combined effects of compressibility and streamwise curvature are demonstrated to be comparable for the selected parameter space. Shear layer growth rates are dominated by the freestream density ratio when streamwise curvature is significant.

Lastly, the performance of lower-order models commonly used in industry for high speed turbulent flows is presented in Chapter 5. Changes to model predictions of turbulent growth rates and turbulent kinetic energy levels resulting from various model modifications are evaluated. Reduced accuracy in model predictions of turbulent kinetic energy magnitudes under curved conditions, even with the inclusion of compressibility and curvature modifications, is demonstrated.

Acknowledgments

This work has been supported by the National Science Foundation Graduate Research Fellowship program (NSF GRFP), the U.S. Department of Energy Office of Science INCITE allocation 4978-4846, the Argonne Leadership Computing Facility (ALCF) Director's Discretionary allocation 6195-6063, the Aerosciences Evaluation and Test Capability (AETC) program office under the Aeronautics Research Mission Directorate (ARMD) at NASA, and the Orion Launch Abort Vehicle project under NASA's Engineering Safety Center (NESC).

Nomenclature

At	Atwood number
D, ε	TKE dissipation
M_c	Convective Mach number
M_g	Gradient Mach number
M_t	Turbulent Mach number
P	TKE production
P_t	Total pressure
Pr	Prandtl number
R	Gas constant
R_{ij}	Reynolds (turbulent) stress tensor
Re	Reynolds number
T	Temperature
Y	Species mass fraction
Δu, $\Delta \bar{u}$	Freestream velocity difference
Γ	Circulation
Π	Pressure dilatation correlation
Π_{ij}	Pressure strain correlation
$\bar{f}$,f'	Reynolds average and fluctuation of field f

δ_{99}	99% thickness
δ_Γ	Circulation thickness
δ_ω	Vorticity thickness
δ_θ	Momentum thickness
γ	Ratio of specific heats
κ	Thermal conductivity
μ	Dynamic viscosity
ρ	Density
τ_{ij}	Viscous (laminar) stress tensor
$\tilde{f}$,f''	Favre (mass) average and fluctuation of field f
$\vec{\omega}$	Vorticity
ξ	Entropy constant
$_0$	Initial value
c	Speed of sound
e	Internal energy
k	Turbulent kinetic energy (TKE)
p	Pressure
r_c	Centerline radius
s_ρ	Ratio of freestream densities
u, v, w	Cartesian velocity components (streamwise, transverse, spanwise)
u_θ, u_r, u_z	Cylindrical velocity components (streamwise, transverse, spanwise)
y_c	Centerline location
θ, r, z	Cylindrical coordinate system (streamwise, transverse, spanwise)
x, y, z	Cartesian coordinate system (streamwise, transverse, spanwise)

CC	Compressibility modification
CFD	Computational fluid dynamics
DNS	Direct numerical simulation
LES	Large eddy simulation
RANS	Reynolds-averaged Navier-Stokes
RC	Rotation/curvature modification
SA	Spalart-Allmaras model
SST	Shear stress transport
TKE	Turbulent kinetic energy (k)

Contents

Abstract **iv**

Acknowledgments **vi**

1 Introduction **1**

1.1 Motivation . . . 1
1.2 Outline . . . 3
1.3 Highlights . . . 3

2 Compressibility effects on turbulent shear layers **5**

2.1 Introduction . . . 5
2.2 Methodology . . . 11
2.2.1 Governing equations . . . 11
2.2.2 Initial conditions . . . 11
2.2.3 Boundary conditions . . . 13
2.2.4 Discretization . . . 14
2.3 Compressibility effects on turbulent statistics in the high-Mach regime . . . 18
2.3.1 Means, turbulent stresses, and turbulent mass fluxes . . . 18
2.3.2 Growth rates . . . 22
2.3.3 Turbulent stress anisotropy . . . 23
2.3.4 Dilatational stresses . . . 25
2.3.5 TKE budgets and pressure-strain rate tensor . . . 28
2.3.6 Turbulence length and time scales . . . 32
2.3.7 Scaling of turbulence statistics . . . 37
2.4 Conclusions . . . 39

3 Variable density effects on turbulent shear layers **40**
3.1 Introduction . . . 40
3.2 Methodology . . . 44
3.2.1 Governing equations . . . 44
3.2.2 Physical parameters . . . 44
3.3 Effects of density variations on turbulent statistics . . . 46
3.3.1 Growth rates and turbulent stresses . . . 46
3.3.2 Mass fluxes . . . 51
3.3.3 Mixing layer centerline and asymmetry . . . 53
3.3.4 Turbulent scales and internal regulation . . . 57
3.4 Decomposition of density fluctuations . . . 61
3.5 Viscous heating effects . . . 64
3.6 Conclusions . . . 68

4 Streamwise curvature effects on turbulent shear layers **69**
4.1 Introduction . . . 69
4.2 Methodology . . . 76
4.2.1 Governing equations . . . 76
4.2.2 Numerical methods . . . 77
4.2.3 Physical parameters . . . 84
4.2.4 Initial conditions . . . 85
4.2.5 Boundary conditions . . . 87
4.2.6 Effect of WENO5 on disturbance energy . . . 87
4.3 Visualization and vortical structures . . . 90
4.4 Curvature effects on turbulent statistics . . . 96
4.4.1 Mean profiles and turbulent stresses . . . 96
4.4.2 Growth rates . . . 104
4.4.3 Stable vs. unstable configuration . . . 107
4.4.4 Effects of increasing curvature intensity . . . 110
4.4.5 Comparison to compressibility effects . . . 114
4.4.6 Combination with variable density effects . . . 116
4.5 Conclusions . . . 127

5 RANS model evaluation **128**
5.1 Introduction: modeling approaches . . . 128
5.1.1 Mean equations of motion . . . 129

5.1.2 Review of compressibility modifications to model equations 130
5.1.3 Review of variable density modifications 134
5.1.4 Review of rotation/curvature modifications 135
5.2 Evaluation of closure approximations 137
5.2.1 Pressure strain tensor 137
5.2.2 Turbulent mass flux 138
5.3 Interactions between RANS model corrections 139
5.3.1 Numerical methods for RANS calculations 140
5.3.2 Turbulent kinetic energy profiles 141
5.3.3 Growth rates 145

6 Conclusions **148**

A Temporal shear layer windowing **152**

B Curved shear layer profiles **154**

C Miscellaneous evolution equations **178**

List of Tables

2.1 Comparison to previously published high resolution simulations of temporal shear layers: initial and final Reynolds numbers based on momentum and vorticity thicknesses, and final values of the Kolmogorov scale η compared to the grid resolution. . . . 10

2.2 Parameters, domains, and grid resolutions for $s = 1$ cases studied. All cases use $N_x \times N_y \times N_z = 1024 \times 1448 \times 512$ uniformly spaced grid points. . . . 15

2.3 A brief comparison of key flow parameters with previous studies. N/A indicates 'not available'. . . . 15

2.4 Peak values of kinematic stress components, defined as Eqn. 2.9. Values of $R_{ij}^{(dd)}$ and $R_{ij}^{(sd)}$ are scaled by 10^{-4}. . . . 27

3.1 Parameters, domains, and grid resolutions for cases studied. All cases use $N_x \times N_y \times N_z = 1024 \times 1448 \times 512$ uniformly spaced grid points. . . . 45

3.2 A brief comparison of parameter ranges with previous studies on compressible, variable density mixing layers. The Atwood number is related to the density ratio by $At = (1 - s_\rho)/(1 + s_\rho)$. . . . 46

4.1 Summary of conditions for centrifugal stability of disturbances in streamwise curved flows. . . . 74

4.2 Case names and corresponding parameter spaces organized by curvature intensity δ/r_c, compressibility M_c, density ratio ρ_2/ρ_1 and velocity ratio u_2/u_1. Total pressure P_t and entropy constant $\xi = p/\rho^\gamma$ are also specified for each freestream. . . . 85

4.3 Physical parameters and curvature levels during initial and turbulent 'asymptotic' growth for unity density ratio cases . . . 86

4.4 Growth rates of δ_Γ for unity density ratio at increasing curvature and compressibility levels. . . . 114

4.5 Growth rates of δ_{99} for variable density cases at $M_c = 0.2$ at weak and strong curvature levels. N/A indicates the data is not available for this case. 117

5.1 Modifications for compressibility (CC) and rotation/curvature (RC) effects to standard models considered in this chapter. 141

List of Figures

1.1 Concept vehicles with exhibiting plumes with streamwise curvature. 2

2.1 Schematic of computational domain for a temporally evolving shear layer. 12
2.2 Mass averaged transverse velocity, transverse mass flux, and mean pressure profiles over the full computational domain. Line opacity indicates time history, such that the faintest lines occur earlier in simulation time and more opaque lines occur later in simulation time. 14
2.3 Energy spectra in streamwise and spanwise directions along the shear layer centerline at $M_c = 0.2, s_\rho = 1$ near the end of simulation time ($\delta_\theta(t)/\delta_\theta(0) \approx 3.0$). 16
2.4 Two point correlations of velocity components in the streamwise (left) and spanwise (right) directions near the end of simulation time ($\delta_\theta(t)/\delta_\theta(0) \approx 3.0$). 17
2.5 Left: normalized mean velocity, density, pressure and temperature profiles. Right: Turbulent stress profiles normalized by $\Delta\bar{u}^2$. 20
2.6 Turbulent mass flux velocities at various compressibility levels. 21
2.7 Growth rates and shear stress with increasing M_c. 22
2.8 Anisotropic invariant map at $\delta/\delta_0 \approx 3$ for $s_\rho = 1$ and increasing compressibility . . . 24
2.9 Centerline slices of the Ducros sensor to indicate regions of compression and dilatation at (from left to right) $M_c = 0.2$, 0.8 and 2.0. 25
2.10 Filter-associated dissipation, resolved dissipation, and total TKE dissipation profiles plotted versus normalized coordinate $\eta = y/\delta_\theta$. 29
2.11 TKE budget and rate of change normalized by global shear layer scales $\delta_{99}/\Delta u^3$ for $M_c = 2.0, s_\rho = 1$. 30
2.12 Pressure strain components and shear productions of TKE, normalized by global shear layer scales $\delta_{99}/\Delta u^3$. Oscillations in the profiles at are due to insufficient averaging. 30

2.13 TKE budget terms normalized by (left) global shear layer scales $\delta_{99}/\Delta u^3$ and by (right) local scales δ_y/U_δ^3. Oscillations in the profiles at $M_c = 0.2$ are due to insufficient averaging. 31
2.14 Instantaneous planar views of transverse velocity $v/\Delta\bar{u}$. Slices at (left) $z = L_z$ and (right) $y = y_c$ at $M_c = 0.2, 0.8$ and 2.0 from top to bottom. Arrows indicate decorrelation length scales based on v' along x and y axes. Note that the domains are truncated for visualization purposes. 35
2.15 Effect of compressibility on (a) normalized decorrelation lengths δ_y/δ_{99} for v' measured about different y_0, (b) mean velocity difference $U_\delta/\Delta\bar{u}$ across the v' decorrelation length, and (c) various Mach numbers. 36
2.16 Autocorrelation profiles for v' measured about different y_0 for (a) $M_c = 0.2$ and (b) $M_c = 2.0$ at the beginning (black) and end (blue) of self similar spreading. Overall mixing layer thickness δ_{99} is indicated in terms of initial thickness δ_θ^o. 36
2.17 (a) Decorrelation ratios and (b) dimensionless shear (Corrsin number). 36
2.18 (a) $|R_{12}|/(\Delta\bar{u})^2$; (b) $|R_{12}|/U_\delta^2$; (c) Integrated $|R_{12}|$ vs. M_c. 37
2.19 Selected TKE budget terms, integrated and scaled with (a) total thickness δ_{99} and total velocity difference $\Delta\bar{u}$ and with (b) internal scales δ_y and U_δ. 38

3.1 Growth rates and stresses for variable density cases compared to previously published results. 48
3.2 Mean density profiles (top), turbulent shear stress (middle) and turbulent Mach number (bottom) profiles. 49
3.3 Mean profiles for the suite of cases analyzed in this work, shown during the approximately self-similar range. Left column: $s_\rho = 1$; right column: $s_\rho = 7$. From top to bottom: $M_c = 0.2, 0.8, 2.0$. 50
3.4 Profiles of streamwise and transverse turbulent mass fluxes and at various compressibility levels for $s_\rho = 1$ (left) and $s_\rho = 7$ (right). 51
3.5 Mean transverse velocity $\tilde{v}/\Delta\bar{u}$ and mean transverse mass flux $\bar{\rho}\bar{v}$ for $s_\rho = 7$. 53
3.6 Contribution to growth rate using different definitions of the centerline, y_c. 55
3.7 Definitions of centerline y_c: (left) centerline positions at two instances in time; (right) centerline position drift in time compared to shear layer bounds at the denser (blue) and lighter (orange) freestreams. Note that density, velocity, and mass fraction profiles have been normalized to range from zero to one. 56
3.8 Transverse velocity decorrelation profiles centered about various y_0 at low and high compressibility levels. 57

3.9 Decorrelation scales centered about various y_0; (a) and (b) decorrelation scale; (c) and (d) decorrelation velocity scale; (e) length scale ratios about the centerline y_c. . 59
3.10 Magnitude profiles of TKE production P, TKE dissipation D, and streamwise component of pressure strain Π_{11} at $s_\rho = 7$. Left column: scaling by $\delta_{99}/\Delta\bar{u}^3$; right column: scaling by δ_y/U_δ^3. 60
3.11 Comparison of density variance profiles across M_c at $s_\rho = 1$ (left) and $s_\rho = 7$ (right) at several snapshots in time. 63
3.12 Profiles of excess mean temperature compared to a reference temperature. 65
3.13 Profiles of mean internal energy budget scaled by U_δ^3 with mean terms in solid lines and turbulent terms in dashed lines. 67

4.1 Computational domain and setup 76
4.2 An annotated view of the grid system used for the present study, decimated in the r and θ directions for visualization. 78
4.3 Reynolds stresses and TKE production at increasing levels of grid resolution for case $\delta_0/r_c = 0.001, M_c = 0.2, u_2/u_1 = 0.4$ and $\rho_2/\rho_1 = 7$. 79
4.4 Several snapshots in time of streamwise (left) and spanwise (right) energy spectra for an unstable, high speed and unity density ratio case ($\delta_0/r_c = 0.001, M_c = 0.2, \rho_2/\rho_1 = 7, u_2/u_1 = 0.4$) along the shear layer centerline during the period of turbulent growth. 80
4.5 Effect of RK4 time step size for case $\delta_0/r_c = 0.01, M_c = 0.8, u_2/u_1 = 0.1$ and $\rho_2/\rho_1 = 7$. 81
4.6 Effect of time integration method for case $\delta_0/r_c = 0.001, M_c = 0.2, u_2/u_1 = 0.4$ and $\rho_2/\rho_1 = 7$. 82
4.7 Autocorrelations of u_r'' for case $\delta_0/r_c = 0.01, M_c = 0.2, u_2/u_1 = 1.9$ and $\rho_2/\rho_1 = 1$ at various points in time. Contour levels vary from 0.1 to 1.0 in increments of 0.1. . 83
4.8 Initial profiles of pressure, density, streamwise velocity, and normalized Eckhoff criterion for selected cases at $\delta_0/r_c = 0.01$, $M_c = 0.8$, and different density ratios. . . . 87
4.9 Effect of initial conditions on growth rates for conditions $\delta/r_c = 0.010, M_c = 0.2, \rho_2/\rho_1 = 1, u_2/u_1 = 0.5$. 88
4.10 Effect of boundary conditions for 2D test case at conditions $\delta/r_c = 0.001, M_c = 0.2, \rho_2/\rho_1 = 1, u_2/u_1 = 1.9$. 88
4.11 Effect of numerical method for convective terms on a test case at conditions $\delta/r_c = 0.010, M_c = 0.8, \rho_2/\rho_1 = 7, u_2/u_1 = 0.1$. 89
4.12 Spanwise velocity fields of stable (top) and unstable (bottom) cases for $M_c = 0.8$ and $\delta_0/r_c = 0.01$. The domain has been truncated in the radial extent for visualization purposes. 90

4.13 Instantaneous normalized streamwise vorticity at contour levels $\omega_\theta \delta_{99}/\Delta u \in [-5, 5]$ along a spanwise $(r - z)$ plane for $u_2 > u_1$ cases. The domain has been truncated for visualization purposes. 92
4.14 Effect of increasing curvature intensity on profiles of streamwise vortex stretching for unstable cases at low and high compressibility, $\rho_2/\rho_1 = 1$ and $u_2 > u_1$. 92
4.15 Instantaneous visualizations of normalized streamwise velocity fluctuations at contour levels $u''_\theta/\Delta u \in [-0.5, 0.5]$ along a streamwise $(\theta - z)$ plane for centrifugally unstable cases at $\rho_2/\rho_1 = 1$ during transitional times. 94
4.16 Instantaneous visualizations of normalized streamwise velocity fluctuations at contour levels $u''_\theta/\Delta u \in [-0.5, 0.5]$ along a streamwise $(\theta - z)$ plane for centrifugally unstable cases at $\rho_2/\rho_1 = 1$. The streamwise extent has been truncated by 50% for visualization purposes. 95
4.17 Mean density profiles $\bar{\rho}(r)$ centered at the innitial radius of curvature, r_c. 98
4.18 Comparison of turbulent stress magnitudes at low speeds and a unity density ratio $(\delta_0/r_c = 0.001, M_c = 0.2, \rho_2/\rho_1 = 1, u_2/u_1 = 0.5)$. 99
4.19 Normalized turbulent shear stress profiles $R_{12}/(\Delta\bar{u}^2)$ for selected cases to show (a) compressibility, (b) variable density, and (c) centrifugal instability effects. 100
4.20 Selected TKE (a,b) and turbulent shear stress (c,d) budget terms normalized by $\delta_{99}(\Delta u)^3$ at moderate curvature $(\delta_0/r_c = 0.01)$ and high compressibility $(M_c = 0.8)$ for two unity and variable density cases. Oscillations present due to averaging window. 103
4.21 Definition of δ_{99} computed from the mean circulation $\tilde{\Gamma}$. 104
4.22 Average growth rates of δ_{99} for selected cases to highlight (a) compressibility, (b) variable density and (c) centrifugal instability effects. 106
4.23 Mean profiles of stable and unstable configurations at $M_c = 0.8$ and $\delta_0/r_c = 0.01$. . 108
4.24 Thickness and growth rate measures for stable and unstable cases at $M_c = 0.8$ and $\delta_0/r_c = 0.01$. Dotted lines indicate the times at which averaging for turbulent statistics begins, which corresponds to approximately a 99% $\delta/\delta_0 = 2.5$. 109
4.25 Evolution of thicknesses and growth rates for stable (top) and unstable (bottom) cases at $M_c = 0.8$. 110
4.26 Evolution of TKE and R_{12} for stable (top) and unstable (bottom) cases at $M_c = 0.8$. 111
4.27 Normalized turbulent mass flux profiles for stable (top) and unstable (bottom) configurations. 112
4.28 Profiles of Ri_f (solid lines) and Φ (dashed lines) for high speed stable (left) and unstable (right) cases with increasing curvature intensity. 113
4.29 Curvature effects on the evolution of the Eckhoff discriminant $\Phi = \frac{1}{\rho}\frac{d\rho}{dr} - \frac{u_\theta^2}{c^2 r}$ at varying compressibility levels for $\rho_2/\rho_1 = 1$ and $u_2 > u_1$. 115

4.30 Turbulent stress anisotropy maps for cases at $M_c = 0.2$ (top) and $M_c = 0.8$ (bottom) and $\rho_2/\rho_1 = 1$ for centrifugally stable (left) and unstable (right) configurations. . . 116
4.31 Thickness evolution for variable density cases at $\delta_0/r_c = 0.01$ and $M_c = 0.2$ 117
4.32 Normalized shear stress profiles corresponding to Fig. 4.31 118
4.33 Curvature effects on the evolution of the stability criterion profiles at varying density ratios ρ_2/ρ_1 of 1/7 (blue), 1 (orange), and 7 (green); Ri_f defined in Eqn. 4.6. . . . 122
4.34 Normalized growth rates compared to stability criterion corresponding to Fig. 4.33 (at $M_c = 0.2$). Similarly to Fig. 4.33, colors of blue, orange and green represent density ratios of $\rho_2/\rho_1 = 1/7, 1$ and 7, respectively. The square markers correspond to cases with weak curvature, and the circle markers correspond to cases with stronger curvature. Finally, the top or bottom fill of the marker indicates the velocity ratio, with top-filled markers indicating $u_2 < u_1$ and vice versa for bottom-filled markers. . 123
4.35 Turbulent stress anisotropy maps for cases at moderate curvature $\delta_0/r_c = 0.01$, $M_c = 0.2$ and $\rho_2/\rho_1 = 1/7, 1, 7$ (top to bottom). 124
4.36 Spanwise component of baroclinic torque for cases at moderate curvature $\delta_0/r_c = 0.01$, $M_c = 0.2$ and $\rho_2/\rho_1 = 1/7, 1, 7$. 125
4.37 Normalized spanwise vorticity $\omega_z\delta_{99}/\Delta u$ for cases at moderate curvature $\delta_0/r_c = 0.01$, $M_c = 0.2, u_2 > u_1$ and $\rho_2/\rho_1 = 1/7, 1, 7$ (top to bottom). 126

5.1 Streamwise pressure strain component compared to M_t-based scaling models: (a) profiles with increasing M_c at $s_\rho = 1$ from *PadeOps* data; (b) trend in integrated profiles compared to models by Pantano and Sarkar [103] and Fujiwara et al. [48]. . 138
5.2 Turbulent mass fluxes and comparison to model by Dussauge and Quine [39] in dashed lines. 139
5.3 Comparison of TKE profiles of curved shear layers at $M_c = 0.8$ with low and high curvature levels for $\rho_2/\rho_1 = 1$, eddy-resolved data labelled as 'LES'. 143
5.4 Comparison of TKE profiles of curved shear layers at $M_c = 0.8$ with low and high curvature levels for $\rho_2/\rho_1 \neq 1$, eddy-resolved data labelled as 'LES'. 144
5.5 Collapse of mean profiles using SA model at $\delta_0/r_c = 0.001$ and $M_c = 0.8$. 146
5.6 Effect of compressibility corrections on growth rates compared to eddy-resolved data (labelled 'LES') for $\delta_0/r_c = 0.001$ and $\rho_2/\rho_1 = 1$. 146
5.7 Peak turbulent Mach number values with increasing M_c. 147

A.1 Transverse velocity field before (top) and after (bottom) windowing and filtering for $M_c = 0.8, s_\rho = 7$ 153

A.2 Instantaneous variances of transverse velocity, pressure and density before and after windowing and filtering for $M_c = 0.8, s_\rho = 7$ . . . 153

B.2 Slices of u_r at $\delta/\delta_0 = 2.5$ and $\delta_0/R_0 = 0.001, M_c = 0.2$ . . . 155
B.3 Slices of u_r at $\delta/\delta_0 = 2.5$ and $\delta_0/R_0 = 0.001, M_c = 0.8$ . . . 156
B.4 Slices of u_r at $\delta/\delta_0 = 2.5$ and $\delta_0/R_0 = 0.010, M_c = 0.2$ . . . 157
B.5 Slices of u_r at $\delta/\delta_0 = 2.5$ and $\delta_0/R_0 = 0.010, M_c = 0.8$ . . . 158
B.6 Initial profiles of pressure, density, streamwise velocity, and normalized Eckhoff criterion for cases at (top row) $\delta_0/r_c = 0.001$ and $M_c = 0.2$; (middle row) $\delta_0/r_c = 0.010$ and $M_c = 0.2$; (bottom row) $\delta_0/r_c = 0.001$ and $M_c = 0.8$. . . . 160
B.7 Normalized mean circulation profiles $(\tilde{\Gamma} - \Gamma_{min})/(\Gamma_{max} - \Gamma_{min})$ . . . 161
B.8 Mean streamwise velocity $\tilde{u}_\theta$ . . . 162
B.9 Mean pressure $\bar{p}$ . . . 163
B.10 Mean temperature $\bar{T}$ . . . 164
B.11 Mean momentum $\bar{\rho}\tilde{u}_\theta$ . . . 165
B.12 Normalized magnitude of R_{12}: $|\sqrt{\overline{\rho u_\theta'' u_r''}/\bar{\rho}\Delta\bar{u}^2}|$ . . . 166
B.13 Normalized magnitude of R_{11}: $|\sqrt{\overline{\rho u_\theta'' u_\theta''}/\bar{\rho}\Delta\bar{u}^2}|$ . . . 167
B.14 Normalized magnitude of R_{22}: $|\sqrt{\overline{\rho u_r'' u_r''}/\bar{\rho}\Delta\bar{u}^2}|$ . . . 168
B.15 Normalized magnitude of R_{33}: $|\sqrt{\overline{\rho u_z'' u_z''}/\bar{\rho}\Delta\bar{u}^2}|$ . . . 169
B.16 Normalized turbulent shear stress profiles: $R_{12}/(\Delta\bar{u}^2) = \overline{\rho u_\theta'' u_r''}/(\bar{\rho}\Delta\bar{u}^2)$ . . . 170
B.17 Anisotropy component b_{12} . . . 171
B.18 Anisotropy component b_{11} . . . 172
B.19 Anisotropy component b_{22} . . . 173
B.20 Anisotropy component b_{33} . . . 174
B.21 Normalized streamwise turbulent mass flux $\overline{\rho' u_\theta'}/(\bar{\rho}\Delta\bar{u})$ . . . 175
B.22 Normalized radial turbulent mass flux $\overline{\rho' u_r'}/(\bar{\rho}\Delta\bar{u})$ . . . 176
B.23 Baroclinic torque acting on spanwise vorticity . . . 177

Chapter 1

Introduction

1.1 Motivation

Many aerospace applications involve high-speed jet plumes that are influenced by multiple complex turbulence mechanisms. A deeper understanding of turbulence in these flows is paramount to improving computational fluid dynamics (CFD) analyses applied to vehicle design and safety evaluation. The Orion Launch Abort Vehicle and Mars lander concept vehicles, depicted in Fig. 1.1, are examples of present and future vehicles whose aerodynamics are strongly affected by rocket plumes. The full dynamics of the flow field associated with these flows can be described using the Navier-Stokes equations, but conducting simulations with eddy-resolving methods (such as large eddy simulations (LES) or direct numerical simulations (DNS)) are extremely computationally expensive. Typical production simulations of these vehicles and similar configurations are conducted using more cost effective methods, such as Reynolds-averaged Navier-Stokes (RANS) simulations, which resolve the mean flow field and use models for turbulent quantities. Improvements in the understanding of turbulence mechanisms, and in the accuracy of lower order models used in CFD, are needed for these flows. These are two separate challenges. The present work addresses the challenge of characterizing the behavior of turbulence in retropropulsive jet plumes by providing turbulence data to assist the current understanding of turbulence physics and to enable the improvement of current lower order models. The work described here is the first of several steps that will be needed to improve the accuracy of CFD for these advanced aerospace concepts.

Several aspects of complex turbulence in plumes have been documented, and a few notable studies will be briefly higlighted. Early experiments by Kamotani and Greber [61] indicated that velocity and temperature fluctuations in circular turbulent jets, both heated and unheated, are mainly determined by momentum ratios and weakly dependent on density ratio. In the past decade,

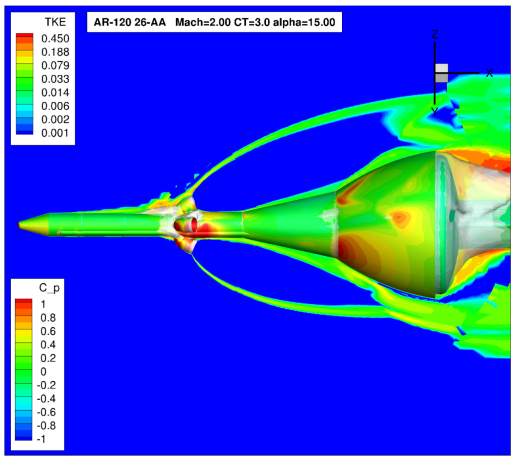

(a) The Orion Launch Abort Vehicle with a curved plume shear layer highlighted by green TKE contours [27].

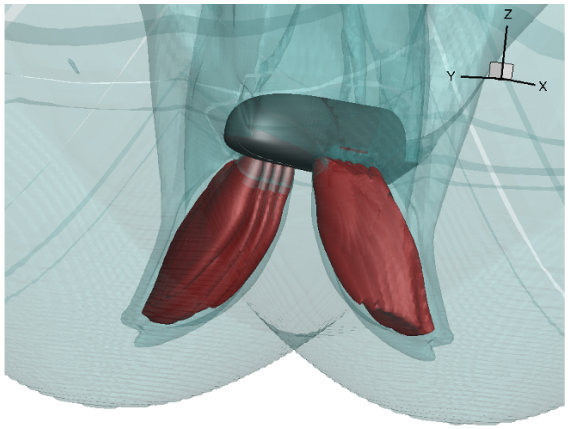

(b) The CobraMRV, a mid lift-to-drag concept vehicle for Mars descent, under supersonic retropropulsive conditions [87].

Figure 1.1: Concept vehicles with exhibiting plumes with streamwise curvature.

Bridges and Wernet [17, 18] published a thorough overview of turbulence statistics from various experiments on hot, subsonic jets with the purpose of improving aero-acoustic predictions. Jets in crossflow are another application in which the shear layers exhibit strong streamwise curvature. Recently, Nair et al. [95] performed experiments to explore the formation of vortical structures in a reacting jet in crossflow. Jet momentum flux ratios and crossflow density ratios were independently varied, and it was observed that the growth rate of shear layer vorticies depended mainly on the momentum flux ratio and heat release effects. Several high fidelity computational studies of jets in crossflow have also been carried out using a variety of numerical methods [63, 5, 71]. Another numerical study specifically focused on the shear layers present in low speed jets in cross flow was conducted by Iyer and Mahesh [56], where the authors observed that the jets' shear layer instability and other characteristics were significantly altered by the jet mixing velocity ratio and the jet exit profile. Regan and Mahesh [110] also studied the global linear stability of low speed jets in crossflow, and observed that upstream or downstream travelling shear layer instabilities dominate jet dynamics depending on the jet velocity ratio. These studies helped establish a solid foundation to emphasize the importance of shear layers in jet plume dynamics. Despite this progress, the present understanding of turbulent mixing in the shear layers of rocket-motor exhaust plumes remains deficient in many respects. Most prior simulation studies focused on turbulent mixing have been limited to a single turbulence mechanism, for example, compressibility or density gradient effects. Limited work has been pursued at the intersection of multiple turbulence mechanisms. The aim of

this work is to bridge this gap in knowledge by examining the behavior of turbulent shear layers and systematically adding levels of complexity in the form of compressibility, variable density, and streamwise curvature effects.

1.2 Outline

In this work, several suites of high resolution simulations of turbulent shear layers are run and observations on turbulent shear layer growth rates, stresses, anisotropy, and other statistics are presented. All of the simulations conducted are of temporally developing shear layers. In Chapter 2, the effect of compressibility on turbulent shear layers with unity density ratio and zero streamwise curvature is investigated. A new turbulent length and velocity scale inspired by a sonic eddy hypothesis is introduced and shown to scale turbulent stresses and key terms in the evolution of TKE. Chapter 3 focuses on variable density effect on the characteristics of turbulent mixing, again without the effects of streamwise curvature. Trends with increasing compressibility and the importance of mixing layer asymmetry are identified. Chapter 4 presents data and observations for shear layers which include streamwise curvature effects. The combined effects of compressibility and streamwise curvature are presented, followed by the combined effects of density variation and streamwise curvature. The performance of RANS models commonly used in industry for high speed turbulent flows is presented in Chapter 5. The changes to model predictions of turbulent growth rates and TKE levels resulting from modifications for compressibility and streamwise curvature effects are evaluated. Finally, conclusions for each section of this work and some avenues of future research are summarized in Chapter 7.

1.3 Highlights

Key contributions of this work and the corresponding chapters are given below.

- Under highly compressible conditions, turbulent length scales which are 'internally regulated' by acoustic communication and reduce significantly as a fraction of the overall shear layer thickness are proposed (Ch. 2)
- Dilatational velocities and pressure-dilatation magnitudes are determined to remain small even at high convective Mach numbers (Ch. 2)
- Shear layer centerlines and turbulent stresses in variable density shear layers are biased towards the less-dense freestream, which reduces the turbulent mixing of the mean momentum profile and corresponding growth rates (Ch. 3)

- Internal regulation is also identified under variable density conditions; profiles of TKE production, dissipation and pressure strain are collapsed using 'effective' eddy scales (Ch. 3)
- A database of temporally developing mixing layers at two compressibility levels, three curvature levels and three density ratios is presented (Ch. 4)
- In the present parameter space, compressibility and stabilizing curvature have comparable effects on growth rates; the shear layer density ratio dominates observed growth rates when streamwise curvature is significant (Ch. 4)
- Discrepancies in growth rate data between eddy-resolved simulations and RANS simulations with dilatation-based compressibility modifications are identified (Ch. 5)
- Reduced accuracy in SA and SST model predictions of TKE under curved conditions, even with the inclusion of compressibility and curvature modifications, is demonstrated (Ch. 5)

Chapter 2

Compressibility effects on turbulent shear layers

2.1 Introduction

The mixing process between two co-flowing streams at different velocities, densities and temperatures has remained of fundamental interest in the turbulence physics community. The applications motivating the study of this flow include the acoustics in jet noise, the internal flow of fuel and air mixtures in air-breathing vehicles, and the external flow and associated loads on a variety of aerospace vehicles. This chapter includes a selective review of the literature pertinent to compressible turbulent mixing.

It is well known that flow compressibility has a stabilizing effect on turbulence. In compressible mixing layers, an obvious effect of compressibility in free shear flows manifests as a suppressed growth rate; this has been demonstrated numerous times in both experiment and scale resolving calculations, like direct numerical simulations (DNS). For the shear layer between two freestream flows, denoted with subscripts 1 and 2, common governing parameters include the velocity ratio u_1/u_2 and the density ratio ρ_1/ρ_2. The velocity difference Δu and the shear layer thickness δ, which has numerous definitions, are used as the characteristic velocity and length scale to define various dimensionless numbers and compressibility measures. The most common compressibility metric for shear layers is the convective Mach number:

$$M_c = \frac{\Delta u}{c_1 + c_2} \tag{2.1}$$

where c_1 and c_2 represent the speed of sound in each freestream. This Mach number gives the ratio of shearing to acoustic communication as seen by eddies advected in the mixing region. The effects of various freestream property ratios have been extensively documented in both experimental and numerical studies over the past several decades.

Previous studies

In the landmark experiments of helium and nitrogen shear layers by Brown and Roshko [19], advected eddies forming large scale structures in the mixing region were observed. Brown and Roshko concluded that shear layer growth rates were effected more by compressibility than by variable density effects. Other studies also observed large scale structures and vortex pairing in compressible shear layers. Chinzei et al. [28] reported large scale structures in supersonic shear layers and correlated spreading rates with the freestream velocity ratio and a characteristic Mach number defined with the velocity difference across the shear layer. Dimotakis [36] used the available experimental data to propose functions for entrainment ratios and growth rates dependent on velocity and density ratios by considering vortex convection velocities. This dependence gives the convection speed as $U_c = (1 + rs^{1/2})/(1 + s^{1/2})$, where r is the freestream velocity ratio and s is the freestream density ratio. This form of U_c is the same as the mean speed for equal densities, and predicts that a heavy, high speed fluid will 'drag' mixed vorticies along. For unity density ratio cases, the growth rate was derived as $\delta/x \sim (1 - r)/(1 + r)$. Papamoschou and Roshko [105] performed experiments at up to $M_c = 1.9$ and observed growth rate reduction beginning in the subsonic M_{c1} range, and also analyzed that perturbations within a vortex sheet decay away from the sheet at a rate dependent on M_{c1}. Large scale amalgamation was not observed in these experiments. Like Chinzei et al. [28], the authors note that for the same density and velocity ratio, the supersonic shear layer still exhibited lower growth rates compared to the incompressible shear layer. Elliott and Samimy [43] compared turbulent shear layers at intermediate convective Mach numbers (at M_c of 0.5,0.64, and 0.81) and also did not observe dominance by coherent large scale structures with increasing compressibility. The authors report profiles for skewness and flatness to indicate turbulence intermittency at the shear layer edges, which they believed contributed to growth rate reduction. Goebel and Dutton [49] studied shear layers characterized by the relative Mach number $M_r = \Delta u/\bar{c}$, instead of M_c, citing the lack of stagnation pressure balance and isentropic stagnation point in high speed layers which lack large scale vortex pairing. Supersonic shear layer experiments by Hall et al. [52] suggested that growth rates are relatively insensitive to incident shock and expansion waves impinging on the shear layer. Debisschop and Bonnet [34] used laser anemometry to provide more detailed measurements of mean and fluctuating velocity fields at intermediate compressibility levels ranging from $M_c = 0.52$ to $M_c = 0.64$. A similar lack of large scale structures as Elliott and Samimy

[43] was observed. Skewness of streamwise velocity fluctuations was noted to be much larger in the subsonic regime, compared to Wygnanski and Fiedler [140], with positive skewness implying a higher occurrence of fluctuations greater than the mean velocity. Slessor et al. [120] considered compressibility as a means of conversion between kinetic and thermal energy and used previous experimental data to proposed a new compressibility measure. The authors argue a central issue is that the convective velocity used for convective Mach numbers, U_c, is not defined uniquely among different experiments, and show that the parameter $\Pi_c = \max(\sqrt{\gamma_i - 1}/a_i)\Delta u$ provides a better collapse of shear layer growth rates. Rossmann et al. [113] studied highly compressible mixing layers with up to $M_c = 2.25$ and noted that the flow appeared to be more dominated by elongated, streamwise vorticies compared to observations by Papamoschou and Roshko [105]. Structures in the high speed case at $M_c = 1.7$ appeared to have inefficient internal mixing but rapid entrainment. Urban and Mungal's measurements of two-component velocity fields at $M_c = 0.25, 0.63$ and 0.73 also indicated reduced transverse communication in the mixing layer. These observations by Rossmann et al. [113] and Urban and Mungal [133] are consistent with the 'sonic eddy' hypothesis by Breidenthal [15] and Day et al. [33]'s co-layer concept, which will be revisited later in this chapter. Most recently, experiments by Kim et al. [65] indicated that streamwise anisotropy increasing, transverse and spanwise normal stress anisotropies decreasing, and the shear anisotropy remaining constant. Mapping the invariants of the Reynolds stress anisotropy tensor indicated that the turbulent motions become increasingly dominated by the streamwise component of velocity as compressibility increased. Anisotropy mapping for the present data will also be presented later in this chapter.

In addition to a multitude of linear stability analyses on modal perturbations in shear layers, pioneering simulations of eddy structures in mixing layers were pursued in parallel with early experimental studies. Early high fidelity calculations focused on vortex dynamics in the shear layer. Lele [74] detailed vortex roll up and pairing and the associated acoustic radiation from these phenomena in both temporal and spatial shear layers. Sandham and Reynolds [114] studied the three dimensional instabilities in temporal mixing layers at high Mach numbers and the resulting large scale structures, and confirmed the dominance of oblique instability waves with increasing compressibility. Papamoschou and Lele [104] studied the simplified configuration of a single vortex and the associated disturbance field in a compressible mixing layer, and concluded vortex communication in the mean flow direction is strongly inhibited at high M_c. Several early calculations of fully turbulent shear layers pursued self similarity with varying success. Rogers and Moser [112]'s DNS of incompressible mixing layers were initialized with turbulent boundary layers and exhibited self similarity in mean profiles and linear growth rates, but did not show organized pairing of large scale structures. Vreman et al. [135] produced shear layer DNS at compressibility levels ranging from $M_c = 0.2$ to $M_c = 1.2$ and showed a collapse of mean and turbulent stress profiles, but asserted that

the results are not fully self-similar. From this study, it was observed that the pressure dilatation and dilatational contribution to dissipation were not significant. Instead, Vreman's analysis of the integrated TKE and Reynolds stress evolution equations demonstrated that reduced pressure fluctuations and the pressure strain term were responsible for observed growth rate reductions. Freund et al. [47] performed DNS of a temporally developing, annular shear layer and observed similar characteristics of Vreman et al.'s planar shear layers. The annular shear layers indicated a decrease in transverse (radial) length scale and demonstrated an alternative scaling using the mean velocity difference across this large eddy length scale, rather than the total velocity difference Δu. Vreman et al.'s observations on the reduction of the pressure strain correlation were also supported by temporally developing shear layers by Pantano and Sarkar [103] across a similar M_c range. Pantano and Sarkar [103] argued that the finite speed of sound in compressible flows introduces a finite time delay in communication and thus increases decorrelation between pressure and velocity fluctuations. While many early DNS of the turbulent shear layer were for the temporal configuration, Lui and Lele [82] performed calculation of spatially developing shear layers at $M_c = 0.4$ and $M_c = 0.6$. Although the calculations showed linear growth rates and collapsed profiles, the observations on the TKE budget indicated that a fully self similar state was not achieved.

Flow development prior to the self similar stage has also been an active area of research. Vortex roll up and pairing studies were conducted by Lele [74] and Sandham and Reynolds [114], and more recently Kourta and Sauvage [69] provided DNS of temporal supersonic mixing layers at $M_c = 1.2$ and $M_c = 1.6$ with a focus on Λ structures during transition and the character of shocklets in the flow. Similar transition characteristics were also observed in the spatial shear layer DNS by Zhou et al. [146] at $M_c = 0.6$ and by Zhang et al. [145] at M_c's ranging from 0.4 to 1.

Several numerical studies have also provided both statistical and structural insight into the finer scales of turbulent structures in the compressible mixing layer. Vaghefi and Madnia [134] studied the topology and dissipating behavior at the turbulent/non-turbulent interface on temporally developing shear layers with M_c ranging from 0.2 to 1.8, and observed that distribution of flow topologies differs in the turbulent region compared to the mixing layer boundary. Jahanbakhshi and Madnia [58] also focused on the turbulent/non-turbulent region of the shear layer, specifically characterizing the entrainment processes at the interface as 'nibbling' with vorticity diffusion and 'engulfing' of external, irrotational fluid. At higher M_c, the probability of highly concave or convex features at the interface decreases, reducing the average entrained mass flux across the interface and the growth rate into the freestream flow. Arun et al. [3] similarly examined the streamline topology in shear layers with $M_c \geq 1.2$, and conclude that shear-dominated topologies show more effective energy redistribution via pressure strain correlation. However, the proportion of vortex-dominated topologies was found to increases with increasing M_c, which offers a new explanation for previous observations of the reduction in the pressure strain correlation. The study observed that vortices

are more aligned in the streamwise direction at higher M_c, but gradually shift to more spanwise angles with progress in time. Arun's data indicated approximate but not perfect self-similarity. Lastly, Li et al. [76] studied spatially developing shear layers at $M_c = 0.3, 0.5, 0.7$ using DNS and specifically focused on energy exchange mechanisms in the transitional and early turbulent regions.

Breidenthal [15]'s sonic eddy hypothesis assumes that supersonic eddies are 'completely impotent' at entrainment because they rotate more quickly than information can propagate across them, and thus only eddies with a subsonic rotational Mach numbers can directly engulf fluid. As a result, at high speeds, it is hypothesized that increasingly smaller eddies are responsible for shear layer growth. A related concept on the role of smaller vorticies was proposed later by Day et al. [33]. From linear stability analysis, Day identified 'co-layer' conditions in which the mixing layer is formed by two sets of vorticies, instead of a roll-up by a single vortex. These two concepts about communication and the relationship between pressure fluctuations and responding velocity fluctuations form the backbone of this work on compressibility effects.

Present objectives

The present work aims to characterize the asymptotic effects of compressibility on the structure and scales of turbulence in the high Mach number regime. High resolution simulations of temporally developing, compressible mixing layers without density gradients are conducted across a range compressibility levels which span convective Mach numbers of $M_c = [0.2, 0.4, 0.8, 1.2, 1.6, 2.0]$. Results on shear layer growth rates and turbulent stresses are first validated against previously published experimental and data. Further analysis of results in the self-similar regime provides insights into turbulent structures in this comprehensive parameter space. At high M_c, the energy-containing eddies do not span the entire shear layer thickness. Their spatial scale and intensity appear to be internally regulated and suggest an alternative scaling for the Reynolds stresses, turbulence budgets and growth rates. This chapter focuses on this evidence and the internal scaling defined by the *effective velocity difference* seen by the eddies. The results are interpreted in relation to the 'multi-layered' mixing proposed by [106] and [33], and the 'sonic eddy hypothesis' by [15]. Finally, we propose a scaling of terms in the turbulent kinetic energy (TKE) budget and Reynolds stresses using the effective velocity difference across eddy decorrelation scales.

Table 2.1: Comparison to previously published high resolution simulations of temporal shear layers: initial and final Reynolds numbers based on momentum and vorticity thicknesses, and final values of the Kolmogorov scale η compared to the grid resolution.

Study	M_c	s_ρ	$[L_x, L_y, L_z]$	$[N_x, N_y, N_z]$	$[\Delta_x, \Delta_y, \Delta_z]$	$Re_{\theta,0}$	Re_θ	$Re_{\omega,0}$	Re_ω	$\eta/\Delta x$
Moser (1993) [93]	0.00	1.0	125 , ∞ , 31.25	512 , 210 , 192	0.244 , , 0.163	800	2,420	1,370	10,800	
Vreman (1996) [135]	0.20	1.0	59 , 59 , 59	192 , 193 , 192	0.307 , 0.306 , 0.307	50	338	200		
	0.60	1.0	68 , 59 , 68	192 , 193 , 192	0.354 , 0.306 , 0.354	50	275	200		
	0.80	1.0	26.7 , 60 , 26.7	144 , 221 , 160	0.185 , 0.271 , 0.167	140	840	560		
	1.20	1.0	39.9 , 59 , 22.1	320 , 513 , 192	0.125 , 0.115 , 0.115	100	675	400		
Pantano (2002) [103]	0.30	1.0	345 , 172 , 86	512 , 256 , 128	0.674 , 0.672 , 0.672	160	1,520	640	10,026	0.340
	0.70	1.0	172 , 129 , 86	256 , 192 , 128	0.672 , 0.672 , 0.672	160	1,360	640	7,790	0.330
	0.70	2.0	172 , 129 , 86	256 , 192 , 128	0.672 , 0.672 , 0.672	160		640	8,590	0.330
	0.70	4.0	172 , 129 , 86	256 , 192 , 128	0.672 , 0.672 , 0.672	160		640	8,330	0.300
	0.70	8.0	172 , 129 , 86	256 , 192 , 128	0.672 , 0.672 , 0.672	160		640	7,404	0.260
	1.10	1.0	345 , 172 , 86	512 , 256 , 128	0.674 , 0.672 , 0.672	160	1,760	640	13,640	0.380
Kourta (2002) [69]	1.20	1.0	40.14 , 30 , 22.9	385 , 257 , 193	0.104 , 0.117 , 0.119	150		600		
	1.60	1.0	29.91 , 30 , 11.91	253 , 513 , 193	0.118 , 0.058 , 0.062	200		800		
Fortune (2004) [46]	0.08	2.0	30.64 , 60 , 30.64	150 , 257 , 150	0.204 , 0.122 , 0.204	100		400		
	0.10	1.0	30.64 , 60 , 30.64	150 , 257 , 150	0.204 , 0.122 , 0.204	100		400		
	0.33	2.0	30.64 , 60 , 30.64	150 , 257 , 150	0.204 , 0.122 , 0.204	100		400		
	0.40	1.0	30.64 , 60 , 30.64	150 , 257 , 150	0.204 , 0.122 , 0.204	100		400		
Kleinman (2008) [67]	0.90	1.0	2000 , 2000 , 750	340 , 213 , 84	5.882 , 4.680 , 8.929	35	233	14		
	0.90	1.0	2000 , 2000 , 750	680 , 425 , 168	2.941 , 2.340 , 4.464	69	485	28		
	0.90	1.0	2000 , 2000 , 750	2050 , 1251 , 512	0.976 , 0.790 , 1.465	207	1,442	83		
	0.90	1.0	2000 , 2000 , 750	2050 , 1251 , 512	0.976 , 0.790 , 1.465	414	2,848	166		
Buchta (2014) [21]	0.75	1.0	120 , 200 , 80	1536 , 2048 , 512	0.078 , 0.098 , 0.156	60	1,970			
	1.25	1.0	120 , 200 , 80	1536 , 2048 , 512	0.078 , 0.098 , 0.156	60	1,970			
	1.75	1.0	120 , 200 , 80	1536 , 2048 , 512	0.078 , 0.098 , 0.156	60	1,970			
Vaghefi (2015) [134]	0.20	1.0	300 , 150 , 100	1261 , 631 , 421	0.238 , 0.238 , 0.238		0	0	12,060	0.772
	0.80	1.0	250 , 180 , 100	1051 , 757 , 421	0.238 , 0.238 , 0.238		0	0	13,590	0.981
	1.20	1.0	300 , 250 , 100	1261 , 1051 , 421	0.238 , 0.238 , 0.238		0	0	15,340	1.112
	1.80	1.0	300 , 250 , 100	1261 , 1051 , 421	0.238 , 0.238 , 0.238		0	0	16,800	1.322
Almagro (2017) [2]	0.00	1.0	461 , 368 , 173	1536 , 851 , 576	0.300 , 0.200 , 0.300	160	1,313	640	6,300	0.625
	0.00	2.0	461 , 368 , 173	1536 , 851 , 576	0.300 , 0.200 , 0.300	160	1,115	640	5,800	0.667
	0.00	4.0	461 , 368 , 173	1536 , 851 , 576	0.300 , 0.200 , 0.300	160	1,066	640	6,500	0.769
	0.00	8.0	461 , 368 , 173	1536 , 851 , 576	0.300 , 0.200 , 0.300	160	909	640	7,000	1.111
Buchta (2017) [20]	0.45	1.0	1536 , 1600 , 512	1536 , 1601 , 512	1.000 , 0.999 , 1.000	60	2,100			
	0.75	1.0	1536 , 1600 , 512	1536 , 1601 , 512	1.000 , 0.999 , 1.000	60	2,100			
	1.25	1.0	1536 , 1600 , 512	1536 , 1601 , 512	1.000 , 0.999 , 1.000	60	2,100			
	1.75	1.0	1536 , 1600 , 512	1536 , 1601 , 512	1.000 , 0.999 , 1.000	60	2,100			
Arun (2019) [3]	0.20	1.0	314 , 147 , 79	512 , 256 , 128	0.614 , 0.575 , 0.614	160	1,760	640	8,495	0.415
	0.50	1.0	314 , 147 , 79	512 , 256 , 128	0.614 , 0.575 , 0.614	160	2,000	640	8,273	0.418
	0.75	1.0	314 , 147 , 79	512 , 256 , 128	0.614 , 0.575 , 0.614	160	1,920	640	8,160	0.441
	0.90	1.0	314 , 147 , 79	512 , 256 , 128	0.614 , 0.575 , 0.614	160	2,080	640	9,544	0.442
	1.20	1.0	314 , 147 , 79	512 , 256 , 128	0.614 , 0.575 , 0.614	160	2,160	640	11,112	0.465
Matsuno (2020) [84]	0.20	1.0	150 , 200 , 75	1024 , 1448 , 512	0.146 , 0.138 , 0.146	1,000	2,870	4,000	11,793	0.573
	0.20	7.0	150 , 200 , 75	1024 , 1448 , 512	0.146 , 0.138 , 0.146	1,000	2,328	4,000	14,830	0.993
	0.40	1.0	150 , 200 , 75	1024 , 1448 , 512	0.146 , 0.138 , 0.146	1,000	6,238	4,000	29,079	0.397
	0.80	1.0	100 , 125 , 50	1024 , 1448 , 512	0.098 , 0.086 , 0.098	1,000	7,259	4,000	36,291	0.332
	0.80	7.0	100 , 125 , 50	1024 , 1448 , 512	0.098 , 0.086 , 0.098	1,000	6,913	4,000	44,853	0.615
	1.20	1.0	100 , 100 , 50	1024 , 1448 , 512	0.098 , 0.069 , 0.098	1,000	9,895	4,000	48,332	0.356
	1.60	1.0	80 , 80 , 40	1024 , 1448 , 512	0.078 , 0.055 , 0.078	1,000	13,316	4,000	65,328	0.425
	2.00	1.0	80 , 80 , 40	1024 , 1448 , 512	0.078 , 0.055 , 0.078	1,000	16,933	4,000	87,493	0.409
	2.00	7.0	80 , 80 , 40	1024 , 1448 , 512	0.078 , 0.055 , 0.078	1,000	12,043	4,000	116,951	0.582

2.2 Methodology

2.2.1 Governing equations

The Navier-Stokes equations for compressible flow were solved in conservative form on a uniform, Eulerian grid.

$$\frac{\partial \rho}{\partial t} + \frac{\partial}{\partial x_i}(\rho u_i) = 0 \tag{2.2}$$

$$\frac{\partial \rho u_i}{\partial t} + \frac{\partial}{\partial x_i}(\rho u_i u_j) = \frac{\partial p}{\partial x_i} + \frac{\partial \tau_{ij}}{\partial x_j} \tag{2.3}$$

$$\frac{\partial \rho E}{\partial t} + \frac{\partial}{\partial x_i}\left[u_i(\rho E + p)\right] = \frac{\partial}{\partial x_i}(\tau_{ij} u_j - q_i) \tag{2.4}$$

In Eqn. 2.2-2.4 above, E is the total energy, τ_{ij} is the viscous stress tensor, and q_i is the component of Fourier heat conduction, defined below.

$$E = \frac{p}{\rho(\gamma - 1)} + \frac{1}{2} u_i u_i$$

$$\tau_{ij} = 2\mu \left(S_{ij} - \frac{1}{3} \frac{\partial u_k}{\partial x_k} \delta_{ij} \right)$$

$$S_{ij} = \frac{1}{2} \left(\frac{\partial u_i}{\partial x_j} + \frac{\partial u_j}{\partial x_i} \right)$$

$$q_i = -\kappa \frac{\partial T}{\partial x_i}$$

Each of the freestreams (denoted 1 and 2) has a constant $\gamma_1 = \gamma_2 = \gamma = 1.4$ and nondimensional gas constants $R_1 = R_2 = R_u$, where R_u is the universal gas constant. The equations are closed by the ideal gas equation of state:

$$p = \rho R T$$

The present chapter focuses on shear layers without density variations; the multi-species formulation will be detailed in Ch. 3.

2.2.2 Initial conditions

For the temporally growing mixing layer, the domain is periodic in the streamwise ($x \in [0, L_x]$) and spanwise ($z \in [0, L_z]$) directions. Upper and lower freestream constants are denoted 1 and 2, respectively. The typical velocity and length scales are the difference in freestream velocities

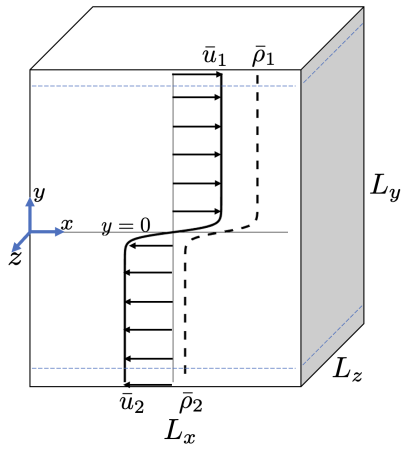

Figure 2.1: Schematic of computational domain for a temporally evolving shear layer.

$\Delta\bar{u} = \bar{u}_1 - \bar{u}_2$ and the initial momentum thickness $\delta_\theta(0)$, where the momentum thickness is defined as a transverse integral over the computational domain ($y \in [{}^{-L_y}/_2, {}^{L_y}/_2]$):

$$\delta_\theta(t) = \frac{1}{\rho_0(\Delta\bar{u})^2}\int_{-L_y/2}^{L_y/2} \bar{\rho}\left(\tfrac{1}{2}\Delta\bar{u} - \tilde{u}_1\right)\left(\tfrac{1}{2}\Delta u + \tilde{u}_1\right) dy \tag{2.5}$$

The shear layer can also be characterized by the 99% thickness based off the mean velocity profile:

$$\frac{\bar{u}(y_+)}{\Delta u/2} = 0.99 \qquad \frac{\bar{u}(y_-)}{\Delta u/2} = -0.99 \qquad \delta_{99} = y_+ - y_- \tag{2.6}$$

The base flow fields are initialized with a hyperbolic tangent profile for the streamwise velocity, as given in Eqn. 2.7. The upper freestream has a velocity of $\Delta u/2$ and the lower freestream has a velocity of $-\Delta u/2$. All other mean velocity components are set to zero. The density and pressure are set to a uniform value of $\rho_0 = 1$ and $p_0 = 1$.

$$\bar{u}(y) = \frac{\Delta\bar{u}}{2}\tanh\left(\frac{y}{2\delta_0}\right) \tag{2.7}$$

Following the initialization of this flow as detailed by Kleinman and Freund, several modal perturbations (with random phases α, β in the streamwise and spanwise direction) on velocity components are imposed on the mean flow. These perturbations have a velocity potential specified

below and evolve into turbulence after an initial period of nonlinear growth. No perturbations to density, pressure, or temperature were applied.

$$\phi(x,y,z) = \sum_{i,j}^{m} \frac{0.15}{4\pi^2 k_x k_z} \cos(k_x x + \alpha_i)\cos(k_z z + \beta_i) g(\xi)$$
$$g(\xi) = e^{-5\xi^2} \left[\sin(\xi) + 10\xi\cos(\xi)\right]$$

Cases at $M_c > 0.8$ were initialized using the turbulent velocity fluctuations from the case at $M_c = 0.2$ to reduce the computational cost of transition to turbulence. The seeded turbulence created a period of brief transition due to dilatational perturbations before reaching equilibrium with the base state. This equilibrium with the base state and beginning of the asymptotic growth period was determined from the collapse of mean profiles of velocity and turbulent stresses, as discussed in section 2.3.2.

2.2.3 Boundary conditions

Early experimental observations have recorded that incident waves, such as those originating from an initial splitter plate, do not affect shear layer growth rates [52]. However, strong expansion and compression waves observed in the experiments by Rossmann et al., Kim et al. at higher compressibility levels show evidence for interactions between the turbulent shear layer region and waves reflecting off tunnel walls. A cleaner numerical setup without reflected waves is desirable. Regions of thickness $5\delta_0$ at the top and bottom of the domain were subjected to Gaussian filtering at each Euler time step [129]. The Gaussian filtering was applied to the primitive variables ρ, u_i and p. For spatial derivatives in the i^{th} direction, anti-symmetric boundary conditions were applied for for each conservative variable except for the i^{th} component of momentum, which used symmetric boundary conditions.

Figure 2.2 shows several profiles including the entire domain for the most compressible case. The mass averaged transverse velocity $\tilde{v}$ shows a nonzero freestream profiles as the shear layer grows, with fluid being pushed away from the mixing region. At the boundaries, the normalized mean transverse velocity remains less than 1% of the total velocity different Δu. While in the mean, the flow moves away from the mixing region, the turbulent fluctuations transport mass into the mixing layer. The transverse mass flux is positive below the shear layer and negative above the shear layer, which is consistent with positive entrainment. The turbulent mass flux is documented more thoroughly later in this chapter. Lastly, mean profiles of static pressure normalized by the reference pressure ($p_0 = 1$) indicate a slight drift in the mean pressure at $M_c = 0.2$ and $M_c = 0.8$

cases, and a larger drift of 15% at $M_c = 2.0$. Mean pressure profiles remain symmetric despite these drifts in absolute magnitude.

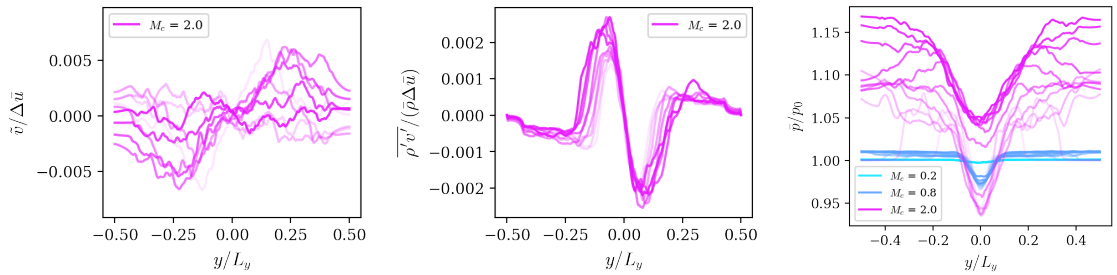

Figure 2.2: Mass averaged transverse velocity, transverse mass flux, and mean pressure profiles over the full computational domain. Line opacity indicates time history, such that the faintest lines occur earlier in simulation time and more opaque lines occur later in simulation time.

2.2.4 Discretization

Spatial derivatives were computed with 10^{th} order compact finite difference schemes [75], an 8^{th} order compact filter was applied to conservative variables at each time step for numerical stability, and the system is time advanced with a low-storage 4^{th} order Runge-Kutta scheme. The computation domain and resolutions for the six unity density ratio cases in this chapter are given in Table 2.2. The effect of the numerical filter can be observed in Fig. 2.10 at various compressibility levels. At higher compressibility levels, the maximum magnitude of the dissipation of TKE due to the filter is $\approx 10\%$ of the resolved viscous dissipation of TKE.

Domain sizes were validated with two point correlations of velocity fluctuations along the shear layer centerline. The profiles for these autocorrelations for all three velocity components in the streamwise and spanwise directions for the lowest and highest compressibility levels are shown in Fig. 2.4. The autocorrelations decrease sharply for all velocity components at $M_c = 0.2$. This suggests that the domain size is at least large enough to contain the largest eddies of the flow in the streamwise and spanwise directions. At $M_c = 2.0$, the streamwise velocity autocorrelation R_{uu} shows a delayed decay until a streamwise separation distance of $s/L_x \approx 0.4$ and a spanwise separation distance of $s/L_z \approx 0.6$. The computational domain for this case should be increased by at least 150% for improved convergence of turbulent statistics.

As shown in Fig. 2.3, energy spectra of velocities and density have been taken in the streamwise and spanwise directions and show a decay of seven decades, which suggests sufficient resolution of the small scales in the flow. The Reynolds numbers reached at the end of simulation time and resolutions of the Kolmogorov scale for the presented cases are comparable to several notable mixing

layer studies in Table 2.3. Although the Kolmogorov scale is not fully resolved, a significant range of the dissipative scales are resolved to study the dynamics of energy containing eddies.

Table 2.2: Parameters, domains, and grid resolutions for $s = 1$ cases studied. All cases use $N_x \times N_y \times N_z = 1024 \times 1448 \times 512$ uniformly spaced grid points.

M_c	s	$\frac{1}{\delta_\theta^\circ}(L_x \times L_y \times L_z)$	$\frac{1}{\delta_\theta^\circ}(\Delta x \times \Delta y \times \Delta z)$
0.2	1	$150 \times 200 \times 75$	$0.146 \times 0.138 \times 0.146$
0.4	1	$150 \times 200 \times 75$	$0.146 \times 0.138 \times 0.146$
0.8	1	$100 \times 100 \times 50$	$0.098 \times 0.069 \times 0.098$
1.2	1	$100 \times 100 \times 50$	$0.098 \times 0.069 \times 0.098$
1.6	1	$80 \times 80 \times 40$	$0.078 \times 0.055 \times 0.078$
2.0	1	$80 \times 80 \times 40$	$0.078 \times 0.055 \times 0.078$

Table 2.3: A brief comparison of key flow parameters with previous studies. N/A indicates 'not available'.

Study	M_c	Re_θ°	Re_θ	Re_ω	$\eta/\Delta x$
Pantano & Sarkar (2002)	1.1	160	1,760	13,640	0.380
Vaghefi (2014)	1.8	N/A	N/A	16,800	1.322
Buchta & Freund (2017)	1.75	60	2100	N/A	N/A
Arun et al (2019)	1.2	160	2,080	11,112	0.465
Present work	2.0	1000	3,800	18,480	0.409

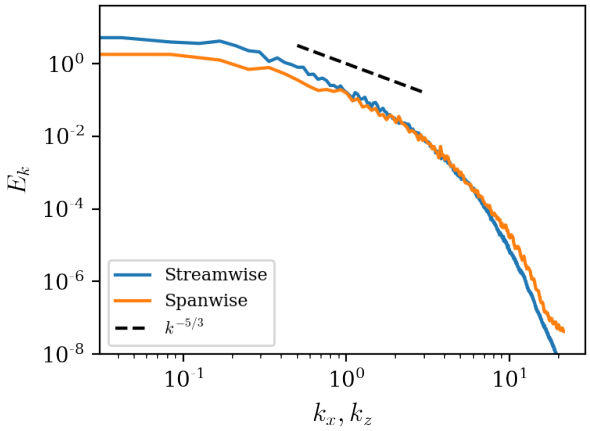

Figure 2.3: Energy spectra in streamwise and spanwise directions along the shear layer centerline at $M_c = 0.2, s_\rho = 1$ near the end of simulation time ($\delta_\theta(t)/\delta_\theta(0) \approx 3.0$).

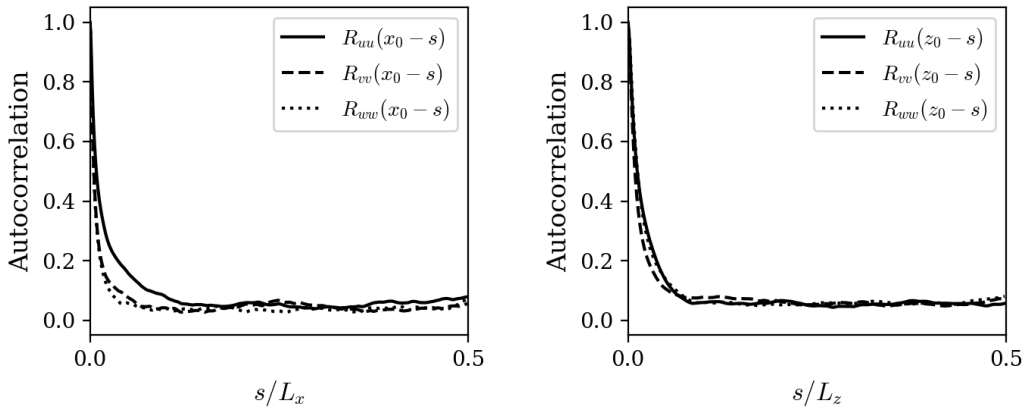

(a) $M_c = 0.2$

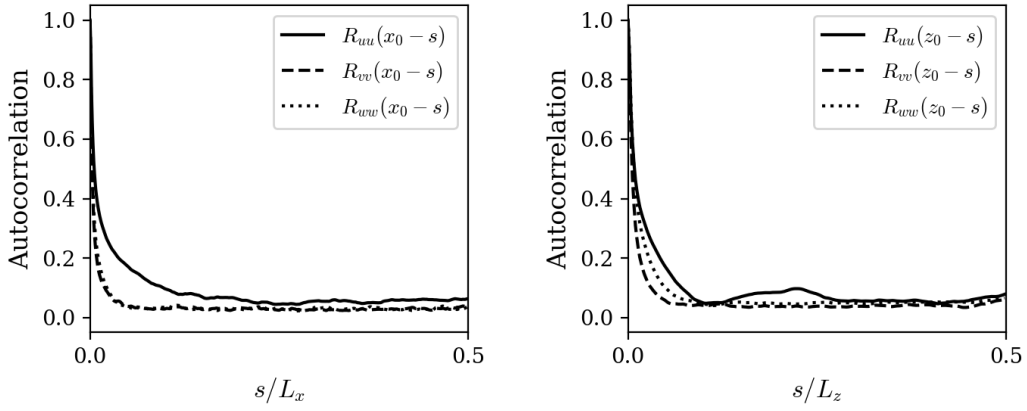

(b) $M_c = 2.0$

Figure 2.4: Two point correlations of velocity components in the streamwise (left) and spanwise (right) directions near the end of simulation time ($\delta_\theta(t)/\delta_\theta(0) \approx 3.0$).

2.3 Compressibility effects on turbulent statistics in the high-Mach regime

In this section, the effects of increasing convective Mach number on mean flow field profiles, turbulent fluctuations, and turbulent growth rates are presented, followed by analysis of the dilatational and anisotropic properties of the flow. Line opacity indicates time history, such that the faintest lines occur earlier in simulation time and more opaque lines occur later in simulation time. Error bars on data points representing mean values over time indicate the standard deviation about the mean during the averaging window. Likewise, profiles plotted in a single solid line with a similarly colored translucent envelope indicate the planar mean value and corresponding standard deviation at each transverse (y) location. Planar averages can be computed in the statistically homogenous and periodic directions, x and z. Both Reynolds and mass (Favre [44]) averaging are leveraged in this work; the notation for a field q under Reynolds and Favre decomposition are given below.

$$\begin{aligned} q(x,y,z,t) &= \bar{q}(y,t) + q'(x,y,z,t) \quad \text{Reynolds decomposition} \\ &= \tilde{q}(y,t) + q''(x,y,z,t) \quad \text{Favre decomposition} \end{aligned}$$

where

$$\bar{q}(y,t) = \frac{1}{L_x L_z} \int_0^{L_x} \int_0^{L_z} q(x,y,z,t) dx dz$$

$$\tilde{q} = \frac{\overline{\rho q}}{\bar{\rho}} \qquad \overline{q''} \neq 0 \qquad \overline{\rho q''} = 0 \qquad \overline{\rho}\tilde{q} = \bar{\rho}\tilde{q}$$

2.3.1 Means, turbulent stresses, and turbulent mass fluxes

Mean profiles at low, moderate and high compressibility levels are shown in Fig. 2.5 versus the normalized transverse coordinate $(y - y_c)/\delta_{99}$, where the centerline y_c corresponds to $\tilde{u}(y_c) = 0$. For unity density ratio cases, this centerline remains near $y = 0$. The profiles are not plotted for the full time history of the flow, but for the interval of time over which a linear growth rate is achieved and the mean streamwise velocity profile can be collapsed. The time and thickness range for this period of growth is indicated in Fig. 2.7. Note that this does not necessarily correspond to a collapse in all the mean profiles of primitive variables. In particular, the mean temperature profile in the most compressible case has a markedly slow rate of convergence compared to other variables. Thermodynamic variables (density, pressure and temperature) are normalized by the mean freestream values at each time instance, and not the constant reference values. The mean pressure profile forms a local minimum in the mixing layer region, where turbulent kinetic energy accounts for a portion of the normal stresses and displaces some of the thermodynamic pressure.

The normal and shear turbulent stresses are shown in the right column of Fig. 2.5. These components of the mass-averaged Reynolds stress tensor are given below.

$$R_{ij} = \frac{\overline{\rho u_i'' u_j''}}{\bar{\rho}} = \widetilde{u_i'' u_j''} \tag{2.8}$$

The present data is consistent with previous numerical studies by Vreman et al. [135], Pantano and Sarkar [103], and other experimental results (see Fig. 2.7c). All the turbulent stress magnitudes decrease with increasing compressibility, and continue to decrease monotonically with increasing M_c beyond those in previous investigations. The streamwise component of stress R_{11} is dominant, followed the spanwise component R_{33}, at all compressibility levels, which is consistent with experimental measurements of turbulent shear layers [65] and turbulent shear flows in general.

The turbulent mass flux profiles are shown in Fig. 2.6, normalized by the mean density and total velocity difference. As compressibility increases, the mass flux normalized by Δu increases notably. Both the streamwise and transverse mass flux profiles are anti-symmetric about the centerline, consistent with a symmetric spreading rate in these unity density ratio cases. This anti-symmetric behavior remains at all compressibility levels. The streamwise turbulent mass flux is negative at the bottom of the shear layer and positive at the top of the shear layer, indicating that this streamwise turbulent transport of mass follows the mean streamwise velocity. In contrast, as previously mentioned, the transverse turbulent mass flux shows the opposite profile across the shear layer, indicating that mass is entrained into the mixing region by the transverse velocity fluctuations. For the highest compressibility case at $M_c = 2.0$, the mass flux profile is nonzero in the freestreams due to to the presence of stronger Mach waves.

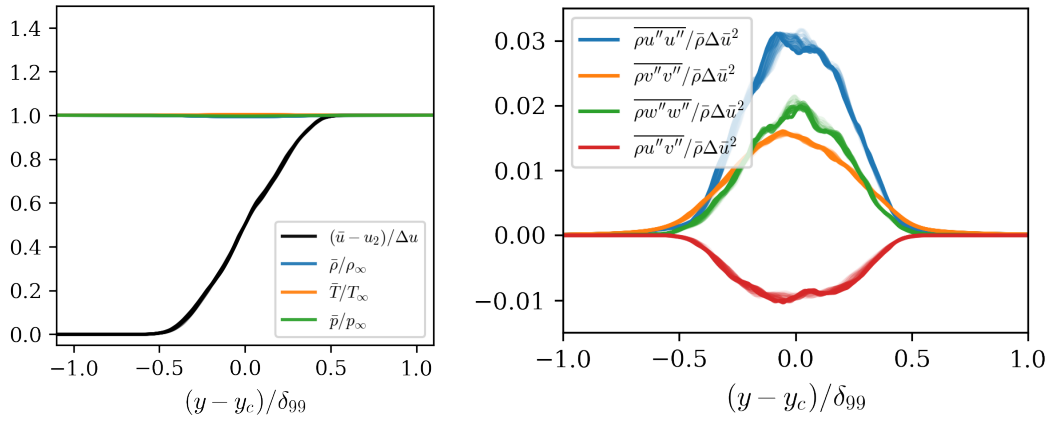

(a) $M_c = 0.2$

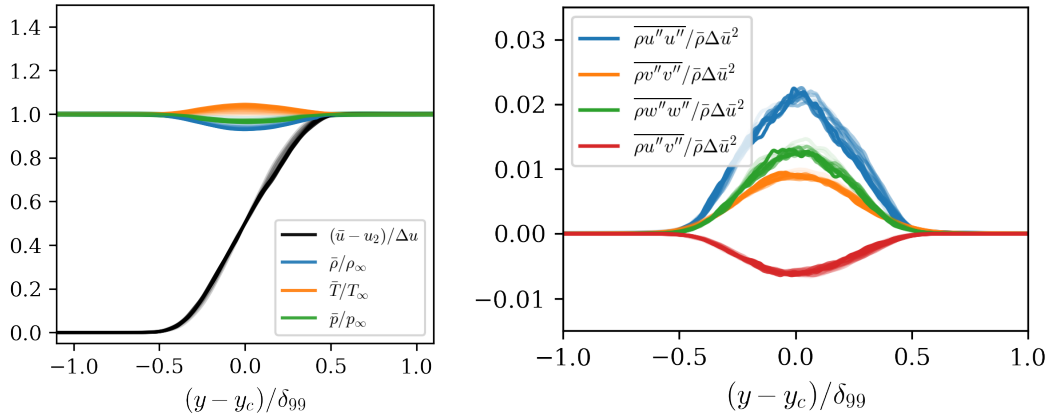

(b) $M_c = 0.8$

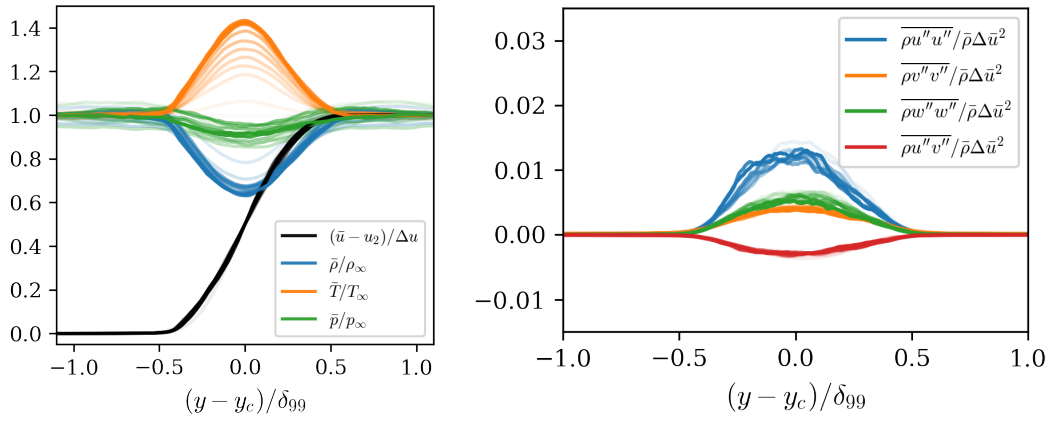

(c) $M_c = 2.0$

Figure 2.5: Left: normalized mean velocity, density, pressure and temperature profiles. Right: Turbulent stress profiles normalized by $\Delta\bar{u}^2$.

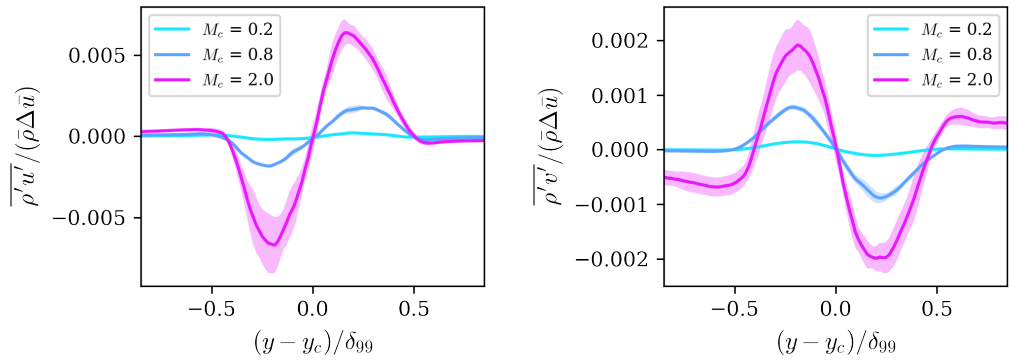

(a) Streamwise (b) Transverse

Figure 2.6: Turbulent mass flux velocities at various compressibility levels.

2.3.2 Growth rates

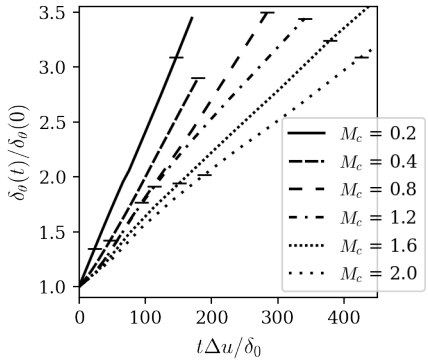

(a) Evolution of momentum thickness vs. convective time

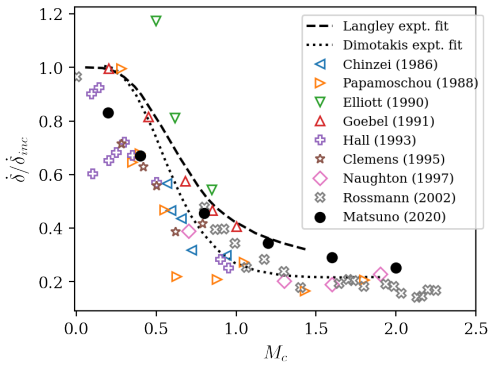

(b) Growth rates normalized by incompressible values

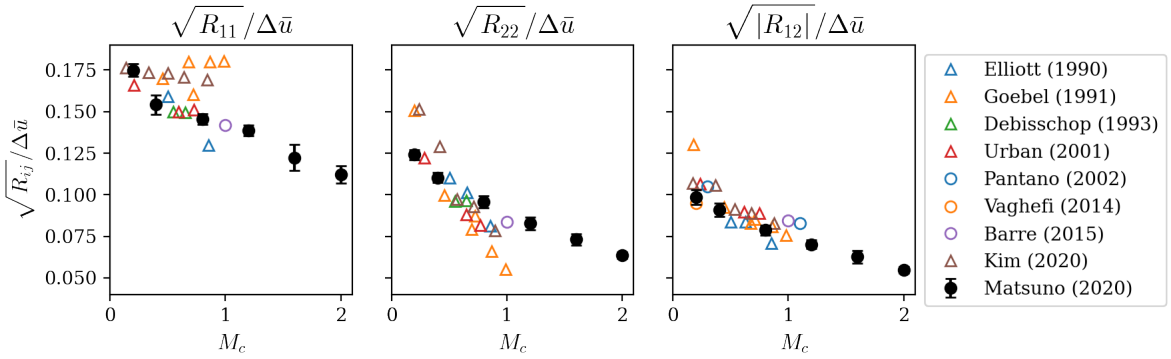

(c) Peak turbulent stress magnitudes compared to previous studies.

Figure 2.7: Growth rates and shear stress with increasing M_c.

The temporal evolution of the momentum thickness, defined in Eqn. 2.5 becomes linear after an initial period of transition. As depicted in figure 2.7a, this constant rate of growth decreases monotonically with increasing M_c. Intersecting tick marks indicate the duration of the self-similar regime, which is determined from collapse of the Reynolds shear stress profiles R_{12}. All error bars presented in this study represent the standard deviation due to temporal variations from the average value in this self-similar regime. Examples of this collapse and temporal variability are given in Fig. 2.5.

Figure 2.7b shows the well-known departure from the incompressible growth rate $\dot{\delta}_{inc}$, with $\dot{\delta}_{inc} = 0.018$ as used by Pantano and Sarkar [103] for $s_\rho = 1$. A drastic reduction occurs near $M_c \sim 0.5$, followed by an asymptotic approach to a normalized growth rate $\dot{\delta}_\theta/\dot{\delta}_{inc} \approx 0.2$. The

growth rates computed for the present data show good agreement with well known experimental results ([28, 105, 43, 49, 52, 30, 96, 113]), though the spread in experimental data at the subsonic region is worth consideration. Different studies have used different values for the incompressible growth rates, which propagates some uncertainty to the 'normalized' values at higher M_c. Despite this experimental spread, the drastic reduction of the growth rate with respect to each study's selected incompressible value remains evident. Figure 2.7c compares the present data to previously published studies. Numerical simulation data are plotted with open circles; present results for $s_\rho = 1$ are shown with black filled circles. Peak magnitudes of turbulent stresses are also consistent with previously published experimental results at lower M_c, ([43, 49, 34, 133, 8, 65]), though there exists some spread in the normal stress components R_{11} and R_{22}. In particular, there is considerable discrepancy in the peak stress trends recorded by Goebel and Dutton [49] and Kim et al. [65]; the cause of this discrepancy has not yet been identified. Other studies do not offer much data past $M_c \approx 1$; present data indicates that turbulent stress magnitudes continue to decrease with increasing M_c. The reduction in the turbulent stress magnitudes across M_c is not of the same magnitude as the reduction of the momentum thickness growth rate. However, the decrease in the turbulent shear stress confirms that the velocity fluctuations, which drive the spread of the mixing layer, decrease in a manner consistent with the observed growth rates and previous experimental observations.

2.3.3 Turbulent stress anisotropy

The present understanding of compressibility effects on the turbulent stresses can be supplemented using anisotropy invariant maps (AIMs). These maps are formed using the stress anisotropy tensor, b_{ij},

$$b_{ij} = \frac{\widetilde{u_i'' u_j''}}{2k} - \frac{1}{3}\delta_{ij} \qquad k = \frac{1}{2}\widetilde{u_k'' u_k''}$$

which can be diagonalized to provide information about the magnitude and directionality of anisotropy in the flow. AIMs map the eigenvalues of b_{ij}, $\lambda_1 \geq \lambda_2 \geq \lambda_3$, onto a two-dimensional plane bounded by limiting states of one-, two-, and three-component turbulence. The one-component (1C) state represents strong fluctuation directionality in one direction. The two-component (2C) state indicates a more disk-like bias in the fluctuations, while the three-component (3C) state indicates the

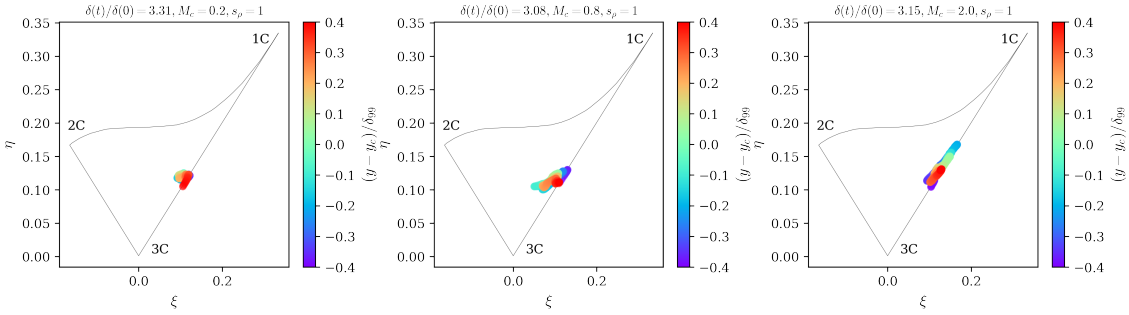

(a) $M_c = 0.2$ (b) $M_c = 0.8$ (c) $M_c = 2.0$

Figure 2.8: Anisotropic invariant map at $\delta/\delta_0 \approx 3$ for $s_\rho = 1$ and increasing compressibility

turbulent fluctuations are mainly isotropic. The invariant mapping onto the Lumley triangle used the coordinates based off the second and third principal components of anisotropy:

$$II = \frac{1}{2} b_{ij} b_{ji} = \lambda_1^2 + \lambda_1 \lambda_2 + \lambda_2^2$$
$$III = \frac{1}{3} b_{ij} b_{jk} b_{ki} = -\lambda_1 \lambda_2 (\lambda_1 + \lambda_2)$$

Alternatively, the turbulence triangle proposed by Choi and Lumley [29] uses the following coordinates to provide a more detailed view of the isoptropic, 3C corner:

$$\xi^3 = \frac{III}{2} \qquad \eta^2 = \frac{II}{2}$$

Compressibility has a known effect on turbulence anisotropy–the b_{11} component of the anisotropy tensor increases with increasing compressibility. Although normal stress components $R_{ii}/\Delta u^2$ decrease overall with increasing M_c, the streamwise component R_{11} becomes an larger proportion of total TKE as the other normal stresses, R_{22} and R_{33}, decrease more rapidly with M_c (see Fig. 2.5 and 2.7). This increase in anisotropy can be observed on the Choi anisotropy map in Fig. 2.8. In these figures, markers are colored by the location within the shear layer, with red and purple markers representing regions near the shear layer edges, respectively. The character of turbulence mainly falls along the 1C-3C region of the map at all compressibility levels. However, the mapping of the $M_c = 2.0$ data shows a tendency towards the 1C corner, which indicates a preference in the flow towards one component of anisotropy [65].

2.3.4 Dilatational stresses

The influence of dilatational dissipation was often considered to explain growth rate reductions in early numerical investigations of compressible turbulent mixing layers. Later studies, such as those by Pantano and Sarkar [103] at $M_c = 1.1$ and by Li et al. [76] at $M_c = 0.7$, indicated that fluctuations related to dilatation were not significant enough to explain the drastic growth rate reduction. These previously published observations on dilatation in mixing layers is in agreement for even the most compressible case at $M_c = 2.0$.

Eddy shocklets along the shear layer centerline are visualized in Fig. 2.9 using a modified Ducros sensor, defined as $-\theta|\theta|/\left[\theta^2 + \omega_j\omega_j + 10^{-32}\right]$, where $\theta = u_{j,j}$ is the velocity dilatation and $\omega_i = \varepsilon_{ijk}u_{k,j}$ is the vorticity. The modified Ducros sensor [37, 122] identifies shocks with sensor values near 1. Regions of dilatation and compression are sparse at $M_c = 0.2$, and become more frequent with increasing M_c. At the highest compressibility level, small shocklets are uniformly distributed along the centerline.

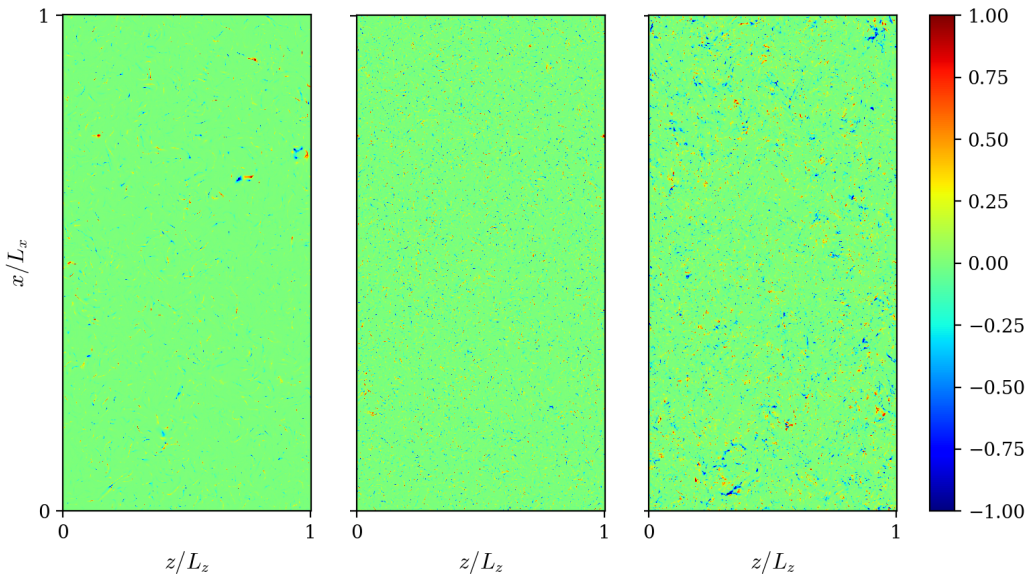

Figure 2.9: Centerline slices of the Ducros sensor to indicate regions of compression and dilatation at (from left to right) $M_c = 0.2$, 0.8 and 2.0.

$$\overline{u_i' u_j'} = \underbrace{\overline{u_i^{(s)} u_j^{(s)}}}_{R_{ij}^{(ss)}} + \underbrace{\overline{u_i^{(d)} u_j^{(d)}}}_{R_{ij}^{(dd)}} + \underbrace{\overline{u_i^{(s)} u_j^{(d)}} + \overline{u_i^{(d)} u_j^{(s)}}}_{R_{ij}^{(sd)}} \tag{2.9}$$

The effects of solenoidal and dilatational contributions to kinematic (non-mass averaged) turbulent stresses provide another assessment of compressibility effects on turbulent behavior. As defined in Eqn. 2.9, the solenoidal, dilational, and mixed components of the stress are referred to as $R_{ij}^{(ss)}$, $R_{ij}^{(dd)}$ and $R_{ij}^{(sd)}$. Beginning with the fluctuating velocities u_i', the field can be split into its solenoidal and dilatational components via Helmholtz decomposition, solved using the formulation by Corral and Jimenez [31] for 1D Poisson equations on infinite and semi-infinite domains with spectral methods. The present computational domain is planar-periodic in the x and z directions, so the Poisson equation for the fluctuating velocities (where primes have been dropped for notation) simplifies to a 1D equation:

$$\vec{u} = \bigtriangledown \times \vec{b} + \bigtriangledown \phi = \vec{u}^{(s)} + \vec{u}^{(d)} \tag{2.10}$$

$$\bigtriangledown \cdot \vec{u} = \bigtriangledown^2 \phi \tag{2.11}$$

$$i(k_x \hat{u} + k_z \hat{w}) + \frac{d\hat{v}}{dy} = -(k_x^2 + k_z^2)\hat{\phi} + \frac{d^2\hat{\phi}}{dy^2} \tag{2.12}$$

$$\hat{f}(y) = -k^2 \hat{\phi} + \frac{d^2\hat{\phi}}{dy^2} \tag{2.13}$$

This nonhomogenous ordinary differential equation may be solved exactly as an integral expression of the two linearly independent solutions, $e^{\pm ky}$. The numerical analysis is simplified by the homogenous nature of u fluctuations and its scalar potential ϕ in the far field as $y \to \pm\infty$, as well as the compact support of the right hand side $\hat{f}$ about the shear layer centerline, $y = 0$. With these boundary conditions, the domain is can be treated as periodic over the interval of L_y. Then, a solution to the scalar potential $\phi(y)$ of Fourier basis in the vertical y direction can be assumed, with $k_y = m\pi/L_y$. While the domain is not physically periodic in this transverse direction, a window to filter out freestream fluctuations, such as Mach waves for the high compressibility cases, is applied

Table 2.4: Peak values of kinematic stress components, defined as Eqn. 2.9. Values of $R_{ij}^{(dd)}$ and $R_{ij}^{(sd)}$ are scaled by 10^{-4}.

M_c	R_{11}	$R_{11}^{(dd)}$	$R_{11}^{(sd)}$	R_{22}	$R_{22}^{(dd)}$	$R_{22}^{(sd)}$	R_{12}	$R_{12}^{(dd)}$	$R_{12}^{(sd)}$
0.2	0.031	0.001	0.084	0.016	0.001	-0.187	-0.010	-0.000	0.099
0.4	0.026	0.006	0.252	0.013	0.006	-0.546	-0.009	-0.001	0.422
0.8	0.023	0.113	1.363	0.009	0.084	-1.165	-0.007	-0.020	0.433
1.2	0.024	0.730	2.229	0.009	1.238	-2.321	-0.007	-0.845	1.363
1.6	0.020	0.820	1.743	0.007	0.778	-2.688	-0.005	-0.439	1.456
2.0	0.021	0.775	1.919	0.006	0.822	-1.827	-0.005	-0.466	1.652

outside the shear layer region to numerically facilitate periodic treatment. This windowing process is detailed in Appendix A.

$$\hat{f} = \sum_{m=0}^{N_y-1} \hat{\hat{f}} e^{im\pi y/L_y} \tag{2.14}$$

$$\hat{\hat{\phi}}_L = -\frac{\hat{\hat{f}}}{k^2 + k_y^2} \tag{2.15}$$

$$\hat{\phi}(y) = \hat{\phi}_L(y) + a_+ e^{k(y-L_y)} + a_- e^{-k(y+L_y)} \tag{2.16}$$

$$a_+ = -\tfrac{1}{2k}\left[k\hat{\phi}_L(L_y/2) + \hat{\phi}'_L(L_y/2)\right] \tag{2.17}$$

$$a_- = -\tfrac{1}{2k}\left[k\hat{\phi}_L(L_y/2) - \hat{\phi}'_L(L_y/2)\right] \tag{2.18}$$

The (kinematic) normal stresses of interest in this problem, $R_{11} = \overline{u'u'}, R_{22} = \overline{v'v'}$, which are positive by definition, have mixed products of dilational and solenoidal components which are negative. Table 2.4 gives the peak values of average stress components for each M_c. While the magnitudes of the dilatational and mixed components of the stresses do not show a particularly significant trend, besides a general increase with increasing M_c, the sign of the individual components can be compared. For example, the shear stress $R_{12} = \overline{u'v'}$ has a negative profile while $R_{12}^{(sd)}$ is positive. This trend of negating values, and associated cancellation of both R_{22} and R_{12}, is consistent with increasing convective Mach number. Nevertheless, because the magnitude of the dilatational and mixed components of the kinematic stresses are small, the present data supports the notion that dilatational effects are not the cause for stress and growth rate reductions observed in highly compressible mixing layers.

2.3.5 TKE budgets and pressure-strain rate tensor

A series of related interactions between mean kinetic energy, mean internal energy, and turbulent kinetic energies exist in compressible flows. Production transfers energy between the mean and turbulent flow, while baropycnal work and pressure-dilatation terms transfer turbulent kinetic energy to internal energy of the mean state.

$$\frac{\partial}{\partial t}(\bar{\rho}R_{ij}) + \frac{\partial}{\partial x_k}(\bar{\rho}\tilde{u}_k R_{ij}) = \underbrace{-\bar{\rho}\left(R_{ik}\frac{\partial \tilde{u}_j}{\partial x_k} + R_{jk}\frac{\partial \tilde{u}_i}{\partial x_k}\right)}_{\text{Production } P_{ij}} \underbrace{- \overline{\left(\tau'_{jk}\frac{\partial u''_i}{\partial x_k} + \tau'_{ik}\frac{\partial u''_j}{\partial x_k}\right)}}_{\text{Dissipation } D_{ij}} + \underbrace{\overline{p'\left(\frac{\partial u''_i}{\partial x_j} + \frac{\partial u''_j}{\partial x_i}\right)}}_{\text{Pressure strain } \Pi_{ij}}$$
$$- \frac{\partial}{\partial x_k}\underbrace{\left(\overline{\rho u''_i u''_j u''_k} + \overline{p' u''_i}\delta_{jk} + \overline{p' u''_j}\delta_{ik} - \overline{\tau'_{jk}u''_i} - \overline{\tau'_{ik}u''_j}\right)}_{\text{Turbulent transport } T_{ijk}} + \underbrace{\overline{u''_i}\left(\frac{\partial \bar{\tau}_{jk}}{\partial x_k} - \frac{\partial \bar{p}}{\partial x_j}\right) + \overline{u''_j}\left(\frac{\partial \bar{\tau}_{ik}}{\partial x_k} - \frac{\partial \bar{p}}{\partial x_i}\right)}_{\text{Mass flux coupling } \Sigma_{ij}} \tag{2.19}$$

$$\frac{\partial}{\partial t}(\bar{\rho}k) + \frac{\partial}{\partial x_j}(\bar{\rho}\tilde{u}_j k) = \underbrace{-\bar{\rho}R_{ij}\frac{\partial \tilde{u}_i}{\partial x_j}}_{\text{Production } P} - \underbrace{\overline{\tau'_{ij}\frac{\partial u''_i}{\partial x_j}}}_{\text{Dissipation } D} - \underbrace{D^f}_{\text{Dissipation via filter}}$$
$$- \frac{\partial}{\partial x_j}\underbrace{\left(\frac{1}{2}\overline{\rho u''_j u''_i u''_i} + \overline{u''_j p'} - \overline{\tau'_{ij}u''_i}\right)}_{\text{Turbulent transport } T} - \underbrace{\overline{u''_i}\frac{\partial \bar{p}}{\partial x_i}}_{\text{Baropycnal work } B} + \underbrace{\overline{p'\frac{\partial u''_i}{\partial x_i}}}_{\text{Pressure dilatation } \Pi} \tag{2.20}$$

$$D^f = \frac{1}{\Delta t}\sum_{N_{RK}}\left(\frac{1}{2}\overline{\rho}^f \widetilde{u_i}^f \widetilde{u_i}^f - \frac{1}{2}\overline{\rho}\widetilde{u_i}\widetilde{u_i}\right) \tag{2.21}$$

The evolution equation of turbulent stresses R_{ij}, with $R_{ij} = \widetilde{u''_i u''_j}$, is given Eqn. 2.19. The evolution equation for TKE, $k = \frac{1}{2}\widetilde{u''_i u''_i}$, is the trace of Eqn. 2.19, and given explicitly in Eqn. 2.20. The resolved dissipation D and the numerical dissipation D^f due to the dealiasing filter are computed as given in Eqn. 2.21. The superscript ^{f} denotes a field variable after filtering is applied and $N_{RK} = 4$ is the number of Runge-Kutta steps used in the simulation. Figure 2.10 shows that the numerical dissipation of the filter is small compared to the resolved dissipation. At intermediate compressibility levels, the maximum magnitude of the numerical dissipation is $\leq 10\%$ of the resolved dissipation, which is comparable to previous DNS studies of this problem [103]. For higher speed cases, the filtered dissipation composes a large proportion of the total dissipation. In subsequent figures, the TKE dissipation shown is the total of both the resolved and filter-associated dissipation.

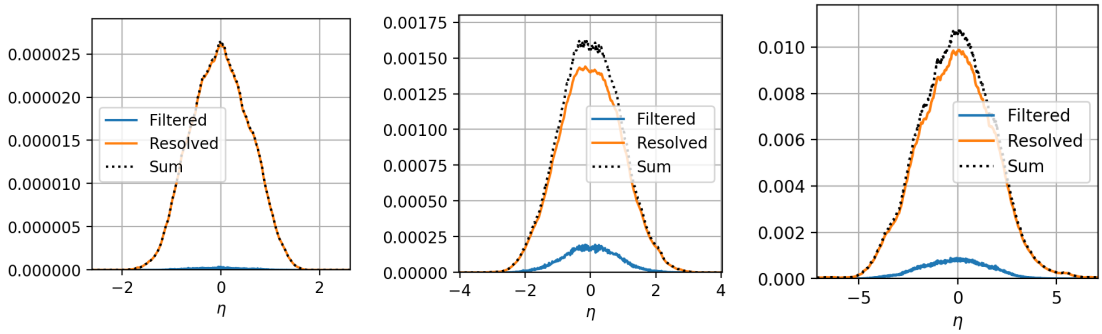

(a) $M_c = 0.2$ (b) $M_c = 0.8$ (c) $M_c = 2.0$

Figure 2.10: Filter-associated dissipation, resolved dissipation, and total TKE dissipation profiles plotted versus normalized coordinate $\eta = y/\delta_\theta$.

Profiles of TKE budget terms normalized by the total velocity and length scales Δu and δ_{99} are shown in the left column of Fig. 2.13. Consistent with profiles presented by Pantano and Sarkar [103], the TKE budget is dominated by production, dissipation, and turbulent transport terms. Some oscillations are present in the profiles due to insufficient averaging in time. The TKE budget of the case with the most stringent grid resolution requirements, $M_c = 2.0$, has a peak residual is about 15% of the peak TKE production, as shown in Fig. 2.11. The numerical truncation inherent in the manipulation of terms required to derive the TKE budget in the form given in Eqn. 2.20 contributes to this residual. As expected, the baropycnal term B remains inactive for these unity density ratio cases. The pressure dilatation term Π also has an almost negligible contribution to the TKE budget, even for the most compressible case at $M_c = 2.0$. The right column of Fig. 2.13 includes the same TKE budget, but scaled using 'internal' eddy scales which will be discussed in detail in section 2.3.6.

Although the pressure dilatation term, which is the trace of the pressure strain rate tensor Π_{ij}, remains small in the TKE budgets of present data, the individual components of Π_{ij} play an important role in the evolution of the turbulent stresses. This pressure strain correlation redistributes TKE among the components of the Reynolds stresses tensor, and is one of the crucial but unclosed terms in Reynolds stress transport models. The normal components of Π_{ij} are shown in Fig. 2.12; the profiles of shear stress production P_{12} are coplotted for comparison. The streamwise component Π_{11} dominates over the transverse and streamwise components, which again reflects observed anisotropy [65]. Overall pressure strain rate components decrease with increasing M_c, which is consistent with observations by Pantano and Sarkar [103] and Li et al. [76]. The scaling of the streamwise pressure strain rate component is also covered in section 2.3.6.

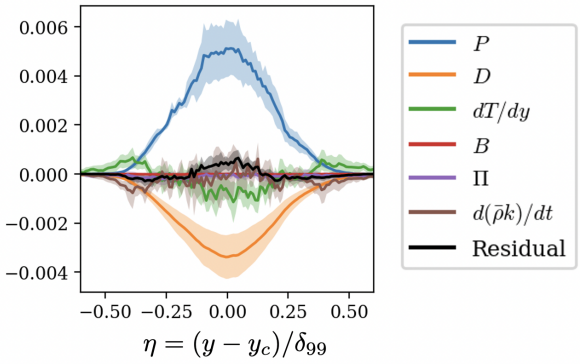

Figure 2.11: TKE budget and rate of change normalized by global shear layer scales $\delta_{99}/\Delta u^3$ for $M_c = 2.0, s_\rho = 1$.

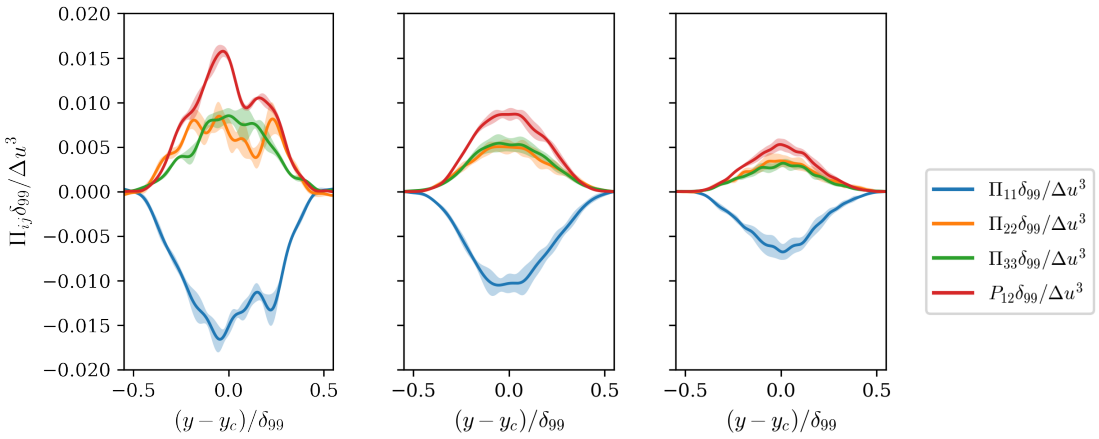

(a) $M_c = 0.2$ (b) $M_c = 0.8$ (c) $M_c = 2.0$

Figure 2.12: Pressure strain components and shear productions of TKE, normalized by global shear layer scales $\delta_{99}/\Delta u^3$. Oscillations in the profiles at are due to insufficient averaging.

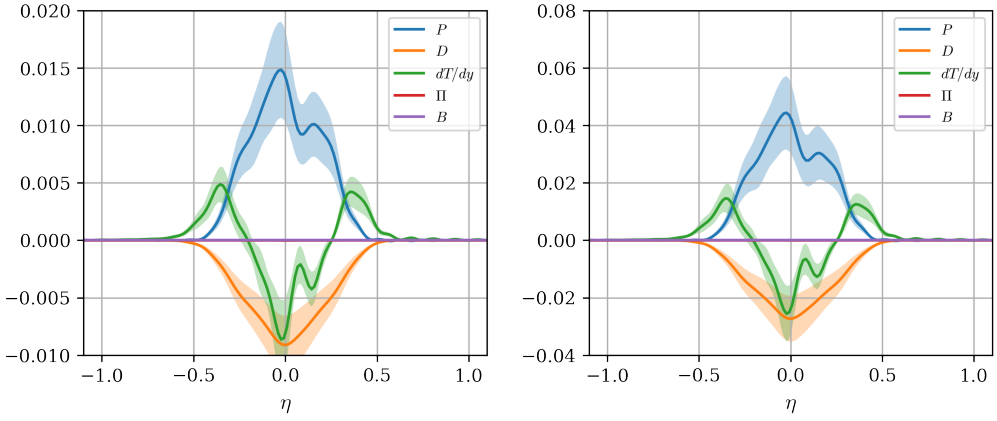

(a) $M_c = 0.2$

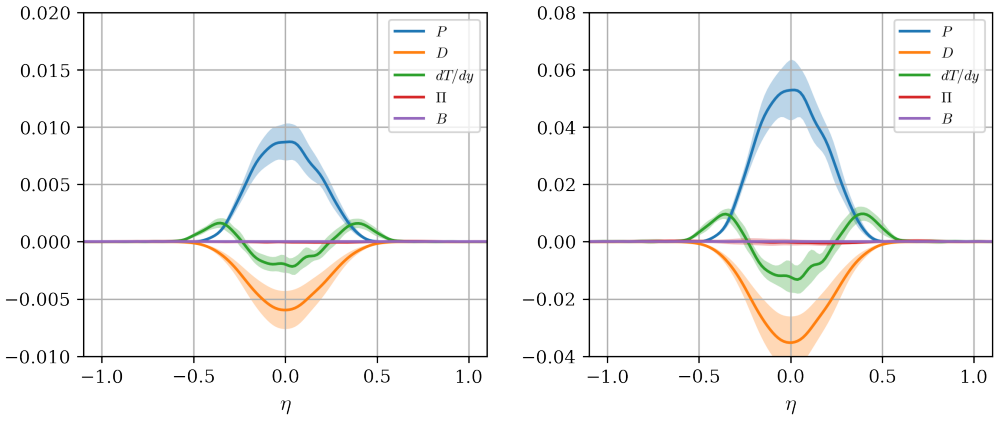

(b) $M_c = 0.8$

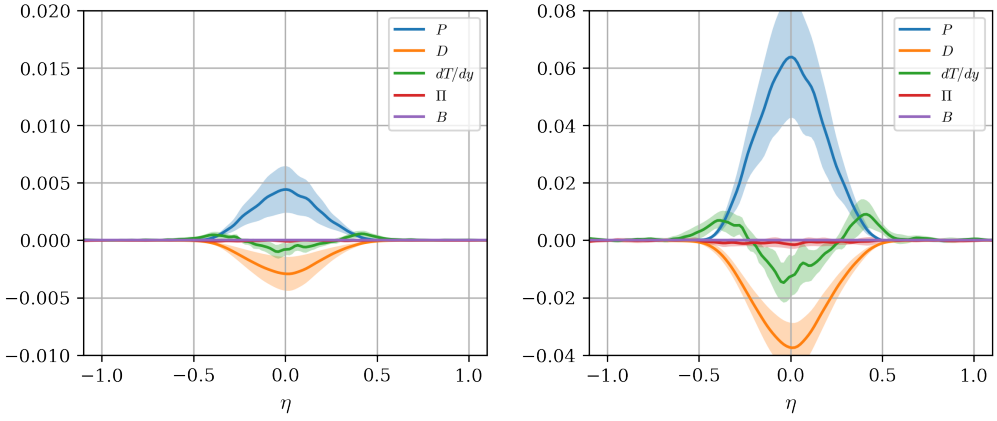

(c) $M_c = 2.0$

Figure 2.13: TKE budget terms normalized by (left) global shear layer scales $\delta_{99}/\Delta u^3$ and by (right) local scales δ_y/U_δ^3. Oscillations in the profiles at $M_c = 0.2$ are due to insufficient averaging.

2.3.6 Turbulence length and time scales

Visualizations of transverse velocity across the mixing layer are shown for the lowest and highest M_c cases in Figure 2.14. The domains (truncated for visual comparison) are scaled by the total mixing layer thickness δ_{99} to allow for a direct comparison of eddy length scales. The scale disparity between the two cases is qualitatively obvious; in this section the turbulent scales are discussed quantitatively and used to propose an alternative explanation for growth rate reduction.

In addition to the thickness measures $\delta_{99}, \delta_\omega$ and δ_θ, which characterize the mean velocity profile, a decorrelation length scale is used to characterize the effect of increasing M_c on the energy-containing scales. This length scale, δ_y, is defined in 2.22 using a pair of points symmetrically placed around an anchor point y_0 at a mutual separation distance of δ_y. A decrease in the correlation to 0.1 is used to define this length scale, with the anchor point $y_0 = y_c$ at the shear layer center, where $\tilde{u}(y_c) = 0$. This decorrelation length of the fluctuating transverse velocity in the transverse direction characterizes the transverse size of energy containing eddies in an average sense.

$$\frac{\overline{v'(y_0 - \delta_y/2)v'(y_0 + \delta_y/2)}}{\overline{v'(y_0)v'(y_0)}} = 0.1 \tag{2.22}$$

The transverse length scale as a fraction of total mixing layer thickness decreases significantly from the quasi-incompressible case at $M_c = 0.2$ to the highly compressible case at $M_c = 2.0$. Figure 2.15a shows the transverse correlation length for the fluctuating transverse velocity and the effect of shifting the anchor point to $y_c \pm \delta_{99}/4$. Present data indicates a three-fold decrease (from low to high M_c) in δ_y along the centerline, and nearly a four-fold decrease in δ_y for points offset from the centerline. Figure 2.15a also indicates that δ_y measured about y_c is the minimum decorrelation length in the mixing layer at each M_c. The occurrence of minimum length scale about the centerline y_c is intuitive–mean shear, TKE production, and turbulent stress magnitudes also peak along the centerline.

The mean velocity difference across the average decorrelation length scale centered about anchor point y_0, defined as U_δ in 2.23, is also an important turbulent statistic of these eddies. The behavior of this velocity scale, plotted in 2.15b matches the familiar reduction of normalized growth rates shown in Figure 2.7b.

$$U_\delta = \tilde{u}\left(y_0 + \tfrac{\delta_y}{2}\right) - \tilde{u}\left(y_0 - \tfrac{\delta_y}{2}\right) \tag{2.23}$$

The time scales of turbulent motions are also inherently linked to the reported decorrelation length scales δ_y. The most obvious time scale of interest is that of the acoustic scale set by the mean speed of sound $\bar{c} = \overline{\sqrt{\gamma p/\rho}}$, which effectively defines the reach of acoustic communication in a mean sense. A second time scale to consider is the one associated with eddy distortion due to the shearing of the mean flow, which corresponds to the the centerline (maximum) shear $S = d\tilde{u}/dy$. Finally,

the turbulent time scales associated with the turbulent velocity fluctuations and shear stresses are considered. In this discussion, these time scales are also interpreted as the Mach numbers defined below.

$$M_t = \left. \frac{\sqrt{\widetilde{u_i'' u_i''}}}{\bar{c}} \right|_{y_c} \tag{2.24}$$

$$M_{t,v} = \left. \frac{\sqrt{\widetilde{v'' v''}}}{\bar{c}} \right|_{y_c} \tag{2.25}$$

$$M_\tau = \left. \frac{\sqrt{|\widetilde{u'' v''}|}}{\bar{c}} \right|_{y_c} \tag{2.26}$$

$$M_g = \left. \frac{S \delta_y}{\bar{c}} \right|_{y_c} \tag{2.27}$$

The turbulent Mach numbers, M_t, represent the ratio of the mean acoustic time scale to the time scale of turbulent fluctuations. The M_t of the present simulations are comparable to previously published DNS of CHIT [57], and can be used to compare statistics such as pressure fluctuation skewness at equivalent M_t [84]. As shown in Figure 2.15c, while M_t shows saturation at the highest M_c, the turbulent Mach number defined using only the transverse component of TKE, $M_{t,v}$, indicates saturation at lower levels of compressibility, as further evidence for the pronounced effect of compressibility on the fluctuating transverse velocity. Freund et al. [47] showed the beginning of a saturated regime for these timescale ratios for an annular mixing layer. The present M_t and $M_{t,v}$ show this trend at higher M_c in a self-similar shear layer.

A friction Mach number, M_τ, of the turbulent mixing layer can be defined using the turbulent shear stress. In the present simulations, $M_\tau \leq 0.5$. Even at the lowest M_c cases, M_τ remains much larger than the M_τ encountered in turbulent boundary layers of high speed, compressible flows [14]. As a complement to M_τ's description of turbulent shear, the gradient Mach number, M_g describes the compressibility effect of mean shear, and represents the ratio of the the acoustic timescale to the mean deformation timescale. Unlike M_t, this time scale ratio does not show a clear plateau, although such a tendency is suggested by the data. Studies at even higher M_c are required to fully demonstrate this saturation.

Even in the most compressible case, each of the Mach numbers investigated in Figure 2.15c remain subsonic. The 'sonic-eddy hypothesis', as proposed by Breidenthal, would suggest that since acoustic communication across these eddies is possible, these eddies remain coherent and participate in entrainment. Present data indicates that even in the M_c range of significant growth rate reduction, the energy-containing eddies are subsonic. Assuming that eddies of scale δ_y are

active in entrainment the relative shear across these eddies appears directly related to the growth rate behavior. At lower M_c, these eddies span across a large portion of the overall mixing layer thickness, whereas at high M_c, the mixing layer consists of several 'colayers' of energy-bearing eddies. Figure 2.16 indicates that several autocorrelation profiles can fit within the mixing layer thickness at $M_c = 2.0$, and that this structure is consistently maintained during the self-similar regime. Such behavior suggests an internal regulation mechanism which limits the formation of still larger scales in the higher M_c mixing layers.

From Figure 2.15c, the turbulent Mach number M_t and transverse turbulent Mach number $M_{t,v}$ reach a plateau of approximately 0.5 and 0.2, respectively. The latter suggests that sound has sufficient time to ricochet 2-3 times across the transverse correlation scale during eddy turnover. Motions at still larger scales are evidently unable to remain coherent. They may correspond to acoustic response, but not rotational eddies. Figure 2.17a shows the ratio of correlation scales along x and y directions, δ_x/δ_y , and along the z and y directions, δ_z/δ_y against M_c. A data processing error invalidates the corresponding plot in Matsuno and Lele [84]. Note that these ratios are relatively constant. The $M_c = 2.0$ point is an outlier since it may be affected by the smaller domain size in x. The internal regulation mechanism which limits the transverse scale to a decreasing fraction of the total shear layer thickness δ_{99} also limits the correlation scales in the x and z directions and maintains approximately the same ratio in correlation scales. All of these trends are consistent with acoustic communication as the regulation mechanism for maintaining coherent eddying motions. Figure 2.17b shows the dimensionless shear number, or Corrsin number, $S\delta_y/\sqrt{R_{ii}} = M_g/M_t$ and $S\delta_y/\sqrt{R_{22}} = M_g/M_{t,v}$ against M_c. These measures are relatively constant with M_c, which affirms that the regulation is not associated with an increased importance of shear with M_c, but with acoustic communication limiting the turbulence length scales in the flow.

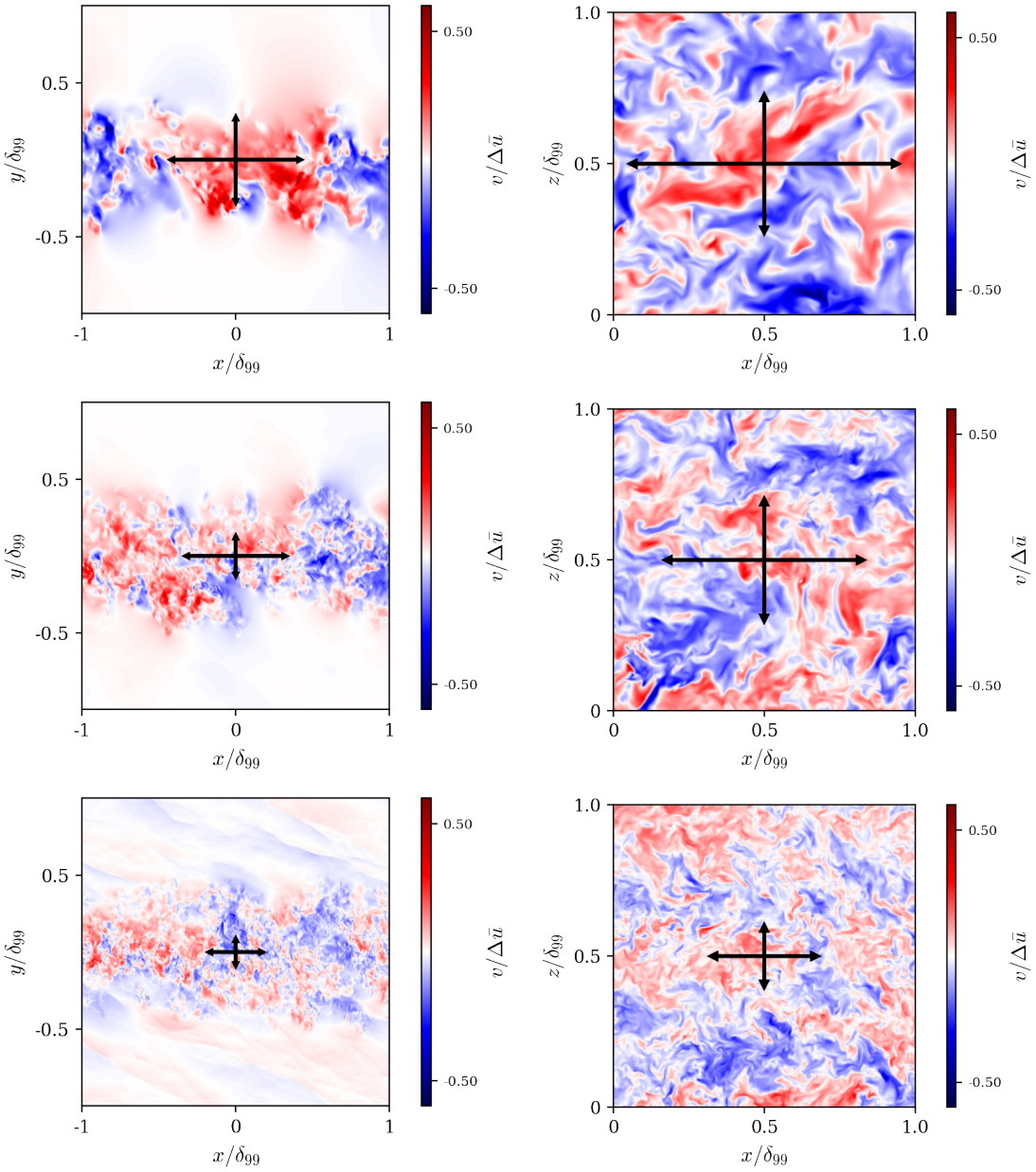

Figure 2.14: Instantaneous planar views of transverse velocity $v/\Delta\bar{u}$. Slices at (left) $z = L_z$ and (right) $y = y_c$ at $M_c = 0.2, 0.8$ and 2.0 from top to bottom. Arrows indicate decorrelation length scales based on v' along x and y axes. Note that the domains are truncated for visualization purposes.

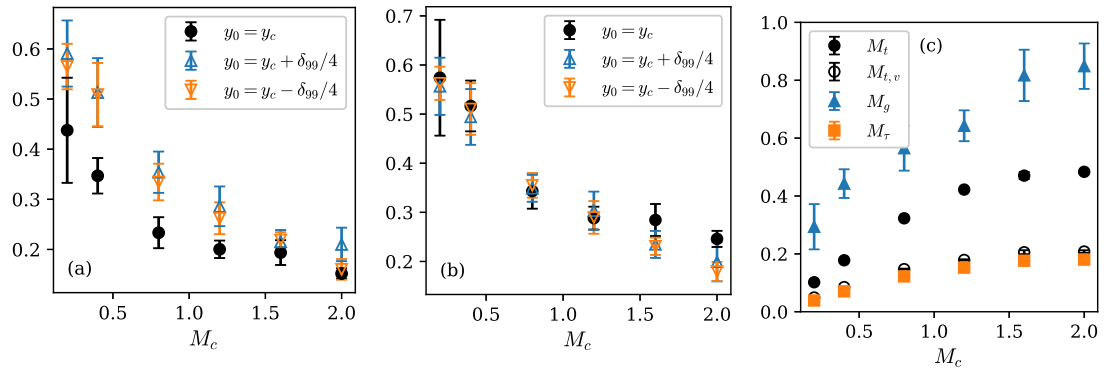

Figure 2.15: Effect of compressibility on (a) normalized decorrelation lengths δ_y/δ_{99} for v' measured about different y_0, (b) mean velocity difference $U_\delta/\Delta\bar{u}$ across the v' decorrelation length, and (c) various Mach numbers.

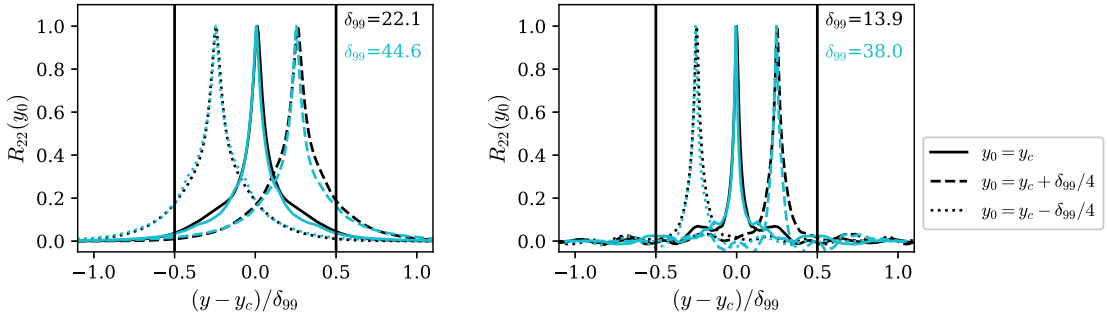

Figure 2.16: Autocorrelation profiles for v' measured about different y_0 for (a) $M_c = 0.2$ and (b) $M_c = 2.0$ at the beginning (black) and end (blue) of self similar spreading. Overall mixing layer thickness δ_{99} is indicated in terms of initial thickness δ_θ^o.

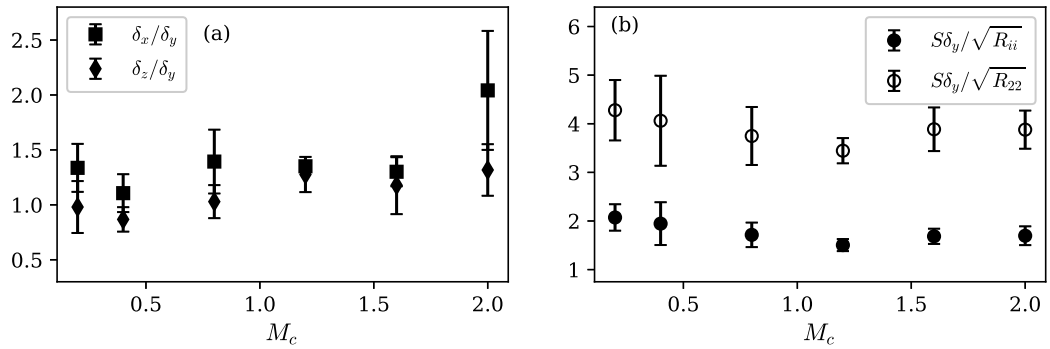

Figure 2.17: (a) Decorrelation ratios and (b) dimensionless shear (Corrsin number).

2.3.7 Scaling of turbulence statistics

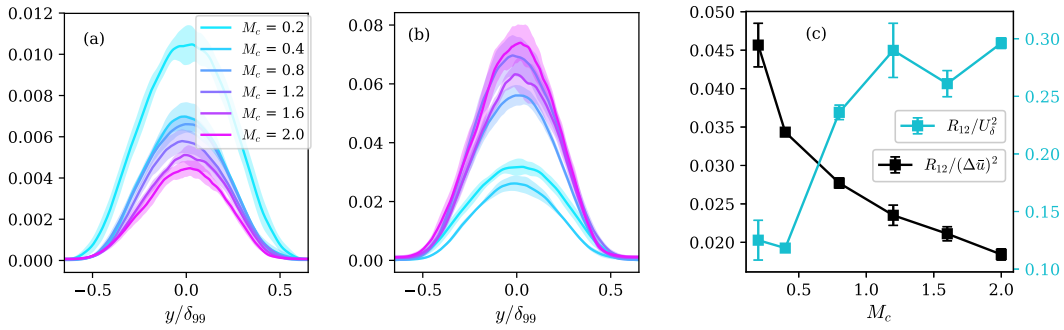

Figure 2.18: (a) $|R_{12}|/(\Delta\bar{u})^2$; (b) $|R_{12}|/U_\delta^2$; (c) Integrated $|R_{12}|$ vs. M_c.

Like all turbulent flows, the compressible mixing layer is an inherently multi-scale phenomena. Several length and velocity scales can be identified, but some scales will provide more satisfactory representations of the flow's turbulent behavior. For the present data, the external and internal length and velocity scales can be compared to which scale is representative in the high-Mach regime.

Profiles of shear stress magnitudes $|\overline{u'v'}|$ scaled using the total velocity difference $\Delta\bar{u}$ and the effective velocity scale U_δ are shown in Figure 2.18. Whereas scaling using $\Delta\bar{u}$ indicates a steady decline in the shear stress magnitude, scaling using U_δ^2 results in a clear separation between Reynolds stress profiles at low versus high M_c.

Similarly, TKE budget terms may be scaled using either the overall mixing layer scales or the internal scales associated with transverse velocity decorrelation. The right column of Figure 2.13 compares the TKE budgets at low, intermediate and high compressibility levels when scaled by the global mixing layer scales $\delta_{99}/(\Delta\bar{u})^3$ and by the internal scales δ_y/U_δ^3. Figure 2.19 shows integrated TKE production P, TKE dissipation D, and pressure strain component Π_{11} again scaled by global and local scales. Considering the evolution equation for the Reynolds stresses given in Eqn. 2.19, the streamwise pressure strain component $\Pi_{11} = 2\overline{p'(du''/dx)}$ plays an important role in shear layer mixing by transferring energy out of R_{11} to other turbulent stresses.

The integrated TKE production term is related to the growth rate definition offered by Vreman et al. [135], such that the values plotted in Figure 2.19a represent $\dot{\delta}_\theta \times \rho_0\delta_{99}/(2\delta_\theta\Delta\bar{u})$. TKE dissipation normalized with internal scales transforms the trend of a monotonic, progressive decrease with M_c to an approximately constant value for $M_c > 0.2$. Internally scaled TKE production and streamwise pressure strain Π_{11} show a similar asymptotic behavior past $M_c \sim 0.8$. The asymptotic approach towards constant production, pressure-strain, and dissipation, as well as evidence for constant turbulent shear stress magnitudes using the effective velocity scale U_δ further suggests the

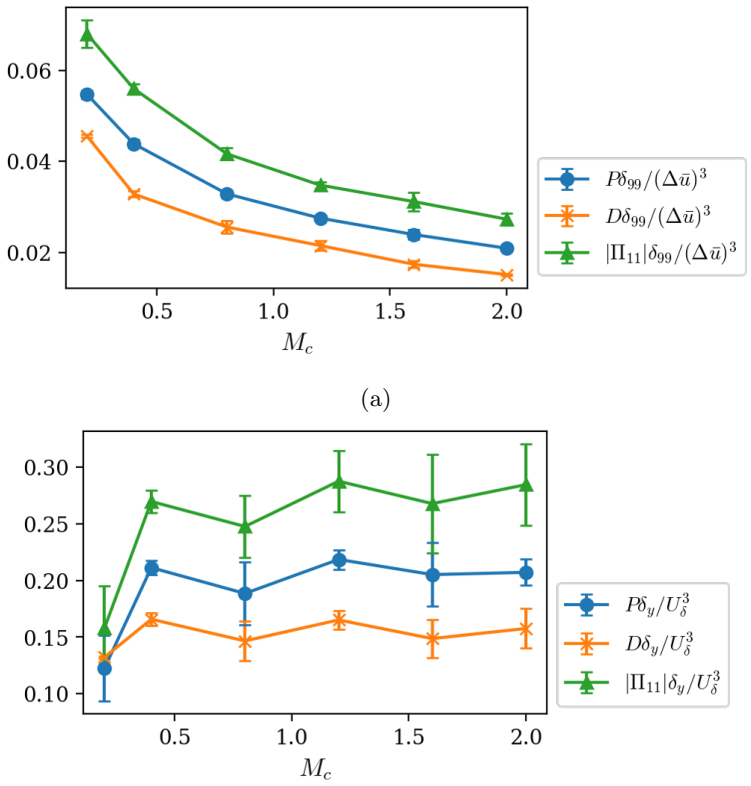

Figure 2.19: Selected TKE budget terms, integrated and scaled with (a) total thickness δ_{99} and total velocity difference $\Delta\bar{u}$ and with (b) internal scales δ_y and U_δ.

importance of δ_y as the defining length scale associated with turbulent mixing. This distinction may improve length scale-based turbulence models.

2.4 Conclusions

High resolution simulations of temporally developing, compressible shear layers were conducted at a range of convective Mach numbers. The highest compressibility level of this study was previously unexplored using turbulence-resolving simulations, and present data shows the extension of previously published turbulent statistics at moderate compressibility levels into this high-Mach regime. Reduction of growth rates, turbulent normal and shear stresses, and TKE budget terms are confirmed to be consistent with previous experimental and numerical results. Anisotropic invariant maps indicate consistency with previously observed trends of increased streamwise anisotropy with increasing compressibility levels. The contributions of dilatational effects in the form of pressure dilatation and dilatational components of kinematic stresses are demonstrated to be small. The scales governing the turbulent structures in mixing layers with notable compressibility effects were examined. As M_c increases, turbulence length scales including the transverse length scale reduce significantly as a fraction of the overall shear layer thickness. These length scales appear to be limited by acoustic communication. Turbulence-associated Mach numbers show saturation at higher levels of compressibility, but remain subsonic even at the highest compressibility level. The mechanism of internal regulation results in adaptation of spatial and temporal scales of shear layer turbulence with increasing compressibility, as inferred from two-point correlations. This internal regulation reduces the effective velocity scale, suppresses pressure fluctuations and lowers the mixing layer growth rate.

(To Table of Contents)

Chapter 3

Variable density effects on turbulent shear layers

3.1 Introduction

Variable density mixing remains highly relevant in high-speed propulsion and other compressible flows for aerospace applications, manifesting in features such as acoustic fluctuations, shock waves, heating from chemical reactions, and/or phase transformations. The turbulence in these applications is especially complex, given that density variations can result from a combination of thermal fluctuations, compositional changes from fluids with different molar masses, phase inhomogeneities and chemical reactions. Acoustic fluctuations and dilatational effects are also relevant, which gives rise to the interest in combinations of compressibility and variable density effects. The joint effects of compressibility and density variations are less commonly studied than the canonical shear layer problem without density variations, although variable density effects on turbulent mixing have remained a relevant topic of interest for several decades. A selective review of the literature pertinent to mixing in variable density shear layers is given below.

Previous studies

Brown and Roshko's experimental observations of turbulent mixing between nitrogen and helium streams were among the first to show the dominance of large, coherent structures at all density ratios. One of Brown's main conclusions was that the density ratio across the mixing layer had a relatively small effect on the spreading rate compared to compressibility effects. Later, Papamoschou and Roshko [105] conducted a suite of mixing layers with varying velocity and density

ratios and observed both low spreading rates and the formation of large scale structures. From this study, it was determined that using the convective Mach number of each freestream, M_{c1} or M_{c2}, approximately collapses the spreading rates for the cases studied. The authors also noted that compared to previous supersonic shear layer studies, their observed spreading rates were substantially reduced and large scale structures were present in a larger variety of conditions. Goebel and Dutton [49] did not observe large scale, organized structures in their compressible turbulent mixing layers. Similarly, while Clemens and Mungal [30] observed that two-dimensional rollers are dominant at lower M_c, the shear layer showed more three-dimensional features at higher M_c. The same large scale structures as those observed in the supersonic shear layers observed by Papamoschou and Roshko were not identified by either Goebel or Clemens.

In numerical studies, the terms 'heavy' and 'light' are used to refer to the higher and lower density freestreams, although the influence of gravity is not included in these studies. Several numerical studies of two-dimensional, spatially developing mixing layers have been conducted with the intent of quantifying the effects of density ratio on both transitional and long term shear layer growth. Among others, Reinaud et al. conducted Lagrangian simulations of transitional, inviscid shear layers at density ratios ranging from 1 to 6; the data indicated that the baroclinic torque acting on the vorticity field is sensitive to perturbations and ought to provide a rapid route to turbulence for variable density shear layers. Later, Lopez-Zazueta et al. [81] further investigated the evolution of these baroclinic perturbations and compared differences between unity and variable density ratio Kelvin-Helmholtz vorticies. The role of vorticity and baroclinic torque was also implicit in the self-similar growth of mixing layers as studied by Kennedy and Gatski [64]. Kennedy integrated the similarity equations for steady, two-dimensional, non-reacting mixing of a binary gas mixture at convective Mach numbers ranging from 0.2 to 1.2. The shear layers were composed of a fast and light stream flowing past a slow and denser stream to mimic a hydrogen and nitrogen mixing layer. This study emphasized that the traditional practice of defining the shear layer thickness solely off the velocity gradient in incomplete, and that the tails of the mixture fraction and density profiles should also be accounted for in describing the shear layer growth. Lastly, this study also emphasized that the majority of the vorticity and mixing occurs in the lighter fluid stream, which was also supported by later DNS. Soteriou and Ghoniem [123] studied two-dimensional, incompressible, and inviscid spatially developing shear layers with a Lagrangian transport element method. Authors observed that as the density ratio increased, earlier and more intense vortex roll up observed and pairing interactions more prominent, which increased the mixing layer region. This contrasted with other studies which indicated that increasing the density ratio decreased the mixing layer growth rate, but that this could be attributed to two-dimensional effects. Bretonnet et al. [16] revisited the idea of asymmetric peak mixing in variable density shear layers with a study focused on centerline drift and advective growth for laminar mixing layers. The authors concluded that the generation

of a transverse velocity field is a critical variable density effect, and that this can be attributed to either diffusive effects, such as mass or temperature mixing, or by dissipative effects, such as kinetic heating. Diffusive effects from either mass or temperature mixing had the same effect of causing the mean velocity gradient to drift away from the mean density gradient, essentially decoupling the velocity shear region and the density-mixing region. On the other hand, dissipative effects were observed to produce a transverse velocity via dilatation due to heat release effects in the shear region. The study overall concluded that while multiple mechanisms exists, the overall variable density effect is that the shear layer shifts into the lighter fluid.

Studies of turbulent shear layers under variable density conditions have also indicated this asymmetric growth of the mixing region. Pantano and Sarkar's DNS of compressible, turbulent shear layers at $M_c = 0.7$ and density ratios of s_ρ ranging from 1 to 8 indicated that the the dividing centerline shifts into the low density stream as a function of the s_ρ. Turbulent shear stress magnitudes were not observed to decrease significantly with s_ρ, and Pantano concluded that increasing s_ρ decreases momentum mixing efficiency and this the turbulent growth rate. More recent investigations of variable density have also been enlightening, though they have been conducted in the incompressible regime. Almagro et al. [2] performed direct numerical simulations of low speed mixing layers at the same density ratios as Pantano, and observed that energy in small scales decreased gradually with increasing density ratio from analysis of the spectral energy distribution in velocity and temperature in the mixing region. Baltzer and Livescu [6] similarly performed direct numerical simulations of incompressible mixing layers with a focus on mixing layer asymmetry and density distribution, and visually identified a difference in turbulent scales from the low to high density sides of the shear layer. Similarly, in Livescu [79]'s review of variable density effects in canonical turbulent flows, it was summarized that turbulent features differ in light and heavy fluids, and that lighter fluids mix faster than heavier ones. In the turbulent mixing layer, this discrepancy of mixing rates results in an asymmetric mixing layer, with a larger thickness present on the lighter fluid side. Most recently, Morgan [90] studied scalar mixing in a temporal shear layer at $s_\rho = 3$ and used these results to calibrate model coefficients in the $k - L - a - V$ turbulence model.

Extensive work also exists on variable density shear layers with increased complexity. Among many others, notable studies include Okong'o and Bellan's DNS of supercritical temporal mixing layer to study high-pressure transitional mixing behavior, Ferrer et al.'s study of the effects of compressibility and heat release in high speed mixing layers with reactive chemistry, and Borghesi et al.'s simulation of an air and n-dodecane jet's ignition at diesel-relevant conditions. While relevant to the applications of this research, these configurations with more complex chemistry are beyond the scope of this thesis chapter.

Present objectives

Previous studies have provided insight into the contribution of density variations to reduced growth rates, but further investigation across a range of compressibility levels is necessary to assist with turbulence modeling efforts. In this chapter, the following questions on mixing layers with density variations are addressed:

- What are the effects of density variations on turbulent mixing and how do these effects vary with increasing compressibility?
- Are the compressibility effects on characteristic turbulent scales in variable density shear layers the same as those observed in mixing layers with equal freestream densities?
- What are the contributions of fluctuations in molecular weight, dilatation, and temperature to density fluctuations?

In this chapter, differences in mixing layer growth rates and other turbulent statistics between unity and variable density ratio cases are discussed and compared to previously published literature at constant compressibility values. To fully separate the effects of compressibility from the effects of density variations, a set of high fidelity simulations at a density ratio of 7 were conducted and used to compare with the unity density ratio shear layer calculations detailed in Ch. 1. Turbulent stress asymmetry and consistent selection of shear layer centerlines are discussed. The analysis of 'internal regulation' from Ch. 1 is applied to the variable density shear layers.

Lastly, the data is processed to isolate the variable density and compressibility effects can be isolated from each other. A method to identify density fluctuations due to compositional, temperature and pressure related fluctuations is proposed. The mean temperature profiles are also decomposed into a mixture component and a separate component introduced by viscous, aerodynamic heating.

3.2 Methodology

3.2.1 Governing equations

In addition to mass conservation and the Navier-Stokes equations in conservative form (Eqn. 2.2-2.4 in Ch. 2), the evolution equation for species mass fractions are also solved. The mass fraction for the species a and its corresponding evolution equation is given as

$$\begin{aligned} Y_a &= \frac{\rho_a}{\rho} \\ \frac{\partial \rho Y_a}{\partial t} + \frac{\partial}{\partial x_i}(\rho Y_a) &= \frac{\partial J_a}{\partial x_i} \end{aligned} \tag{3.1}$$

where ρ is the mixture density, and $J^{(a)}$ is the diffusion mass flux for species a. Species mixing is computed with a Fickian diffusion approximation [129]:

$$J_i = -\rho \left(D_i \bigtriangledown Y_i - Y_i \sum_{i=0}^{n_s} D_j \bigtriangledown Y_j \right) \tag{3.2}$$

For M species, compatibility with the continuity equation imposes the following constraint:

$$\sum_{a=1}^{M} J_a = 0$$

The thermodynamic properties of each species and the mixture are given below for completeness:

$$R_a = \frac{R_u}{MW_a} \qquad R_{mix} = \sum_{a=1}^{M} Y_a R_a$$

For the present configuration at density ratio of $s_\rho = 7$ and a universal gas constant $R_u = 1$, $MW_2 = 1.75$ and $MW_2 = 0.25$. The numerical methods for time intergration, spatial derivatives and solution filtering for these variable density flows are the same as those used in Ch. 2.

3.2.2 Physical parameters

$$M_c = \frac{\Delta \bar{u}}{c_1 + c_2} \qquad s_\rho = \frac{\rho_1}{\rho_2} \qquad Re_\theta^0 = \frac{\Delta \bar{u} \delta_\theta(0)}{\nu} \qquad Re_\omega^0 = \frac{\Delta \bar{u} \delta_\omega(0)}{\nu} \tag{3.3}$$

The convective Mach number M_c quantifies the compressibility of the base flow, while the Reynolds numbers establish the range of viscous scales which may develop under turbulence. Documentation comparing domain sizes, Reynolds numbers, and Kolmogorov scale resolution for this problem and previously published DNS studies is offered in Table 2.3. Pantano's similar study up to $M_c = 1.1$

and with variable density effects studied at a single $M_c = 0.7$ [103], but previously available data has generally been insufficient to clearly isolate compressibility effects from density effects over the full range of M_c. The suite of cases presented in this work are shown in Table 3.1. Cases with $s_\rho = 1$ serve as the single fluid reference cases for cases at $s_\rho = 7$. These variable density cases each have the temperature ratio $T_1/T_2 = 0.51$ and molecular weight ratio $MW_1/MW_2 = 7$. The freestreams in these cases are both mixtures and not pure fluids; for example the top freestream has mass fractions $Y_1 = 0.875, Y_2 = 0.125$. The two freestreams are split by the centerline defined nominally as $\tilde{u}(y_c) = 0$; various definitions of y_c are explored in a later section.

Each case was run at the same initial Reynolds numbers $Re_\theta^0 = 1000$ and $Re_\omega^0 = 4000$, Prandtl number $Pr = 0.7$, and Schmidt number $Sc = 1$. Initial conditions and modal velocity perturbations are consistent with those detailed in Ch. 1. Mean profiles of the variable density cases listed in Table 3.1 are shown in Fig. 3.3. Individual lines on each plot represent a single snapshot in time. Profiles are plotted for several snapshots within the self-similar range of this study, though perfect self-similarity was difficult to achieve at high M_c due to limitations on the computational domain and due to viscous dissipation in the highest M_c case with $s_\rho = 7$. Similar computational limitations in the $M_c = 2.0, s_\rho = 7$ case account for the slight departure of mean variables from the nominal free-stream value above $(y - y_c)/\delta_{99} = 0.6$. Differences in the mean temperature profile across the M_c range occur at both $s_\rho = 1$ and $s_\rho = 7$ as a result of aerodynamic heating, which will be discussed at the end of this chapter.

Table 3.1: Parameters, domains, and grid resolutions for cases studied. All cases use $N_x \times N_y \times N_z = 1024 \times 1448 \times 512$ uniformly spaced grid points.

M_c	s_ρ	T_1/T_2	$\frac{1}{\delta_\theta^0}(L_x \times L_y \times L_z)$	$\frac{1}{\delta_\theta^0}(\Delta x \times \Delta y \times \Delta z)$
0.2	1	1.00	$150 \times 200 \times 75$	$0.146 \times 0.138 \times 0.146$
0.2	7	0.51	$150 \times 200 \times 75$	$0.146 \times 0.138 \times 0.146$
0.8	1	1.00	$100 \times 100 \times 50$	$0.098 \times 0.069 \times 0.098$
0.8	7	0.51	$100 \times 100 \times 50$	$0.098 \times 0.069 \times 0.098$
2.0	1	1.00	$80 \times 80 \times 40$	$0.078 \times 0.055 \times 0.078$
2.0	7	0.51	$80 \times 80 \times 40$	$0.078 \times 0.055 \times 0.078$

Table 3.2: A brief comparison of parameter ranges with previous studies on compressible, variable density mixing layers. The Atwood number is related to the density ratio by $At = (1 - s_\rho)/(1 + s_\rho)$.

Study	M_c	At
Pantano (2002) [103]	0.7	0, 0.33, 0.60, 0.77
Almagro (2017) [2]	0	0, 0.33, 0.60, 0.77
Baltzer (2020) [6]	0	0, 0.25, 0.50, 0.75, 0.87
Matsuno (2020) [84]	0.2, 0.8, 2.0	0, 0.75
Morgan (2021) [90]	0	0.25

3.3 Effects of density variations on turbulent statistics

In this section, the effect of non-unity density ratio and convective Mach number on mean flow field profiles, turbulent fluctuations, and turbulent growth rates are presented, followed by analysis of the asymmetric behavior of the flow. Line opacity indicates time history, such that the faintest lines occur earlier in simulation time and more opaque lines occur later in simulation time. Error bars on data points representing mean values over time indicate the standard deviation about the mean during the averaging window. Likewise, profiles plotted in a single solid line with a similarly colored translucent envelope indicate the planar mean value and corresponding standard deviation at each transverse (y) location.

3.3.1 Growth rates and turbulent stresses

The normalized growth rates of the momentum thickness, defined in 2.5, become linear after an initial period of transition, and decrease significantly with increasing convective Mach number. Rates are normalized by incompressible growth rates $\dot{\delta}_{inc} = 0.018, 0.013$ [103] for $s_\rho = 1, 7$ cases, respectively. Figure 3.1 shows the effect of density ratio on normalized growth rates, and Fig. 3.1b gives the ratio of the growth rate for $s_\rho = 7$ compared to $s_\rho = 1$. These values indicate a 50-60% drop in the momentum thickness growth rate, which is in the range of growth rate reductions observed by previous studies at a similar Atwood numbers (see Fig. 3.1c). Complete decoupling between compressibility and variable density effects on shear layer growth has been assumed in previous experimental studies [105, 52]. However, Almagro et al. compared their numerical simulations of incompressible mixing layers to Pantano and Sarkar's compressible mixing layer (at $M_c = 0.7$) and observed a weak dependence on density ratio effects between the incompressible and compressible configurations. Likewise, the present data trend in Fig. 3.1b is not perfectly flat and has a slight trend with increasing M_c which suggests that the effect of density ratio on growth rates may be larger at lower compressibility levels.

Profiles of kinematic Reynolds stresses $R_{ij} = \overline{u_i' u_j'}$ against the self-similar coordinate $(y - y_c)/\delta_{99}$ have been shown to reflect well known asymmetry in [84]. The shift of the Reynolds stress peaks and mixing layer centerline y_c (defined as $\tilde{u}(y_c) = 0$) was noted early on by Brown & Roshko [19]. As discussed by Pantano & Sarkar, this shift of peak turbulent stress towards the lower density region results in reduced momentum transport $\overline{\rho u'' v''}$, and thus the significant reduction in growth rate [103]. The kinematic turbulent shear stresses R_{12} plotted in Fig. 3.1d show a noticeable intrusion into the lower density fluid (present data has been plotted against $-y$ instead of y for consistent comparison to data from Almagro et al. [2] and Baltzer and Livescu [6]), confirming that the lighter fluid is more prone to turbulent fluctuations and mixing compared to the heavier fluid. Note that the present data in Fig. 3.1d is plotted by $-y$ to match with the reference data. This asymmetry remains present with increasing compressibility, as seen in Fig. 3.2. Mass weighted mean and turbulent stress profiles are shown in Fig. 3.3. There exists a noticeable decrease in peak stress magnitudes across the M_c range at both $s_\rho = 1$ and $s_\rho = 7$, but mass-weighted turbulent stress profiles show more asymmetry at $s_\rho = 7$ compared to $s_\rho = 1$.

The turbulent Mach number, $M_t = \sqrt{2k}/\bar{c}$, compares the velocity scales of turbulent fluctuations with respect to the speed of sound. As shown in Fig. 3.2, present data indicates that the turbulent Mach number profile across the shear layer shows similar behavior at $s_\rho = 1$ and $s_\rho = 7$, with the exception that the profiles at $s_\rho = 7$ are slightly less broad near the centerline. Peak M_t values are elevated at $s_\rho = 7$. Although TKE profiles are elevated in the lighter fluid region, similar asymmetry is not apparent in the turbulent Mach number because the speed of sound along the lighter fluid is also elevated compared to the speed of sound in the heavier fluid.

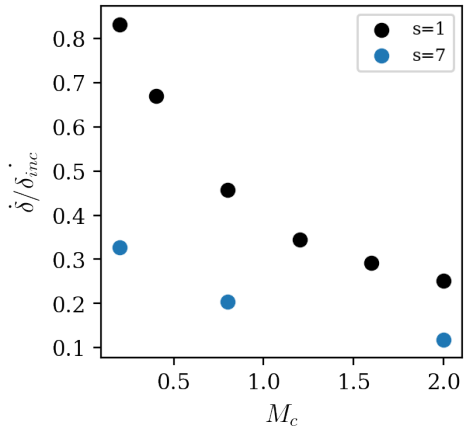

(a) Momentum thickness growth rates normalized by corresponding incompressible values

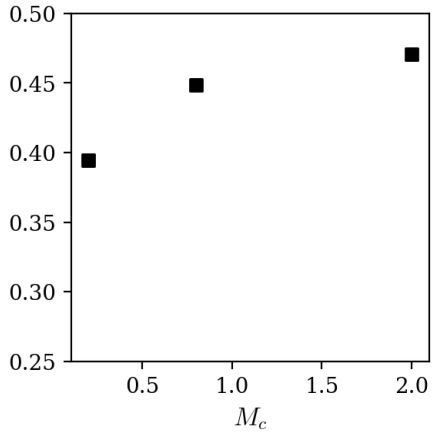

(b) Ratio of variable density ratio to unity density ratio growth rates, $\dot{\delta}(s_\rho = 7)/\dot{\delta}(s_\rho = 1)$

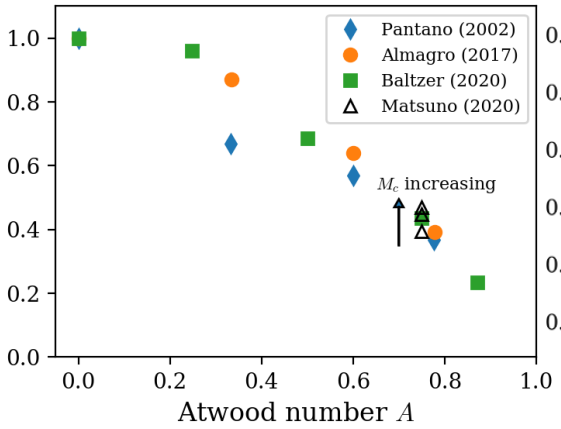

(c) Variable density growth rates normalized by growth rates at $A = 0$ cases compared to previously published DNS [2, 6, 103].

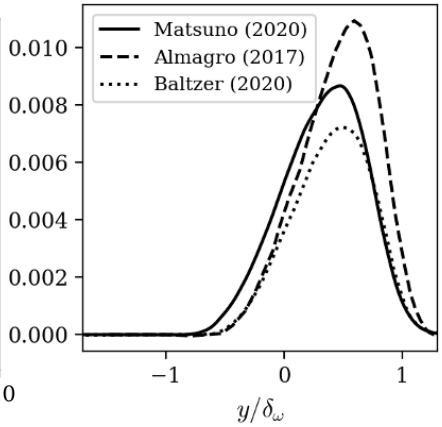

(d) Comparison of present kinematic $|R_{12}| = |\overline{u'v'}|$ at $M_c = 0.2$ to Almagro [2] and Baltzer [6] data at $M_c = 0$.

Figure 3.1: Growth rates and stresses for variable density cases compared to previously published results.

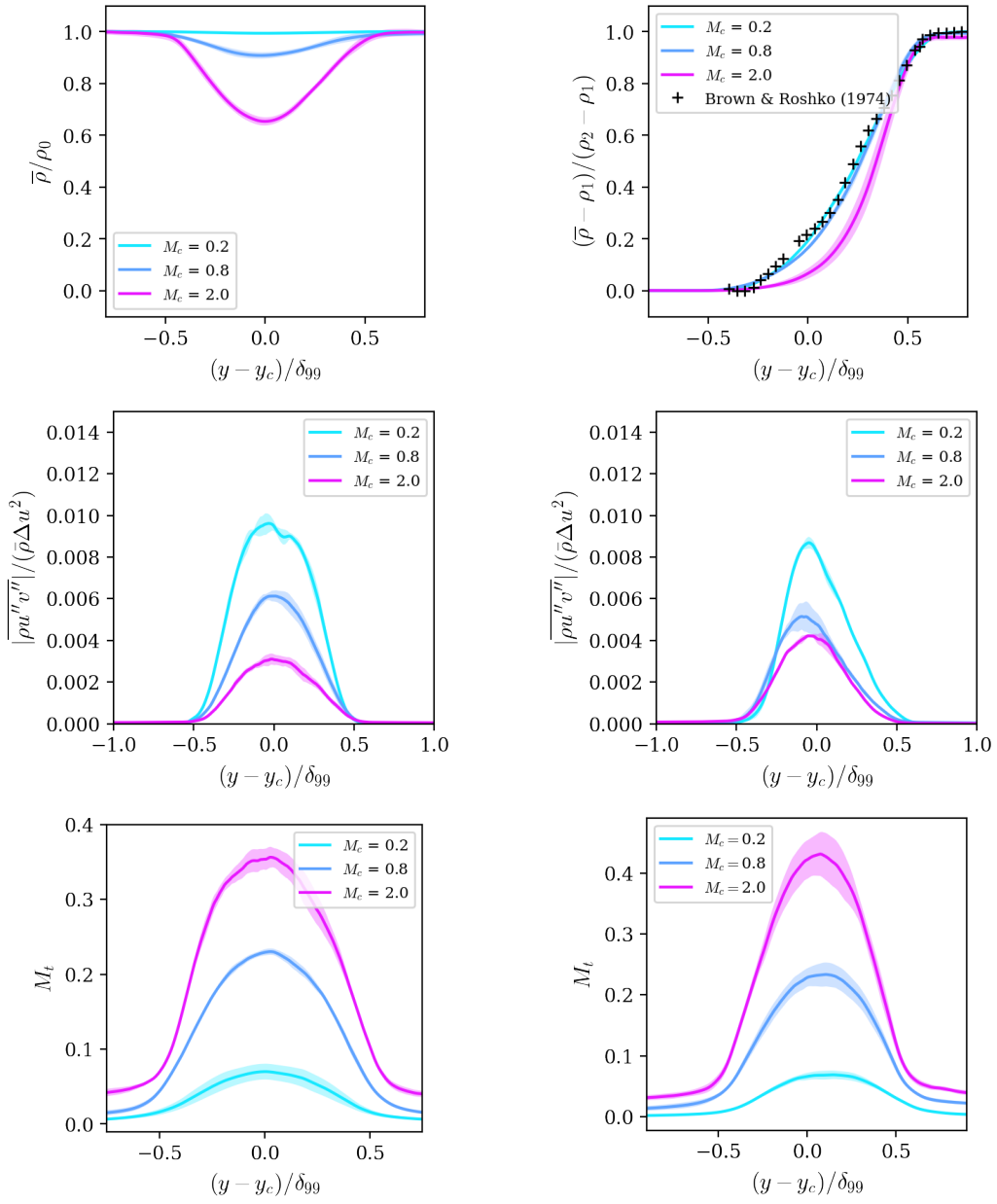

(a) $s_\rho = 1$ (b) $s_\rho = 7$

Figure 3.2: Mean density profiles (top), turbulent shear stress (middle) and turbulent Mach number (bottom) profiles.

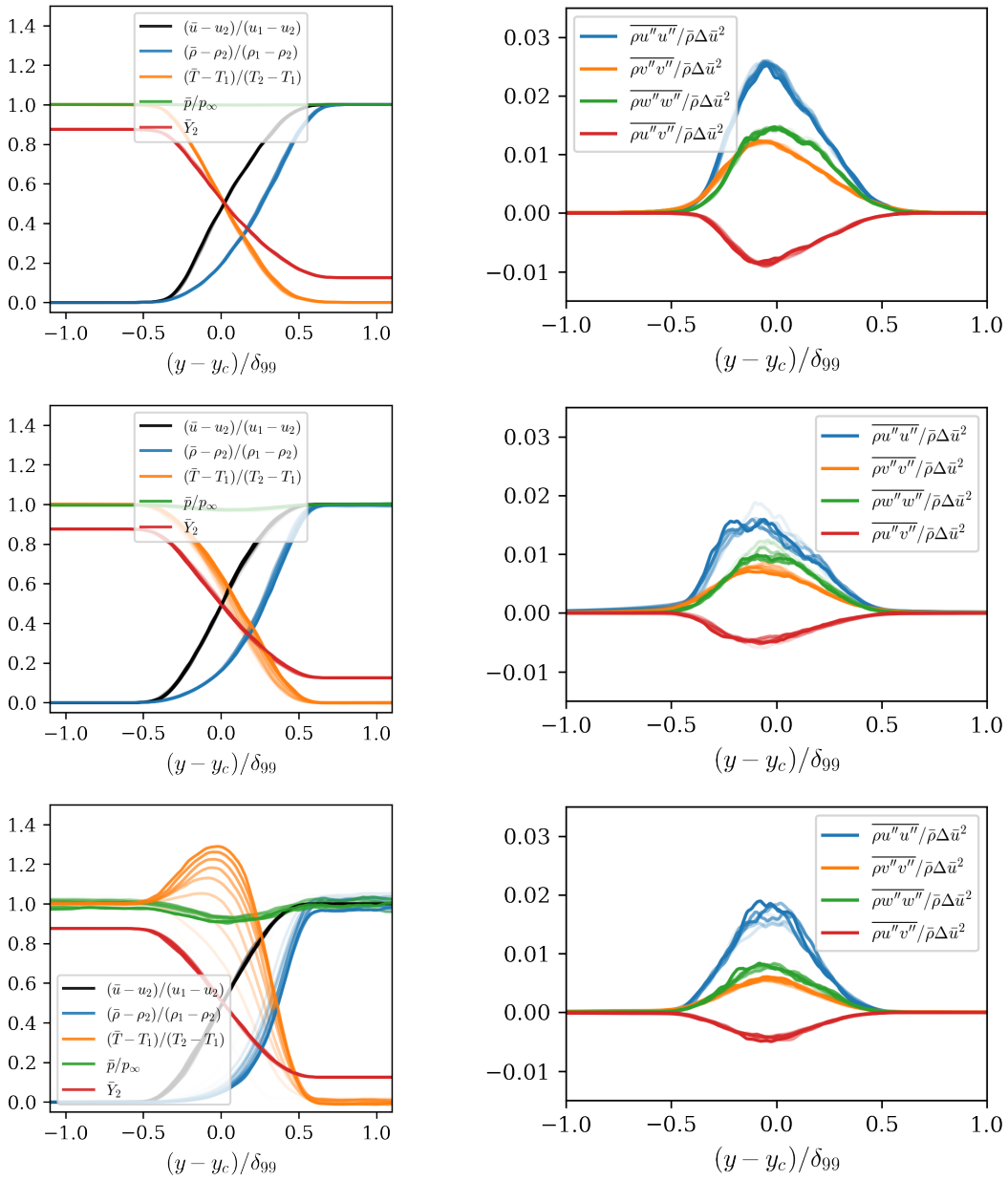

(a) $s_\rho = 1$ (b) $s_\rho = 7$

Figure 3.3: Mean profiles for the suite of cases analyzed in this work, shown during the approximately self-similar range. Left column: $s_\rho = 1$; right column: $s_\rho = 7$. From top to bottom: $M_c = 0.2, 0.8, 2.0$.

3.3.2 Mass fluxes

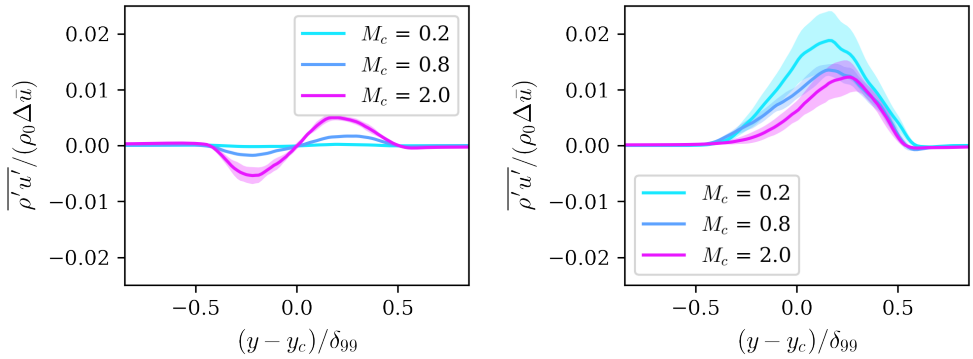

(a) Streamwise turbulent mass flux

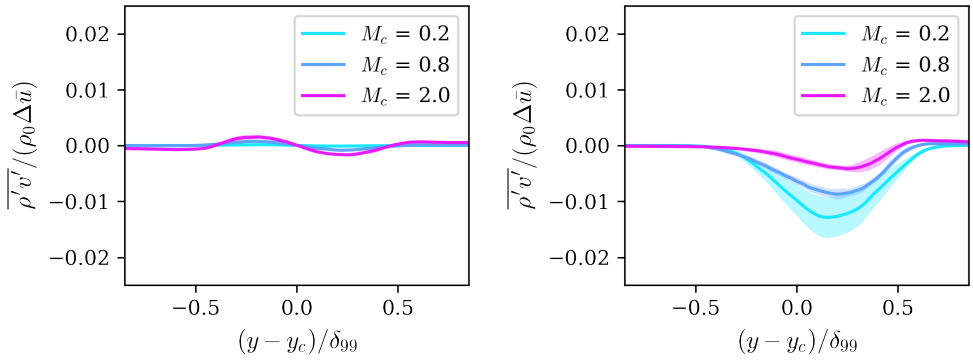

(b) Transverse turbulent mass flux

Figure 3.4: Profiles of streamwise and transverse turbulent mass fluxes and at various compressibility levels for $s_\rho = 1$ (left) and $s_\rho = 7$ (right).

Variable density effects are also evident in turbulent mass flux profiles, $\overline{\rho' u_i'}$. Streamwise and transverse turbulent mass fluxes are anti-symmetric about the centerline for $s_\rho = 1$ at $M_c = 0.2, 0.8$ and 2.0. For both the streamwise and transverse components, the peak mass flux occurs closer to the edges of the mixing layer, with a minimum mass flux at the centerline. This indicates that most of the transfer of mass due to turbulent fluctuations occurs due to entrainment from each of the freestreams into the turbulent region. In contrast, a complete change in mass flux profiles occurs when a mean density variation is present. The peak mass flux occurs near the centerline instead of the mixing layer edges, and the magnitude of the mass fluxes are also greatly increased at $s_\rho = 7$ compared to $s_\rho = 1$. Baltzer and Livescu showed, at the limit of $M_c \to 0$, that mass flux profiles peak in the denser fluid because large-scale disturbances form on the heavy fluid side which correspond

to "large displacements of largely unmixed fluids relative to the background density gradient". The authors claimed this leads to larger density fluctuations on the heavy side compared to the lighter side with fine-scale turbulent features and smaller density fluctuations, and this in turn biases the mass flux to the heavy fluid side. In the present data, both the streamwise and transverse mass flux are also skewed towards the denser freestream occurs at all compressibility levels. This appears to indicate that mass transfer due to turbulent fluctuations occurs mainly from turbulent stirring of the mean density gradient rather than the mean velocity gradient. The interaction between these mean mass flux and the turbulent mass fluxes are discussed below.

$$\frac{\partial \bar{\rho}}{\partial t} = -\frac{\partial}{\partial x_j}(\bar{\rho}\bar{u}_j + \overline{\rho' u'}) \tag{3.4}$$

In the Reynolds-averaged mass equation, written explicitly in Eqn. 3.4, the divergence of turbulent mass flux and mean mass flux contribute to the evolution of the mean density profile. In the present shear layer configuration, only the $\frac{d}{dy}(\bar{\rho}\bar{v} + \overline{\rho' v'})$ is nonzero due to flow homogeneity in the x and z directions. For the available variable density cases, the turbulent mass flux $\overline{\rho' v'}$ serves to reduce the mean mass flux $\bar{\rho}\bar{v}$ (see Fig. 3.5), with this reduction effectively decreasing with increasing M_c. Correspondingly, the source terms driving the evolution of $\bar{\rho}$ become relatively larger at high M_c; this is consistent with the larger changes (more pronounced curvature) in the variable density $\bar{\rho}$ seen at $M_c = 2.0$ compared to $M_c = 0.2$ and 0.8. The normalized mean density profiles at $s_\rho = 7$ compare well with Brown & Roshko's mean density profile at the same density ratio in a low speed, $He - N_2$ mixing layer, but shows differences when compared to the supersonic mixing layer. A trend emerges where the mean density profiles exhibit more curvature for higher speed mixing layers compared to the low speed ones. Pronounced curvature in $\bar{\rho}$ is also evident with $s_\rho = 1$ at high M_c, caused by aerodynamic heating (i.e. viscous dissipation). This dip in density at $M_c = 2.0, s_\rho = 1$ within the turbulent region is directly proportional to the peak in temperature seen in Fig. 3.3; the rise in mean temperature deepens the concavity of mean density, which in turn drives the turbulent mass flux.

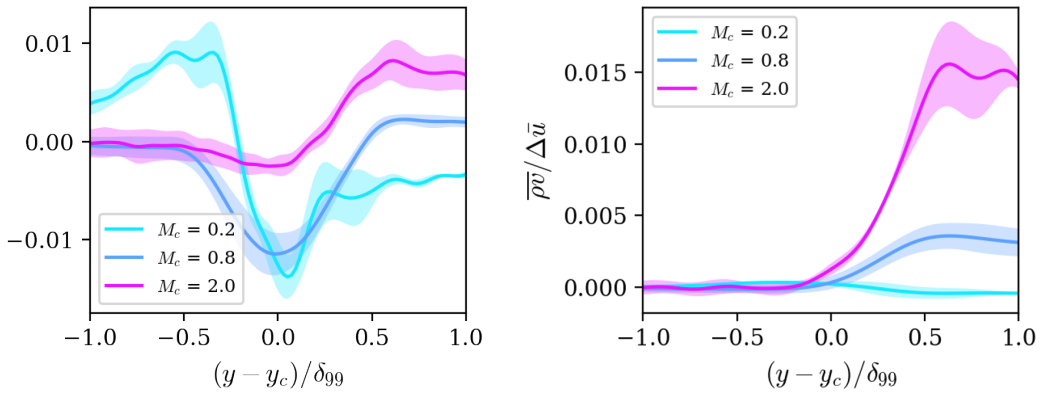

Figure 3.5: Mean transverse velocity $\tilde{v}/\Delta\bar{u}$ and mean transverse mass flux $\bar{\rho}\bar{v}$ for $s_\rho = 7$.

3.3.3 Mixing layer centerline and asymmetry

Several previous studies of incompressible mixing layers have recorded asymmetric spreading of the mixing layer. The present data also presents a consistent trend of preferential spreading towards the lighter fluid region at all compressibility levels. To quantitatively assess this asymmetry, first consider several candidates to define the shear layer centerline, y_c, in Eqn. 3.5 below.

$$\bar{\rho}(y_c) = \frac{\rho_1 + \rho_2}{2} = \rho_0 \qquad \tilde{u}(y_c) = 0 \qquad Y_1(y_c) = Y_2(y_c) \tag{3.5}$$

The centerline can be defined by the location of 'neutral' density, or the location of the mean density of the freestreams. Alternatively, the location of zero mean streamwise velocity can also be used a centerline definition, which is common for the counter-current, temporal shear layer configuration, where each freestream has a velocity of $\pm\Delta U$. Lastly, using the location of equivalent mass fractions is also considered to represent a dividing centerline between the two freestreams. The left column of Fig. 3.7 clarifies the behavior of the centerline using each of the definitions above, using the mean profiles for streamwise velocity, density and mass fraction normalized to range from zero to unity across the mixing layer. The mean profiles at two instances in time are shown to indicate that the behavior is consistent during the turbulent evolution of the flow. A distinct difference arises between the centerline defined by the mean density compared to the alternative definitions. This discrepancy increases slightly with M_c. Excluding the mean-density defined y_c, all other centerline definitions indicate that the shear layer centerline drifts into the lighter fluid. This intuitively makes sense–the mixed, heavier fluid gradually pushes into the freestream, lighter fluid due to its higher momentum. This is also consistent with information from profiles of the transverse

turbulent mass flux in Fig. 3.4, which indicate that mass transport via turbulent fluctuations occurs downward (into the lighter fluid region).

The right column of Fig. 3.7 shows the evolution of the shear layer bounds into the denser (blue) and lighter (orange) freestreams, as defined by δ_{99}. The velocity-defined centerline, corresponding to $\tilde{u} = 0$, and the density-defined centerline, corresponding to $\bar{\rho} = \rho_0$, are shown in solid and dashed lines, respectively. In these figures, the preferential spreading of the shear layer towards to the lighter fluid side can be observed, particularly in the $M_c = 0.2$ case. The ratio of growth rate of the shear layer boundary from the chosen shear layer centerline into the heavy (top) and light (bottom) freestreams are given in the legend as $\dot{\delta}_{top}/\dot{\delta}_{bot}$ in each of the legends provided. Using the velocity-defined centerline, the rates of spreading into the heavy and light fluids are approximately unity across the compressibility levels. In contrast, the density-defined centerline suggests that the heavier fluid contributes very little to the overall growth rate. This difference between the centerline based upon mean density compared to mean velocity appears exaggerated at the highest compressibility case at $M_c = 2.0$. This may be related to the previously mentioned increase in concavity of the mean density profile as aerodynamic heating increases the mean temperature near the main mixing region at the velocity-based centerline.

Baltzer also showed that the contribution of the momentum thickness growth from the lighter fluid was much greater than that of the heavier fluid at $M_c = 0$. By splitting the momentum thickness growth rate into two integral components–the contribution from the lighter fluid, and the contribution of the heavier fluid, the dependence of growth rate ratios on the centerline definition can be alternatively confirmed. Baltzer previously used the density definition of y_c in Eqn. 3.6 to examine these contributions to the total shear layer growth.

$$\dot{\delta}_\theta = -\frac{2}{\rho_0(\Delta\bar{u})^2}\left(\int_{-L_y/2}^{y_c} \bar{\rho}\widetilde{u''v''}\frac{\partial\tilde{u}}{\partial y}dy + \int_{y_c}^{L_y/2} \bar{\rho}\widetilde{u''v''}\frac{\partial\tilde{u}}{\partial y}dy\right) \tag{3.6}$$

In Fig. 3.6a, our data confirms Balter's observation (plotted at $M_c = 0$) remains true across the available range of compressibility levels using the mean density definition of the shear layer centerline. Again, as previously discussed, differences arise when using alternative shear layer centerline definitions. As shown in Fig. 3.6b, using the centerline defined by velocity indicates that both 'sides' of the shear layer contribute almost equally to the total growth rate, with a slightly larger contribution by the heavier fluid side.

Turbulent mixing, TKE, and production of TKE are concentrated at the region of the peak streamwise velocity gradient, which occurs more closely to the centerline as defined by velocity rather than density. Thus, throughout this work, the centerline defined by the mean streamwise velocity is used to collapse profiles of mean and turbulent quantities. As discussed in the following

section 3.3.4, this choice of the shear layer centerline is also relevant in the selection of characteristic turbulent scales.

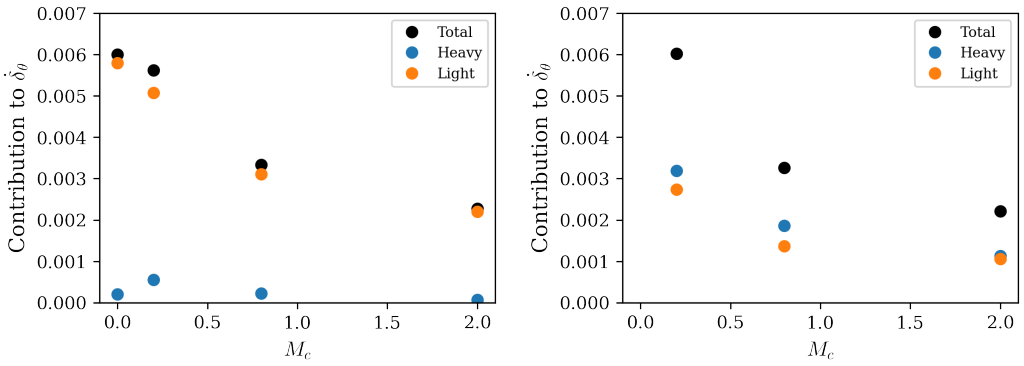

(a) $\bar{\rho}(y_c) = \rho_0$ (b) $Y_1(y_c) = Y_2(y_c)$

Figure 3.6: Contribution to growth rate using different definitions of the centerline, y_c.

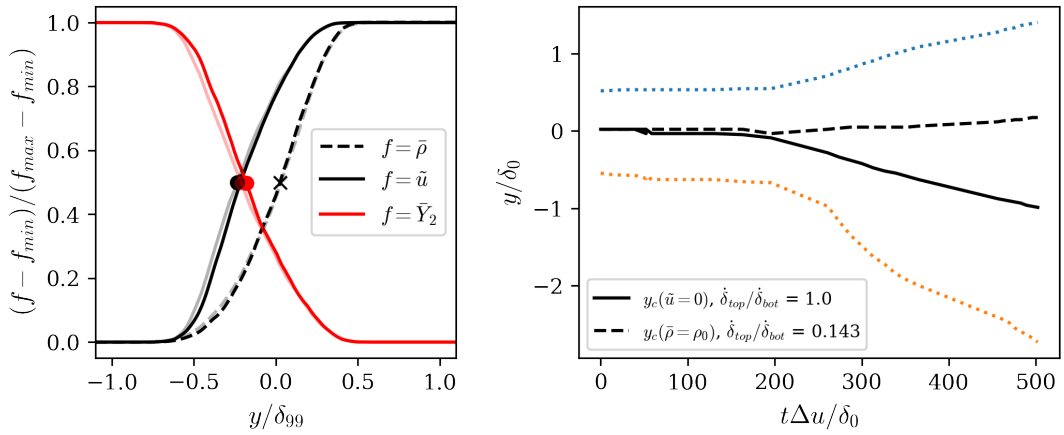

(a) $M_c = 0.2, s_\rho = 7$

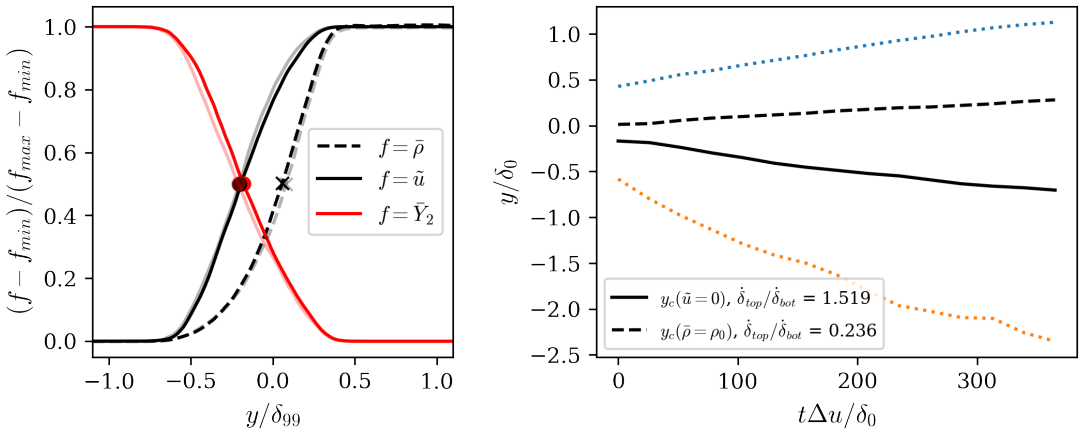

(b) $M_c = 0.8, s_\rho = 7$

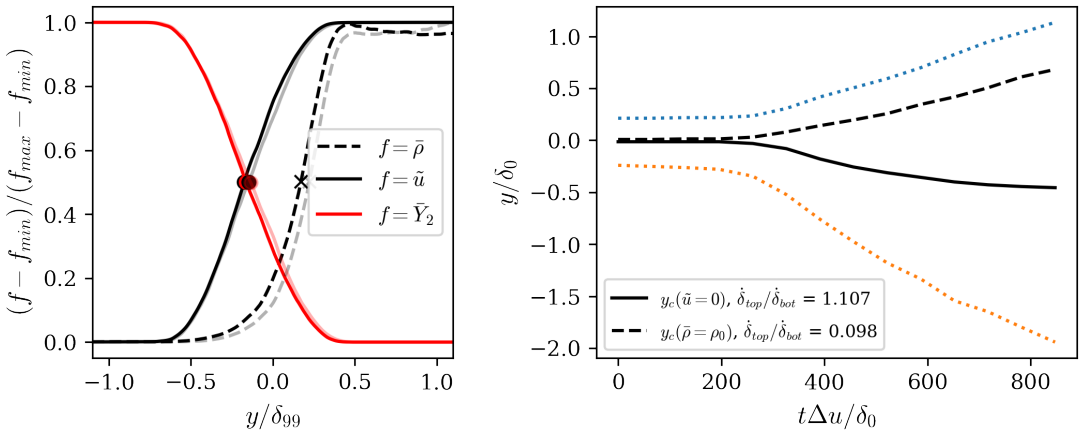

(c) $M_c = 0.2, s_\rho = 7$

Figure 3.7: Definitions of centerline y_c: (left) centerline positions at two instances in time; (right) centerline position drift in time compared to shear layer bounds at the denser (blue) and lighter (orange) freestreams. Note that density, velocity, and mass fraction profiles have been normalized to range from zero to one.

3.3.4 Turbulent scales and internal regulation

Following the discussion in Ch. 1, internal regulation refers to the scaling of turbulent quantities with respect to the integral lengthscales within the mixing layer rather than the external scales across the mixing layer–such as the 99% thickness δ_{99} and the total velocity difference $\Delta\bar{u}$. In this section, the data for $s_\rho = 7$ will be analyzed from the view of internal regulation and compared to similar scales at $s_\rho = 1$. The definition of the decorrelation function using transverse velocity fluctuations $v\prime$ about anchor point y_0 is written explicitly again in Eqn. 2.22.

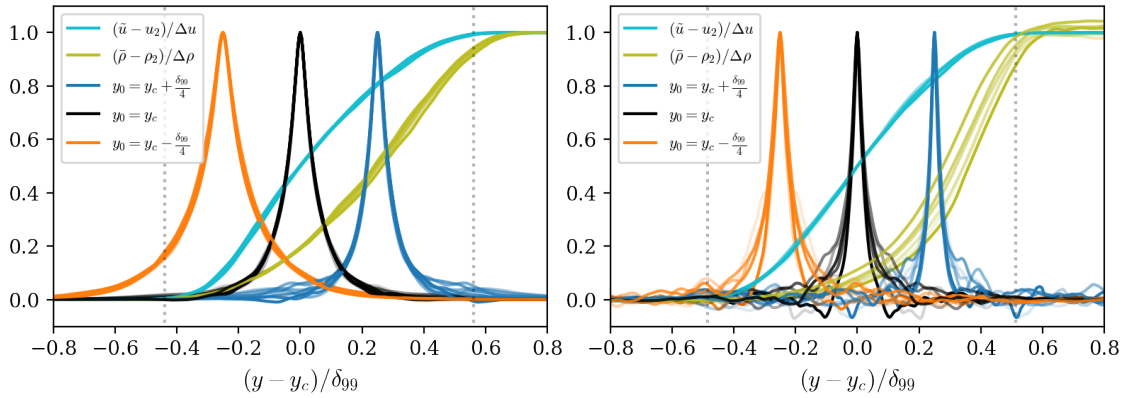

(a) $M_c = 0.2, s_\rho = 7$ autocorrelation profiles

(b) $M_c = 2.0, s_\rho = 7$ autocorrelation profiles

Figure 3.8: Transverse velocity decorrelation profiles centered about various y_0 at low and high compressibility levels.

The behaviors of the decorrelation length scale δ_y ('internal' or 'effective' length scales) at low and high compressibility levels are shown in Fig. 3.8. Profiles of the autocorrelations used to define the decorrelation scale are superimposed on the normalized mean velocity profile $\tilde{u}$ in cyan, the normalized mean density profile $\bar{\rho}$ in green, along with the upper and lower bounds of the 99% thickness. Decorrelation profiles with anchor points at the velocity-defined centerline are shown in black; profiles with anchor points offset by $\delta_{99}/4$ into the lighter and heavier fluid are shown in orange and blue, respectively. Two characteristics of these decorrelation profiles warrant discussion.

First, notable change in the overall span of the decorrelation occurs between low and high compressibility levels. At low M_c, a significant portion of the autocorrelation remains above the decorrelation threshold past the lower boundary of the mixing region, whereas the autocorrelations are completely contained within the mixing region at high M_c. This trend is consistent across the M_c range for $s_\rho = 1$ cases. The monotonic decrease in the internal length scales as a function of M_c, for both centerline and off-centerline anchors y_0, are shown in Figs. 3.8a and 3.8b. The

corresponding decrease in the internal velocity scale U_δ, where U_δ is the mean velocity difference across an eddy sized δ_y at y_c, can be observed in Figs. 3.8c and 3.8d.

Second, the decorrelation scale is asymmetric across the shear layer centerline. This asymmetry was discussed further in subsection 3.3.3 above, in the context of the mean profiles of velocity and density. Present data indicates that the scales defined by turbulent fluctuations are also asymmetric when sampled at equal distances $\delta_{99}/4$ from the centerline. At all compressibility levels, the transverse decorrelation scale δ_y in the heavier fluid region (at $y_c + \delta_{99}/4$) is larger than δ_y in the lighter fluid region (at $y_c - \delta_{99}/4$). This contrasts with the distribution of lengthscales at $s_\rho = 1$, in which case the off-centerline decorrelations are consistently but symmetrically larger than the centerline value. The internal length and velocity scales in the lighter fluid, plotted with orange markers, have values which are larger in magnitude than the scales near the velocity-defined centerline, plotted in black markers. The internal length and velocity scales in the denser fluid, plotted with blue markers, have values which are more similar in magnitude but slightly smaller than the scales near the velocity-defined centerline. This variation in the internal length and velocity scales is notable, since it is the scales defined about the centerline which show most promising scaling of turbulent statistics (as discussed later in Fig. 3.10).

For completeness, streamwise and spanwise decorrelation lengths ratios at the centerline defined by velocity for $s_\rho = 7$ are shown in Fig. 3.9e and show similar behavior to those at $s_\rho = 1$, with the streamwise-transverse decorrelation ratio δ_x/δ_y always slightly larger than the spanwise-transverse one, δ_z/δ_y. Note that at $M_c = 2.0$ for both $s_\rho = 1$ and $s_\rho = 7$, error bars are especially large due to difficulty in achieving true self-similarity.

Profiles of turbulent production P, dissipation D, and the streamwise component of pressure strain $\Pi_{11} = 2\overline{p'\partial u''/\partial x}$ are shown in Fig. 3.10. When scaled by total shear layer scales $\Delta\bar{u}^3/\delta_{99}$, turbulent production, dissipation and pressure strain decrease monotonically with increasing M_c. In contrast, normalizing by internal quantities U_δ^3/δ_y, measured at the shear layer centerline defined by $\tilde{u}(y_c) = 0$, collapses the profiles across the M_c range. Similar behavior was observed for corresponding quantities at $s_\rho = 1$ [85]. The consistent collapse in data for both $s_\rho = 1$ and $s_\rho = 7$ suggests the dependency on internal scales is a compressibility effect and likely not a variable density effect. As in Ch. 1, this can be interpreted as internal regulation arising from a sonic limitation on eddies which actively entrain fluid.

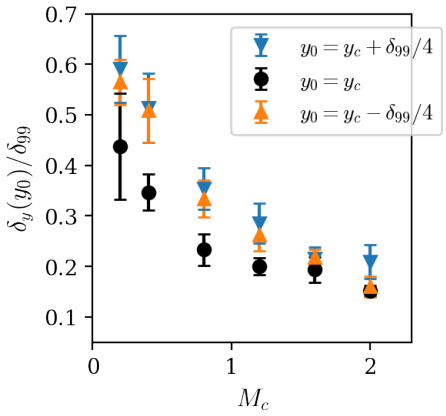

(a) δ_y/δ_{99} measured about various y_0 for $s_\rho = 1$

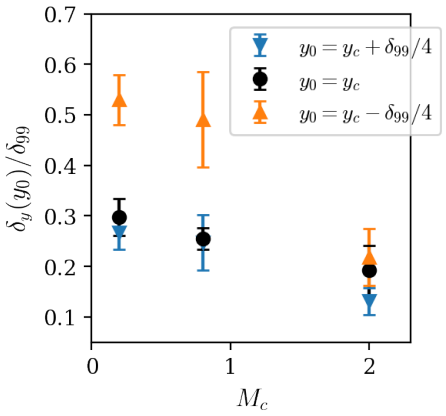

(b) δ_y/δ_{99} measured about various y_0 for $s_\rho = 7$

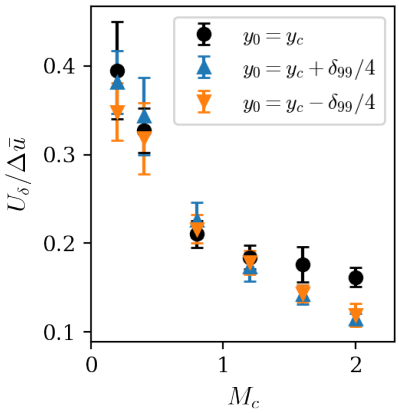

(c) U_δ measured about various y_0 for $s_\rho = 1$

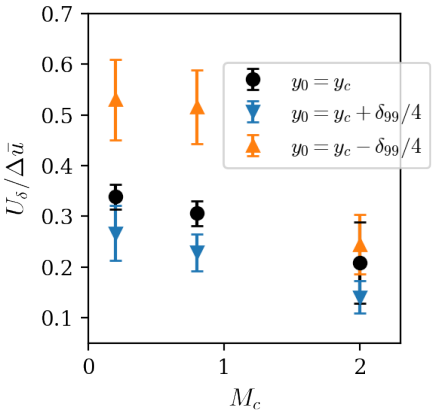

(d) U_δ measured about various y_0 for $s_\rho = 7$

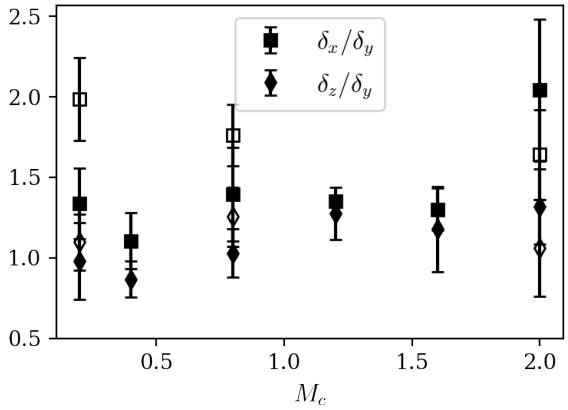

(e) Lengthscale ratios at $s_\rho = 1$ (filled markers) and $s_\rho = 7$ (open markers)

Figure 3.9: Decorrelation scales centered about various y_0; (a) and (b) decorrelation scale; (c) and (d) decorrelation velocity scale; (e) length scale ratios about the centerline y_c.

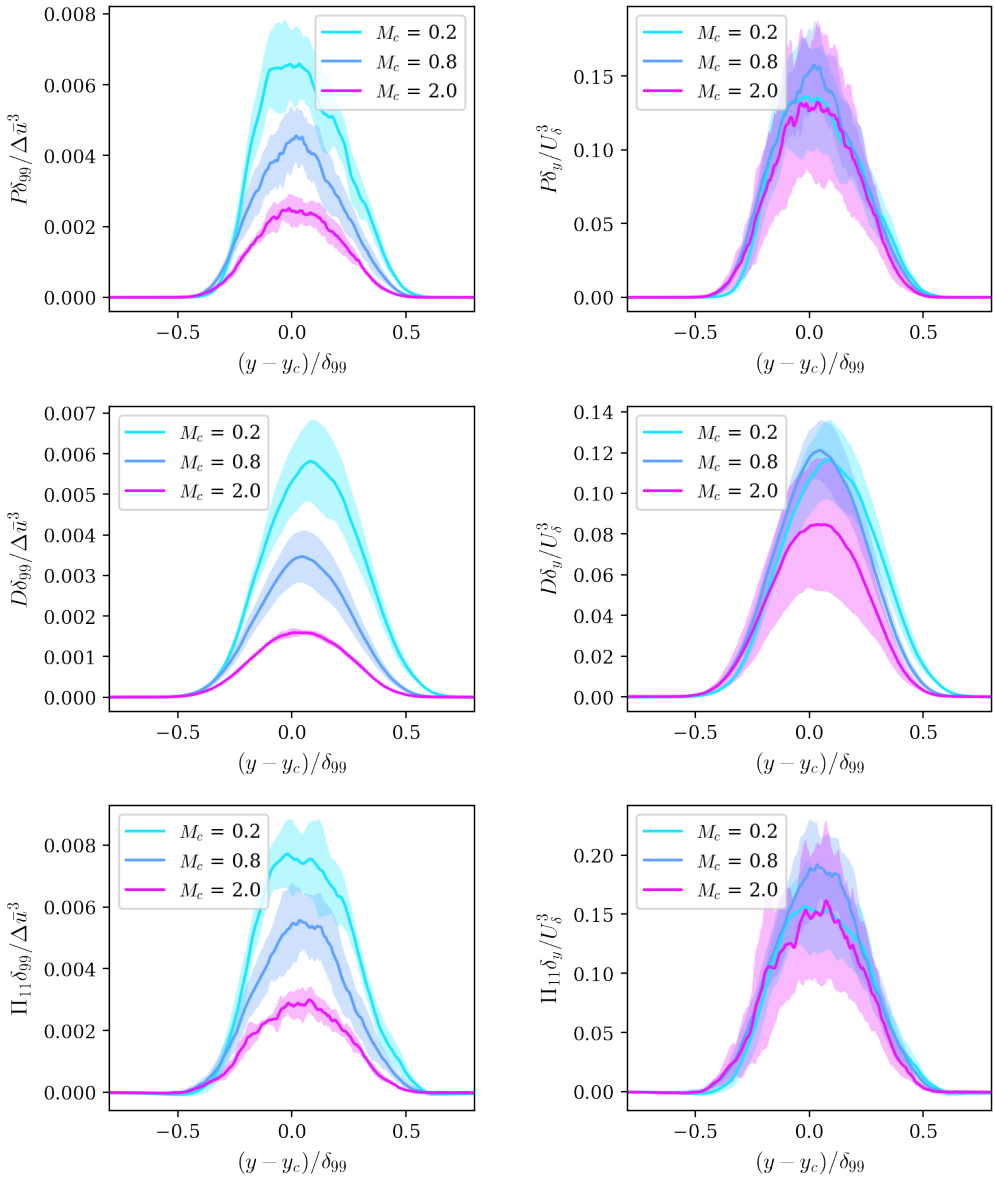

Figure 3.10: Magnitude profiles of TKE production P, TKE dissipation D, and streamwise component of pressure strain Π_{11} at $s_\rho = 7$. Left column: scaling by $\delta_{99}/\Delta\bar{u}^3$; right column: scaling by δ_y/U_δ^3.

3.4 Decomposition of density fluctuations

The goal of this section of work is to examine density variations in the compressible shear layer for the available variable density cases. Mechanisms contributing to density fluctuations may be categorized as compositional changes, adiabatic fluctuations, and thermal effects. The contribution from each of these mechanisms and its correlation with density fluctuations is given below.

Compositional variation

The density field associated with compositional changes, ρ_m, is the density field which would result from isobaric mixing of the pure fluids without compressibility effects. The resulting mixture density variation is then taken as the fluctuation from the mean density $\bar{\rho}_m$. Pure species densities associated with Y_1 and Y_2 are ρ_1 and ρ_2, respectively; $\bar{q}$ represents the planar (x and z) average of field q.

$$\frac{1}{\rho_m} = \frac{Y_1}{\rho_1} + \frac{Y_2}{\rho_2} \qquad \rho'_m = \rho - \rho_m \tag{3.7}$$

Adiabatic variation

The density field associated with adiabatic compression and expansion, ρ_a, is the density which would result purely from isentropic dilatation for a given pressure field. The reference state in the Eulerian frame is defined by the background mean density and pressure which varies in y.

$$\rho_a = \bar{\rho}\left(\frac{p}{\bar{p}}\right)^{1/\gamma} \qquad \rho'_a = \rho - \rho_a \tag{3.8}$$

Isobaric variation

The density field associated with thermal effects ρ_T, is defined as the density fluctuations solely due to temperature fluctuations from the mean temperature, $\bar{T}$. These density fluctuations represent hypothetical variations which would occur for a given departure from the mean temperature while holding the local pressure and local mass fractions constant.

$$\rho_T = \bar{\rho}\frac{\bar{T}}{T} \qquad \rho'_T = \rho - \rho_T \tag{3.9}$$

The density fluctuation magnitudes associated with each of the density fields defined in Eqns. 3.7-3.9 are compared across the M_c range in Fig. 3.11. Each variance is normalized by the mean density, $\bar{\rho}$. The full density variance is shown in black. An initial observation regarding the shape of these profiles emerges–with increasing M_c, the steepness and skewness of the profiles at $s_\rho = 7$

increases. This is consistent with the difference in curvature of the mean density profiles observed in Fig. 3.2, and is likely a result of the peaked heating region at higher M_c. The profiles of density variance at $s_\rho = 1$ are symmetric and indicate larger variance at the shear layer edges. In general, it can also be observed that the density fluctuation magnitudes are significantly reduced in the $s_\rho = 1$ case compared to the $s_\rho = 7$ cases, this is especially clear at low M_c. At incompressible conditions of $M_c = 0.2$, the total density variance is almost identical to the adiabatic density variance ρ'_a, indicating that the density fluctuations are almost entirely adiabatic. At higher M_c, a difference can be observed between the total and the adiabatic density fluctuation profiles, which indicates that not all fluctuations are perfectly adiabatic.

The mixture-based and isobaric-based fluctuations, ρ'_m and ρ'_T follow the general profile of the total density fluctuations, but have reduced magnitudes. At $M_c = 0.8, 2.0$ and $s_\rho = 7$, the isobaric-based density fluctuations are larger than that of the mixture-based fluctuations, although some statistical variation is present for the case at $M_c = 2.0$. At higher M_c, the profile for these fluctuations also do not decay to zero into either the lighter of the heavier freestream region. This persistence of density fluctuations into the heavy fluid region at high M_c can be attributed to the presence of stronger Mach waves at the $M_c \geq 0.8$ configuration. It is important to note that the different density fluctuations defined in Eqns. 3.7-3.9 are not mutually independent or 'orthogonal'. Further interpretation of this density decomposition is ongoing.

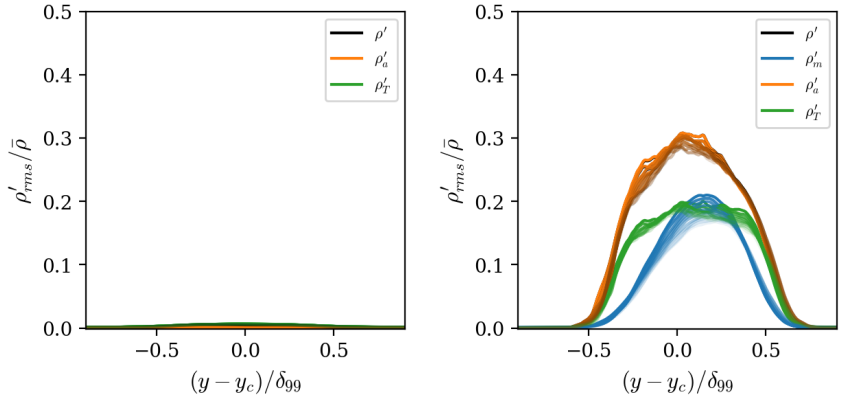

(a) $M_c = 0.2$

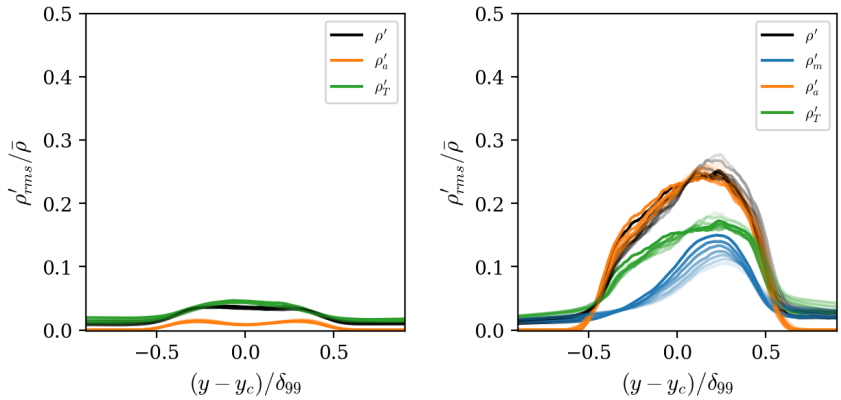

(b) $M_c = 0.8$

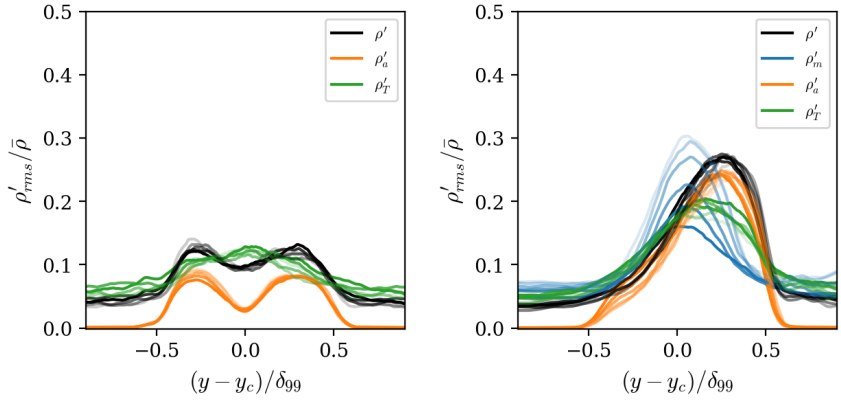

(c) $M_c = 2.0$

Figure 3.11: Comparison of density variance profiles across M_c at $s_\rho = 1$ (left) and $s_\rho = 7$ (right) at several snapshots in time.

3.5 Viscous heating effects

At increased compressibility levels, aerodynamic heating due to viscous dissipation cane be observed. This excess in temperature profiles is measured with respect to either the freestream temperature, $T_{ref} = T_0$ for $s_\rho = 1$ cases, or with respect to the mixture temperature defined off a mixing progress variable χ for $s_\rho = 7$ cases:

$$\chi = \frac{Y - Ymin}{Y_{max} - Y_{min}} \tag{3.10}$$

$$T_{mix} = T_1(1-\chi) + T_2\chi \tag{3.11}$$

In Fig. 3.12, the temperature rise for both $s_\rho = 1$ and $s_\rho = 7$ are shown. The two sets of profiles show a similar magnitude of increase in excess temperature with increasing compressibility, with the peak value of $\bar{T} - T_{ref} \approx 0.4$ for $s_\rho = 1$ and $s_\rho = 7$. Freund et al. observed similar rise in peak temperature in annular mixing layers at high compressibility levels, and noted that the effect scales similarly to M_c. The present data supports this argument, with Fig. 3.12c indicating that the peak rise in temperature scales quadratically with M_c. A parabolic fit is plotted through the scattered data to clarify this dependence.

The observed heating effect with increase compressibility can be further understood by considering various contributions to the evolution of internal energy of the flow. The internal energy budget equation is written as in Eqn. 3.13 below.

$$\frac{D}{Dt}(\rho e) = -p\frac{\partial u_k}{\partial x_k} + \tau_{ij}\frac{\partial u_i}{\partial x_j} - \frac{\partial q_k}{\partial x_k} \tag{3.12}$$

$$\frac{\partial}{\partial t}(\overline{\rho e}) = -\frac{\partial}{\partial x_j}(\overline{\rho u_j e}) - \left(\bar{p}\frac{\partial \bar{u}_k}{\partial x_k} + \overline{p'\frac{\partial u_k'}{\partial x_k}}\right) + \left(\bar{\tau}_{ij}\frac{\partial \bar{u}_i}{\partial x_j} + \overline{\tau_{ij}'\frac{\partial u_i}{\partial x_j}'}\right) - \frac{1}{Pr}\frac{\partial}{\partial x_k}\left(\bar{\mu}\frac{\partial \bar{T}}{\partial x_k} + \overline{\mu'\frac{\partial T'}{\partial x_k}}\right) \tag{3.13}$$

The mean and turbulent components of advection, pressure dilatation, dissipation, and heat conduction are shown in Fig. 3.13. The mean component of terms are plotted with solid lines and the turbulent components are are plotted with dashed lines. Statistical noise is present and especially large at higher M_c. The mean internal energy budget terms for $s_\rho = 7$ cases are qualitatively similar in profile to those of the $s_\rho = 1$ cases, aside from the case at low compressibility. Turbulent dissipation (plotted in orange), mean advection (plotted in red) and mean pressure dilatation (plotted in blue) are the largest contributors to the evolution of internal energy. For $s_\rho = 1$ cases, similarly to TKE profiles, the dissipative and advective transport components are symmetric across the mixing layer. Turbulent dissipation contributes to heating while advective transport spreads

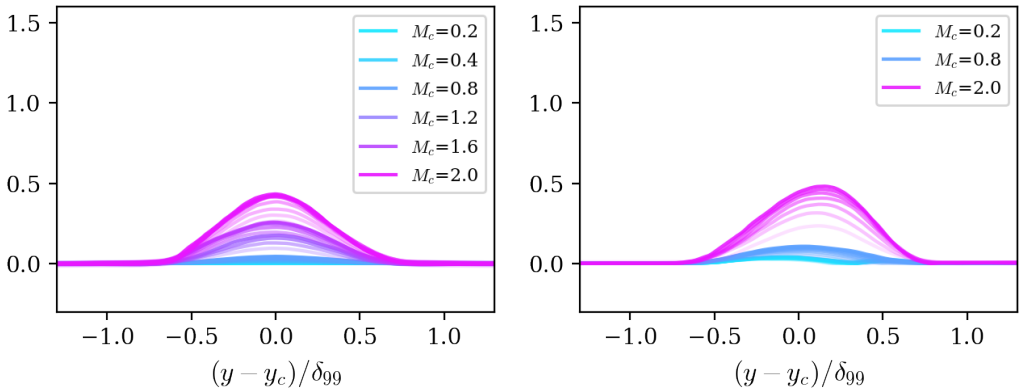

(a) Heating at $(\bar{T} - T_\infty)/T_\infty$ at $s_\rho = 1$ (b) Heating at $(\bar{T} - T_{mix})/(T_2 - T_1)$ at $s_\rho = 7$

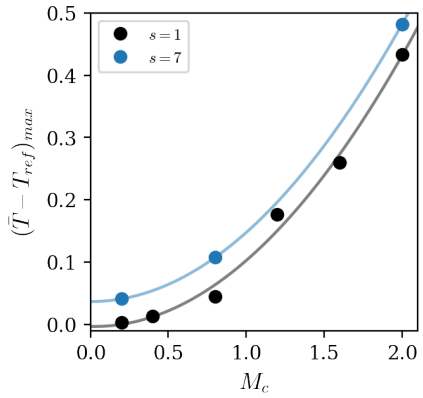

(c) Peak excess temperature

Figure 3.12: Profiles of excess mean temperature compared to a reference temperature.

this contribution as the shear layer spreads with nonzero transverse velocity. Across the compressibility range, the profiles show a similar qualitative shape with magnitudes of turbulent viscous dissipation, mean advection, and mean pressure dilatation peaking in the centerline. These magnitudes decrease monotonically when scaled by the global velocity $\Delta\bar{u}^3$. Similarly to the trends of integrated TKE dissipation for $s_\rho = 1$, the peak dissipation profiles show consistent scaling with U_δ^3 in Fig. 3.13b. Overall, at both $s_\rho = 1$ and $s_\rho = 7$, the dissipation of TKE is a significant contributor to increasing the internal energy of the flow in the turbulent region; there is only heat generation and energy transfer within the shear layer. This energy is not generated in the freestream regions and does not escape in the form of heat to the freestream regions ($dT/dy = 0$ is zero outside the mixing region), so heat is both generated and accumulated in the turbulent mixing region. As shown in Fig. 3.3, the difference in satisfactory collapse between mean streamwise velocity and mean temperature profiles is evident. The mean streamwise velocities at all compressibility levels quickly collapse to a single, similar, profile. In contrast, the temperature profile shows increasing amounts of drift with increasing M_c. The gradual increase in temperature in the mixing layer region implies that the speed of sound gradually increases as well, and that the local Mach number decreases. In the context of internal scales and acoustic limitations, this drift in the speed of sound would result in internal scales which are larger than their hypothetical counterpart in a flow without aerodynamic heating. The interpretation of the observed rise in temperature due to accumulation of heat suggests that over very long time scales, perfect similarity for this shear layer configuration may not exist. A deviation or drift in temperature profile due to viscous heating may have a similarity solution and the rate of this drift may show dependence on a reference Mach number. This similarity analysis and determination of this heating time scale is an avenue of future work.

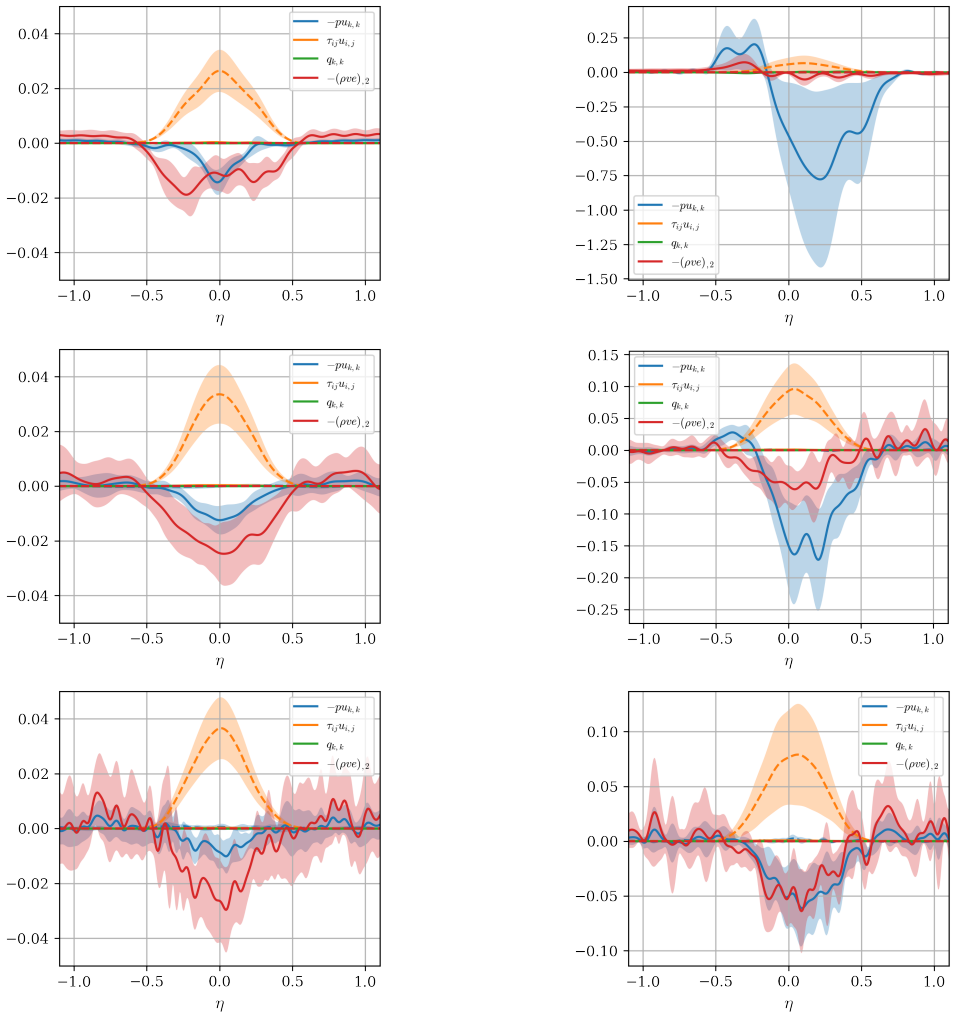

(a) $s_\rho = 1$ (b) $s_\rho = 7$

Figure 3.13: Profiles of mean internal energy budget scaled by U_δ^3 with mean terms in solid lines and turbulent terms in dashed lines.

3.6 Conclusions

In this work, the effect of the mean density variation in the flow independent from the effect of compressibility is demonstrated. Present data comparing thickness growth rates and shear layer decorrelation scales suggests that compressibility and variable density effects cannot be completely decoupled. At $s_\rho = 7$, growth rates decrease with increasing M_c in a similar manner to $s_\rho = 1$ growth rates, though the decrease from $M_c = 0.2$ to $M_c = 2.0$ is not as dramatic at $s_\rho = 7$. Furthermore, the shift in mean velocity profile compared to the mean density profile is also documented to occur consistently at all studied compressibility levels. This offset between the location of turbulent mixing and the location of mean density gradient reduces the momentum mixing efficiency, as seen by turbulent stress profiles which become biased towards the lighter fluid region. Two definitions of the shear layer centerline are compared; the centerline defined by the streamwise velocity profile moves into the lighter freestream region and indicates approximately similar contributions to shear layer growth rates from both sides of the mixing layer. The centerline as defined by mean density gradually moves into the denser fluid region; this definition of the mixing layer centerline implies that the lighter fluid is responsible for most of the mixing layer growth in the turbulent regime. This work also demonstrated that the centerline definition should be considered in the selection of characteristic turbulent scales. Decorrelation length scales are found to be asymmetric about the shear layer centerline, with larger decorrelation scales occurring in the lighter fluid. Internal regulation also occurs at $s_\rho = 7$, which allows for the scaling of TKE production, dissipation and pressure strain to be collapsed when normalized by the 'effective' eddy scales when centered about the velocity-defined centerline. A comparison of density variances associated with compositional, adiabatic, and isobaric effects were examined. Across the M_c range, density fluctuations associated with multi-species mixing were significantly larger than those associated with adiabatic and isobaric effects. Lastly, aerodynamic heating was observed at both variable and unity density ratios and the corresponding temperature excess scales quadratically with compressibility.

(To Table of Contents)

Chapter 4

Streamwise curvature effects on turbulent shear layers

4.1 Introduction

Many aerospace applications involve high-speed jet plumes with complex flow physics and multiple turbulence mechanisms. A comprehensive understanding of turbulence in these flows is essential in developing and improving numerical methods for such vehicle design and analysis, and is currently lacking. In particular, the shear layers in these rocket-motor exhaust plumes exhibit streamwise curvature, along with pressure gradients, shock waves, and other complexities. An area which has not been well studied is the joint effect of streamwise curvature, compressibility, and variable density effects in mixing layers. The combination of all three influences on turbulent mixing result in a complex mixture of the following three instability mechanisms in the flow.

- The Kelvin-Helmholtz (KH) instability, associated with planar shear layers as characterized in the previous chapters of this work, exists for parallel flows with $u_2 \neq u_1$ and an inflection point in the velocity profile. This instability results in spanwise vortical structures which pair and amalgamate.
- The Rayleigh-Taylor (RT) instability, which arises from the opposition of a body force and the fluid's density gradient, is also applicable in the curved shear layer configuration due to centripetal acceleration. When a heavier fluid is accelerated into a lighter fluid, three-dimensional bubble and spike-like features are produced at the two fluids' interface.

- The Taylor-Görtler (TG) instability, associated with centripetal acceleration in wall-bounded flows with streamwise curvature, produces streamwise vortical structures.

This section introduces previous work specifically on the characterization of centrifugal stability rather than on KH, RT or TG instabilities individually.

Previous studies

Several qualitative arguments on the proposed stability in vortical flows have been formulated. Beginning at low complexity with an incompressible, inviscid and uniform density fluid undergoing rotation, [109] derived a criterion for centrifugal stability by comparing fluid parcels' kinetic energy in concentric cylinders of fluid. Rayleigh postulated that the circulation of a flow, $\Gamma = u_\theta r$, must increase in the outer radial direction for the flow to be centrifugally stable. This criterion for stability is given by the discriminant Φ in Eqn. 4.1.

$$\Psi = \frac{1}{r^3}\frac{d\Gamma^2}{dr} = \frac{2u_\theta}{r}\left(\frac{u_\theta}{r} + \frac{du_\theta}{dr}\right) > 0 \tag{4.1}$$

The variable density equivalent of Rayleigh's stability criterion for incompressible flows was later proposed [131, 136] by considering the conservation of mass and angular momentum of an incompressible fluid parcel.

$$\frac{d}{dr}(\rho\Gamma^2) > 0 \tag{4.2}$$

In another consideration of restorative forces, an analogy between the phenomena in turbulent shear flow under buoyancy and under streamwise curvature was drawn early on by Bradshaw [12, 13] for incompressible curved flows. The Richardson number for stratified flows represents the ratio of buoyant to shear effects; a corresponding Richardson number (as defined in Eqn. 4.4) to represent the ratio of curvature to shear effects is positive for centrifugally stable flows. A flux Richardson number represents the ratio of buoyant to shear production of TKE in stratified flows and acts a measure of dynamic stability, or the persistence of turbulence compared to the stabilizing effect of buoyancy. The definition of Bradshaw's flux Richardson number, $Ri_f^{(B)}$ in Eqn. 4.5, was proposed

based on the close correlation between temperature and streamwise velocity fluctuations, where $\overline{u'_\theta u'_r}$ is the kinematic shear stress.

$$S = \frac{u_\theta / r}{du_\theta / dr} \tag{4.3}$$

$$Ri = \frac{2u_\theta}{r^2}\frac{\partial \Gamma}{\partial r} \Big/ \left(\frac{\partial u_\theta}{\partial r}\right)^2 = 2S(1+S) \tag{4.4}$$

$$Ri_f^{(B)} = \frac{2\overline{u'_\theta u'_r}\frac{u_\theta}{r}}{\overline{u'_\theta u'_r}\frac{1}{r}\frac{\partial u_\theta r}{\partial r}} = \frac{2S}{1+S} \tag{4.5}$$

Several decades later, Nagata and Kasagi [94] presented a similar flux Richardson number for curvature effects on turbulent channel flows, with a specific focus on the effects of increasing curvature on turbulence intensity. Similarly to the Ri_f defined in Eqn. 4.5, Nagata and Kasagi's version can be written considering the production of turbulent stresses $R_{\theta\theta}$ and R_{rr}. Nagata suggested using the first term of $P_{\theta\theta}$ as the shear production term and $R_{12}\tilde{u}_\theta / r$ as the centrifugal production term of $P_{\theta\theta}$ and P_{rr}, with R_f as the balance between these shear and centrifugal terms. Alternatively, R_f can also be defined as the ratio of the radial stress production to streamwise stress production, as given in Eqn. 4.6. This form of flux Richardson number is revisited in evaluation of stability in the present cases.

$$\begin{aligned} P_{\theta\theta} &= -2\overline{u'_\theta u'_r} r \frac{\partial}{\partial r}\left(\frac{\tilde{u}_\theta}{r}\right) - 4\overline{u'_\theta u'_r}\frac{\tilde{u}_\theta}{r} \\ P_{rr} &= 4\overline{u'_\theta u'_r}\frac{\tilde{u}_\theta}{r} \\ Ri_f &= -\frac{P_{rr}}{P_{\theta\theta}} \end{aligned} \tag{4.6}$$

Formal stability analyses have also been conducted to evaluate centrifugal stability. Eckhoff and Storesletten [41] gave the stability criterion for disturbances in a swirling, compressible flow using a generalized progressing wave-expansion method (generalized Wentzel–Kramers–Brillouin (WKB)):

$$\Phi = \frac{u_\theta^2}{r}\left(\frac{1}{\rho}\frac{d\rho}{dr} - \frac{u_\theta^2}{c^2 r}\right) > 0 \tag{4.7}$$

Leibovich and Stewartson [73] gave the sufficient condition for the stability of columnar vortices which are unbounded, homogeneous, inviscid, and subject to 3D, exponentially growing disturbances with large azimuthal wavenumbers: (WKB-type asymptotic analysis)

$$u_\theta \left(\frac{d\Omega}{dr}\right)^2 \frac{d\Gamma}{dr} = \frac{u_\theta}{r}\left(\frac{du_\theta}{dr} - \frac{u_\theta}{r}\right)\left[\left(\frac{du_\theta}{dr}\right)^2 - \left(\frac{u_\theta}{r}\right)^2\right] > 0 \tag{4.8}$$

where the angular velocity is $\Omega = u/r$. Eckhoff [40] (1984) later asserted that the criterion for exponentially growing disturbances (the disturbances which satisfy Eqn. 4.7 typically grow algebraically), is given as:

$$\frac{u_\theta^2}{r}\left(\frac{du_\theta}{dr} - \frac{u_\theta}{r}\right)^2\left(\frac{1}{\rho}\frac{d\rho}{dr} - \frac{u_\theta^2}{c^2 r}\right) + \frac{2u_\theta}{r}\left(\frac{du_\theta}{dr} - \frac{u_\theta}{r}\right)\left[\left(\frac{du_\theta}{dr}\right)^2 - \left(\frac{u_\theta}{r}\right)^2\right] < 0 \tag{4.9}$$

Eckhoff [40] proved that in the homogeneous and incompressible limit, the first term in Eqn. 4.9 is zero and Leibovich's incompressible criterion (Eqn. 4.8) can be recovered.

The stability analyses above were formulated for swirling, vortical or helical flows. The following works presented the numerical solutions to linear stability equations of spatially developing mixing layer with modest levels of streamwise curvature. In many cases, the the focus of the studies were the formation of streamwise, TG-type vorticies. The effect of curvature on the development of the profiles of the base flow were typically neglected. Liou [78] (1994) presented the linear, inviscid, hydrodynamic stability of slightly curved, spatial shear layers using a shooting method. Hyperbolic tangent velocity profiles and an assumption of parallel flow were used. Curvature levels varied from $\delta/R = [0, 0.025, 0.05]$, which corresponds to $Ri_f = [0.0488, 0.0952]$ for stable cases as $Ri_f = [-0.0513, -0.105]$ for unstable cases, with Ri_f as defined in Eqn. 4.5. Analysis indicated that instability modes in the form of streamwise vortex pairs were possible. Hu et al. [54] (1994) also studied the save problem as Liou, and determined that (i) curvature effect on Rayleigh modes were minimal and (ii) nonzero curvature allows the formation of an unstable, 3D mode which becomes the dominant mode as the curvature wavelength decreases. Otto et al. [100] (1996) extended this analysis for Lock's (1951) velocity profile, to account for non-parallel effects, and argue that the hyperbolic tangent profile is insufficient to studying spatial stability. Spanwise vortex pairs were also found to form in unstable cases. Stability analysis by Otto indicated that centrifugal instability modes in the form of longitudinal vorticies are supported in curved, incompressible mixing layers if the centerline curves into the faster stream. Zhuang [147] (1999) also studied the linear stability of the inviscid, spatial shear layer but included density variations of $\rho_2/\rho_1 = [0.2, 1, 5]$ and a wake deficit in the velocity profile. Hyperbolic tangents were used to define the mean velocity and density profiles, and streamwise vortex pairs were also identified. Otto et al. [101] further developed their

previous study to include effects of buoyancy by adding a mean temperature gradient in the flow. Temperature and velocity profiles followed a hyperbolic tangent profile, under the argument that stability results are qualitatively similar to using a more exact profile. Streamwise evolution of the flow was not considered, so only small time and length scales were considered. For the flow to be unstable to longitudinal vorticies, the curvature and temperature profile must satisfy Eqn. 4.10. The inner to outer radial freestream ratios are $\beta_u = u_{inner}/u_{outer} = u_2/u_1$, $\beta_t = T_{inner}/T_{outer} = T_2/T_1$, the Görtler number $G = 2\delta Re^{1/2}/r_c$ is large ($1 << G << Re$) and Gr is the Grashof number, $Gr = \alpha_V g \delta^3 T_1/\nu^2$ where α_V is the coefficient of volume expansion ($\alpha_V = 1/T$ for an ideal gas), g is the acceleration due to gravity and ν is the kinematic viscosity.

$$\frac{G}{Gr} > \begin{cases} \frac{\beta_t - 1}{\beta_u(\beta_u - 1)}, & \beta_t > 1 \quad \text{(stably stratified)} \\ \frac{\beta_t - 1}{(\beta_u - 1)}, & \beta_t < 1 \quad \text{(unstably stratified)} \end{cases} \tag{4.10}$$

The parameters proposed by Otto et al. [101] in Eqn. 4.10 correspond to Eqn. 4.11 when gravitational acceleration is replaced with centrifugal acceleration.

$$2Re^{1/2}\frac{T}{T_1}\frac{r}{r_c}\left(\frac{\nu}{u_\theta \delta_0}\right)^2 > \begin{cases} \frac{\beta_t - 1}{\beta_u(\beta_u - 1)}, & \rho_2/\rho_1 > 1 \quad \text{(stably 'stratified')} \\ \frac{\beta_t - 1}{(\beta_u - 1)}, & \rho_2/\rho_1 < 1 \quad \text{(unstably 'stratified')} \end{cases} \tag{4.11}$$

Sarkies and Otto [118] looked at the linear stability of compressible, spatially developing mixing layers with temperature gradients. The results suggested that compressibility has a stabilizing effect, and that the stability of the flow is sensitive to changes in the temperature ratio β_t. Changes in curvature and velocity ratio have similar effects compared to the incompressible case in that streamwise vorticity is generated when the slower stream curves into the faster stream. However, if the faster stream curves into a cooler and slower stream, centrifugal instabilities can also be observed. As the lower stream M_1 increases, the layer is more unstable to thermal modes, which appear at lower values of β_t. The results were found to be largely independent of the velocity ratio β_u. Görtler modes with a cooler, faster stream ($\beta_t < 1$ and $\beta_u > 1$) were found to be more unstable to a wider range of wavenumbers compared to uncooled configurations ($\beta_t = 1$).

More recently, other studies of vorticies with smoothly varying density gradients have also been conducted. Joly et al. [60] studied RT-type behavior during the breakdown of 2D incompressible, inviscid, constant circulation vorticies with heavy cores. Sipp et al. [119] reviewed the criteria for centrifugal stability in an incompressible, non-homogenous Lamb-Oseen vortex. The parameters

N^2, N_w^2 and the Rayleigh discriminant Ψ defined in Eqn. 4.1 was used to characterize the density variation of the vortex:

$$N^2 = -\frac{u_\theta^2}{r}\frac{1}{\rho}\frac{d\rho}{dr} \qquad N_w^2 = -\frac{1}{4}\left(\frac{\partial u_\theta}{\partial r} - \frac{u_\theta}{r}\right)^2 \tag{4.12}$$

If density increases in the radial direction, $-N^2$ is defined similarly to the square of the buoyancy (Brunt-Väisälä) frequency, with gravity replaced with u_θ^2/r. While N_w^2 is always a negative quantity, the stability discriminant of $N_w^2 - N^2$ can be positive depending on the density gradient. Vortices with a heavy vortex core ($N > 0$) were mainly considered, though several instabilities may occur with various combinations of N^2 and Ψ:

$N^2 = 0$: A homogeneous vortex flow, Kelvin-Helmholtz unstable

$N^2 > 0$: Rayleigh-Taylor instability may occur

$N^2 > \Psi$: A very heavy vortex core, centrifugally unstable

$N^2 \leq \Psi$: Centrifugally stable (Leibovich [72], Howard [53]), KH & RT unstable

$0 < N^2 < \Psi$: No general sufficient condition for instability

$N^2 < N_w^2$: A very light vortex core, stable to all perturbations (Lalas (1975), Warren (1975) and Fung (1983))

Table 4.1: Summary of conditions for centrifugal stability of disturbances in streamwise curved flows.

Reference	VD	Comp.	Parameter(s)	Condition for stability
Rayleigh (1917)[109]	no	no	$\Psi = \frac{1}{r^3}\frac{d\Gamma^2}{dr}$	$\Psi > 0$
Synge (1933)[131]	yes	no		$\frac{d\rho\Gamma^2}{dr} > 0$
Bradshaw (1969)[12]	yes	no	$S = \frac{u_\theta/r}{du_\theta/dr}, Ri = 2S(1+S)$	$Ri > 0$
Eckhoff (1978)[41]	yes	yes	$\Phi = \frac{u_\theta^2}{r}\left(\frac{1}{\rho}\frac{d\rho}{dr} - \frac{u_\theta^2}{c^2 r}\right)$	$\Phi > 0$
Leibovich (1983)[73]	no	no		$\left(\frac{d\Omega}{dr}\right)^2 \frac{d\Gamma}{dr} > 0$
Eckhoff (1984)[40]	yes	yes		Eqn. 4.7
Sipp (2005)[119]	yes	no	$N^2 = -\frac{u^2}{r}\frac{1}{\rho}\frac{d\rho}{dr}$, $N_w^2 = -\frac{1}{4}\left(\frac{\partial u_\theta}{\partial r} - \frac{u_\theta}{r}\right)^2$	$N_w^2 - N^2 > 0$

Selected characterizations of centrifugal stability from the multitude of studies above summarized given in Table 4.1. Columns 'VD' and 'Comp.' indicate whether the formulation of the stability criterion included variable density and compressibility effects, respectively.

Experimental studies on streamwise curvature effects on turbulent mixing have been conducted in addition to the theoretical and numerical research detailed above. Several studies of streamwise curvature effects in turbulent boundary layers have been carried out by Jeans and Johnston [59],

Wang et al. [137], but similar experiments of curved shear layers across a comparable parameter space are more sparse. Experimental studies of curved mixing layers into the compressible range have also not been conducted, as early experiments focused on incompressible conditions. Margolis and Lumley [83] studied incompressible shear layers in a wind tunnel with unstable and stable configurations. Stability was defined by the angular momentum gradient, with increasing angular momentum in the radial direction correlated with stable conditions. The data suggested that for both configurations, while the mean flow is self-similar, the turbulent quantities are not, and so the total flow is not self-similar. Turbulence intensities were observed to increase rapidly for the unstable case, compared to the stable case, which was attributed to the importance of the turbulent transport of TKE. Wyngaard et al. [141] observed that Margolis's measurements indicated that the production and dissipation of TKE are approximately in balance. However, it was observed that in the stable case, the dissipation rates were orders of magnitude larger than those measured in unstable cases when calculated using isotropic relationship $\epsilon = 15\nu\overline{u_{,x}^2}$. Later, Castro and Bradshaw [24] studied the turbulence behavior in planar impinging jet flow. With this more complex configuration, the jet shear layer in the impingement region experiences non-constant, stabilizing curvature (of a maximum thickness to radius ratio of 0.2) before returning to a classic planar shear layer. The data showed that the return from a curved to a planar mixing layer involved some non-monotonic behavior, with turbulent stresses, triple products and energy dissipation rates overshooting then decreasing to planar values once the curvature region subsided. Castro noted that this behavior was also observed in curved boundary layer flows, and postulated that the suppression of turbulent transport, which results in increased turbulence intensity where TKE production is maximum, is caused by larger eddies which have long time scales and longer recovery times from stabilizing curvature effects.

Later experimental studies, however, did not give evidence for the dependence of turbulent structures on streamwise curvature. Plesniak et al. [107, 108] conducted experiments of nearly incompressible, mildly curved mixing layers, and observed that shear layers grew approximately linearly and that vortical structures that developed were related to upstream disturbances rather than the Taylor-Görtler instability. Similarly, Karasso and Mungal [62]'s experiments of reacting, curved mixing layers with a focus on scalar mixing and hydrodynamic instabilities indicated that unstable curvature did not increases mixing efficiency. Finally, Wang [136] characterized the stability of a spatially developing, curved mixing layer according to the KH, RT and TG instability mechanisms. The density and velocity ratio were varied independently in the experiment, and Wang highlighted flow conditions under which each mechanism dominated. The dynamics of observed large scale structures in the mixing layer were found to depend mainly on the density and velocity ratio rather than the streamwise curvature.

Present objectives

High resolution simulations of turbulent mixing layers with streamwise curvature in the compressible regime have not been conducted, under either unity or variable density ratio conditions. The primary goal of this work is to improve the understanding of these complex turbulent mixing layers influenced by compressibility, density variations, and curvature via eddy-resolving simulations. Temporally developing shear layers at low and high compressibility levels, and stable and unstable curvature configurations, and non-negligible density ratios are analyzed to improve the current understanding of the fundamental physics behind turbulent mixing in flows with multiple physical effects. Metrics for shear layer thicknesses and growth rates, including a discussion of their evolution for stable and unstable configurations, are presented. The effects of increasing curvature intensity on turbulent statistics are demonstrated. The analogy between centrifugal and buoyancy effects, following work by Bradshaw [13] and Nagata and Kasagi [94], is also evaluated. Finally, compressibility and curvature effects for the present parameter range are compared.

Throughout this work, profiles are shown with lines of varying opacity. Each line's opacity indicates its instance in time, with more translucent profiles occurring earlier in simulation time and more opaque profiles occurring later. Notation used throughout this work are the centerline radius r_c, the centerline streamwise position $s = r_c\theta$, and the normalized transverse coordinate $(r - r_c)/\delta_{99}$. This thickness measure is defined in section 4.4.2.

4.2 Methodology

4.2.1 Governing equations

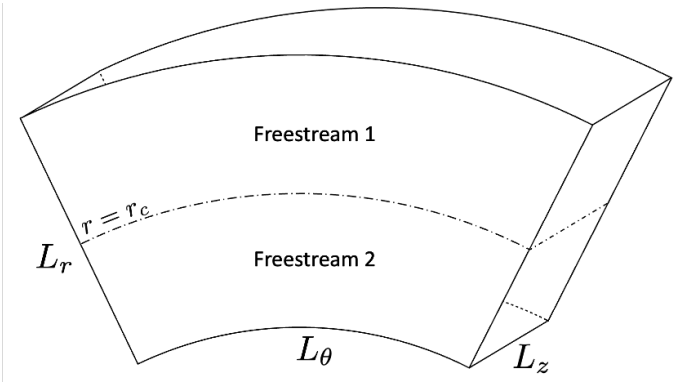

Figure 4.1: Computational domain and setup

The Navier-Stokes equations for the compressible flow of an ideal gas are solved in generalized curvilinear coordinates using the overset grid flow solver OVERFLOW[22]. The governing equations for the conservation of mass, momentum, and energy are consistent with Eqn. 2.2-2.4 in Ch. 2, but with velocity components $u_1 = u_\theta, u_2 = u_r, u_3 = u_z$ and the cylindrical coordinate index notation below.

In cylindrical coordinates, the scalar gradient $\frac{\partial f}{\partial x_j}$, divergence $\frac{\partial f_i}{\partial x_i}$ and vector gradient $\frac{\partial f_i}{\partial x_j}$ are:

$$\frac{\partial f}{\partial x_i} = \begin{bmatrix} \frac{1}{r}\frac{\partial f}{\partial \theta} & \frac{\partial f}{\partial r} & \frac{\partial f}{\partial z} \end{bmatrix}$$

$$\frac{\partial f_i}{\partial x_i} = \frac{1}{r}\frac{\partial f_\theta}{\partial \theta} + \frac{1}{r}\frac{\partial r f_r}{\partial r} + \frac{\partial f_z}{\partial z}$$

$$\frac{\partial f_i}{\partial x_j} = \begin{bmatrix} \frac{1}{r}\frac{\partial f_\theta}{\partial \theta} + \frac{f_r}{r} & \frac{\partial f_\theta}{\partial r} & \frac{\partial f_\theta}{\partial z} \\ \frac{1}{r}\frac{\partial f_r}{\partial \theta} - \frac{f_\theta}{r} & \frac{\partial f_r}{\partial r} & \frac{\partial f_r}{\partial z} \\ \frac{1}{r}\frac{\partial f_z}{\partial \theta} & \frac{\partial f_z}{\partial r} & \frac{\partial f_z}{\partial z} \end{bmatrix}$$

With the symmetric viscous stress tensor, using $\lambda = -2\mu/3$:

$$\begin{aligned} \tau_{ij} &= \lambda \frac{\partial u_k}{\partial x_k}\delta_{ij} + \mu\left(\frac{\partial u_i}{\partial x_j} + \frac{\partial u_j}{\partial x_i}\right) \\ &= -\frac{2}{3}\mu\frac{\partial u_k}{\partial x_k}\delta_{ij} + \mu \begin{bmatrix} 2\left(\frac{1}{r}\frac{\partial u_\theta}{\partial \theta} + \frac{u_r}{r}\right) & \frac{1}{r}\frac{\partial u_r}{\partial \theta} - \frac{u_\theta}{r} + \frac{\partial u_\theta}{\partial r} & \frac{\partial u_\theta}{\partial z} + \frac{1}{r}\frac{\partial u_z}{\partial \theta} \\ \frac{1}{r}\frac{\partial u_r}{\partial \theta} - \frac{u_\theta}{r} + \frac{\partial u_\theta}{\partial r} & 2\frac{\partial u_r}{\partial r} & \frac{\partial u_r}{\partial z} + \frac{\partial u_z}{\partial r} \\ \frac{\partial u_\theta}{\partial z} + \frac{1}{r}\frac{\partial u_z}{\partial \theta} & \frac{\partial u_r}{\partial z} + \frac{\partial u_z}{\partial r} & 2\frac{\partial u_z}{\partial z} \end{bmatrix} \end{aligned}$$

The dynamic viscosity μ follows Sutherland's law, with reference values μ_0, T_0, and constant $S = 199.0R$:

$$\mu = \mu_0\left(\frac{S}{T_0} + 1\right)\left(\frac{T}{T_0}\right)^{3/2}\left(\frac{S}{T_0} + \frac{T}{T_0}\right)^{-1} \qquad \frac{T}{T_0} = \frac{\gamma}{R_{gas}(\gamma - 1)}(e - \frac{1}{2}u_k u_k)$$

The divergence of the viscous stresses is given by:

$$\frac{\partial \tau_{ij}}{\partial x_j} = \begin{bmatrix} \frac{1}{r}\frac{\partial \tau_{\theta\theta}}{\partial \theta} + \frac{1}{r}\frac{\partial r\tau_{r\theta}}{\partial r} + \frac{\partial \tau_{\theta z}}{\partial z} + \frac{\tau_{r\theta}}{r} \\ \frac{1}{r}\frac{\partial \tau_{r\theta}}{\partial \theta} + \frac{1}{r}\frac{\partial r\tau_{rr}}{\partial r} + \frac{\partial \tau_{rz}}{\partial z} - \frac{\tau_{\theta\theta}}{r} \\ \frac{1}{r}\frac{\partial \tau_{z\theta}}{\partial \theta} + \frac{1}{r}\frac{\partial r\tau_{rz}}{\partial r} + \frac{\partial \tau_{zz}}{\partial z} \end{bmatrix}$$

4.2.2 Numerical methods

The Navier-Stokes equations for the compressible flow of an ideal gas are solved in generalized curvilinear coordinates using the overset grid flow solver OVERFLOW [9, 98, 97, 102]. Simulation

of the present problem on curvilinear and stretched grids motivated the switch from *PadeOps* to OVERFLOW. The grid system used in this study is shown in Fig. 4.2, with a 'mixing' mesh to encompass the turbulent and near-turbulent regions, and two 'buffer' regions. These buffer grids included mesh stretching in the radial direction for computational efficiency and additional numerical damping of any freestream disturbances. The grid stretching ratio linearly increases from 1.0 to a maximum of 1.1 over a 10 grid points from the mixing region to facilitate smoothness of metric terms and derivatives at the mixing and buffer grid interface. The grid encompassing the mixing region was designed to have approximately uniform and isotropic spacing about the radius of curvature to avoid relying on assumptions about turbulent structure anisotropy. The isotropic spacing translates to $\Delta r = \Delta z \approx \Delta s$, where s is the streamwise coordinate at radius r. The streamwise coordinate s was used to specify the azimuthal domain size for consistency in streamwise eddy-convection space between the low and high curvature cases. The domain sizes are $r \in [r_c - 40\delta_0, r_c + 40\delta_0]$, $s \in [-100\delta_0, 100\delta_0]$, and $z \in [-20\delta_0, 20\delta_0]$, discretized with $N_\theta \times N_r \times N_z = 1000 \times 320 \times 200$ points. This domain size and resolution is the same across all cases, unless otherwise noted. The isotropic mixing layer region extends from $r \in [r_c - 30\delta_0, r_c + 30\delta_0]$ and resolves the initial shear layer with about 30 points.

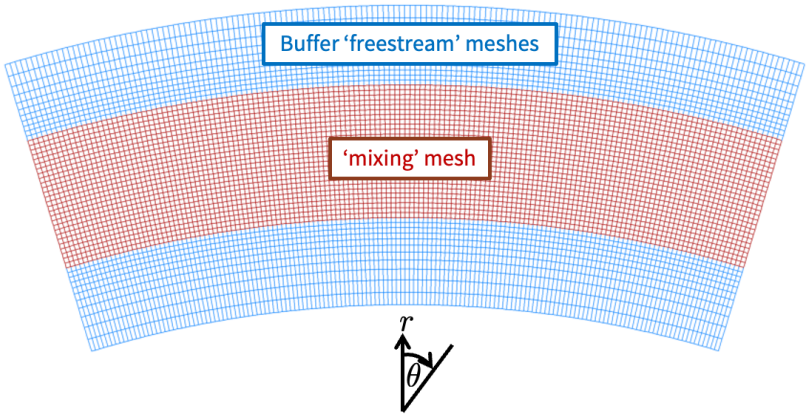

Figure 4.2: An annotated view of the grid system used for the present study, decimated in the r and θ directions for visualization.

The appropriate grid resolution was selected by comparing both evolution of the turbulent shear stress and TKE production on a coarse, medium, and fine grid. The grid resolution in each coordinate direction is increased by a factor of $\sqrt{2}$ from the coarse to medium to fine grid. Figure 4.3 indicates that the change from the medium to fine resolution grid gives less than 10% difference in the shear stress. Similarly, the statistical fluctuations in the shear stress are large on the coarse

grid but decrease significantly for calculations on the medium and fine grid. A similar convergence can be seen in the profiles of TKE production, though statistical noise is still present at the finest resolution. The presented cases have been run at the finest grid resolution.

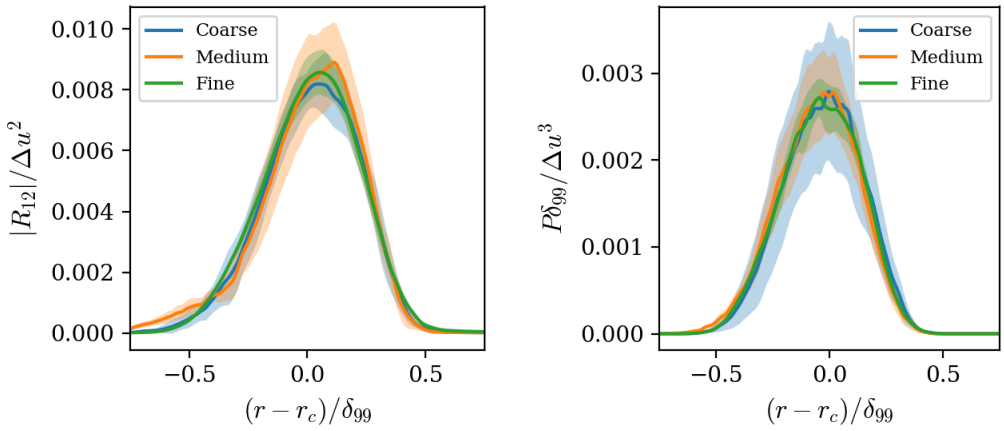

(a) Shear stress $R_{12}/\Delta u^2$

(b) TKE production P

Figure 4.3: Reynolds stresses and TKE production at increasing levels of grid resolution for case $\delta_0/r_c = 0.001, M_c = 0.2, u_2/u_1 = 0.4$ and $\rho_2/\rho_1 = 7$.

Convective fluxes were computed with 5^{th} order WENO[132] and no SGS model was used. As a result, the calculations have small amounts of resolved dissipation, and the non-physical dissipation of the numerical scheme dominates. WENO-like schemes have been identified as vastly inferior to higher order central finite difference schemes [89, 122] in the study of turbulence. Since WENO schemes require more grid points to resolve similar turbulent scales captures by the central finite difference schemes, they are considered inefficient for simulations of turbulence. A brief comparison of WENO and second order central differences is below in section 4.2.6. A range of scales useful in studying the physics in this flow can be identified. The streamwise and spanwise energy spectra at multiple instances in time for an unstable, low speed and variable density case are shown in Fig. 4.4, normalized by the total TKE along the centerline. Two grid resolutions are shown, which correspond to the cases which are also referenced in Fig. 4.3. In the streamwise direction, the spectra shows a reduction in magnitude from large to small scales of 10^5. For the spanwise direction, the reduction in magnitude from large to small scales is about 10^3. Both spectra do not indicate an accumulation of energy in the high wavenumber region. The high wavenumber region does not resolve the appropriate physics of viscous dissipation at the smallest eddy scales. The inertial range of scales which exists at both the medium and fine scale grids have a similar drop in magnitude in the high wavenumber regime, mainly due to the numerical dissipation.

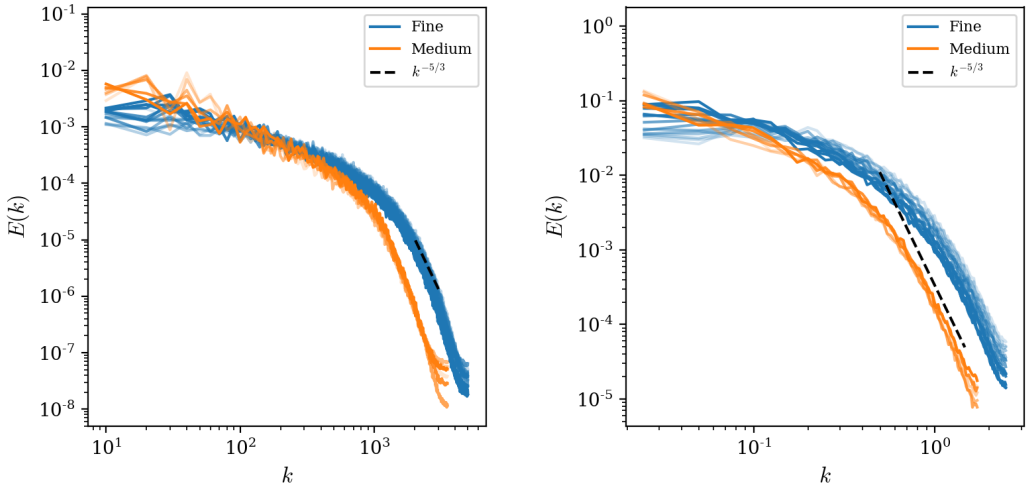

Figure 4.4: Several snapshots in time of streamwise (left) and spanwise (right) energy spectra for an unstable, high speed and unity density ratio case ($\delta_0/r_c = 0.001, M_c = 0.2, \rho_2/\rho_1 = 7, u_2/u_1 = 0.4$) along the shear layer centerline during the period of turbulent growth.

Time integration was conducted with 4^{th} order Runge-Kutta (RK4) and dependence of the shear layer growth rates on time step size was determined to be small. As shown in Fig. 4.5, the growth rate differs very little with different time steps using RK4 time integration. When Δt is reduced from 0.001 to 0.0005, the average growth rate during convective time $t^* = t\Delta u/\delta_0 \in [20, 40]$ differs by less than 3%. The sensitivity of results to the selected time integration method was also evaluated. As shown in Fig. 4.6, the order of accuracy of time integration also did not change the observed growth rates. Use of either RK4 or second order backwards differentiation (BDF2) gave the same growth rate and range of shear stress and TKE production magnitudes for the same configuration. All cases in this study were conducted using RK4 and a timestep of $\Delta t = 0.001$.

The computational domain size can be validated using two point correlations of turbulent structures about the centerline of the shear layer. The evolution of radial velocity fluctuation u_r'' autocorrelations are shown in Fig. 4.7 at $\delta_0/r_c = 0.01, M_c = 0.2, u_2/u_1 = 1.9$ and $\rho_2/\rho_1 = 1$. These conditions are associated with one of the moderately curved shear layers where the domain is challenged by two features of the flow. The first challenge is that larger scale structures typically form at this low M_c and the domain must be large enough to contain multiple of these coherent flow features for meaningful statistics to be extracted. The second challenge is that the growth rate for this configuration is higher than the growth rates for stable configurations, so the domain must be large enough that the period of turbulent spreading is sufficiently long for collection of statistics.

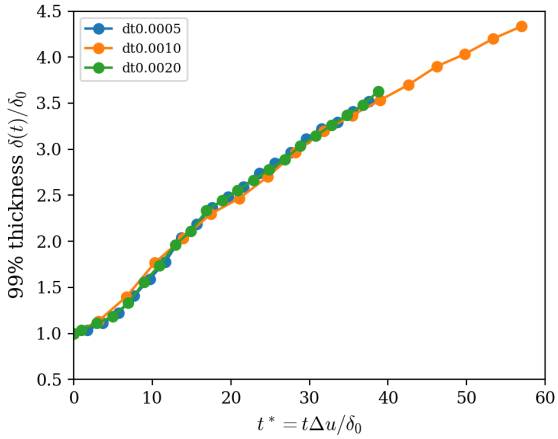

Figure 4.5: Effect of RK4 time step size for case $\delta_0/r_c = 0.01, M_c = 0.8, u_2/u_1 = 0.1$ and $\rho_2/\rho_1 = 7$.

The autocorrelations for this condition are shown at early, mid and late times during the turbulent development. At early times, notable correlation can be observed between the velocity fluctuations applied in the initial conditions. At the later times shown in the two contour plots below, the autocorrelations demonstrate that the domain is sufficiently large in the streamwise and spanwise direction with satisfactory decorrelation in u_r''.

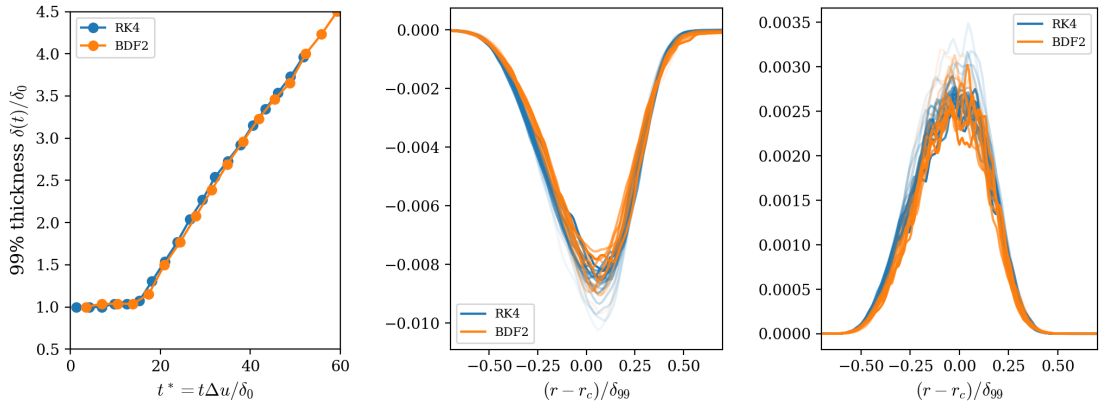

(a) Evolution of δ_{99} (b) Shear stress R_{12} (c) TKE production P

Figure 4.6: Effect of time integration method for case $\delta_0/r_c = 0.001, M_c = 0.2, u_2/u_1 = 0.4$ and $\rho_2/\rho_1 = 7$.

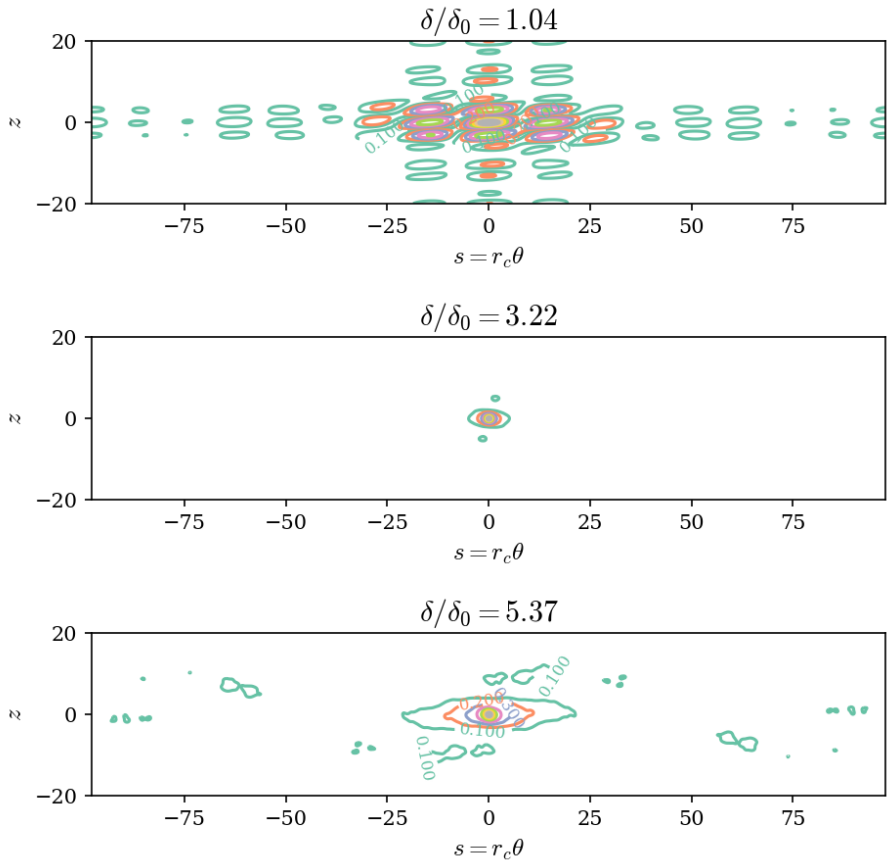

Figure 4.7: Autocorrelations of u_r'' for case $\delta_0/r_c = 0.01, M_c = 0.2, u_2/u_1 = 1.9$ and $\rho_2/\rho_1 = 1$ at various points in time. Contour levels vary from 0.1 to 1.0 in increments of 0.1.

4.2.3 Physical parameters

The temporally developing curved shear layer configured as two co-annular streams which are periodic spanwise (z) direction and azimuthally periodic in the streamwise (θ) direction. In the remainder of this chapter, the outer and inner radial freestream values are denoted with subscripts 1 and 2, respectively. The streamwise velocity, u_θ, satisfies the pressure gradient relation to be consistent with the chosen radius of curvature along the shear layer centerline, r_c. The initial conditions for the curved shear layer are set such that vorticity is zero everywhere except within the shear layer region. As such, the inner and outer radial freestream flows have constant total pressure P_t, constant circulation $\Gamma = ru_\theta$, and are homoentropic. In contrast to the planar shear layer, the velocity difference across the curved shear layer is non-constant as the shear layer thickness grows. Definitions of shear layer thicknesses will be discussed further in the results section below.

$$M_c = \frac{\Delta u}{c_1 + c_2} \qquad \rho_2/\rho_1 \qquad \delta_0/r_c$$

$$\delta_\Gamma = \frac{1}{(\Delta\Gamma)^2}\int_{R_2}^{R_1} (\Gamma_1 - \tilde{\Gamma})(\tilde{\Gamma} - \Gamma_2)dr \tag{4.13}$$

The physical parameters governing this flow are the curvature intensity, the convective Mach number, the velocity ratio, and the density ratio across the shear layer. The curvature intensity, defined as the ratio of the (initial) shear layer thickness compared to the radius of curvature, is selected to range from $\delta_0/r_c = 0.001$ to $\delta_0/r_c = 0.01$, where δ_0 is the initial thickness defined from the mean circulation profile, $\delta_\Gamma(0)$. The convective Mach number, $M_c = \Delta u/(c_1 + c_2)$, a measure of the mean flow's compressibility, was selected to be $M_c = 0.2$ and 0.8 in order to provide cases with a combination of compressibility and curvature effects. Likewise, the density ratio ρ_2/ρ_1 was chosen to be $1/7, 1, 7$ at each compressibility and curvature ratio. These density ratios were selected for comparison with the previous chapters' work and for validation using previously published literature [136, 103, 84]. The parameter space and freestream constants for the present cases at unity and variable density conditions are given in Table 4.2. A subset of ten nominally unity density ratio configurations, $\rho_2/\rho_1 = 1$, were selected for analysis in order to focus on simple curvature effects due to kinematics, without large mean density gradient effects. These cases are summarized in Table 4.3. Definitions of the shear layer thickness and growth rate are discussed in section 4.4.2. The middle column of Table 4.3 indicates the range of curvature δ_Γ/r_c during turbulent growth from which statistics are collected.

Table 4.2: Case names and corresponding parameter spaces organized by curvature intensity δ/r_c, compressibility M_c, density ratio ρ_2/ρ_1 and velocity ratio u_2/u_1. Total pressure P_t and entropy constant $\xi = p/\rho^\gamma$ are also specified for each freestream.

Case ID	δ_0/r_c	P_{t1}	P_{t2}	ξ_1	ξ_2	ρ_2/ρ_1	u_2/u_1	M_c
dR001_Mc02_rr0.1_uu2.6	0.001	0.82	0.82	1.00	16.00	0.143	2.636	0.202
dR001_Mc02_rr1.0_uu0.5	0.001	1.16	0.82	1.00	1.00	1.001	0.529	0.201
dR001_Mc02_rr1.0_uu1.9	0.001	0.82	1.16	1.00	1.00	1.001	1.882	0.200
dR001_Mc02_rr7.0_uu0.4	0.001	0.82	0.82	16.05	1.00	7.001	0.377	0.203
dR001_Mc08_rr0.1_uu7.5	0.001	0.82	1.95	1.00	15.50	0.144	7.483	0.805
dR001_Mc08_rr1.0_uu0.2	0.001	6.20	0.82	1.00	1.00	1.005	0.219	0.800
dR001_Mc08_rr1.0_uu4.5	0.001	0.82	6.30	1.00	1.00	1.005	4.506	0.800
dR001_Mc08_rr7.0_uu0.1	0.001	1.92	0.82	15.59	1.00	7.002	0.133	0.801
dR010_Mc02_rr0.1_uu2.6	0.010	0.82	0.82	1.00	15.95	0.144	2.633	0.204
dR010_Mc02_rr1.0_uu0.5	0.010	1.15	0.82	1.00	1.00	1.009	0.521	0.204
dR010_Mc02_rr1.0_uu1.9	0.010	0.82	1.18	1.00	1.00	1.010	1.868	0.200
dR010_Mc02_rr7.0_uu0.4	0.010	0.82	0.82	16.05	1.00	7.032	0.369	0.207
dR010_Mc08_rr0.1_uu7.4	0.010	0.82	2.00	1.00	16.00	0.144	7.378	0.809
dR010_Mc08_rr1.0_uu0.2	0.010	5.75	0.82	1.00	1.00	1.046	0.207	0.800
dR010_Mc08_rr1.1_uu4.3	0.010	0.82	6.90	1.00	1.00	1.052	4.277	0.803
dR010_Mc08_rr7.0_uu0.1	0.010	1.90	0.82	15.15	1.00	7.001	0.130	0.805

4.2.4 Initial conditions

Each freestream in the curved shear layer is vorticity-free in the mean flow. The shear layer region is centered about the centerline radius r_c with an initial thickness of δ_0. The initial values for the constant freestream total pressure, P_t, and entropy, ξ_i, for each freestream $i = 1, 2$ are set according to Eqn. 4.14-4.15. Both streams have the same ratio of specific heats, $\gamma = 1.4$, and gas constant R_g. The density gradient is due to thermal effects, rather than different species densities.

$$P_t(r) = P_{t,1}g + P_{t,2}(1-g) \tag{4.14}$$

$$\xi(r) = \xi g + \xi(1-g) \tag{4.15}$$

$$g(r) = \frac{1}{2}\left[1 + \tanh\left(\frac{r - r_c}{\delta_0}\right)\right]$$

The streamwise velocity profiles are set by the circulation as $u_\theta = \Gamma/r$, and the pressure profile is computed by integrating $dp/dr = \rho u_\theta^2/r$ from the centerline at $r = r_c$ to the upper and lower boundaries, using a reference pressure p_{ref} at the centerline. This reference pressure is set such that the speed of sound at the centerline is a constant c_{ref} for all cases. The initial conditions satisfy potential, inviscid flow except in the initial shear layer region where vorticity is nonzero. To induce turbulence, solenoidal velocity perturbations were added to the shear layer. By selecting

Table 4.3: Physical parameters and curvature levels during initial and turbulent 'asymptotic' growth for unity density ratio cases

M_c	u_2/u_1	$\delta_\Gamma(0)/r_c$	Turb. δ_Γ/r_c	Final $\dot{\delta}_\Gamma/\Delta u(0)$	Final $\Delta u/\Delta u(0)$
0.2	0.5	0.001	0.005 - 0.008	0.071	0.98
	0.5	0.010	0.075 - 0.108	0.035	0.97
	1.9	0.001	0.004 - 0.011	0.069	1.00
	1.9	0.010	0.061 - 0.110	0.140	1.01
0.8	0.2	0.001	0.006 - 0.009	0.036	0.99
	0.2	0.005	0.022 - 0.027	0.018	0.98
	0.2	0.010	0.049 - 0.108	0.018	0.96
	4.5	0.001	0.006 - 0.009	0.025	1.01
	4.6	0.005	0.025 - 0.040	0.061	1.02
	4.8	0.010	0.056 - 0.085	0.079	1.04

simple profiles for each u'_θ and u'_r, the remaining spanwise component of the fluctuating velocity can be solved analytically from the continuity equation to maintain a divergence-free initialization. For u'_θ and u'_r, sinusoidal perturbations are added at selected spatial modes $k_\theta^{(i)} = i2\pi/L_\theta$ and $k_z^{(j)} = j2\pi/L_z$ for $i, j \in [4, 8]$ with amplitude $A(r) = \exp[\sigma(r - r_c)^2]$. These perturbations decay exponentially with a rate of $\sigma = 5$ into the freestreams. The initial perturbation amplitude is $0.05\Delta\bar{u}$ and phases ϕ were chosen randomly for each mode. The chosen form for velocity perturbations is given below.

$$u'_\theta = \sum_{i,j} A(r)\cos(k_\theta^{(i)}\theta + \phi_1)\cos(k_z^{(j)}z + \phi_2) \tag{4.16}$$

$$u'_r = \sum_{i,j} A(r)\sin(k_\theta^{(i)}\theta + \phi_1)\sin(k_z^{(j)}z + \phi_2) \tag{4.17}$$

$$u'_z = \sum_{i,j} \frac{A(r)}{rk_z^{(j)}}\sin(k_\theta^{(i)}\theta + \phi_1)[(1 - 2r(r - r_c))\cos(k_z^{(j)}z + \phi_2) + k_\theta^{(i)}\sin(k_z^{(j)}z + \phi_2)] \tag{4.18}$$

The effect of initial conditions is observed to be small for most cases. The growth rate resulting from three initial conditions are compared for case at $\delta/r_c = 0.010, M_c = 0.2, \rho_2/\rho_1 = 1, u_2/u_1 = 0.5$ in Fig. 4.9. The case labelled 'Phases' was initialized using the same form of perturbations as the 'Original' case, but with different perturbation phases. These two cases show similar behavior during both the transitional and turbulent phases of growth. A third case was initialized using broadband velocity perturbations which are likewise masked to be zero outside the mixing layer region. Though this initialization introduces dilatational velocities into the flow, the turbulent growth remains similar to that of the original initialization method.

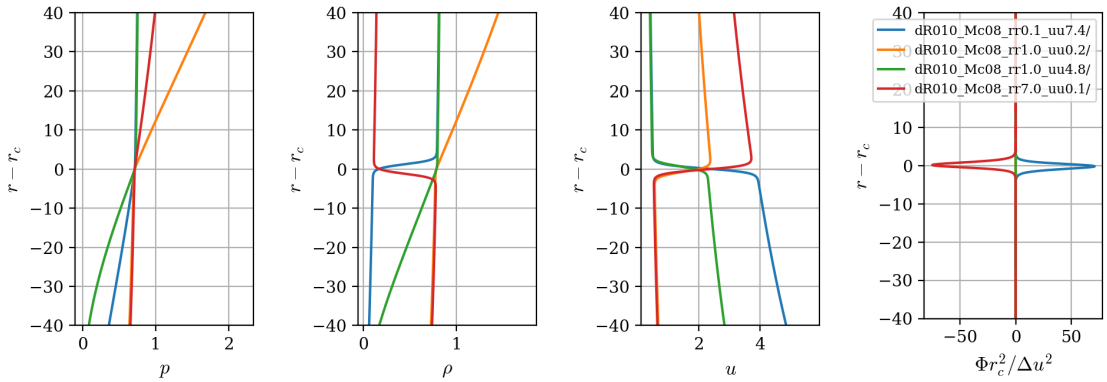

Figure 4.8: Initial profiles of pressure, density, streamwise velocity, and normalized Eckhoff criterion for selected cases at $\delta_0/r_c = 0.01$, $M_c = 0.8$, and different density ratios.

4.2.5 Boundary conditions

The upper and lower boundaries of the domain are adiabatic slips walls with second order pressure extrapolation which enforce zero radial velocity at the wall. The effect of boundary conditions for a simplified problem has been found to be negligible. To test the effect of boundary conditions on the mixing layer growth rates, two calculations with identical initial conditions and numerical methods were run. The test problem was a simplified, 2D version of the mixing layers presented in the main sections at low curvature. The perturbations in this case grow and emit some initial transient waves, but do not become turbulent. In one case, pressures were extrapolated at the upper and lower radial boundaries which acted as a slip wall. In another case, with the exact same initial conditions, these slip walls were instead treated with outflow boundary conditions, in which conservative variables are extrapolated at the boundaaries [23]. As shown in Fig. 4.10, both the cases with pressure-extrapolation and outflow boundary conditions exhibit almost the same evolution of the δ_{99}.

4.2.6 Effect of WENO5 on disturbance energy

The effect of using WENO5 [132] for a simplified problem is shown in Fig. 4.11. A single modal perturbation at $k_\theta = 8\pi/L_\theta$ and $k_z = 8\pi/L_z$ of the form and amplitude given in Eqns. 4.16-4.18 was used to disturb the base flow profile of a case at conditions $\delta/r_c = 0.010, M_c = 0.8, \rho_2/\rho_1 = 7, u_2/u_1 = 0.1$. The grid resolution and domain size mimics that of the grids used in the full turbulent simulations. The evolution of the kinetic energy of the perturbations, normalized by the initial kinetic energy is shown in Fig. 4.11a. The perturbation energy tracked by WENO5 and by the second order central differences shows some discrepancies after a normalized time of $t^* = 2.0$.

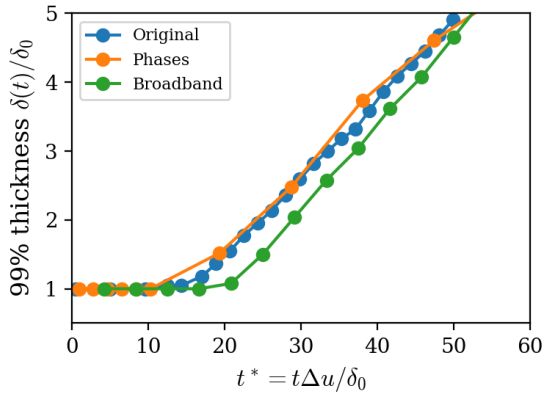

Figure 4.9: Effect of initial conditions on growth rates for conditions $\delta/r_c = 0.010, M_c = 0.2, \rho_2/\rho_1 = 1, u_2/u_1 = 0.5$.

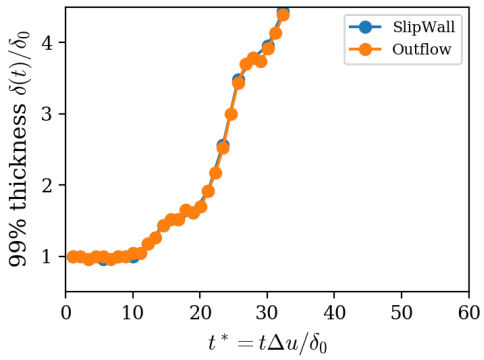

Figure 4.10: Effect of boundary conditions for 2D test case at conditions $\delta/r_c = 0.001, M_c = 0.2, \rho_2/\rho_1 = 1, u_2/u_1 = 1.9$.

This is due in part to some numerical artifacts which appear in the second order central difference case corresponding to the given grid resolution. The final growth rate of the disturbance energy show some difference between the two numerical methods for this simple test case. It is possible that similar differences would appear if the corresponding comparison between second order central differences and WENO5 were conducted for the fully turbulent calculations. Given that conducting this simple, single-mode test case with central differences also required a time step which is ten times finer than that used in the WENO5 case, conducting the calculations with the central differences would have increased the total cost of this study substantially.

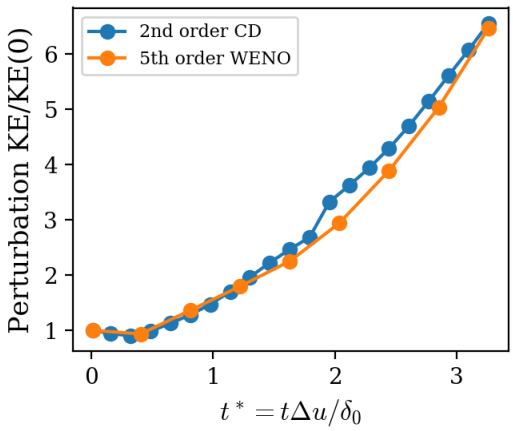

(a) Growth of perturbation kinetic energy (KE)

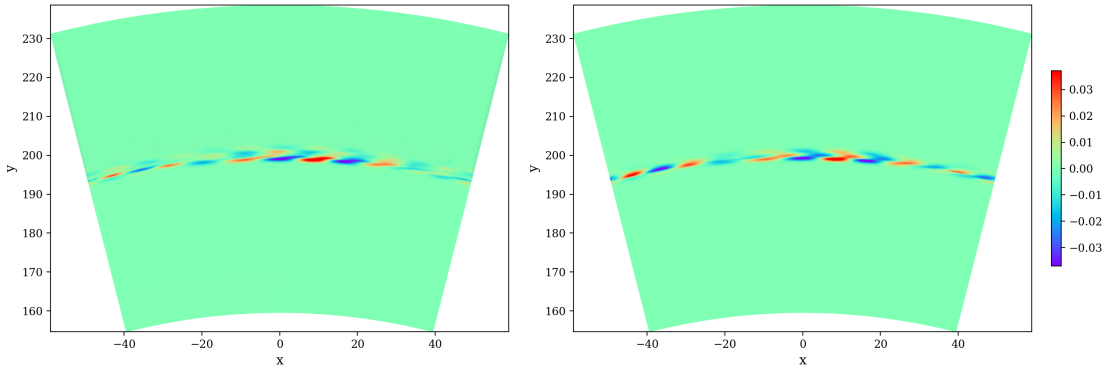

(b) Instantaneous streamwise pressure $p'/(\rho_0 \Delta u^2)$ using central differences at $t^* \approx 1$.

(c) Instantaneous streamwise pressure $p'/(\rho_0 \Delta u^2)$ using WENO5 at $t^* \approx 1$.

Figure 4.11: Effect of numerical method for convective terms on a test case at conditions $\delta/r_c = 0.010, M_c = 0.8, \rho_2/\rho_1 = 7, u_2/u_1 = 0.1$.

4.3 Visualization and vortical structures

In this section, visualization of turbulent structures along various slices of the domain are shown to highlight notable similarities and differences between stably and unstably curved shear layers. The effect of the curvature on fluctuation intensity and vortical features during the transitional and turbulent period of growth are qualitatively discussed.

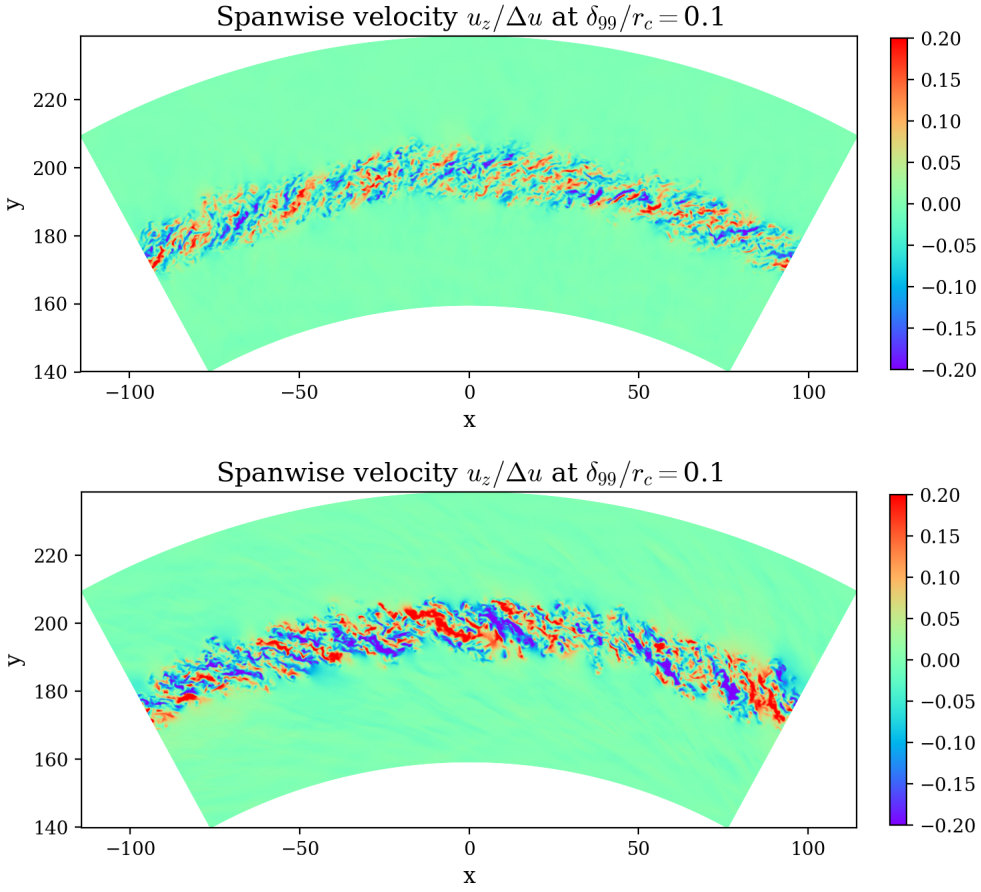

Figure 4.12: Spanwise velocity fields of stable (top) and unstable (bottom) cases for $M_c = 0.8$ and $\delta_0/r_c = 0.01$. The domain has been truncated in the radial extent for visualization purposes.

Instantaneous spanwise velocity fields for the two configurations are shown in Fig. 4.12. In all configurations, the azimuthal flow travels in the clockwise direction. Two distinct differences between the turbulence in the two configurations can be easily observed by comparing these two visualizations. The magnitude of turbulent fluctuations in the unstable case is larger than that of

the stable case (both plots use the same color scale). This difference in turbulent stresses can also be seen in the profiles of TKE in Fig. 4.26. The peak TKE in the unstable case is nearly twice that of the stable case. The striation along the shear layer is opposite for the stable and unstable cases; this direction of shearing for the turbulent eddies is consistent with the streamwise velocity gradient in the two cases. In the stable configurations, the streamwise velocity u_θ is higher along the outer freestream; and in the unstable configurations, u_θ is higher along the inner freestream. The corresponding evolution of mean velocity profiles during multiple snapshots during turbulent growth are plotted by radius r in Fig. 4.23 (a) to show spreading of the shear layer. There is a small, negative velocity gradient in each of the freestream regions in order to ensure that the freestreams are vorticity free. This requirement of constant freestream circulation causes the velocity difference across the shear layer to also change (proportional to r^{-1}) as it spreads, though the change is relatively small (see Table 4.3). For the stable cases, Δu decreases in time, whereas it increases in time for the unstable cases. In planar shear layers, Δu remains constant and the mean shear decreases as the shear layer grows. In the stable configuration, because the velocity difference decreases as the shear layer grows, the mean shear contributing to TKE production and eddy growth are further reduced.

Given the effects of streamwise curvature in boundary layers along a concave or convex surface, structural differences in the mixing layer due to streamwise curvature may be expected. In particular, the presence of Görtler vorticies or other spanwise-coherent structures may be expected to form in the turbulent region. While some qualitative differences can be observed in the mixing layer's spanwise organization while perturbations grow into turbulence, a clear difference in coherent structures between stably and unstably curved cases was not observed when the flow became fully turbulent. This observation remained unaffected by compressibility levels. At both low and high speeds, during periods of well-developed turbulent growth, large-scale spanwise vorticies were not seen in the mixing region.

As the curvature intensity increases, small differences can be observed in instantaneous snapshots of streamwise vorticity for unstable configurations. In Fig. 4.13, spanwise cuts of the streamwise vorticity are compared at similar times of shear layer evolution ($\delta_{99}(t)/\delta_{99}(0) = 1.6$). At low curvature levels, the vortical region is compact and nearly uniform in height across the span of the mixing layer. At higher curvature levels, a slightly less compact region of vorticity is observed in the mixing region. In addition this sparsity, slight stretching of streamwise vorticity can be observed from the anisotropy of contour levels. This effect is more obvious for the low speed cases, where elongated iso-contours of vorticity are seen. The profiles in Fig. 4.14 show the turbulent vortex stretching term of the mean streamwise vorticity transport equation, $\overline{\omega_j' u_{i,j}'}$, normalized by the instantaneous scales. Three profiles at times leading up to the visualization time are plotted to indicate the drift in value during this transient period. Statistical noise is evident in the profiles,

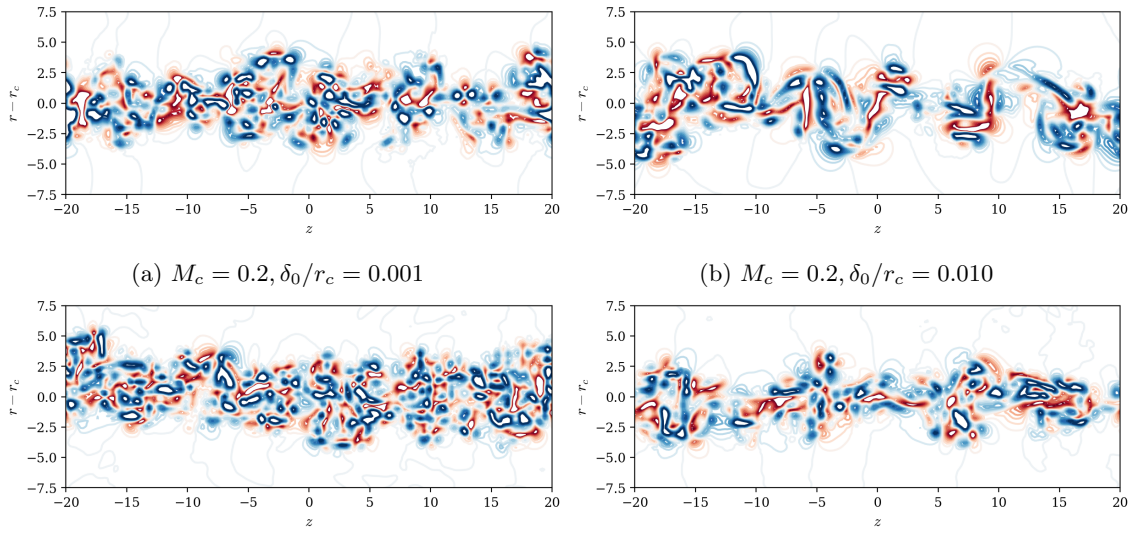

(a) $M_c = 0.2, \delta_0/r_c = 0.001$ (b) $M_c = 0.2, \delta_0/r_c = 0.010$

(c) $M_c = 0.8, \delta_0/r_c = 0.001$ (d) $M_c = 0.8, \delta_0/r_c = 0.010$

Figure 4.13: Instantaneous normalized streamwise vorticity at contour levels $\omega_\theta \delta_{99}/\Delta u \in [-5, 5]$ along a spanwise $(r - z)$ plane for $u_2 > u_1$ cases. The domain has been truncated for visualization purposes.

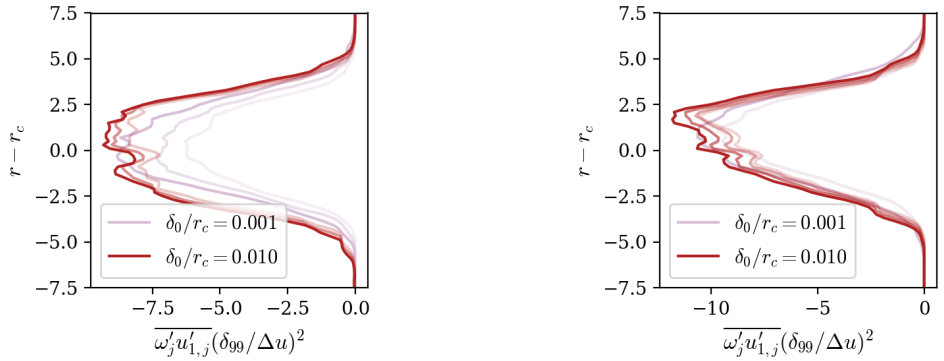

(a) $M_c = 0.2$ (b) $M_c = 0.8$

Figure 4.14: Effect of increasing curvature intensity on profiles of streamwise vortex stretching for unstable cases at low and high compressibility, $\rho_2/\rho_1 = 1$ and $u_2 > u_1$.

but a general form of the vortex stretching profile can be inferred. As seen qualitatively in the instantaneous visualizations, the normalized stretching of streamwise vorticity is slightly amplified for increased curvature intensity.

The intermittent vorticity field also suggests that higher levels of curvature achieve equivalent shear layer thicknesses over a shorter development period. Regions of sparse vorticity may be expected as the shear layer 'falls apart' during the early evolution of unstable cases, compared to stable cases with a restoring force of the freestream pressure gradient. In stable cases, due to the velocity ratio $u_2/u_1 < 1$, the freestream pressure gradient in the radial direction which scales as $dp/dr \sim u^2/r$ is the largest along the outer freestream. As a result, it is possible that vorticies which may otherwise stray into the outer freestream flow from the main mixing region are pushed back by the increasing mean pressure further from the mixing layer.

The visualizations are shown to highlight the differences in the vortical structures during early shear layer evolution. However, as the turbulence developed further, larger vortical structures or roll cells were not observed. Profiles of streamwise velocity fluctuations, u''_θ, during the time period of early shear layer development ($\delta_{99}(t)/\delta_{99}(0) = 1.6$) and fully developed turbulence ($\delta_{99}(t)/\delta_{99}(0) = 3.0$) are shown in Figs. 4.15-4.16. During the early development stage of the shear layer, for the same compressibility level of $M_c = 0.2$ in subfigures (a) and (b), the structure of the fluctuation field is notably different. Coherent elongated streaks can be observed in the higher curvature case, and transition to turbulence has not yet encompassed the entire domain. Notably, in the second figure in Fig. 4.15, transition to turbulence has only occurred between $-50 < s < -5$, and the remainder of the domain exhibits the fastest growing perturbation mode. The inhomogeneity in the transition is typical for mixing layer simulations with randomized modes in the initial perturbations. Similar contrast between the low and high curvature case for subfigures (c) and (d) at $M_c = 0.8$. This again supports the idea that the higher initial level of curvature facilitates shear layer growth for the same unstable velocity ratio and unity density ratio. Later, during the stage of fully developed turbulence, streaks of somewhat coherent streamwise structures are visible, but definite differences in the organization of u''_θ were not observed. The observed lack of large scale turbulent structures in this parameter space during the fully turbulent regime is similar to experimental observations by [59] for incompressible turbulent boundary layers under destabilizing curvature, but largely differs from Wang's observations of incompressible curved mixing layers. In Wang's experiments, shear layers were confined to a relatively narrow channel and the two freestreams were initialled separated with a curved splitter plate. Large scale structures dominated the streamwise visualizations of cases at unity density ratio, but the influence of the experimental facility and channel width on these structures is unknown.

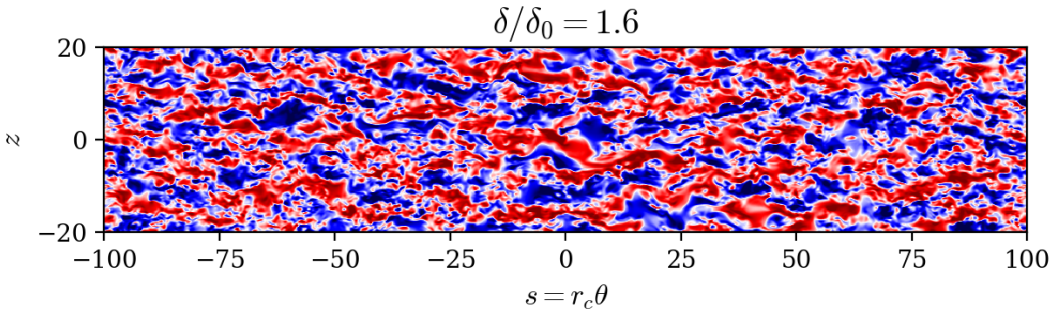

(a) $M_c = 0.2, \delta_0/r_c = 0.001$

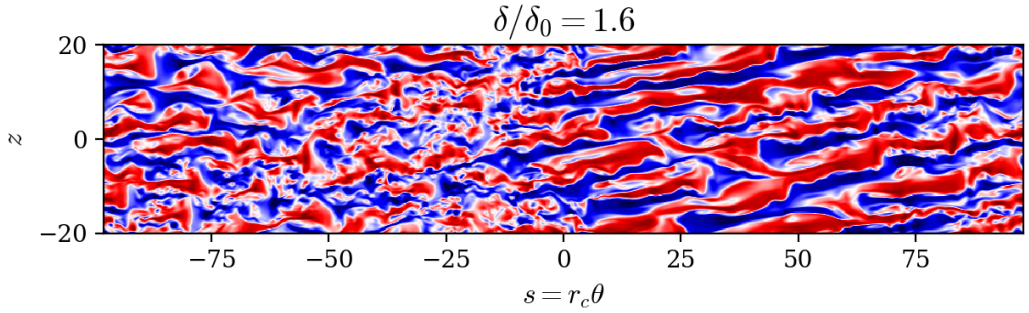

(b) $M_c = 0.2, \delta_0/r_c = 0.010$

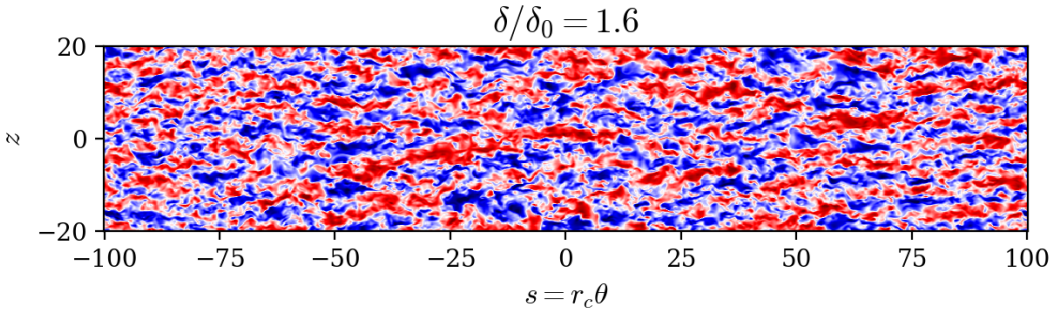

(c) $M_c = 0.8, \delta_0/r_c = 0.001$

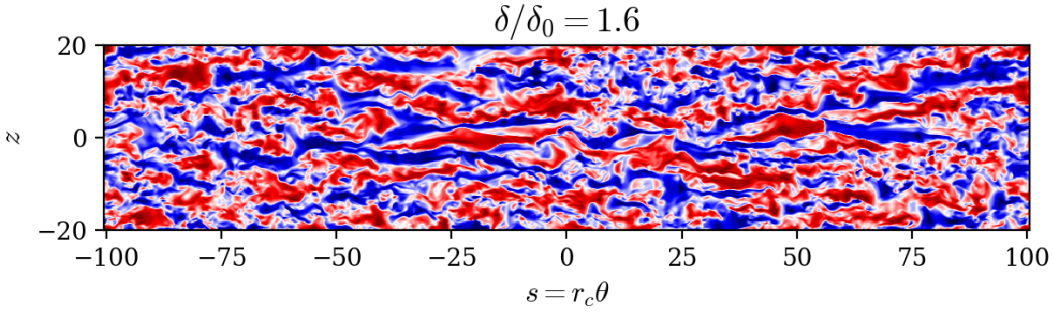

(d) $M_c = 0.8, \delta_0/r_c = 0.010$

Figure 4.15: Instantaneous visualizations of normalized streamwise velocity fluctuations at contour levels $u''_\theta/\Delta u \in [-0.5, 0.5]$ along a streamwise $(\theta - z)$ plane for centrifugally unstable cases at $\rho_2/\rho_1 = 1$ during transitional times.

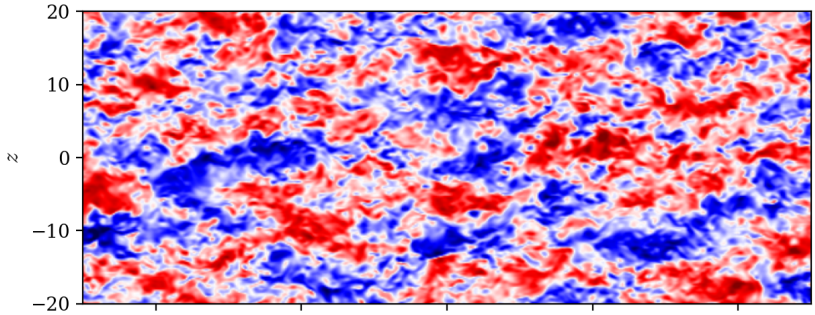

(a) $M_c = 0.2, \delta_0/r_c = 0.001$

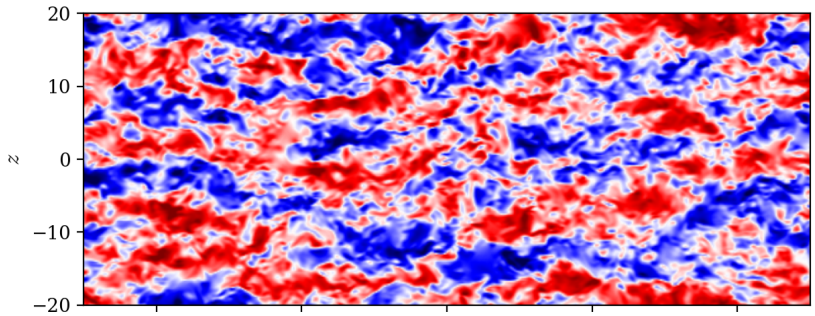

(b) $M_c = 0.2, \delta_0/r_c = 0.010$

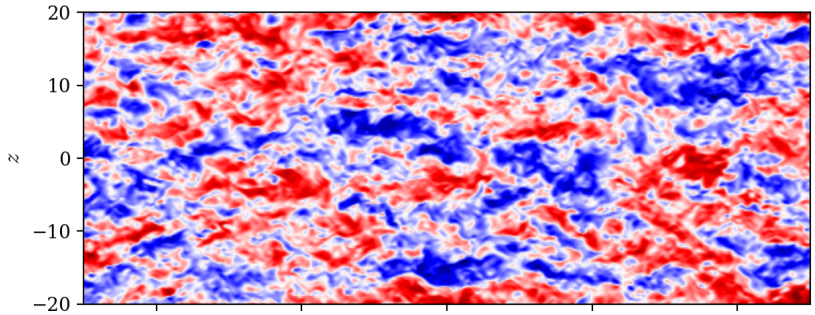

(c) $M_c = 0.8, \delta_0/r_c = 0.001$

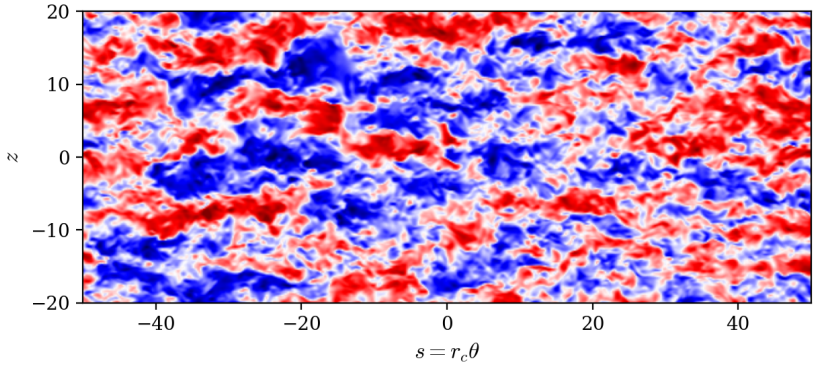

(d) $M_c = 0.8, \delta_0/r_c = 0.010$

Figure 4.16: Instantaneous visualizations of normalized streamwise velocity fluctuations at contour levels $u''_\theta/\Delta u \in [-0.5, 0.5]$ along a streamwise $(\theta - z)$ plane for centrifugally unstable cases at $\rho_2/\rho_1 = 1$. The streamwise extent has been truncated by 50% for visualization purposes.

4.4 Curvature effects on turbulent statistics

This section first discusses the evolution of mean profiles in the flow followed by different measures of shear layer thicknesses and growth rates. After this introduction of shear layer metrics, stably and unstably curved configurations are compared, and the effects of increasing curvature intensity are presented. Lastly, comparison with compressibility effects and combination with variable density effects for the given parameter range are considered.

4.4.1 Mean profiles and turbulent stresses

For all cases, mean profiles of velocity, temperature, pressure and others are given in Figs. B.7-B.11 of Appendix B. The spreading of the shear layer can be observed from the evolution of density profiles shown in Figs. 4.17, with line opacity indicating various snapshots in time. Each subfigure shows a set of cases at the same initial curvature and compressibility level with varying density and velocity ratio. The mean density profiles for the variable density cases plotted in red and blue indicate expected asymmetric spreading of the mixing region, where the mean density profile has a larger spread into the lighter fluid region compared to the denser region. The unity density ratio cases plotted in green and orange demonstrate the extent of the variation in freestream density required for the desired curvature and compressibility levels. The higher compressibility cases at $M_c = 0.8$ and unity density ratio show a slight decrease in mean density inside the mixing region, which is consistent with the aerodynamic heating observed in the simulations presented in the previous chapters.

The turbulent shear stress plays an essential role in shear layer dynamics because it is directly related to the shear layer's growth. Thus, validating the shear stresses of the present simulations with previously published literature has been a high priority in this study. Figure 4.18 compares the trace and shear components of the turbulent stress tensor $R_{ij} = \widetilde{u_i'' u_j''}$ of the present, approximately planar, low speed and unity density ratio data with previously published results. Experimental data are plotted in symbols and numerical data are plotted with solid lines. The shear stress magnitudes are well-aligned with previous data. The normal stress comparisons exhibit slightly larger departures from previous numerical profiles, but peak magnitudes remain within the spread of experimental points. The present calculations using OVERFLOW (labelled 'Matsuno et al. 2022') compare well with prior calculations described in Ch. 2 using *PadeOps* (labelled 'Matsuno & Lele 2020').

The magnitudes of the normal stresses R_{11}, R_{22} and R_{33} and shear stresses R_{12} for all sixteen cases are included for completeness in Appendix B. As expected, the shear stress's sign corresponds to the velocity gradient in each configuration. In configurations with the velocity gradient decreasing

with r across the shear layer ($u_2/u_1 > 1$), the shear stress is negative. In configurations with the velocity gradient increasing with r across the shear layer ($u_2/u_1 < 1$), the shear stress is positive. Expected compressibility, variable density, and curvature effects on the shear stress can be highlighted by examining subsets of the present data in Fig. 4.19. Note that the shear stresses plotted in Fig. 4.19 are Favre-averaged and incorporate density fluctuations.

The compressibility effect on turbulent shear stresses is highlighted in Fig. 4.19a. Four cases at the same level of low curvature and unity density ratio are shown. The shear stress magnitudes decrease from the low speed cases (blue and orange profiles at $M_c = 0.2$) to the high speed cases (red and orange profiles at $M_c = 0.8$). This is consistent with the decrease in growth rates indicated in Fig. 4.22a, to be discussed in the subsequent sections. As demonstrated in the previous chapters on planar shear layers, this decrease in shear stress magnitude with increasing compressibility can be scaled by the effective velocity difference across an eddy lengthscale [85].

The effect of density variations on the shear stresses can be observed in Fig. 4.19b. Four cases at the same level of low curvature and compressibility are shown. Two behaviors can be observed from this figure. First, similarly to the compressibility effect, the mean density gradient across the shear layer serves to reduce the turbulent shear stress. This reduction in shear stress is reflected in the reduction in growth rates between unity and variable density configurations, shown later in Fig. 4.22. Additionally, a clear indication of asymmetry can be observed in the variable density cases. The stress profiles for cases at density ratios $\rho_2/\rho_1 = 1/7$ and 7 are anti-symmetric about the y-axis, with both configurations indicating that the shear stresses skew away from the heavier freestream and into the lighter freestream region. Again, this behavior is well documented in planar shear layers [103, 2, 6, 86]. The effect of curvature can be observed in Fig. 4.19c, where four cases at the same compressibility level and unity density variation are shown. As reflected in the growth rate trends in Fig. 4.22c, increasing curvature increases also shear stresses in centrifugally unstable configurations.

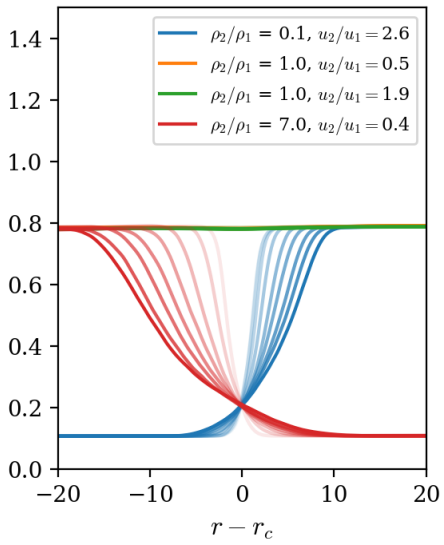

(a) $\delta/R_0 = 0.001$ and $M_c = 0.2$

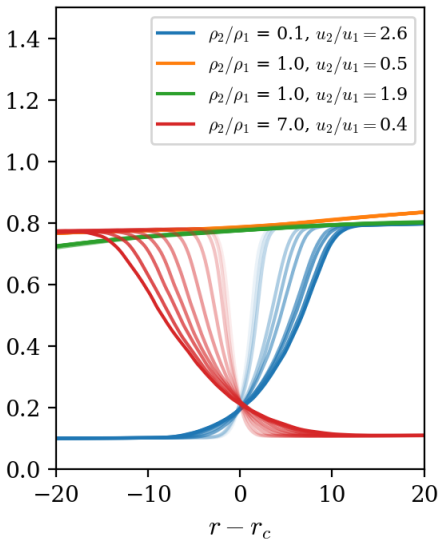

(b) $\delta/R_0 = 0.010$ and $M_c = 0.2$

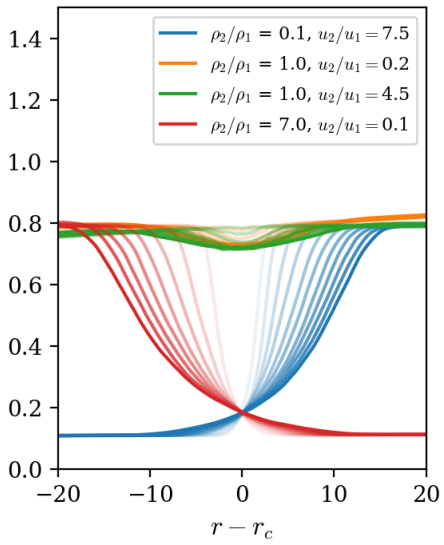

(c) $\delta/R_0 = 0.001$ and $M_c = 0.8$

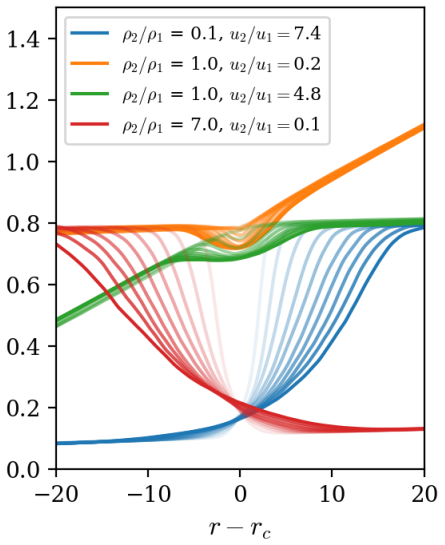

(d) $\delta/R_0 = 0.010$ and $M_c = 0.8$

Figure 4.17: Mean density profiles $\bar{\rho}(r)$ centered at the innitial radius of curvature, r_c.

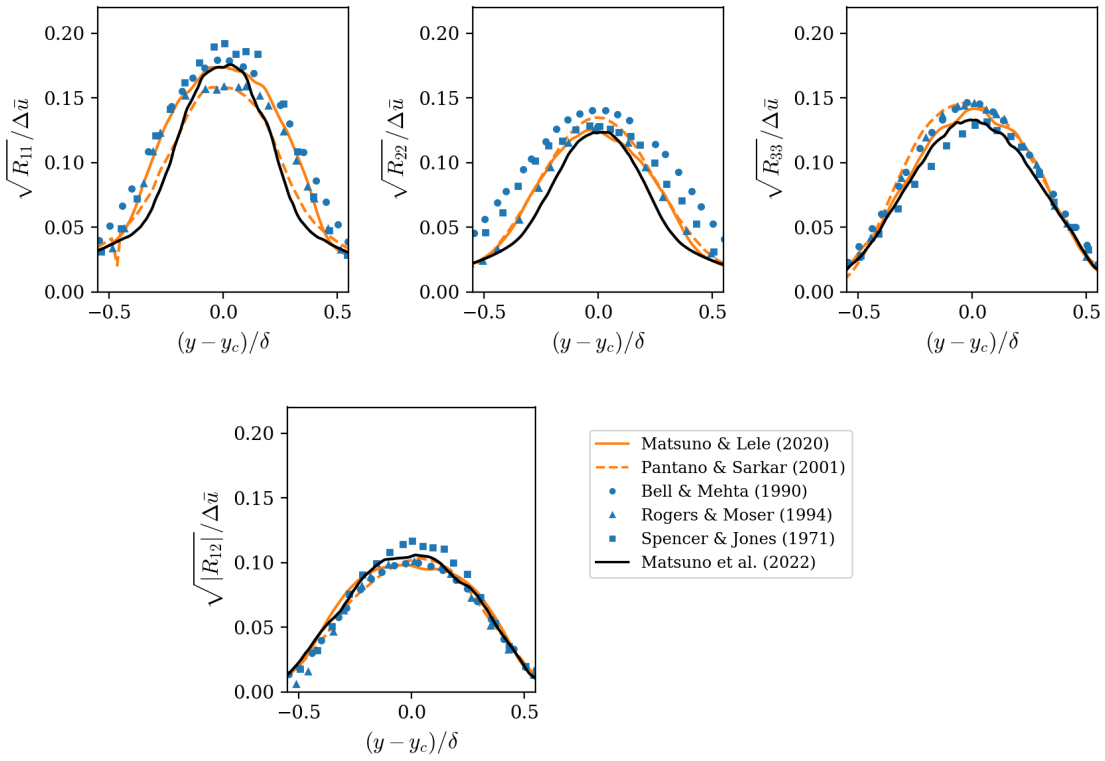

Figure 4.18: Comparison of turbulent stress magnitudes at low speeds and a unity density ratio ($\delta_0/r_c = 0.001, M_c = 0.2, \rho_2/\rho_1 = 1, u_2/u_1 = 0.5$).

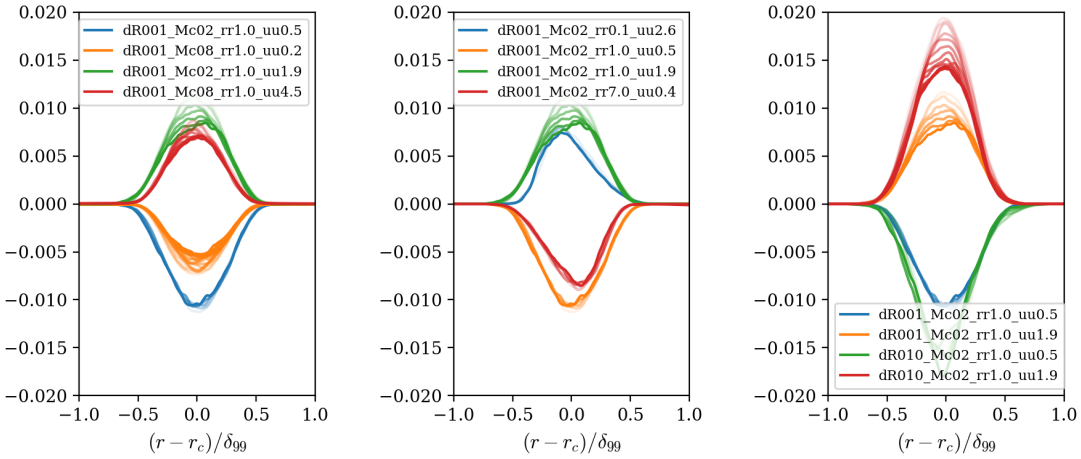

(a) (b) (c)

Figure 4.19: Normalized turbulent shear stress profiles $R_{12}/(\Delta\bar{u}^2)$ for selected cases to show (a) compressibility, (b) variable density, and (c) centrifugal instability effects.

Contributors to TKE and shear stress evolution were also compared to further understand the observed shear stress behaviors across the test matrix. By understanding the important contributors to these budgets, unexpected shear layer growth rates and the mechanisms behind them can be clarified. The evolution equation for TKE $k = \frac{1}{2}\widetilde{u_i'' u_i''}$ and nomenclature for specific terms are given in Eqn. 4.19. Components of the TKE budget are shown in Fig. 4.20. These budget terms exhibit some statistical noise from averaging limitations, but the overall profile form is observable. Comparing the unity density ratio case, shown in Fig. 4.20a, and the variable density case, shown in Fig. 4.20b, there is noticeable asymmetry in the turbulent transport term dT/dr. The transport term is skewed towards the region of lighter fluid, which is consistent with the idea that parcels of lighter fluid are more prone to velocity fluctuations compared to parcels of heavier fluid for the same magnitude of pressure fluctuations. From Figs. 4.20a and 4.20b, it is also observed that the pressure dilatation term Π also contributes significantly to the TKE evolution. In contrast, the contribution of baropycnal work in both the unity and variable density cases is small. TKE dissipation is approximately zero because of the dissipation is instead provided from WENO scheme used.

$$\frac{\partial}{\partial t}(\bar{\rho}k) + \frac{\partial}{\partial x_j}(\bar{\rho}\tilde{u}_j k) = \underbrace{-\bar{\rho}R_{ij}\frac{\partial \tilde{u}_i}{\partial x_j}}_{\text{Production } P} - \underbrace{\overline{\tau_{ij}'\frac{\partial u_i''}{\partial x_j}}}_{\text{Dissipation } D} - \frac{\partial}{\partial x_j}\underbrace{(\frac{1}{2}\overline{\rho u_j'' u_i'' u_i''} + \overline{u_j'' p'} - \overline{\tau_{ij}' u_i''})}_{\text{Turbulent transport } T} - \underbrace{\overline{u_i''}\frac{\partial \bar{p}}{\partial x_i}}_{\text{Baropycnal work } B} + \underbrace{\overline{p'\frac{\partial u_i''}{\partial x_i}}}_{\text{Pressure dilatation } \Pi} \tag{4.19}$$

$$\frac{\partial}{\partial t}(\bar{\rho}R_{ij}) + \frac{\partial}{\partial x_k}(\bar{\rho}\tilde{u}_k R_{ij}) = \underbrace{-\bar{\rho}\left(R_{ik}\frac{\partial \tilde{u}_j}{\partial x_k} + R_{jk}\frac{\partial \tilde{u}_i}{\partial x_k}\right)}_{\text{Production } P_{ij}} - \underbrace{\overline{\left(\tau_{jk}'\frac{\partial u_i''}{\partial x_k} + \tau_{ik}'\frac{\partial u_j''}{\partial x_k}\right)}}_{\text{Dissipation } D_{ij}} + \underbrace{\overline{p'\left(\frac{\partial u_i''}{\partial x_j} + \frac{\partial u_j''}{\partial x_i}\right)}}_{\text{Pressure strain } \Pi_{ij}}$$
$$- \frac{\partial}{\partial x_k}\underbrace{\left(\overline{\rho u_i'' u_j'' u_k''} + \overline{p' u_i''}\delta_{jk} + \overline{p' u_j''}\delta_{ik} - \overline{\tau_{jk}' u_i''} - \overline{\tau_{ik}' u_j''}\right)}_{\text{Turbulent transport } T_{ijk}} + \underbrace{\overline{u_i''}\left(\frac{\partial \bar{\tau}_{jk}}{\partial x_k} - \frac{\partial \bar{p}}{\partial x_j}\right) + \overline{u_j''}\left(\frac{\partial \bar{\tau}_{ik}}{\partial x_k} - \frac{\partial \bar{p}}{\partial x_i}\right)}_{\text{Mass flux coupling } \Sigma_{ij}} \tag{4.20}$$

The evolution equation for R_{12} and nomenclature for specific terms are given in Eqn. 4.20. The sign of the turbulent shear stress is easily predicted from the shear stress production term, which explicitly includes the mean velocity gradient in the radial direction. Components of the shear stress budget of selected cases are shown in Fig. 4.20. The R_{12} production term and the pressure strain component have contributions of similar magnitude to the evolution of R_{12}. This suggests that

at these conditions, the redistribution of energy in fluctuating velocities is considerable compared to the production of shear stress by the mean velocity gradient. The transport of turbulent stress by the fluctuating field, T_{12}, also has a non-negligible effect on the shear stress evolution. Present data suggests that turbulent transport of R_{12} behaves similarly to the transport of TKE in the the present data and in budgets shown by Pantano and Sarkar [103]. Sizable contributions of turbulent transport and pressure strain were also observed in the study of isolated turbulent vorticies by Duraisamy and Lele [38]. Lastly, the contribution of the mass flux coupling term is small in both the unity density ratio and variable density ratio configurations. Note that the mass fluxes are shown in Figs. B.21 and B.22 in Appendix B for completeness. A slight asymmetry can be seen in the mass flux coupling term Σ_{12}, which is skewed away from the lighter fluid freestream. The magnitude of this term is almost negligible compared to the contributions of R_{12} production, pressure strain, and turbulent transport.

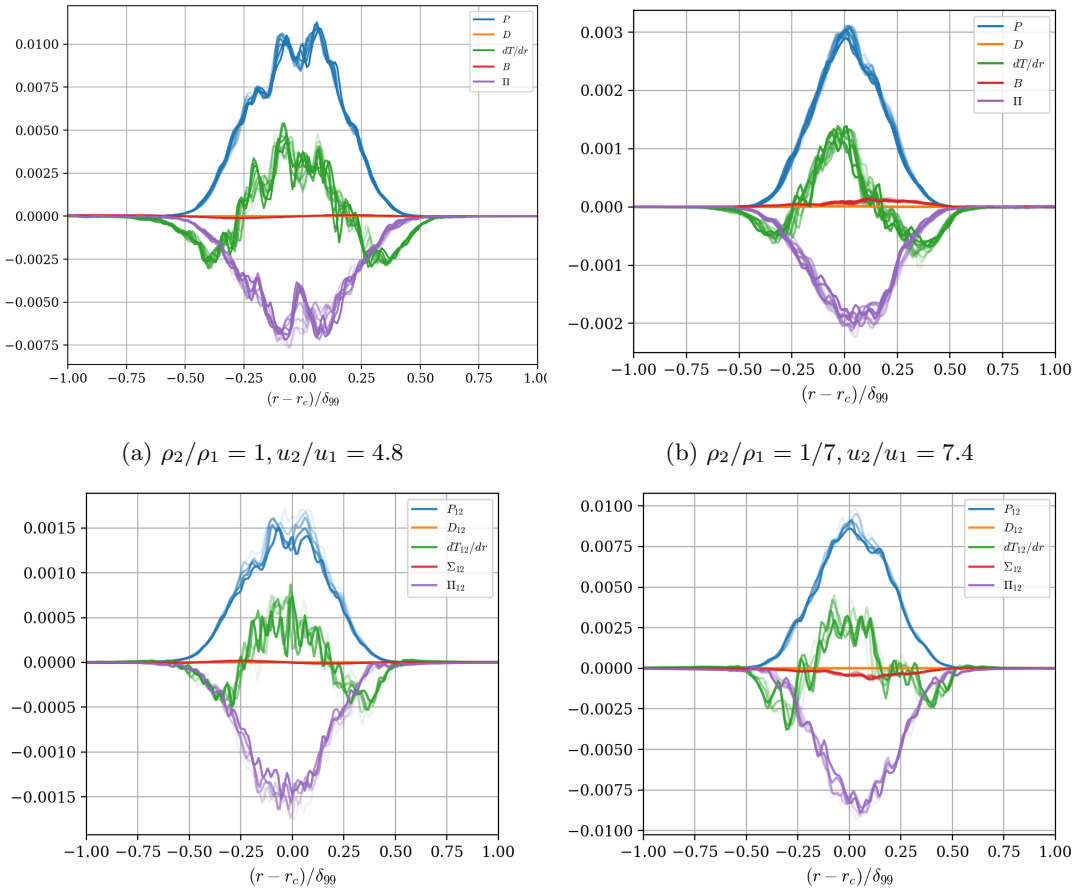

(a) $\rho_2/\rho_1 = 1, u_2/u_1 = 4.8$

(b) $\rho_2/\rho_1 = 1/7, u_2/u_1 = 7.4$

(c) $\rho_2/\rho_1 = 1, u_2/u_1 = 4.8$

(d) $\rho_2/\rho_1 = 1/7, u_2/u_1 = 7.4$

Figure 4.20: Selected TKE (a,b) and turbulent shear stress (c,d) budget terms normalized by $\delta_{99}(\Delta u)^3$ at moderate curvature ($\delta_0/r_c = 0.01$) and high compressibility ($M_c = 0.8$) for two unity and variable density cases. Oscillations present due to averaging window.

4.4.2 Growth rates

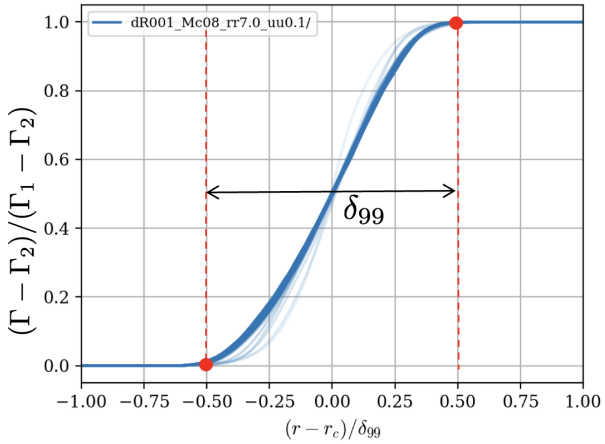

Figure 4.21: Definition of δ_{99} computed from the mean circulation $\tilde{\Gamma}$.

A consistent method of measuring the shear layer thickness and its associated growth rate is essential for characterization of any of the compressibility, variable density and curvature effects sought in this study. One such candidate to identify the shear layer boundary is the 99% thickness, δ_{99}. As shown in Fig. 4.21, this measure is computed from the mass-averaged circulation profile, $\tilde{\Gamma} = r\tilde{u}_\theta$, and is similar to the visual thickness reported by previous experimental studies of planar shear layers.

$$\delta_{99}(t) = |\delta_1| + |\delta_2| \qquad \text{with} \qquad \frac{\tilde{\Gamma}(r_c + \delta_1)}{\tilde{\Gamma}_{max}} = 0.99, \quad \frac{\tilde{\Gamma}(r_c + \delta_2)}{\tilde{\Gamma}_{min}} = 1.01 \tag{4.21}$$

Figure 4.22 shows the evolution of δ_{99} for subsets of shear layers to highlight the individual effects of compressibility, variable density, and curvature effects. Round markers indicate the beginning and end phases of averaging windows. Two cases of approximately planar ($\delta_0/r_c = 0.001$) shear layers are shown in Fig. 4.22a at M_c of 0.2 and 0.8 to show the isolated effect of compressibility on the mixing layer growth rate. As expected, the approximately incompressible case shows a growth rate about twice that of the moderately compressible case.

Figure 4.22b shows the growth rates of δ_{99} for the approximately planar configurations at $M_c = 0.2$ and to confirm the effects of density ratio variation in isolation from compressibility and curvature effects. The variation in growth rates in this group shows two expected behaviors. First, it is expected that unity density ratio planar shear layers with reciprocal velocity ratios exhibit exactly the same growth rates. The corresponding unity density ratio and reciprocal velocity

ratio cases in the present data, plotted with in orange and green markers, also indicate similar growth rates. Note that the green and orange markers are nearly perfectly overlapping. The suppressed growth rates of the variable density cases compared to the unity density ratio cases serve as a second validation of the present data. This growth rate suppression due to variable density effects has been well documented in literature [103, 86] and is expected in the low-curvature configuration.

Lastly, Fig. 4.22c shows two pairs of growth rates for $M_c = 0.2$ and unity density ratio cases to isolate curvature effects. As expected, the reciprocal velocity ratio cases in the low curvature configurations at $\delta_0/r_c = 0.001$ exhibit approximately the same growth rates. In contrast, a difference in growth rate arises for the corresponding velocity and density ratios in the cases with moderate curvature. The configuration with a higher velocity along the inner radial stream ($u_2/u_1 > 1$) grows about 1.5 times faster than the configuration with a higher velocity along the outer radial stream. This result is consistent with both Eckhoff's and Rayleigh's stability criterion. Profiles of Eckhoff's stability criterion for these cases' initial conditions are given in Fig. 4.8 and Appendix B. For the faster growing case (plotted in red), the Eckhoff discriminant Φ is slightly negative, indicating centrifugal instability. For the corresponding reciprocal case at the same curvature intensity (plotted in green), Φ is slightly positive, indicating centrifugal stability. Some unexpected behaviors can also be observed in Fig. 4.22c. The low speed case at moderate curvature (plotted in green) is particularly anomalous. This case is centrifugally stable by Eckhoff's and Rayleigh's criterion, but exhibits a slightly higher growth rate compared to the centrifugally 'neutral' case at $M_c = 0.2$ and $\delta_0/r_c = 0.001$ (plotted in blue). These unexpected trends suggests that a combination of mechanisms may be competing to influence the growth rates, since the effect of initial conditions on this configuration was demonstrated to be small (see Fig. 4.9) compared to the observed discrepancy from the planar growth rate.

Another thickness defined from the mean circulation, which is constant in each of the freestreams, can be computed. Equation 4.22 defines this 'circulation thickness', δ_Γ, which is analogous to the definition of momentum thickness for planar shear layers.

$$\delta_\Gamma(t) = \frac{1}{\rho_0(\Delta\Gamma)^2}\int_{R_2}^{R_1} \bar{\rho}(\Gamma_1 - \tilde{\Gamma})(\tilde{\Gamma} - \Gamma_2)dr \tag{4.22}$$

An expression for the growth rate of the circulation thickness can be defined by taking the time derivative of Eqn. 4.22. This analysis follows a similar derivation of planar shear layer growth

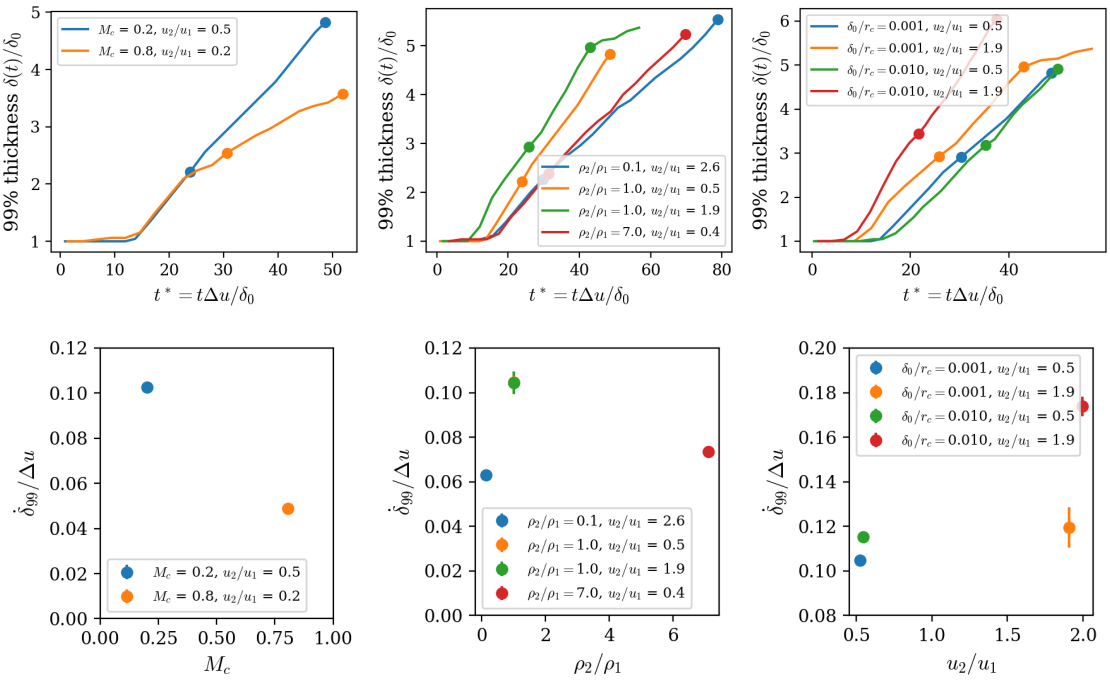

(a) Compressibility effects at $\delta_0/r_c = 0.001, \rho_2/\rho_1 = 1, u_2 < u_1$

(b) Variable density effects at $\delta_0/r_c = 0.001$ and $M_c = 0.2$

(c) Curvature effects at $M_c = 0.2, \rho_2/\rho_1 = 1$

Figure 4.22: Average growth rates of δ_{99} for selected cases to highlight (a) compressibility, (b) variable density and (c) centrifugal instability effects.

rate by Vreman et al., where the integrand is first expanded and rewritten in terms of the mean momentum and kinetic energy equations.

$$\delta_\Gamma(t) = \frac{1}{\rho_{ref}(\Delta\Gamma)^2}\int_{R_2}^{R_1} \bar{\rho}(\Gamma_1 - \tilde{\Gamma})(\tilde{\Gamma} - \Gamma_2)dr \tag{4.23}$$

$$\frac{d\delta_\Gamma}{dt} = \frac{1}{\rho_{ref}(\Delta\Gamma)^2}\int_{R_2}^{R_1} \left[(\Gamma_1 + \Gamma_2)\frac{d(\bar{\rho}\tilde{\Gamma})}{dt} - \frac{d(\bar{\rho}\tilde{\Gamma}^2)}{dt}\right] dr \tag{4.24}$$

The first term in the integrand, $d(\bar{\rho}\tilde{\Gamma})/dt$, can be rewritten in terms of the mean streamwise momentum equation as $r[d(\bar{\rho}\tilde{u}_\theta)/dt]$. The evolution equation for $\bar{\rho}\tilde{u}_\theta$ can be written in divergence form and evaluates to zero at the domain boundaries, so the first term in the integrand is dropped.

The second term, $d(\bar{\rho}\tilde{\Gamma}^2)/dt$, can be rewritten in terms of the evolution of the mean kinetic energy, $K = \tilde{u}_i\tilde{u}_i/2 \approx \tilde{u}_\theta\tilde{u}_\theta/2$ (viscous terms have been neglected):

$$\begin{aligned}
\frac{\partial}{\partial t}(\bar{\rho}\Gamma^2) &= r^2\frac{\partial}{\partial t}(\bar{\rho}K) \\
&= r^2\left[-\frac{\partial}{\partial x_j}(\bar{\rho}\tilde{u}_jK + \tilde{u}_i\overline{\rho u_i'' u_j''}) + \overline{\rho u_i'' u_j''}\frac{\partial \tilde{u}_i}{\partial x_j} - \tilde{u}_i\frac{\partial \bar{p}}{\partial x_i}\right] \qquad \left(\text{with } \frac{\partial}{\partial\theta}, \frac{\partial}{\partial z} = 0\right) \\
&= r^2\left[-\frac{1}{r}\frac{\partial}{\partial r}(r\bar{\rho}\tilde{u}_rK + r\tilde{u}_\theta\overline{\rho u_\theta'' u_r''}) + \overline{\rho u_\theta'' u_r''}\left(\frac{\partial \tilde{u}_\theta}{\partial r} + \frac{\partial \tilde{u}_r}{\partial\theta} - \frac{\tilde{u}_\theta}{r}\right) - \tilde{u}_r\frac{\partial \bar{p}}{\partial r}\right] \quad \text{(with small } \tilde{u}_r\text{)} \\
&= r^2\left[-\frac{1}{r}\frac{\partial}{\partial r}(r\tilde{u}_\theta\overline{\rho u_\theta'' u_r''}) + \overline{\rho u_\theta'' u_r''}\left(\frac{\partial \tilde{u}_\theta}{\partial r} - \frac{\tilde{u}_\theta}{r}\right)\right] \\
&= -\frac{\partial}{\partial r}(r^2\tilde{u}_\theta\overline{\rho u_\theta'' u_r''}) + r\tilde{u}_\theta\overline{\rho u_\theta'' u_r''} + r^2\overline{\rho u_\theta'' u_r''}\left(\frac{\partial \tilde{u}_\theta}{\partial r} - \frac{\tilde{u}_\theta}{r}\right)
\end{aligned}$$

Finally, the expression for instantaneous growth rate of the circulation thickness is given in Eqn. 4.25, with $\rho_{ref} = \bar{\rho}(r_c)$. Similarly to the planar shear layer configuration, the long-term growth rate is dominated by a term which is similar the production of turbulent kinetic energy (TKE).

$$\dot{\delta}_\Gamma = \frac{\partial \delta_\Gamma}{\partial t} = -\frac{1}{\rho_{ref}(\Delta\Gamma)^2}\int_{R_2}^{R_1} r^2\overline{\rho u_\theta'' u_r''}\frac{\partial \tilde{u}_\theta}{\partial r}dr \tag{4.25}$$

4.4.3 Stable vs. unstable configuration

In order to highlight the differences between unstable and stable configurations on turbulent statistics, two cases at $\delta(0)/r_c = 0.01$, $M_c = 0.8$ and $\rho_2/\rho_1 = 1$ will be compared in this section.

The velocity ratio is reciprocal between the stable and unstable cases, and the velocity difference Δu is initially the same. In a temporally developing, planar shear layer the growth rate depends on the velocity difference, and not the freestream velocity ratio. The mean circulation profiles for these cases are plotted by $(r - r_c)/\delta_{99}$ in Fig. 4.23 (b) to show approximate similarity during a subset of the turbulent period. Collapsed profiles of TKE and turbulent shear stress R_{12}, normalized by the instantaneous velocity difference, are also compared. For both the stable and unstable cases, the peak R_{12} magnitude is consistently one third of the TKE magnitude. The shear stress is positive in the unstable case and negative in the stable case, which is consistent considering the production of shear stress is dependent on the mean velocity gradient.

Differences in shear layer evolution can clearly be seen in Fig. 4.24. Transition to turbulence and development into an asymptotically growing turbulent state occurs about twice as quickly for the unstable case compared to the stable case. Even during the peak growth period of the stable shear layer, the growth rate remains less than the growth rate of the planar shear layer, as expected. Two measures of shear layer evolution are shown in Fig. 4.24. The left-most figure shows the evolution

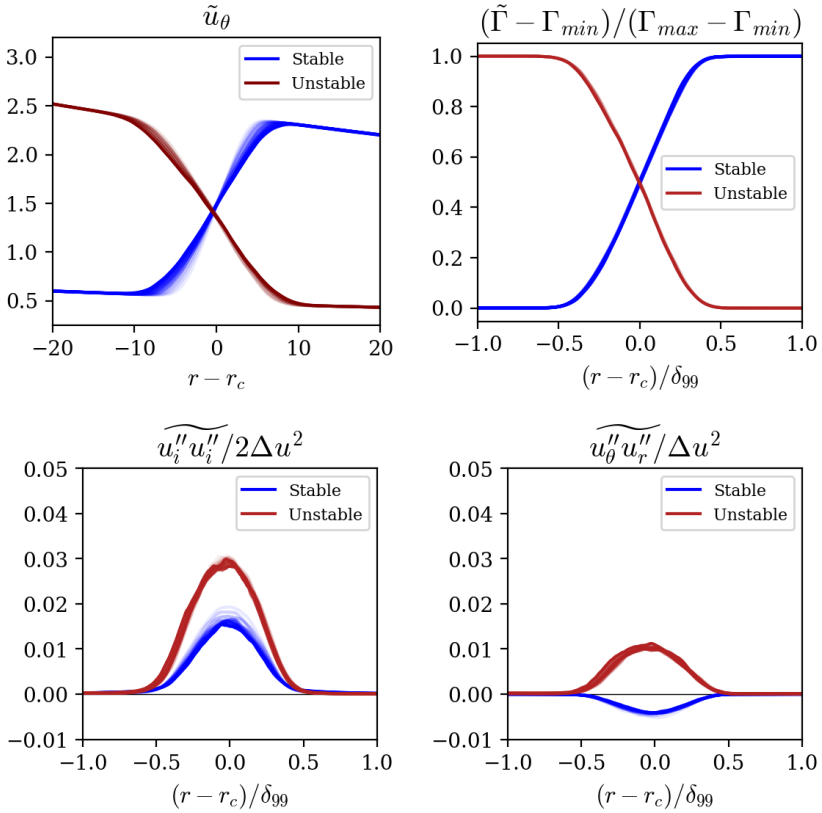

Figure 4.23: Mean profiles of stable and unstable configurations at $M_c = 0.8$ and $\delta_0/r_c = 0.01$.

of the 99% thickness for two high speed shear layers at $M_c = 0.8$ with stabilizing and destabilizing curvature. After a period of transient growth, the flow becomes turbulent once the shear layer has growth to approximately twice its initial δ_{99} thickness. This occurs around a normalized convective time of $t^* = 100$ for the unstable case, and $t^* = 240$ for the stable layer. While the transient growth phase is not a focus of this study, it has been consistently observed that the more stable configurations require a longer transitional period before turbulence begins. Compared to the plot of δ_{99}, the evolution of the circulation thickness is less noisy due to integration across the mixing region. Both time histories of the shear layer thickness definitions are normalized by the initial value and predict the same trend in growth rates with respect to curvature, namely that the destabilizing configuration results in a growth rate four times larger than the stable configuration.

The growth of the circulation thickness normalized by the initial velocity difference, $\dot{\delta}_\Gamma/\Delta u$, indicates approximately three periods of adjustment in the shear layer evolution. First, a period of transient perturbation growth occurs, corresponding to the peaks in growth rates at $t^* = 80$

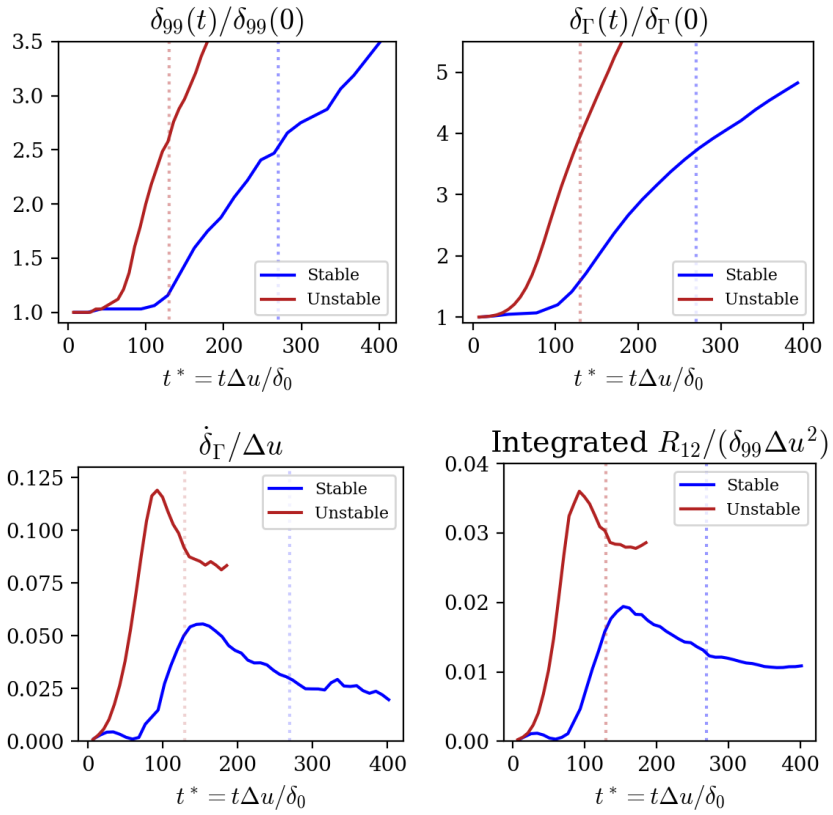

Figure 4.24: Thickness and growth rate measures for stable and unstable cases at $M_c = 0.8$ and $\delta_0/r_c = 0.01$. Dotted lines indicate the times at which averaging for turbulent statistics begins, which corresponds to approximately a 99% $\delta/\delta_0 = 2.5$.

for the unstable case and $t^* = 140$ for the stable case. The second period is a transition to well-developed turbulence, between $t^* \in [80, 130]$ for the unstable case and $t^* \in [150, 270]$ for the stable case. A similar evolution can be seen for the shear stress integrated across the shear layer, when normalized by the instantaneous thickness $\delta_{99}\Delta u^2$. The distinction between this second transitional period and the period of relaxation into an asymptotic state is not clearly defined, but have been estimated from these plots. The corresponding start times of this final phase with respect to the shear layer evolution have been marked with translucent dotted lines in Fig. 4.24. The curvature ratios δ_Γ/r_c during the periods chosen for collection of statistics are given in Table 4.3. In this work, cases are referred to by their initial curvature levels. However, the overall change in curvature intensity seen by the turbulent shear layer are more moderate. For example, while the approximately planar configuration has an initial curvature of 0.001, its final curvature intensity

as measured by δ_Γ/r_c approaches that of the intermediate curvature cases. Lastly, Table 4.3 also presents the final growth rate normalized by the initial velocity difference for each case. These tabulated rates are not perfectly constant, but represent the final turbulent growth rate measured before eddies begin to be constrained by the computational domain.

4.4.4 Effects of increasing curvature intensity

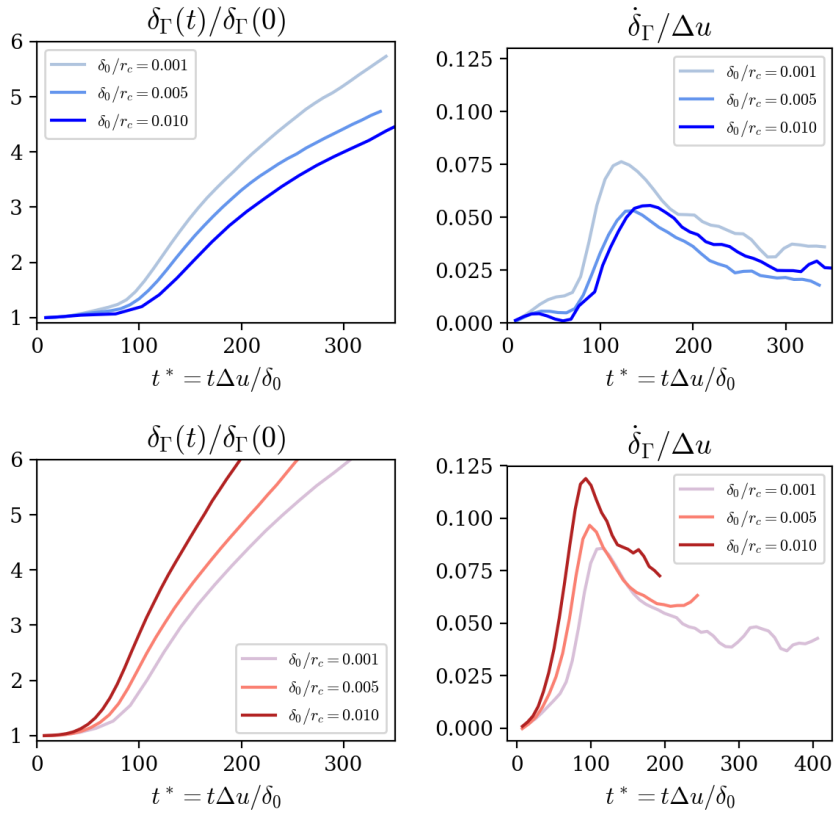

Figure 4.25: Evolution of thicknesses and growth rates for stable (top) and unstable (bottom) cases at $M_c = 0.8$.

The effects of increasing curvature on mixing layer growth rates for both stabilizing and destabilizing curvature are shown in Fig. 4.25. The growth rate for the stable case with intermediate curvature, $\delta_0/r_c = 0.005$, is lower than previously anticipated, and the final growth rate approaches the final growth rate of the higher curvature case. In Fig. 4.26, a similar trend of closeness between TKE and shear stress magnitude can be seen between theses two cases as well. An explanation for this unexpected trend in the stably curved cases remains to be determined.

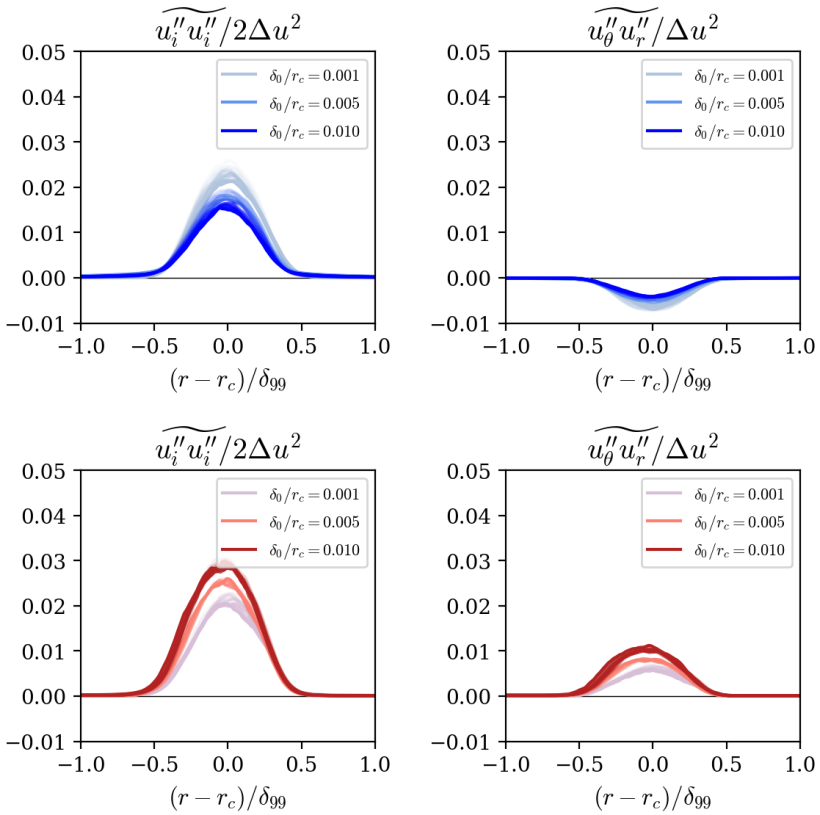

Figure 4.26: Evolution of TKE and R_{12} for stable (top) and unstable (bottom) cases at $M_c = 0.8$.

The curvature intensity appears to influence the transient periods of the stable and unstable growth rates, such that cases with intermediate curvature levels of $\delta_0/r_c = 0.005$ have a thickness growth which is mostly bounded by the lower and higher curvature cases. The asymptotic growth periods between the stable and unstable configurations show some notable differences. The unstable configurations appear to reach their asymptotic growth period more quickly compared to the stable configurations. These periods of growth correspond to the regions where the integrated shear stress also begin to plateau. In contrast, the stabilizing configurations did not exhibit any region of growth which was definitively linear. The upper left two plots in Fig. 4.26 instead show that the δ_Γ in the stable cases have progressively slower growth rates which continue to drift lower until the computational domain is exceeded. Normalized TKE and shear stress profiles for the unstable cases have distinct magnitudes, with the intermediate curvature case sitting evenly between the low and higher curvature cases. In contrast, the difference in TKE and shear stress magnitudes for the stabilizing curvature cases is less evenly distributed. Consistent with the observed growth rates,

the cases with initially higher curvature have similar magnitudes of TKE and shear stress which are distinct from the low curvature case.

Streamwise and transverse turbulent mass flux profiles for stable and unstable configurations are shown in Fig. 4.27. As expected, the direction of turbulent mass transport by the streamwise velocity fluctuations varies with the mean velocity gradient of the base flow. Monotonic changes in the streamwise and radial turbulent mass flux are observed with increasing curvature intensity, but these changes are proportionally small. Again, the $M_c = 0.8$ case with intermediate curvature ($\delta_0/r_c = 0.005$) shows unusual behavior, with some elevated mass flux outside the shear layer region compared to the other stabilizing cases. The transverse turbulent mass flux has qualitatively the same profile for both stable and unstable cases, with differences in magnitude between the most unstable and stable configurations at $\delta_0/r_c = 0.01$. In both stable and unstable configurations, the profiles indicate that radial velocity fluctuations transport mass into the mixing layer.

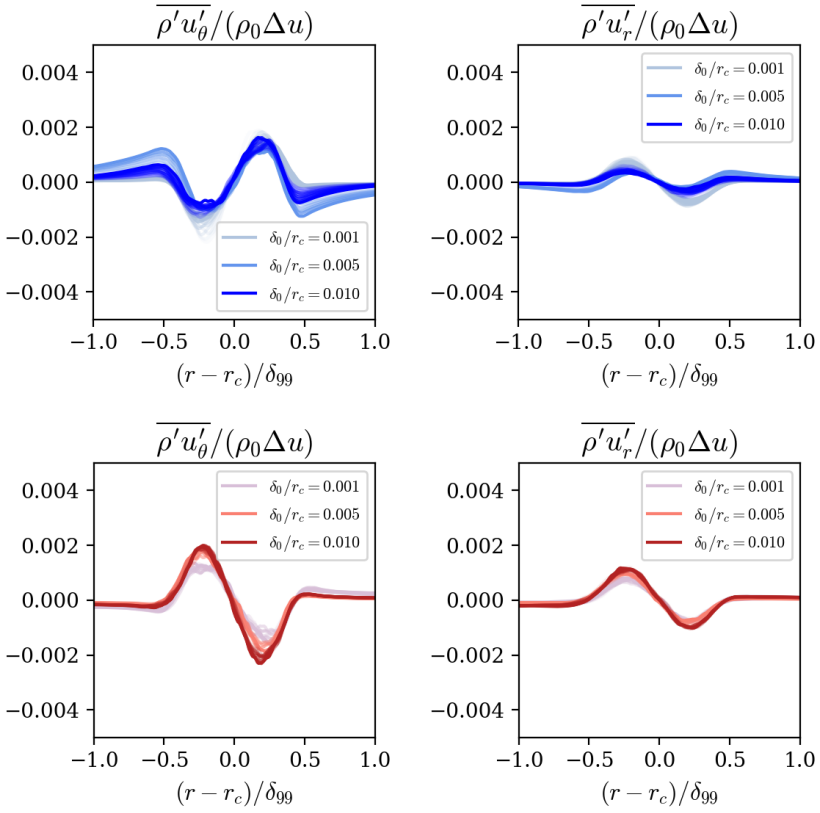

Figure 4.27: Normalized turbulent mass flux profiles for stable (top) and unstable (bottom) configurations.

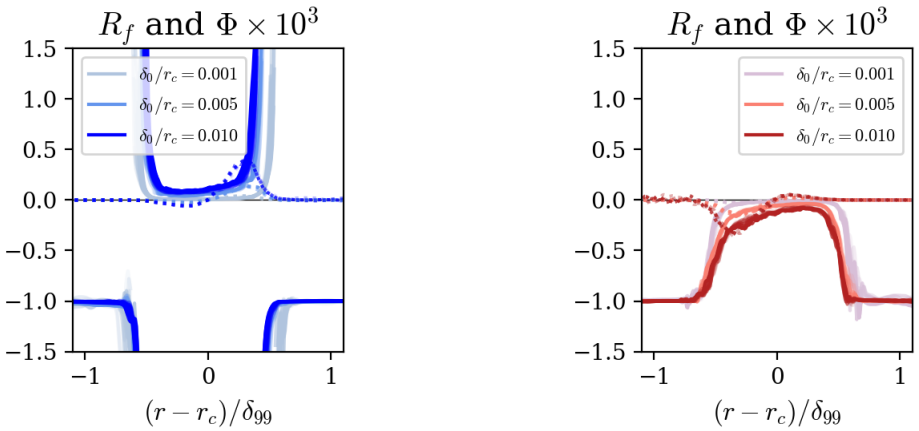

Figure 4.28: Profiles of Ri_f (solid lines) and Φ (dashed lines) for high speed stable (left) and unstable (right) cases with increasing curvature intensity.

The parameter governing the balance between shear production and centrifugal production of turbulent stress can be written similarly to a flux Richardson number Ri_f for stratified flow. Profiles of Ri_f as defined by Eqn. 4.6 by Nagata and Kasagi for stable and unstable flows at $M_c = 0.8$ and $\rho_2/\rho_1 = 1$ are plotted with solid lines in Fig. 4.28. Nagata's definition of Ri_f gives the ratio of turbulent stress production by centrifugal effects to production by shearing; a value of $Ri_f = -1$ indicates that the centrifugal effects cancel the shear production. Both the stable and unstable configurations give $Ri_f \approx -1$ in the freestreams, which implies the two terms in the production of $R_{\theta\theta}$ cancel and the net TKE production is zero. Thus, Nagata's definition of Ri_f confirms that the freestreams should not sustain turbulent stress. Increasing curvature for unstable flows gives a more negative value of Ri_f in the mixing layer and increasing curvature for stable flows gives a more positive value of Ri_f, especially near the mixing layer edges. For the stable cases, the velocity profile includes a local minimum and maximum near the shear layer edges, which results in two discontinuities in Ri_f near the mixing layer edges. An interpretation of these singularities consistent with Nagata's definition of Ri_f would indicate that the edges of the stably curved shear layers have a tendency for instability.

The parameter for Eckhoff's stability criterion, Φ as defined in Eqn. 4.7, is also plotted with dashed lines in Fig. 4.28 to demonstrate the centrifugal stability of the curved shear layer is dependent only on the shear layer region and not on the freestream behavior. The values are similarly as expected, with $\Phi > 0$ for centrifugally stable cases and vice versa for the unstable cases. Peak values of Φ occur for the cases with the highest initial curvature levels. The stability parameters used to categorize this flow, along with the sign of the turbulent shear stress, were summarized in

Table 4.1. A similar characterization of stability for the sets of cases comparing compressibility and variable density effects is included in the remaining subsections below.

Lastly, the present understanding of the turbulent structures in this complex flow can be supplemented by considering the distribution of turbulent fluctuations. Capturing the anisotropic behavior of turbulence is often critical for accurate numerical prediction of a wide variety of complex flows. The Choi and Lumley anisotropy map described in subsection 2.3.3 of Ch. 2 and various parameters for centrifugal stability will be shown in the following subsections to compare compressibility and variable density effects in combination with streamwise curvature.

4.4.5 Comparison to compressibility effects

Compressibility effects in planar shear layers reduce mixing layer growth rates to 20-30% of its 'incompressible' value. For the M_c range in this work, which varies from quasi-incompressible at $M_c = 0.2$ to moderately compressible at $M_c = 0.8$, the data shows $\geq 50\%$ decrease in growth rates. As given in Table 4.3, at low, stabilizing curvatures, the growth rate reduction is $0.036/0.071 = 0.507$. At higher, destabilizing curvatures, the growth rate reduction is $0.079/0.14 = 0.564$. In comparison, the difference in growth rate $\delta_\Gamma/\Delta u$ between the most stable and the most unstable cases gives a factor of four difference at both $M_c = 0.8$ and $M_c = 0.2$. In the present data, the compressibility effect remains relevant across the ranges of curvature intensities explored. The trends observed suggest that, for the given range of curvature intensities, the effects of stabilizing and destabilizing curvature may be just as important as compressibility effects.

Table 4.4: Growth rates of δ_Γ for unity density ratio at increasing curvature and compressibility levels.

M_c	u_2/u_1	$\delta_\Gamma(0)/r_c$	Final $\dot{\delta}_\Gamma/\Delta u(0)$
0.2	0.5	0.001	0.071
	0.5	0.010	0.035
	1.9	0.001	0.069
	1.9	0.010	0.140
0.8	0.2	0.001	0.036
	0.2	0.010	0.018
	4.5	0.001	0.025
	4.8	0.010	0.079

Eckhoff's criterion for centrifugal stability is one of the few which includes the effect of compressibility in the formulation of the problem. The profile of the Eckhoff discriminant Φ is shown in Fig. 4.29 for cases which are centrifugally unstable at unity density ratio. Consistent with the stability criterion, the mean profiles of Φ contain negative values in the mixing layer region along

the side of the shear layer with the faster moving freestream. When normalized by the center radius of curvature, the profiles of $r_c\Phi$ approximately collapse at both low and high compressibility levels. This collapse in profiles of $r_c\Phi$ across curvature levels contrasts with the difference in growth rates due to curvature effects, which suggests that while the Eckhoff criterion correctly predicts stability, it does not necessarily represent the shear layers' affinity for turbulent growth.

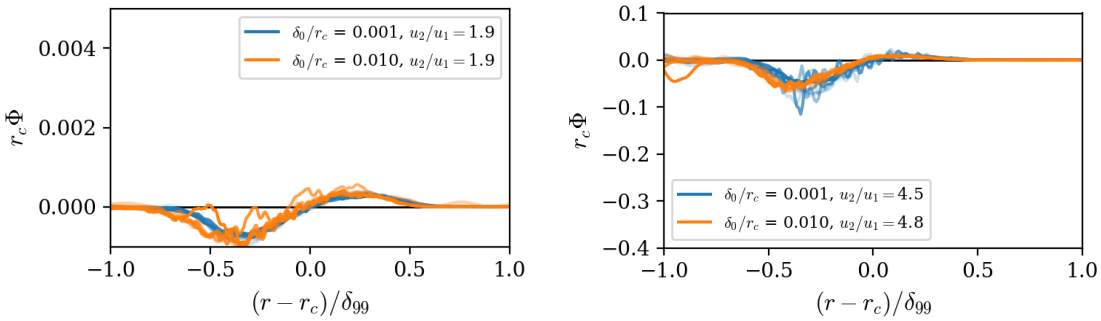

(a) $M_c = 0.2$ (b) $M_c = 0.8$

Figure 4.29: Curvature effects on the evolution of the Eckhoff discriminant $\Phi = \frac{1}{\rho}\frac{d\rho}{dr} - \frac{u_\theta^2}{c^2 r}$ at varying compressibility levels for $\rho_2/\rho_1 = 1$ and $u_2 > u_1$.

Turbulent stress anisotropy maps for the high and low speed cases at ρ_2/ρ_1 are given in Fig. 4.30. Each map shows the character of turbulence anisotropy when the shear layer has become fully turbulent. For both low and high compressibility levels, these anisotropy maps are similar. Both the change in M_c and in δ_0/r_c do not produce distinctly different mappings, with the data in the turbulent region showing mainly 1C-3C turbulence. While an increase in turbulent anisotropy, which would show up as bias in data towards the 1C corner, present data suggests that this compressibility effect is not yet active in the flow. Similarly, increasing curvature effects could possibly manifest as increasing anisotropy if streamwise vortical structures dominated the flow. However, as shown in the previous visualizations, these types of vorticies are not dominant and this anisotropy does not present itself in the data.

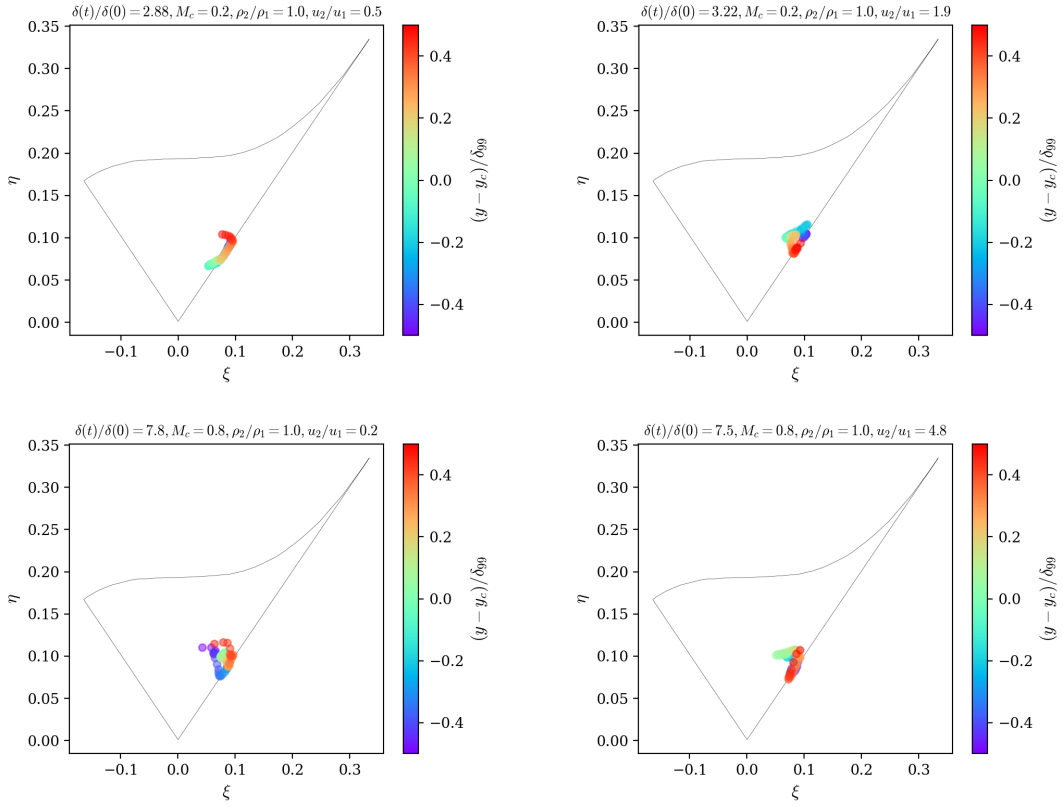

(a) $u_2 < u_1$ (b) $u_2 < u_1$

Figure 4.30: Turbulent stress anisotropy maps for cases at $M_c = 0.2$ (top) and $M_c = 0.8$ (bottom) and $\rho_2/\rho_1 = 1$ for centrifugally stable (left) and unstable (right) configurations.

4.4.6 Combination with variable density effects

Growth rates for variable density cases at moderate curvature and low compressibility levels are given in Fig. 4.31. These can be contrasted with the expected variable density effects in planar shear layers, where the introduction of density variation results in a distinct decrease in the growth rate. In cases with a denser inner stream, plotted in green, growth rates which are comparable to or larger than the corresponding unity density ratio case, plotted in orange. Cases with a denser outer stream indicate a dramatic decrease in the growth rate, regardless of the velocity ratio. In fact, the case plotted in blue in Fig. 4.31a with $u_2/u_1 = 0.6$ and $\rho_2/\rho_1 = 1$ never transitions to turbulence because the flow is too stable to maintain the initial perturbations. These trends in the growth rates are also reflected in the shear stress profiles, given with the same color scheme in Fig. 4.32.

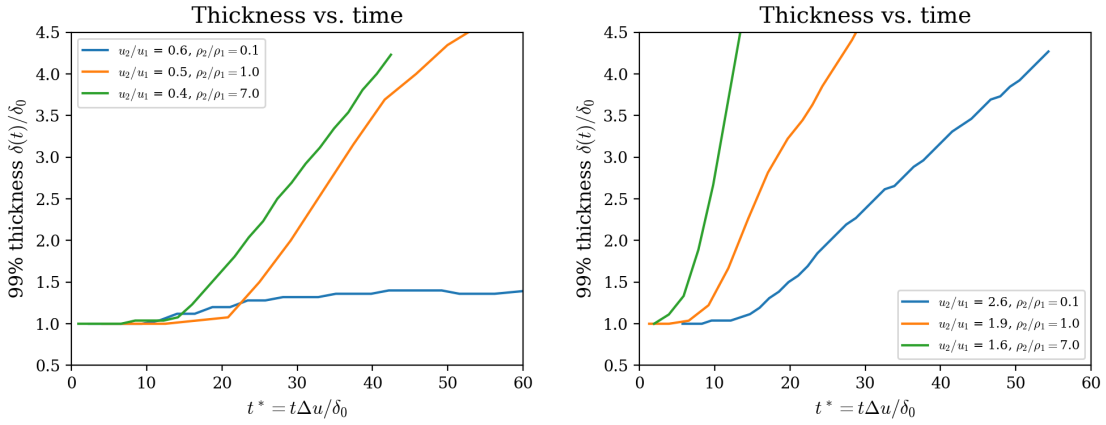

(a) $u_2 < u_1$ (b) $u_2 > u_1$

Figure 4.31: Thickness evolution for variable density cases at $\delta_0/r_c = 0.01$ and $M_c = 0.2$

Cases with a larger density along the inner freestream, plotted in green, show stress magnitudes which are larger the corresponding unity density ratio cases in orange. It is also observed that the shear stress asymmetry is greatly exaggerated in the cases with $\rho_2/\rho_1 = 7$, and is not as obvious in cases with $\rho_2/\rho_1 = 1/7$. This again contrasts with the planar shear layer configuration, in which both density ratios would produce equal and opposite asymmetry into the lighter freestream. The present growth rates and the shear stress asymmetries show distinct differences from corresponding planar shear layer configurations, and the differences can be classified as combined variable density and curvature effects.

Table 4.5: Growth rates of δ_{99} for variable density cases at $M_c = 0.2$ at weak and strong curvature levels. N/A indicates the data is not available for this case.

u_2/u_1	ρ_2/ρ_1	Final $\dot{\delta}_{99}/\Delta u(0)$ $\delta/r_c = 0.001$	Final $\dot{\delta}_{99}/\Delta u(0)$ $\delta/r_c = 0.010$
0.6	1/7	N/A	0.002
0.5	1	0.104	0.048
0.4	7	0.073	0.117
2.6	1/7	0.067	0.082
1.9	1	0.119	0.176
1.6	7	N/A	0.438

Several of the stability criterion in Table 4.1 take into account the density variation across the mixing layers. Each of the stability criterion and corresponding mean profiles are shown in Fig.

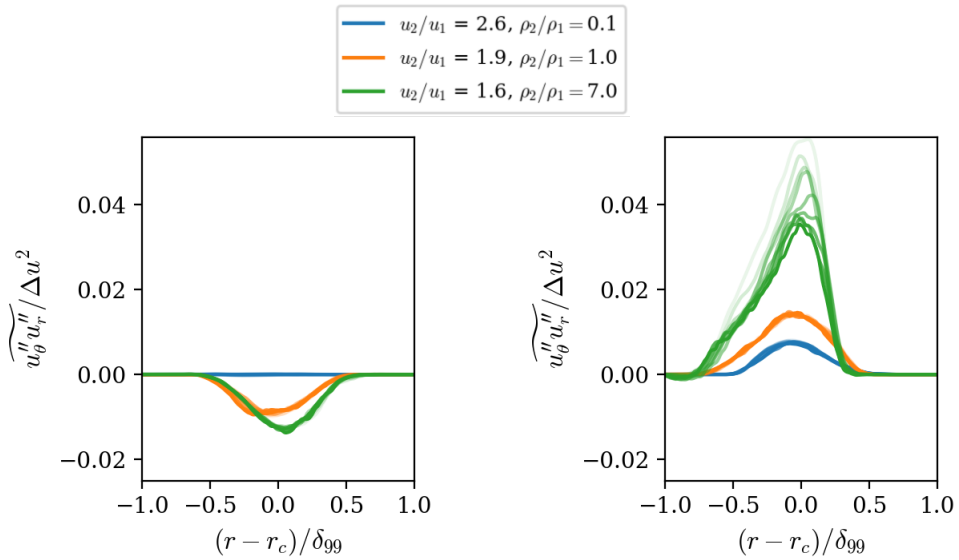

(a) $u_2 > u_1$ (b) $u_2 < u_1$

Figure 4.32: Normalized shear stress profiles corresponding to Fig. 4.31

4.33. The data at $\rho_2/\rho_1 = 1/7$ is currently labelled as $\rho_2/\rho_1 = 0.1$. The left column are the profiles for the cases where the outer stream is faster than the inner stream ($u_2 < u_1$). The velocity ratio is similar for each of cases grouped by subfigures such that the effect of changing the density ratio from $\rho_2/\rho_1 = 1/7$ to $\rho_2/\rho_1 = 7$ can be observed. The stability criterion proposed by Synge which depends on the gradient of angular momentum is indicated in the top left of Fig. 4.33. The case plotted in blue which has the highest peak in the mixing layer reflects logically that the case which is both denser and faster along the outer freestream is centrifugally stable. A similar profile can be observed in the profiles of Sipp's criterion of $N_w^2 - N^2$ and Eckhoff's normalized criterion $r_c\Phi$. For each of these profiles, the unity density ratio case shows profiles which are slightly positive in the mixing region, while the density ratio $\rho_2/\rho_1 = 7$ cases are slightly negative. This implies that the increased density ratio dominates over the 'stabilizing' velocity ratio for this curvature level, and the flow remains prone to centrifugal instability during the period of turbulent growth. The bottom two subfigures show the profiles for Bradshaw's Richardson number (defined in Eqn. 4.4) and Nagata's flux Richardson number (defined in Eqn. 4.6). The profiles of the two quantities are similar in the mixing layer region, and for unity density ratio cases, the Ri_f and Ri are about twice as large compared to the variable density cases. All Richardson numbers are positive in the mixing layer region. Using Ri_f as the sole criterion for stability suggests these configurations are centrifugally stable.

The right column of Fig. 4.33 indicates corresponding stability criterion profiles for cases with a faster inner stream and a slower outer stream, $u_2 > u_1$. Each of the profiles for density ratio of $\rho_2/\rho_1 = 1$ and 7 are centrifugally unstable via Synge, Sipp and Eckhoff's criterion. Interestingly, for the case plotted in blue with a denser, but slower, outer freestream, Eckhoff's criterion suggests no centrifugal instability in contrast to Synge's and Sipp's criterion. Similarly to the Richardson numbers in the cases with $u_2 < u_1$, the magnitude of Ri and Ri_f in the mixing region are approximately the same.

For the parameter space considered, the density ratio dominates the turbulent growth rates. Though most of the centrifugal stability criterion in Fig. 4.33 are formulated for linear stability (excluding Nagata's Ri_f), the criteria by Synge, Sipp and Eckhoff correctly predict the major trends in turbulent growth–configurations with density ratios of $\rho_2/\rho_1 = 1/7$ grow considerably slower than configurations with $\rho_2/\rho_1 = 1$ and 7 for comparable velocity ratios. Similarly, these criterion correctly predict that the configuration with the faster inner stream and $\rho_2/\rho_1 = 7$ is the most unstable of all considered configurations. These distinctions between the most stable ($\rho_2/\rho_1 = 1/7, u_2 < u_1$) and most unstable ($\rho_2/\rho_1 = 7, u_2 > u_1$) variable density configurations is not as clearly indicated in profiles of Ri as defined by Bradshaw and Ri_f as defined in Eqn. 4.6.

The centerline values for the stability criterion proposed by Sipp and the flux Richardson number defined in Eqn. 4.6 are used to compare the trend in growth rates for all the low M_c cases conducted. These trends are shown in Fig. 4.34. The criterion proposed by Sipp in Fig. 4.34a does not give a clear trend in growth rates, though generally the growth rates are clustered according to their density ratio (color). When comparing the trend in growth rates to the flux Richardson number in Fig. 4.34b, the observed growth rate data can be interpreted to decrease from negative to positive R_f, but this trend is also not concretely clear. An alternative scaling for the growth rates can be formulated as a ratio of freestream momenta, defined as β as in Eqn. 4.26.

$$\beta = \frac{\rho_2 U_2^2 - \rho_1 U_1^2}{\rho_2 U_2^2 + \rho_1 U_1^2} = \frac{\rho_2/\rho_1 (U_2/U_1)^2 - 1}{\rho_2/\rho_1 (U_2/U_1)^2 + 1} \tag{4.26}$$

Using β to scale the growth rate data, a trend emerges with lower growth rates occurring at $\beta \to -1$ and high growth rates at $\beta \to 1$. However, scatter exists in this trend, and β does not account for the curvature intensity of the flow. Scaling growth rate data by $\beta\delta/r_c$ as a simple attempt to incorporate the curvature intensity does not decrease scatter or improve the overall growth rate trend. The definition of a more appropriate curvature parameter which also encompasses compressibility effects on growth rates remains a direction of future research.

Turbulent stress anisotropy maps for the low speed cases at $M_c = 0.2$ and ρ_2/ρ_1 are given in Fig. 4.35. Aside from the upper left subfigure, each plot shows the character of turbulence anisotropy when the shear layer has become fully turbulent. Again, as shown in Fig. 4.30, at $M_c = 0.2$ and

unity density ratio, the data in the turbulent region shows mainly clustering in the 1C-3C region. Similar behavior is observed for the case with a lighter but faster inner stream ($\rho_2/\rho_1 = 1/7$ and $u_2/u_1 = 2.6$). The case with a lighter and slower inner stream ($\rho_2/\rho_1 = 1/7$ and $u_2/u_1 = 0.6$) did not reach a state of fully developed turbulence, and the persistence of transitional vortical structures is reflected in the anisotropy mapping. The final row in Fig. 4.35 show the map for the cases with a heavy fluid along the inner freestream. Whether the inner stream or the outer stream is faster, the map indicates a tendency for a larger range of 1C-3C turbulence, where at least part of the mixing region is more 3C than the rest of the mixing layer. This can be interpreted as consistent with an increase in the 3D structures which would be produced by the RT instability, which is supported visually by Fig. 4.37–the protrusions of the vorticity from the mixing region into the freestream regions becomes more pronounced as the inner stream becomes heavier than the outer stream.

$$\frac{\partial \bar{\omega}_i}{\partial t} + \frac{\partial}{\partial x_i}(\bar{u}_j \bar{\omega}_i) = \underbrace{-\frac{\partial}{\partial x_j}(\overline{u_j' \omega_i'})}_{\text{Turb. transport}} \underbrace{- \left(\bar{\omega}_i \frac{\partial \bar{u}_j}{\partial x_j} + \overline{\omega_i' \frac{\partial u_j'}{\partial x_j}} \right)}_{\text{Dilatation prod}} + \underbrace{\frac{1}{\rho^2} \epsilon_{ijk} \left(\frac{\partial \bar{\rho}}{\partial x_j} \frac{\partial \bar{p}}{\partial x_k} + \overline{\frac{\partial \rho'}{\partial x_j} \frac{\partial p'}{\partial x_k}} \right)}_{\text{Baroclinic torque}}$$
$$+ \underbrace{\left(\bar{\omega}_j \frac{\partial \bar{u}_i}{\partial x_j} + \overline{\omega_j' \frac{\partial u_i'}{\partial x_j}} \right)}_{\text{Vortex stretching}} + \underbrace{\nu \frac{\partial^2 \bar{\omega}_i}{\partial x_j x_j}}_{\text{Diffusion}} \quad (4.27)$$

The evolution equation for mean vorticity is given in Eqn. 4.27. In the evolution of vorticity, the baroclinic torque term indicates the production of vorticity due to the alignment or misalignment of the mean pressure and density gradients. In the present flow, the mean pressure gradient is always position and pressure always increases in the outer radial direction in order to satisfy the curvature of the flow. The configurations with density ratios of $\rho_2/\rho_1 = 1/7$ have mean density gradients which align with the mean pressure gradient, which is stabilizing in a mean sense. The configurations with density ratios of $\rho_2/\rho_1 = 7$ have mean density gradients which are misaligned with the mean pressure gradient, which is destabilizing. Of course, these concepts of baroclinic stability are discussed in a mean sense, as the turbulent eddies in the mixing region experience significant instantaneous pressure and density gradients.

$$\frac{1}{\rho^2}(\nabla p \times \nabla \rho) = \frac{1}{\rho^2} \begin{bmatrix} \frac{\partial p}{\partial z}\frac{\partial \rho}{\partial z} - \frac{\partial p}{\partial r}\frac{\partial \rho}{\partial z} \\ \frac{1}{r}\frac{\partial p}{\partial \theta}\frac{\partial \rho}{\partial z} - \frac{\partial p}{\partial z}\frac{1}{r}\frac{\partial \rho}{\partial \theta} \\ \frac{\partial p}{\partial r}\frac{1}{r}\frac{\partial \rho}{\partial \theta} - \frac{1}{r}\frac{\partial p}{\partial \theta}\frac{\partial \rho}{\partial r} \end{bmatrix} \quad (4.28)$$

The baroclinic torque term in cylindrical coordinates is written explicitly in Eqn. 4.28. The baroclinic torque acting on the mean z vorticity is given in Fig. 4.36; profiles for all cases are provided

in Appendix B Fig. B.23. Note that, like all terms of the baroclinic torque, each term in the vector component includes a gradient in one of the homogeneous directions (θ or z). As such, the mean baroclinic torque terms are only nonzero due to correlations between fluctuating pressure and density gradient correlations. The contribution of the mean baroclinic torque to the mean vorticity is small for the unity density ratio cases in orange, as expected. For the case with a faster and denser outer freestream, the mean density and pressure gradients are aligned across the mixing region, and the baroclinic torque is also zero in this case. Regardless of the velocity ratio, the configurations with a denser inner stream, plotted in green in both Fig. 4.36a and 4.36b, indicate antisymmetric baroclinic torque levels which are antisymmetric across the mixing layer. In the most centrifugally unstable case plotted in Fig. 4.36b, with a faster and denser inner stream, the magnitude of the baroclinic torque is an order of magnitude larger than the corresponding centrifugally unstable case Fig. 4.36a. In an interested combination of curvature and compressibility effects, the case with a less dense but faster inner freestream also exhibits considerable amounts of baroclinic torque, and in a manner more similar to the $u_2 < u_1$ configurations. Comparing the reciprocal cases of denser but slower inner freestream (Fig. 4.36a, green) and a lighter but faster inner freestream (Fig. 4.36a, green), the profile of baroclinic torque is similar in form and magnitude. This further points to the complex interactions between the density gradient and curvature effects, as the baroclinic torque profiles are not solely dependent on the mean density and pressure profiles during turbulent growth.

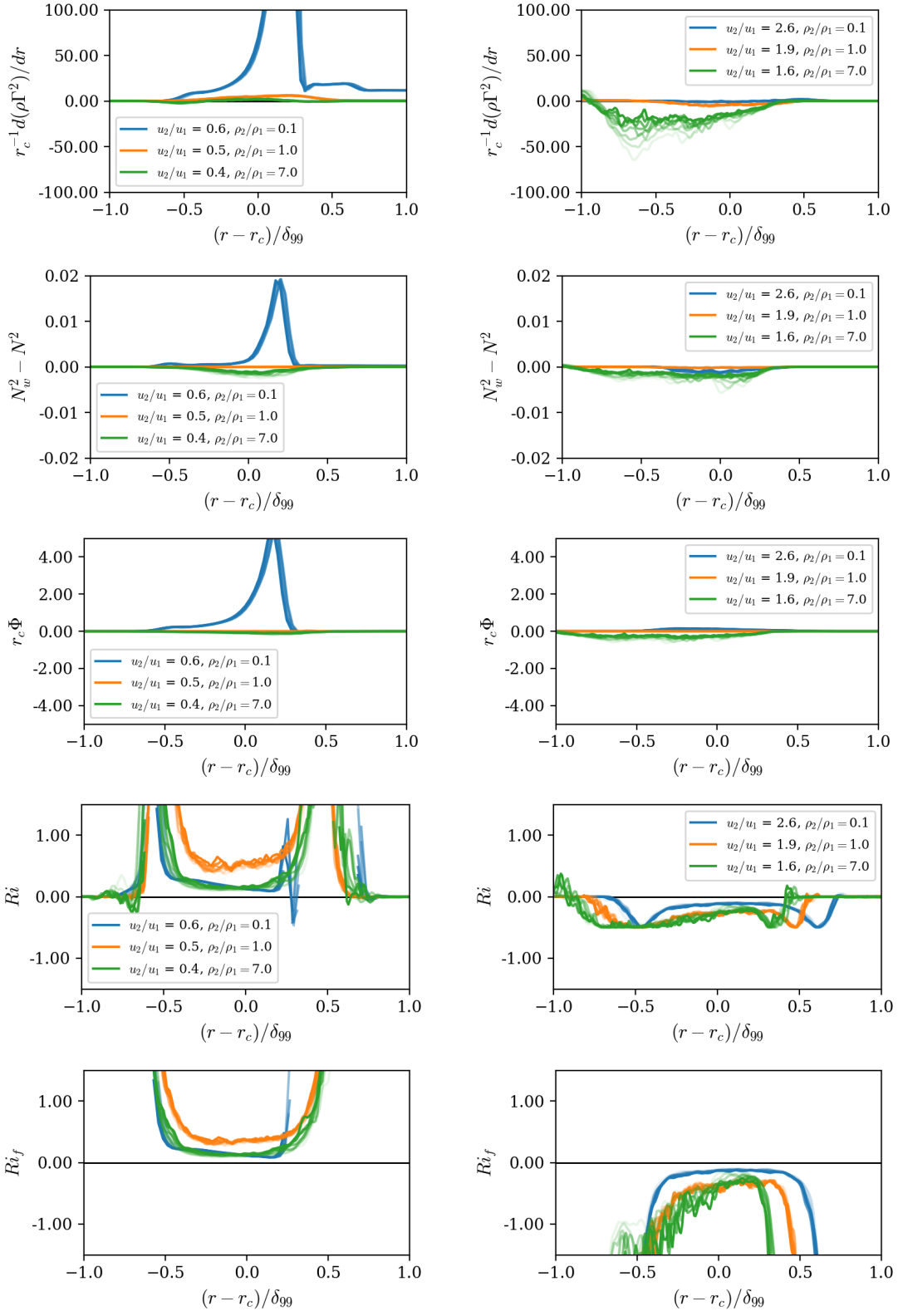

(a) $u_2 < u_1$ (b) $u_2 > u_1$

Figure 4.33: Curvature effects on the evolution of the stability criterion profiles at varying density ratios ρ_2/ρ_1 of 1/7 (blue), 1 (orange), and 7 (green); Ri_f defined in Eqn. 4.6.

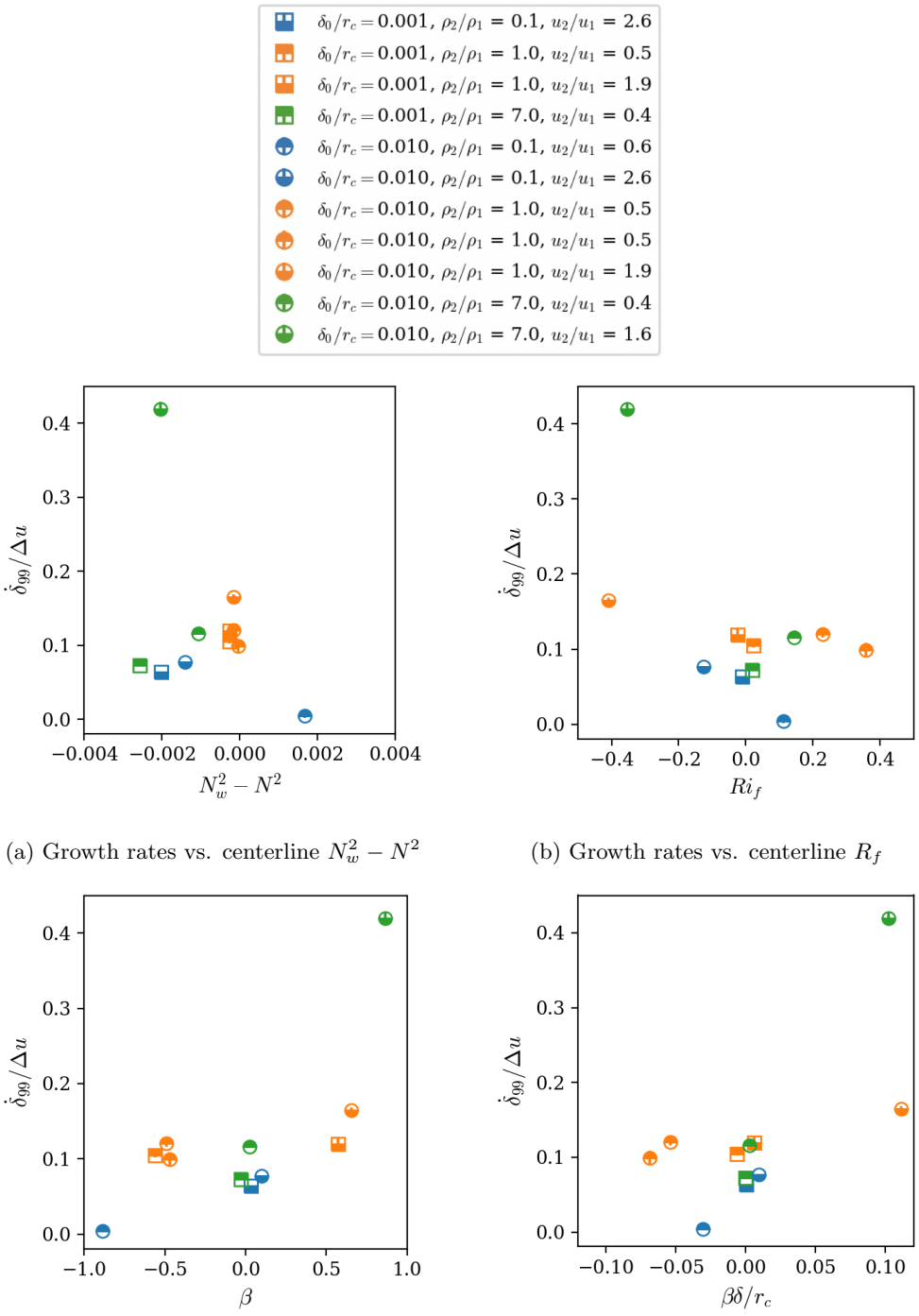

(a) Growth rates vs. centerline $N_w^2 - N^2$

(b) Growth rates vs. centerline R_f

(c) Growth rates vs. angular momentum ratio, *beta*

(d) Growth rates vs. angular momentum ratio scaled by curvature intensity, $\beta\delta/r_c$

Figure 4.34: Normalized growth rates compared to stability criterion corresponding to Fig. 4.33 (at $M_c = 0.2$). Similarly to Fig. 4.33, colors of blue, orange and green represent density ratios of $\rho_2/\rho_1 = 1/7, 1$ and 7, respectively. The square markers correspond to cases with weak curvature, and the circle markers correspond to cases with stronger curvature. Finally, the top or bottom fill of the marker indicates the velocity ratio, with top-filled markers indicating $u_2 < u_1$ and vice versa for bottom-filled markers.

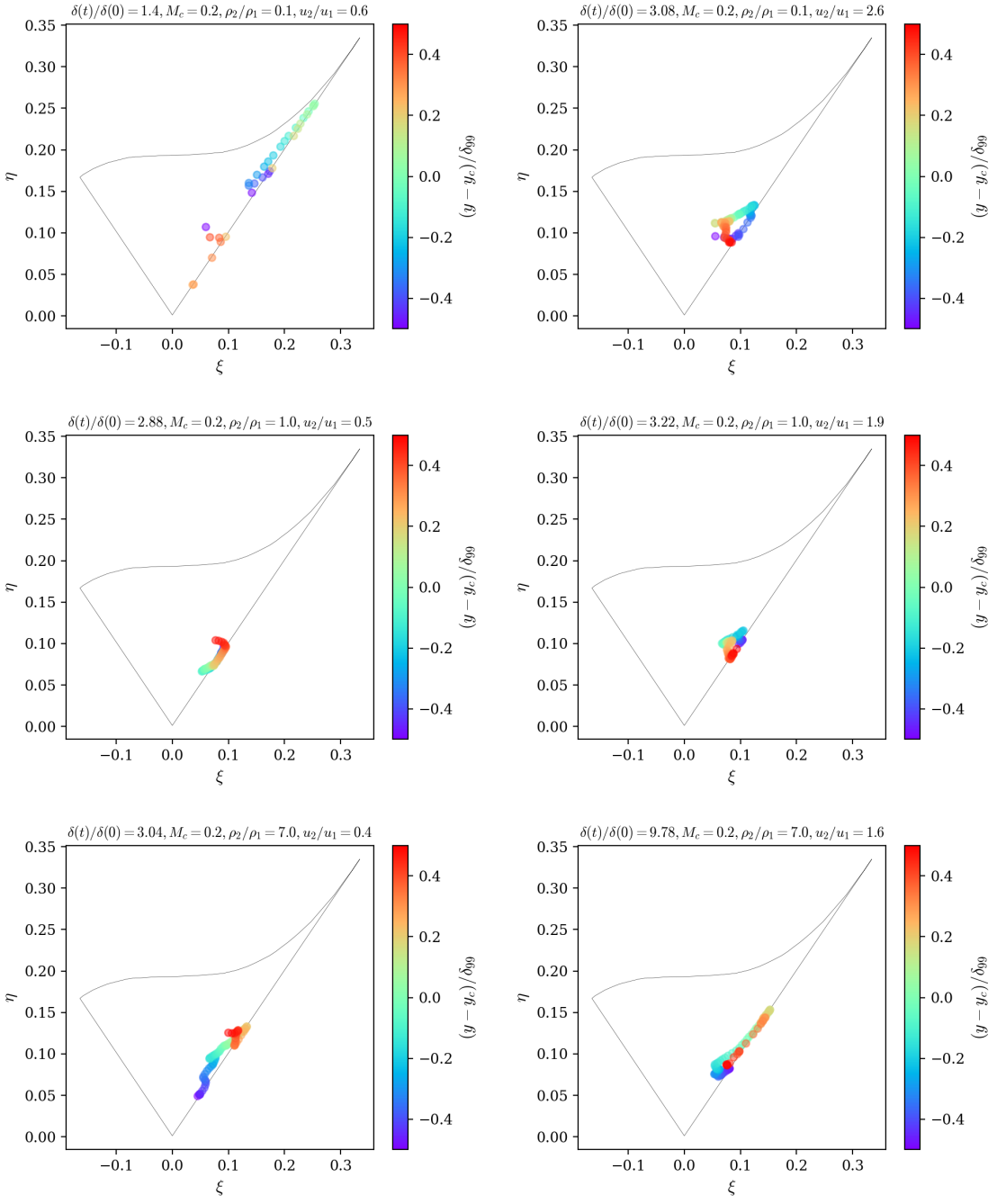

(a) $u_2 < u_1$ (b) $u_2 > u_1$

Figure 4.35: Turbulent stress anisotropy maps for cases at moderate curvature $\delta_0/r_c = 0.01$, $M_c = 0.2$ and $\rho_2/\rho_1 = 1/7, 1, 7$ (top to bottom).

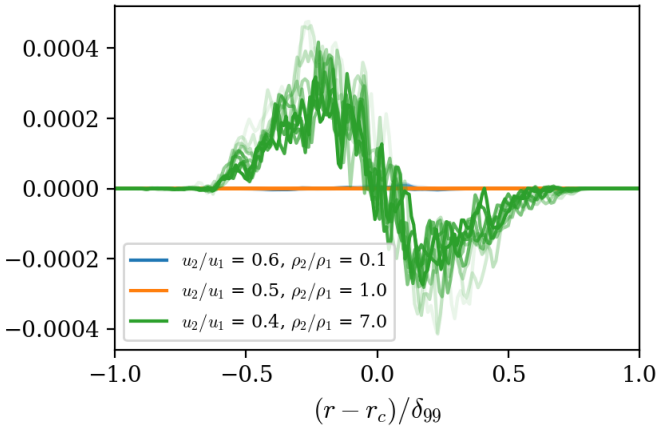

(a) $u_2 < u_1$

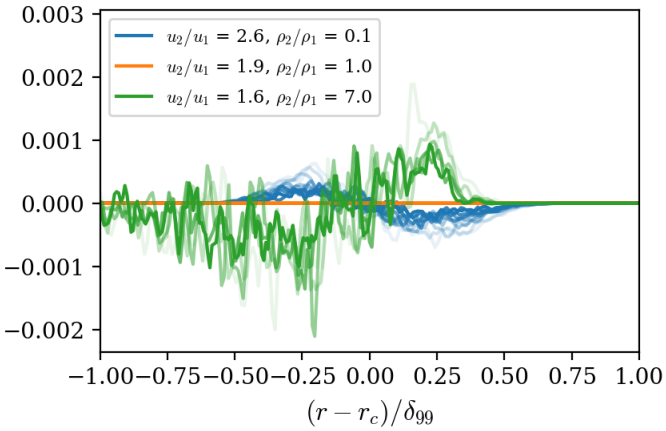

(b) $u_2 > u_1$

Figure 4.36: Spanwise component of baroclinic torque for cases at moderate curvature $\delta_0/r_c = 0.01$, $M_c = 0.2$ and $\rho_2/\rho_1 = 1/7, 1, 7$.

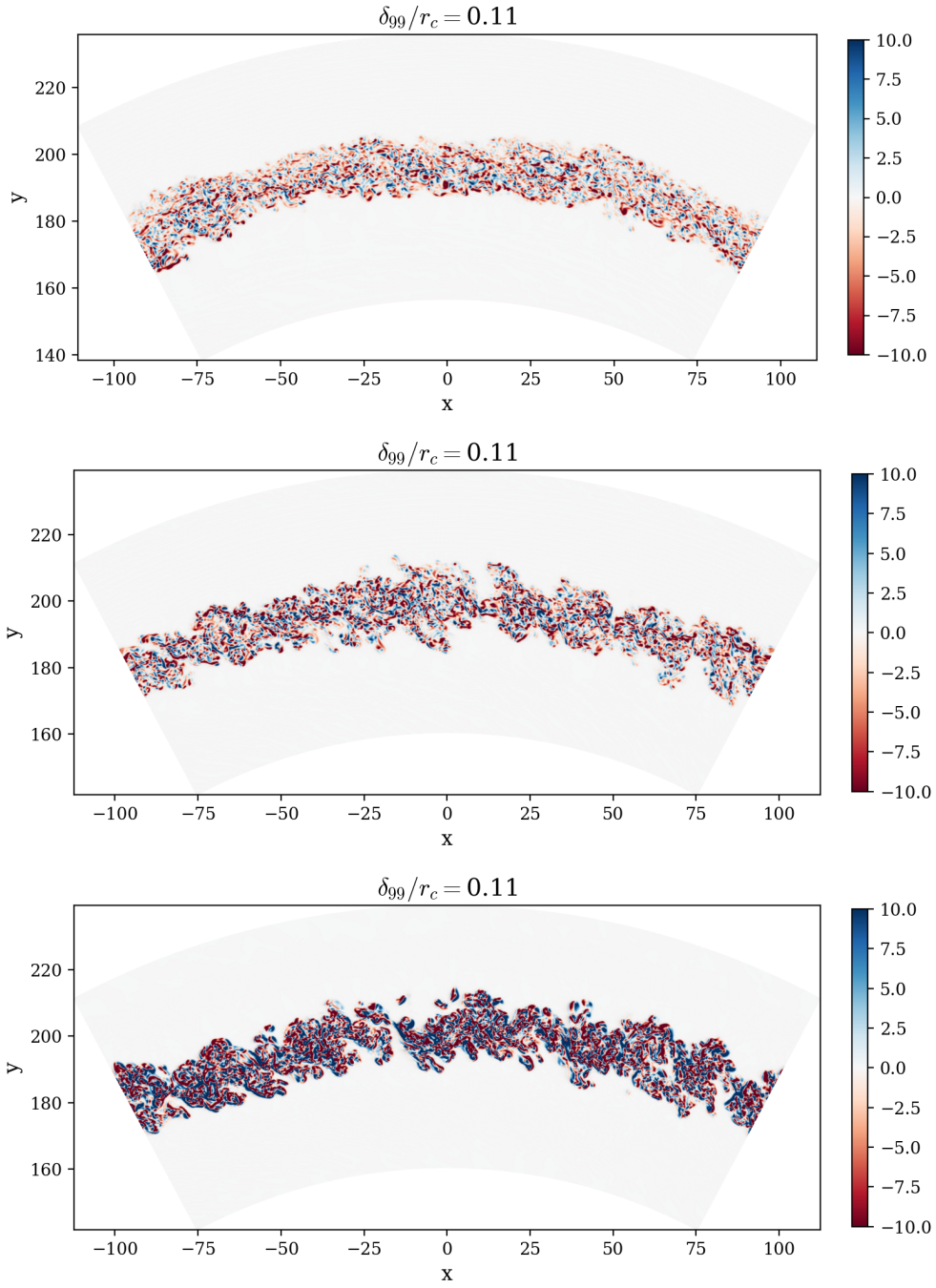

Figure 4.37: Normalized spanwise vorticity $\omega_z \delta_{99}/\Delta u$ for cases at moderate curvature $\delta_0/r_c = 0.01$, $M_c = 0.2, u_2 > u_1$ and $\rho_2/\rho_1 = 1/7, 1, 7$ (top to bottom).

4.5 Conclusions

In this work, the effects of streamwise curvature on turbulent shear layers was examined via eddy-resolving simulations of temporally developing mixing layers at two compressibility levels, three curvature levels and three density ratios. Cases which are approximately planar show good agreement with turbulent stress and growth rate trends of comparable experimental and numerical studies. Stresses at low curvature, low speed and unity density ratio conditions agree well with previously published literature. Budgets of turbulent kinetic energy and shear stress indicate that baropycnal work and mass flux coupling terms, which depend on the mean pressure gradient inherent in these curved flows, remain small in comparison to stress production and turbulent transport at both unity and variable density conditions. For unity density ratio and the present co-flowing shear layers, the centrifugal stability of the flow is determined by the velocity ratio. Increasing the curvature intensity for the unity density ratio cases shows some expected behaviors. Increasing the curvature intensity enhances growth rates and turbulent stresses for centrifugally unstable cases, and vice versa for centrifugally stable cases. Differences in turbulent structure and stress anisotropy were not observed with increasing curvature for unity density ratio cases, at both low and high compressibility cases. Comparison of turbulent growth rates for unity density ratio cases indicate that compressibility and curvature effects for the investigated parameter space are comparable. While criteria developed for linear stability analysis of curved shear layers correctly identify which mixing layers exhibit the slowest or fastest turbulent growth, the corresponding criteria parameters are not necessarily representative of the turbulent growth rates themselves. Lastly, present data demonstrates the combined effects of curvature and variable density effects result in growth rate behavior which is difficult to predict. For example, the present low speed configuration with a denser but slower inner freestream and a reciprocal case with a lighter but faster inner freestream exhibit similar amounts of spanwise baroclinic torque. For comparable velocity ratios, observed growth rates and differences in instantaneous vortical structures are observed with increasing density ratio. Expanding the parameter space beyond the density, velocity, and curvature ratios presented in this chapter would advance the present understanding of these complex interactions between compressibility, variable density and streamwise curvature effects, and is an avenue for future research.
(To Table of Contents)

Chapter 5

RANS model evaluation

5.1 Introduction: modeling approaches

Solving the Reynolds-Averaged Navier-Stokes (RANS) equations is one of the most affordable methods in CFD and remains vital in vehicle design and analysis. However, RANS solvers' deficiencies in capturing complex flow fields, such as those in supersonic retro-propulsive (SRP) flows, are well acknowledged [66, 143]. This work addresses the challenge of modelling turbulence in flows with combinations of compressibility, variable density and rotation/curvature effects by direct comparison of eddy-resolved simulations and RANS calculations. This chapter first introduces the evolution equations associated with turbulence modelling, summarizesme various closure approximations, and compares selected model approximations with eddy-resolved data. Lastly, the performance of standard and modified SA and SST models for shear layers with compressibility and curvature effects are evaluated.

5.1.1 Mean equations of motion

Applying mass averaging to the instantaneous governing equations for transport of mass, momentum, and energy (Eqn. 2.2-2.4) gives the mass-weighted Reynolds-Averaged Navier-Stokes (RANS):

$$\frac{\partial \bar{\rho}}{\partial t} + \frac{\partial}{\partial x_j}(\bar{\rho}\tilde{u}_j) = 0 \tag{5.1}$$

$$\frac{\partial}{\partial t}(\bar{\rho}\tilde{u}_i) + \frac{\partial}{\partial x_j}(\bar{\rho}\tilde{u}_i\tilde{u}_j + \overline{\rho u_i'' u_j''}) = -\frac{\partial \bar{p}}{\partial x_i} + \frac{\partial \bar{\tau}_{ij}}{\partial x_j} \tag{5.2}$$

$$\frac{\partial}{\partial t}(\bar{\rho}\tilde{E}) + \frac{\partial}{\partial x_j}(\bar{\rho}\tilde{u}_j\bar{H}) = \frac{\partial}{\partial x_j}(\bar{\tau}_{ij}\tilde{u}_i + \overline{\tau_{ij}u_i''}) - \tag{5.3}$$

$$\frac{\partial}{\partial x_j}\left(\bar{q}_j + c_p\overline{\rho u_j'' T''} - \tilde{u}_i\overline{\rho u_i'' u_j''} + \frac{1}{2}\overline{\rho u_i'' u_i'' u_j''}\right) \tag{5.4}$$

These evolution equations can be evolved in order to determine mean fields such as $\bar{\rho}$ and $\tilde{u}_i$, given that turbulent terms are modelled. The following terms require modelling in order to 'close' Eqn. 5.1-5.4.

$$\overline{\rho u_i'' u_j''} = \bar{\rho}R_{ij} \qquad c_p\overline{\rho u_j'' T''} \qquad \overline{\tau_{ij}u_i''} \qquad \frac{1}{2}\overline{\rho u_i'' u_i'' u_j''}$$

From left to right, these terms are the turbulent stresses, turbulent heat flux, molecular diffusion of internal energy, and turbulent triple product of velocities (turbulent transport of TKE). Many RANS models neglect the latter two contributions to internal energy, and focus on approximations for the turbulent stresses, $\bar{\rho}R_{ij}$. Closure approximations for the stress tensor comes in many forms. These stresses are either solved directly or defined via constitutive relations to link the stress behavior to the mean flow field. Direct computation of R_{ij} by evolving the Reynolds stress transport equations (Eqn. 2.19) are categorized as second-moment Reynolds stress models, and include further terms which require modelling. These successive levels of approximations required in order to close the model equations is the closure problem or RANS modelling. Constitutive relations for simpler stress models are less computationally expensive in comparison to second-moment models. For example, the common Boussinesq approximation is given in Eqn. 5.5; this approximation simply requires knowledge of a parameter ν_t in order to link the stress tensor to known mean field variables.

$$R_{ij} \approx \nu_t\left(\frac{\partial \tilde{u}_i}{\partial x_j} + \frac{\partial \tilde{u}_j}{\partial x_i} - \frac{2}{3}\frac{\partial \tilde{u}_k}{\partial x_k}\delta_{ij}\right) \tag{5.5}$$

This parameter, ν_t, is the eddy viscosity, which models the dissipation captured in the turbulent energy cascade as a quantity analogous to laminar (molecular) viscosity. The eddy viscosity is

approximately solved using model equations, such as in the Spalart-Allmaras (SA) model equation given in Eqn. 5.6.

$$\frac{\partial \nu_t}{\partial t} + \tilde{u}_j \frac{\partial \nu_t}{\partial x_j} = c_{b1}(1 - f_{t2})S\nu_t + \frac{c_{b1}}{\kappa^2} f_{t2} \left(\frac{\nu_t}{d}\right)^2 + \frac{1}{\sigma}\left[\frac{\partial}{\partial x_j}\left(\nu + \nu_t\right)\frac{\partial \nu_t}{\partial x_j} + c_{b2}\frac{\partial \nu_t}{\partial x_i}\frac{\partial \nu_t}{\partial x_i}\right] \tag{5.6}$$

Spalart and Allmaras [125] provides the definitions of specific model functions and constants. The SA model requires the solution of only one more transport equation in order to provide an approximation of turbulent effects on the mean field (a "one-equation" model). Most turbulence models created to date have been two-equation eddy viscosity models. Considering the dimensions of viscosity, the eddy viscosity can be determined from characteristic length (l) and velocity (v) scales:

$$\nu_t \sim lv$$

Two-equation models typically form a velocity scale by solving a modified form of the evolution equation for TKE, and a second transport equation which provides a turbulence length scale. One commonly applied two-equation model is the SST (shear stress transport) $k - \omega$ model, given in Eqn. 5.7 and 5.8. The model tracks the TKE, k, and the specific turbulent dissipation rate, ω. The eddy viscosity can be approximated as k/ω in regions far from walls.

$$\frac{\partial \rho k}{\partial t} + \frac{\partial}{\partial x_j}(\rho u_j k) = \frac{\partial}{\partial x_j}\left[\left(\mu + \mu_t \sigma_k\right)\frac{\partial k}{\partial x_j}\right] + P - \beta^* \rho \omega k \tag{5.7}$$

$$\frac{\partial \rho \omega}{\partial t} + \frac{\partial}{\partial x_j}(\rho u_j \omega) = \frac{\partial}{\partial x_j}\left[\left(\mu + \mu_t \sigma_\omega\right)\frac{\partial \omega}{\partial x_j}\right] + \frac{\gamma}{\nu_t}P - \beta \rho \omega^2 + 2(1 - F_1)\frac{\rho \sigma_{\omega 2}}{\omega}\frac{\partial k}{\partial x_j}\frac{\partial k}{\partial x_j} \tag{5.8}$$

Refer to Menter [88] for the definitions of specific model functions and constants. While the TKE production $P = \bar{\rho} R_{ij} \tilde{u}_{i,j}$ is defined if the turbulent stresses and mean velocities are known, this modified form of the TKE evolution equation requires approximation of several other terms. The turbulent mass flux, pressure dilatation, and TKE dissipation all require approximation to 'close' the TKE evolution equation (Eqn. 4.19). As shown in Ch. 2 and 3, the turbulent mass flux is greatly enhanced in variable density flows compared to unity density counterparts. Models for this mass flux term will be discussed further in section 5.1.3.

5.1.2 Review of compressibility modifications to model equations

Compressibility modifications to RANS models are designed to mimic the reduction of growth rates and shear stress observed in high speed mixing layers. Existing evaluations of compressibility corrections in turbulence models include Yoder's review of algebraic stress models (ASMs) for jets and shear layers, in which the proposed ASM showed improvements in predictions of mean

velocity profiles and Reynolds stress anisotropy. Barone et al. [7] assessed the compressibility modifications proposed by Zeman, Sarkar et al., Wilcox and found all to be provide a decrease in growth rate but maintain an average error of greater than 10% in the compressibility factor compared to experimental data. Lastly, Aupoix [4] demonstrated that for low speed mixing layers, the influence of velocity ratio on mixing layer growth rates was well captured, but reduction to growth rate due to density differences were not well captured by existing models. This section summarizes notable dilatational and pressure-strain based compressibility modifications for one-equation, two-equation, and second moment turbulence models.

Dilatation-based modifications

Early theories on the reduction of growth rates in compressible turbulent shear layers focused on the contributions of dilatational motions in the flow. Dissipation associated with dilatational velocities, or dilatational dissipation, increases a model's turbulence variable for dissipation and serves as a sink to the TKE of the flow. Similar effects arise from the pressure-dilatation term, which appears explicitly in the exact TKE equation (Eqn. 2.20). Both these dilatational terms serve to effectively reduce the eddy viscosity, μ_t. Models for the dilatational dissipation and pressure-dilatation sink terms were formulated to scale with the compressibility of the flow and are typically dependent on the turbulent Mach number. For an eddy lengthscale of l and kinetic energy k, the time scale of turbulent fluctuations can be approximated as $T_t \sim l/\sqrt{k}$. As mentioned in section on compressibility, the time scale corresponding fto the communication across an eddy can be approximated as $T_c \sim l/c$. The turbulent Mach number presents the ratio of these two time scales, and gives one measure of the compressibility of the flow founded on the scale of turbulent fluctuations.

$$M_t = \frac{T_c}{T_t} = \frac{\sqrt{2k}}{c}$$

For RANS models which track the evolution of k, M_t can be readily computed and used as a compressibility metric. In one equation RANS models, such as SA, the TKE can be approximated as

$$\left[\nu_t^2 \frac{\partial \tilde{u}_i}{\partial x_j}\frac{\partial \tilde{u}_i}{\partial x_j}\right]^{1/2}$$

Spalart [124] gave the equivalent sink term on the RHS of the evolution equation for the eddy viscosity variable ν_t as:

$$\frac{\partial \nu_t}{\partial t} + \tilde{v}\frac{\partial \nu_t}{\partial y} = ... - C_5 \frac{\nu_t^2}{c^2}\frac{\partial \tilde{u}_i}{\partial x_j}\frac{\partial \tilde{u}_i}{\partial x_j}$$

Sarkar et al. [117] modeled the ratio of solenoidal and dilatational dissipation as a function of the turbulent Mach number, based of asymptotic analysis and DNS of compressible, homogeneous, isotropic turbulence (CHIT) with model constant $\alpha_1 = 1$:

$$\frac{\varepsilon_d}{\varepsilon_s} = \alpha_1 M_t^2$$

Zeman [144] also modelled the ϵ_d/ϵ_s using the departure from a reference turbulent Mach number $\xi = M_t - M_{t0}$, with $H(x)$ as the Heaviside step function. This model was tuned for the compressible shear layer without mean density ratio.

$$M_{t0} = 0.1 \qquad \frac{\varepsilon_d}{\varepsilon_s} = H(\xi)\left[1 - e^{-\frac{\xi^2}{0.36}}\right]$$

Wilcox [138] (1992) used a slightly different form and reference M_{t0}, with the aim of improving model performance in compressible flat plate boundary layers. The Sarkar and Zeman models consistently cause a reduction in skin friction in the boundary layer case, although they capture mixing layer compressibility effects well.

$$M_{t0} = 0.25 \qquad \frac{\varepsilon_d}{\varepsilon_s} = H(\xi)(M_t^2 - M_{t0}^2)$$

Suzen and Hoffmann [130] (1998) incorporate Sarkar's compressibility correction for the dissipation ratio and the pressure dilatation in $k-\epsilon$ part of the SST model, and exclude it from the near-wall $k-\omega$ part of the model using a wall blending function.

In addition to dilatational dissipation models, several pressure dilatation models have been formulated. Sarkar [115] suggested that the pressure dilatation term, Π, which appears in the TKE budget as in Eqn. 2.20, should also scale with the M_t, TKE production P, and the solenoidal dissipation rate:

$$\Pi = -0.15\bar{\rho}PM_t + 0.2\bar{\rho}\varepsilon_s M_t^2$$

El Baz and Launder [42] proposed a similar model for Π that includes the mass averaged divergence:

$$\Pi = 3\bar{\rho}\left(\frac{4}{3}k\frac{\partial \tilde{u}_i}{\partial x_i} - P\right)M_t^2$$

Huang et al. [55] used DNS of turbulent channel flow to propose the form

$$\Pi = \bar{\rho}\left(-0.4P + 0.2\varepsilon_s\right)M_t^2$$

Most recently, Li et al. [77] compared the dilatational dissipation models of Sarkar et al. [117], Zeman [144] and Wilcox [138] to DNS of spatially developing compressible turbulent shear layers and conclude that because the dilatational dissipation is dwarfed by solenoidal dissipation, these dilatational dissipation models are unsuitable for at least $M_c \leq 0.7$. Similarly, the pressure dilatation models also overpredict the term's contribution to the TKE budget, even at the compressible case $M_c = 0.7$. The observations that dilatational dissipation and pressure dilatation are negligible in the evolution of TKE are consistent with observations by Vreman et al. [135] and data presented in Ch. 2.

Pressure strain models

After a multitude of studies confirmed that dilatational effects were not the main factor in the stabilizing effect of compressibility, the pressure strain tensor became a candidate for study. The pressure strain tensor contributes to the evolution of the turbulent stresses, as in Eqn. 2.19, and approximations of the pressure strain tensor are directly applicable to Reynolds stress models.

DNS and experimental studies suggested that reduced pressure fluctuations and the corresponding reduction of the pressure strain correlation were the main reasons for dramatic changes in magnitudes of Reynolds stress anisotropy. Present high resolution data also indicates elevated streamwise velocity fluctuations compared to transverse and spanwise components. The pressure strain tensor is responsible for the redistribution of energy among the velocity components, so present data suggests that properly representing the pressure strain tensor is key. Yoder [142] confirmed that models capable of predicting anisotropy and changes in the pressure-strain components are necessary to predict shear layer growth rates, and emphasized that many pressure-strain correlation models are founded on incompressible and locally homogeneous flows. Some notable models which propose a functional dependence of pressure strain components on compressibility are summarized in this section. Pantano and Sarkar [103] proposed that the compressible pressure strain, Π_{ij} and the incompressible pressure strain, Π^I_{ij} are related by the convective Mach number in the highly compressible limit, where the constant $K = 4.5$ was determined empirically.

$$\frac{\Pi_{ij}}{\Pi^I_{ij}} = \frac{1}{KM_c^2} \tag{5.9}$$

Similarly, Fujiwara et al. [48] introduced an M_t-based correction to the incompressible pressure strain where $C_f = 0.02$ is a model constant.

$$\frac{\Pi_{ij}}{\Pi^I_{ij}} = 1 - \exp(-C_f/M_t^2) \tag{5.10}$$

Klifi and Lili [68] developed a version of their pressure strain model to include both the turbulent and the gradient Mach number in the model constants.

$$\frac{\Pi_{ij}}{\bar{\rho}\epsilon} = -C_1\epsilon_s b_{ij} + C_2\frac{k}{\epsilon}\left(S_{ij} - \frac{1}{3}S_{kk}\delta_{ij}\right) + C_3\frac{k}{\epsilon}\left(b_{ik}S_{ij} + a_{jk}S_{ik} - \frac{2}{3}b_{ml}S_{ml}\delta_{ij}\right) + C_4\frac{k}{\epsilon}\left(b_{ik}\Omega_{jk} + b_{jk}\Omega_{ik}\right)$$

With model constants modified from the Launder, Reece, and Rodi [70] model to be functions of M_t. The second model constant was modified in terms of a polynomial in M_t and an exponential of M_g.

$$C_2 = C_\mu g(M_t) \qquad C_\mu = C_{\mu 0} exp(-\beta M_g)$$

Decompositions of the pressure strain tensor have also been proposed. Adumitroaie et al. [1] gave a compressible form of the the pressure strain which split the tensor into its incompressible, compressible, and dilatational components. Gomez and Girimaji [50, 51] give compressible modifications to incompressible pressure strain models from rapid distortion analysis, which considers slow pressure fluctuations that are nonlinear in the fluctuating velocity and fast pressure fluctuations that are linear in the velocity fluctuations. Compared to the model by Adumitroaie et al., Klifi and Lili's demonstration of the model was shown to improve predictions in Reynolds stress anisotropy magnitudes. However, disagreement remained between the Reynolds stress magnitudes predicted using these pressure strain models and experimental data by Goebel and Dutton.Li et al. found that the pressure strain models by Speziale et al. [127] and Wilcox [139] predict the shear component Π_{12} excellently up to $M_c = 0.7$ in unity density ratio, spatially developing shear layers. The M_t-based model by Fujiwara et al. [48] shows much less favorable performance for all Π_{ij} components.

5.1.3 Review of variable density modifications

Notable variable density formulations of second moment turbulence models will be introduced in this section. Analogously to the eddy viscosity model for the turbulent stress tensor, Sarkar and Lakshmanan [116] proposed the following gradient diffusion approximations for the turbulent mass and heat flux, with turbulent Schmidt number Sc_t and turbulent Prandtl number Pr_t:

$$\overline{\rho' u_i'} = \frac{\nu_t}{Sc_t}\frac{\partial \bar{\rho}}{\partial x_i}$$
$$\overline{T' u_i'} = \frac{\nu_t}{Pr_t}\frac{\partial \bar{T}}{\partial x_i}$$

Chassaing [26] gave a thorough review on various closures for variable density turbulence, with a specific focus on turbulent mass flux and energy dissipation rates. Chassaing noted that while

gradient-diffusion type models are attractive for their simplicity, they are not necessarily representative of first order density fluctuations, and concluded that second-order modeling is a more suitable level of closure for turbulence in variable density flows.

Information about the turbulent mass flux is required to captured the dynamics of variable density turbulence. A model for the turbulent mass flux which was formulated for the prediction of 2D supersonic mixing layers was proposed by Dussauge and Quine [39]:

$$\overline{\rho' u_i'} = C^{(i)}(\gamma - 1)M^2 \frac{\bar{\rho}\widetilde{u_i'' u_i''}}{\tilde{u}} \tag{5.11}$$

Where M is the local Mach number, and the model constants are $C^{(1)} = 0.8$ and $C^{(2)} = 1.5$. A comparison to this model is provided later in this chapter. One of the most common models which directly tracks the turbulent mass flux, or the turbulent mass flux velocity, is the Besnard-Harlow-Rauenzahn (BHR) model [10]. The BHR model tracks the mass flux-associated velocity, a_i, Reynolds stresses R_{ij}, the density self-correlation b, TKE dissipation rate ε, turbulent flux of internal energy $S_i\overline{\rho u_i'' e''}$, internal energy fluctuations $\overline{e''}$, and species concentration C_i. Several modifications on the BHR model have been applied a wide variety of compressible, variable density flows. Other models for variable density flows include the Catris & Aupoix model [25], which was formulated specifically for the correction of the log region in boundary layer flows. This model can be applied to both single equation and general two equation RANS models, with access to the turbulent eddy viscosity is $\mu_t = C_\mu \frac{\rho k^2}{\epsilon}$, the turbulent lengthscale $\phi = \rho^n k^m \epsilon^l$, and constants $C_1 = lC_{\epsilon 1} + m$; $C_2 = lC_{\epsilon 2} + m$. Other notable n-equation models include the $k - L$ proposed by Dimonte and Tipton [35], the $k - L - a$ proposed by Morgan and Wickett [91] and the $k - L - a - V$ detailed in Morgan et al. [92]. Models of this form track k number of species, L is some characteristic turbulence length scale, a refers to the mass flux velocity, and V refers to the species mass fraction variance.

5.1.4 Review of rotation/curvature modifications

A selected few models for rotation and curvature modifications to standard RANS model equations are given in chronological order below. One of the earlier modifications was proposed in consideration of wing tip vorticies by Dacles-Mariani et al. [32]. The Dacles-Mariani model suppresses the production term in the Baldwin Barth one equation model. The modification relies on the scalar measure of deformation, S, given below. This formulation reduces eddy viscosity in regions where

the vorticity exceeds the strain rate–it suppresses turbulence in vortex cores, but is inactive in thin shear layers.

$$P = C_1 \nu Re_\tau S \qquad S = |\omega| + 2\min(0, |s| - |\omega|) \qquad \omega = \sqrt{2\Omega_{ij}\Omega_{ij}} \qquad s = \sqrt{2S_{ij}S_{ij}}$$

Spalart and Shur [126] later proposed a rotation-curvature correction for one equation models, without frame rotation, replaces $(1 - f_{t2})$ with $(f_{r1} - f_{t2})$. This model is also known as the Spalart-Shur correction, or SA-RC. Coefficients were tuned based off rotating and curved channel flows; see [126] for more details.

$$\begin{aligned} f_{r1} &= (1 + c_{r1})\frac{2r^*}{1 + r^*}\left[1 - c_{r3}\text{atan}(c_{r2}\hat{r})\right] \\ r^* &= s/\omega \\ \hat{r} &= 2\omega_{ik}S_{jk}D^{-4}\left(\frac{DS_{ij}}{Dt}\right) \\ D^2 &= \frac{1}{2}(S_{ij}S_{ij} + \omega_{ij}\omega_{ij}) \end{aligned}$$

Smirnov and Menter [121] applied the Spalart-Shur modification to two equation models like SST; this model modification is referred to as the rotation-curvature (RC) modification in subsequent sections. The modification is introduced in the production term of both the k and the ω equations:

$$\begin{aligned} f_{r1} &= \max[\min[f_r, 1.25], 0] \\ f_r &= (1 + c_{r1})\frac{2r^*}{1 + r^*}\left[1 - c_{r3}\text{atan}(c_{r2}\hat{r})\right] - c_{r1} \end{aligned}$$

Childs et al. [27]'s modifications to the standard SST $k-\omega$ account for both compressibility and curvature effects. The corrections depends on the magnitude of the dynamics and total pressure gradient, $\hat{\beta} = -\frac{\partial p}{\partial x_i}\frac{\partial p_0}{\partial x_i}$. The compressibility modification is defined similarly to Suzen and Hoffmann's TKE destruction term, with an added factor $F_{MRC}(\hat{\beta}) \in [0, 1]$. The rotation and curvature correction modifies the destruction of the dissipation rate ω:

$$-\beta\rho\omega^2 \quad \rightarrow \quad -g_2\beta\rho\omega^2$$

The dissipation rate is increased or decreased depending on the sign of $\hat{\beta}$ in order to decrease eddy viscosity in regions with stabilizing curvature. Stabnikov and Garbaruk [128] proposed a multiplier

for only the production term in the k equation, which is a modification similar to Spalart & Shur's modification:

$$f_{r1,mod} = \max[f_{r1}, 0]$$
$$f_{r1} = (1 + c_{r1})\frac{1 + c_{r4}}{1 + c_{r4}|r^* - 2|}\left[1 - c_{r3}\text{atan}(c_{r2}\hat{r})\right] - c_{r1}$$

5.2 Evaluation of closure approximations

In this section, data presented in the previous chapters on planar mixing layers will be compared to terms approximated by selected models. In each section, proposed model forms for pressure strain tensor and turbulent mass flux will be compared to present data from eddy-resolving calculations. This evaluation is conducted using the high resolution data from *PadeOps* for purely planar shear layers.

5.2.1 Pressure strain tensor

The components of the pressure strain tensor for unity density ratio, planar shear layer calculations conducted with *PadeOps* at low, moderate and high compressibility levels is shown again for reference in Fig. 5.1. The streamwise component shows monotonically decreasing behavior with increasing compressibility. Again, there exists some statistical variation among each of the profiles due to the averaging period. Integrating the profiles across the shear layer in the y direction gives the trend in Fig. 5.1b. The rate of decrease in the streamwise pressure strain component is reduced with increasing compressibility, with the steepest drop in the integrated value occurring near from $M_c = 0.2$ to $M_c = 0.8$. Models for the compressible pressure strain tensor also shown in terms of integrated values. The Pantano model and the Fujiwara model, defined in Eqn. 5.9 and 5.10, use a reference incompressible value of Π_{ij}^I. In the present comparison, Π_{ij}^I is taken as the value of Π_{ij} at $M_c = 0.2$, and the turbulent Mach numbers match the mean values in Fig. 2.15. The model by Pantano was formulated for the high Mach regime and shows an increase in pressure strain at low $M_c = 0.4$. This is followed by a dramatic decrease at $M_c = 0.8$, where the trend then smoothly decreases similarly to the present data with *PadeOps*. While the high M_c trend qualitatively matches, the values for integrated pressure strain are too small, which suggests some tuning to the model constant K may be necessary. The Fujiwara model similarly shows a sharp decline from $M_c = 0.4$ to $M_c = 0.8$, followed by a slowly decaying trend into the high Mach regime. This model also predicts values which are less than half of what is observed in the present data at

high compressibility levels, though the behavior at lower M_c is improved compared to the Pantano model. Both models appear to exaggerate the decrease with increasing compressibility beyond that observed in the present data.

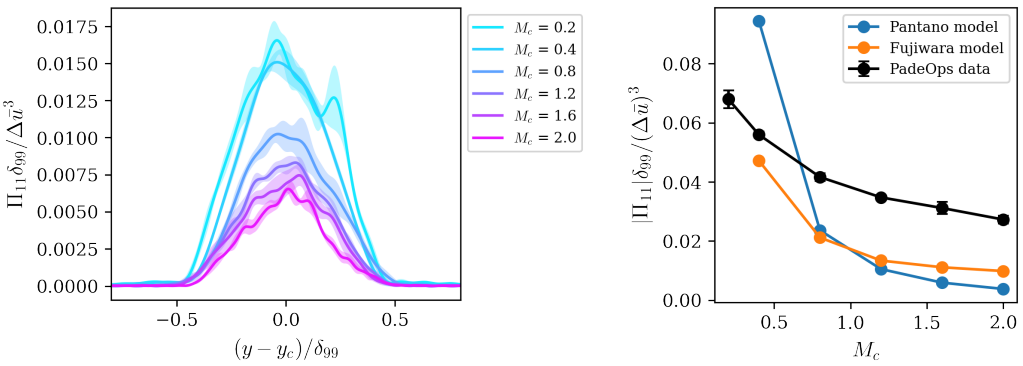

(a) (b)

Figure 5.1: Streamwise pressure strain component compared to M_t-based scaling models: (a) profiles with increasing M_c at $s_\rho = 1$ from *PadeOps* data; (b) trend in integrated profiles compared to models by Pantano and Sarkar [103] and Fujiwara et al. [48].

5.2.2 Turbulent mass flux

The streamwise and transverse turbulent mass flux velocities are compared to the model proposed specifically for supersonic mixing layers by Dussauge and Quine in 5.1.3, and compared with present data in Fig. 5.2. The model relates the mass flux to the turbulent stresses and the local Mach number. Qualitatively, the model shows the correct behavior for the streamwise and transverse mass flux. For unity density ratio cases, the mass flux velocity profiles are anti-symmetric across the mixing layer. The model indicates similar behavior, though the magnitudes predicted by the model do not match the present data. For $s_\rho = 7$ cases, the mass flux shows a bias towards the denser fluid side at $y > y_c$, which is reflected in the model behavior. However, the model incorrectly shows some negative mas flux velocity for the streamwise component in Fig. 5.2c, and shows a large offset between the shear layer centerline and the transverse mass flux in Fig. 5.2d. The turbulent mass flux velocity magnitudes are also not predicted well for $s_\rho = 7$ configurations. With increasing compressibility, the mass flux should decrease, but the model indicates an increase with M_c for the streamwise mass flux velocity. Almost no trend in M_c is observed for the transverse mass flux, likely because the region of the predicted mass flux occurs near the edge of the shear layer into the denser fluid, where the turbulent stress R_{12} is reduced and shows less variation with M_c.

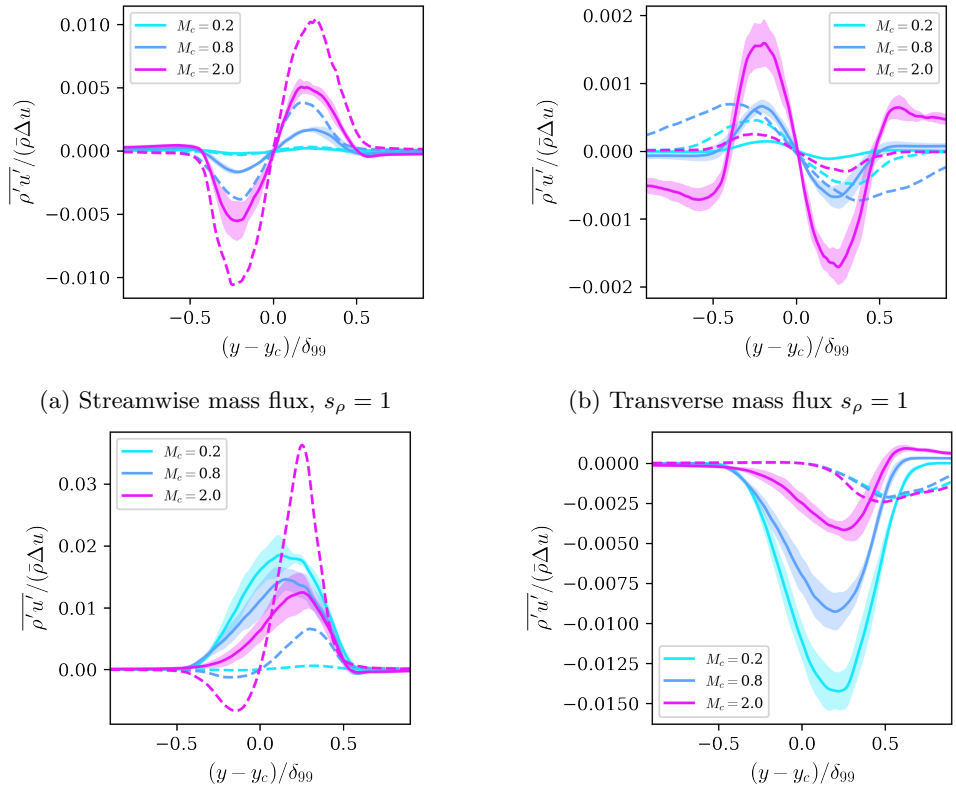

(a) Streamwise mass flux, $s_\rho = 1$

(b) Transverse mass flux $s_\rho = 1$

(c) Streamwise mass flux, $s_\rho = 7$

(d) Transverse mass flux $s_\rho = 7$

Figure 5.2: Turbulent mass fluxes and comparison to model by Dussauge and Quine [39] in dashed lines.

5.3 Interactions between RANS model corrections

Most turbulence model modifications were developed to capture the effects of either compressibility, curvature, or density variations individually. However, these model modifications are often applied simultaneously in complex flow fields, like the ones which arise in SRP. Combinations of model corrections often have unexpected or unintended consequences on the simulated flow field. The main objective of this section is to provide examples of the interactions between commonly applied RANS model corrections. OVERFLOW RANS calculations of both SA and SST are compared to data from eddy resolved simulations using shear layer growth rates and TKE profiles as metrics of model performance. The setup for RANS calculations and validation are introduced, followed by discussion of growth rates with increasing compressibility and presentation of TKE profiles the combination of compressibility, variable density, and curvature effects.

5.3.1 Numerical methods for RANS calculations

The domains for the RANS calculations have the same streamwise (θ) and transverse (r) extent as the same as the previous eddy-resolving calculations. The RANS calculations are run as 2D calculations, given the spanwise periodicity. The azimuthal direction is also periodic, but must be included in the calculations to capture the mean curvature of the flow. Typical RANS calculations for vehicles are under-resolved compared to the grid resolutions used in this work's eddy resolving calculations. To replicate this realistic resolution of RANS calculations for vehicle, the initial shear layer is only resolved with about 5 grid points. Spatial discretization of derivatives and fluxes are the same as the previous calculations (WENO5). Time integration was conducted using second order backwards finite differences and a time step of $\Delta t = 0.1$ with five subiterations to enabled sufficient convergence for integration accuracy. The backwards finite difference scheme was selected over RK4 given the smoothly varying nature of the flow and the lack of high wavenumber features, since eddies were not resolved.

Initial conditions on the eddy viscosity variable ν_t for the SA cases and on k and ω for SST cases are given below; initial values have a Gaussian distribution in the initial mixing layer region which decays into the freestream at a rate of $\sigma = 1.0$:

$$g(r) = e^{-\sigma(r-r_c)^2}$$

The initial eddy viscosity profile for the SA cases were scaled proportional to $\Delta u \delta_{99}$:

$$\nu_t(r) = (C_0 g + C_1)\Delta u \delta_{99}$$

The initial k and ω for the SST cases were scaled with Δu^2 and $\Delta u/\delta_{99}$.

$$k(r) = (C_2 + C_3 g)\Delta u^2$$
$$\omega(r) = (C_4 + C_5 g)\Delta u/\delta_{99}$$

Constants $C_i = [150, 0.1, 0.0001, 0.005, 0.1, 0.0005]$ were selected using rough estimations of the corresponding values from corresponding eddy-resolving calculations, but the RANS calculations did not show particular sensitivity to initial conditions. After a sufficiently long period of growth, the profiles of the turbulent variable collapsed to a single profile. An example of this collapse is given in Fig. 5.5b.

In addition to the two convective Mach numbers of $M_c = 0.2$ and $M_c = 0.8$ of the eddy-resolved calculations, additional RANS cases at compressibility levels of $M_c = 0.1$ and $M_c = 0.5$ were also

conducted to provide more detail of the observed trends in growth rates by the RANS models. These were conduction for the planar ($\delta_0/r_c = 0.001$) and unity density ratio configuration ($\rho_2/\rho_1 = 1$).

The modifications for the SA and SST model are given in Table 5.1. These modifications are not necessarily the most recent and advantageous models for compressible turbulent shear layers, but they are commonly applied for a wide range of complex turbulent applications. As such, the evaluation of these modifications remains relevant. In the remainder of this work, these modifications are referred to as CC and RC for compressibility and rotation/curvature modifications, respectively. Note that the CC modification by Suzen and Hoffmann is the same as that by Sarkar [117] in free shear flows without walls.

Table 5.1: Modifications for compressibility (CC) and rotation/curvature (RC) effects to standard models considered in this chapter.

Model	SA	SST $k-\omega$
CC modification	Spalart [124]	Sarkar [117]
RC modification	Spalart & Shur [126]	Smirnov & Menter [121]

5.3.2 Turbulent kinetic energy profiles

TKE levels from SST calculations of cases with $\rho_2/\rho_1 = 1$ at $M_c = 0.8$ are given in Fig. 5.3, and compared with eddy-resolved calculations (here labelled as 'LES', although no subgrid-scale model has been used). The TKE profiles from standard SST are shown in solid orange lines, SST with rotation/curvature modification in dashed lines, SST with compressibility modification in dotted lines, and SST with both rotation/curvature and compressibility modification in the dashed-dotted lines. At weak curvature levels, shown in Fig. 5.3a and b, the standard SST overpredicts the TKE levels compared to eddy-resolved calculations, but application of the compressibility correction results in surprisingly good agreement. As expected, with weak curvature, application of the rotation/curvature modification does give a large change in the TKE levels. The SST-CC and SST-RC-CC models give the best performance in terms of TKE for these weak curvature cases. In profiles of TKE for cases with stronger curvature, in Fig. 5.3c and d, differences due to the CC and RC modification are more distinct. The RC modification correctly decreases TKE for the centrifugally stable case at $u_2 < u_1$ and increases TKE for the centrifugally unstable case at $u_2 > u_1$. As expected, the CC modification reduces TKE levels in both the unstable and stable configurations. Since both compressibility and curvature effects are active at these flow conditions of $M_c = 0.8$ and $\delta_0/r_c = 0.01$, the SST-CC-RC model may be expected to give the best agreement with the eddy resolving calculations. However, compared to the agreement with cases at weak curvature in Figs. 5.3a and b, the SST-CC-RC model does not show as favorable performance.

A similar comparison of TKE levels is conducted for the cases with increasing curvature at $M_c = 0.8$ and $\rho_2/\rho_1 = 7$ in Fig. 5.4. Similarly to the unity density ratio cases, the variable density cases with weak curvature shows decent agreement with the eddy-resolving calculations in terms of TKE magnitude and asymmetry. Again, the SST-CC-RC model is expected to give the best comparison to the eddy-resolved TKE levels. For $\rho_2/\rho_1 = 1/7$ and $u_2/u_1 > 1$, the magnitudes of the model (SST-RC-CC) and reference ('LES') TKE levels match well, but the asymmetry in the profile is exaggerated. For $\rho_2/\rho_1 = 7$ and $u_2/u_1 < 1$, the SST-RC-CC model captures the symmetry in the profile is relatively well, but the TKE magnitudes are under-predicted. For both the unity and variable density cases, the introduction of streamwise curvature reduces model predictions of TKE, even with the inclusion of compressibility and curvature modifications.

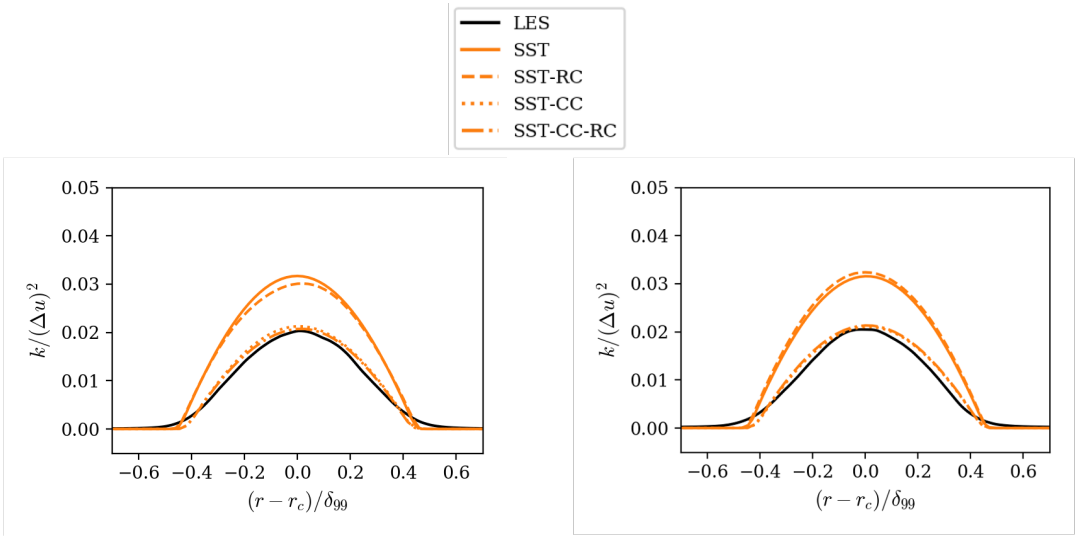

(a) Weak curvature ($\delta_0/r_c = 0.001$), $u_2 < u_1$

(b) Weak curvature ($\delta_0/r_c = 0.001$), $u_2 > u_1$

(c) Strong curvature ($\delta_0/r_c = 0.010$), $u_2 < u_1$

(d) Strong curvature ($\delta_0/r_c = 0.010$), $u_2 > u_1$

Figure 5.3: Comparison of TKE profiles of curved shear layers at $M_c = 0.8$ with low and high curvature levels for $\rho_2/\rho_1 = 1$, eddy-resolved data labelled as 'LES'.

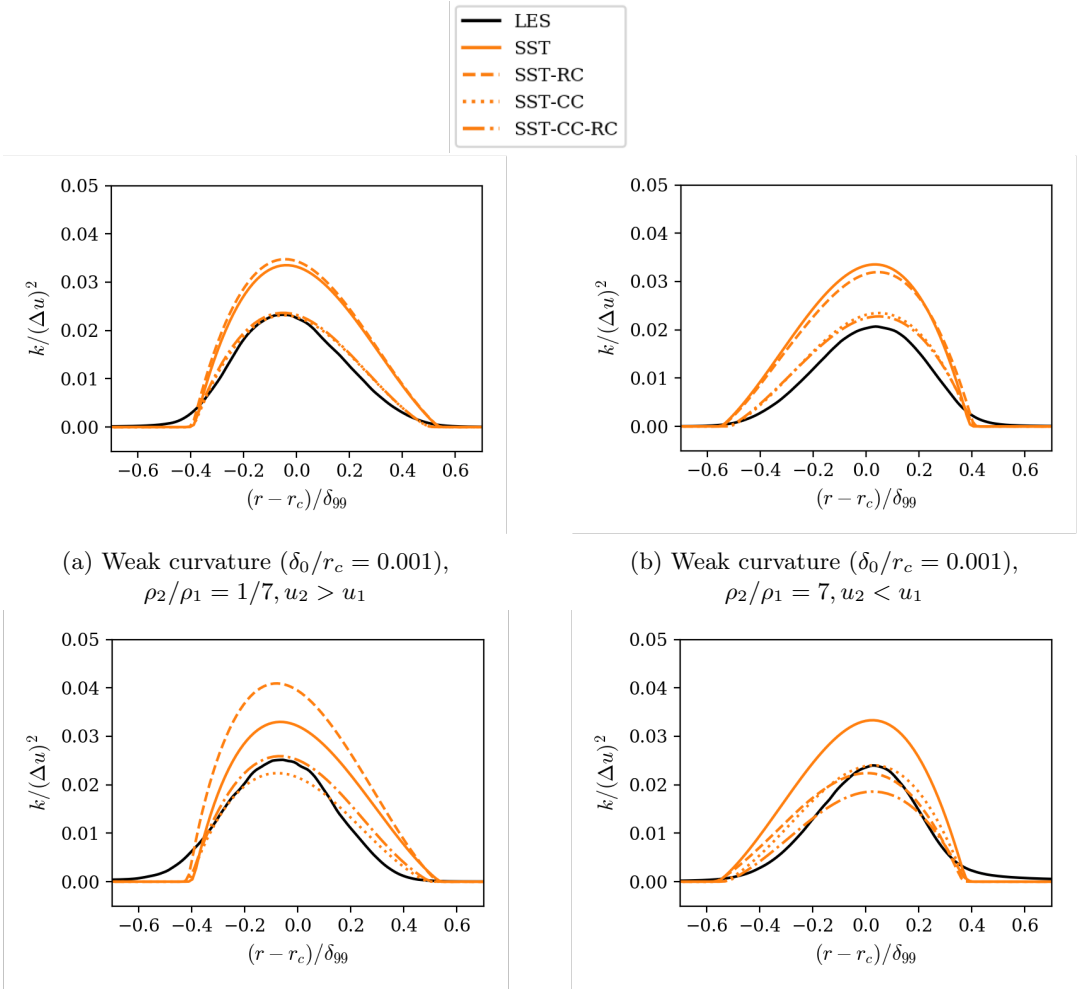

(a) Weak curvature ($\delta_0/r_c = 0.001$), $\rho_2/\rho_1 = 1/7, u_2 > u_1$

(b) Weak curvature ($\delta_0/r_c = 0.001$), $\rho_2/\rho_1 = 7, u_2 < u_1$

(c) Strong curvature ($\delta_0/r_c = 0.010$), $\rho_2/\rho_1 = 1/7, u_2 > u_1$

(d) Strong curvature ($\delta_0/r_c = 0.010$), $\rho_2/\rho_1 = 7, u_2 < u_1$

Figure 5.4: Comparison of TKE profiles of curved shear layers at $M_c = 0.8$ with low and high curvature levels for $\rho_2/\rho_1 \neq 1$, eddy-resolved data labelled as 'LES'.

5.3.3 Growth rates

Mean profiles of streamwise velocity calculated using standard SA for $\delta_0/r_c = 0.001$ and $M_c = 0.8$ are plotted versus radius and normalized transverse coordinate to demonstrate collapse after and brief transient period. Similar behavior can be seen in Fig. 5.5b, where the eddy viscosity profile, ν_t, normalized by external shear layer scales shows collapse to distinct profiles for standard (blue) and corrected (orange) SA.

An example comparison of growth rate trends with increasing compressibility is given in Fig. 5.6. With standard SA and SST, the growth rates show almost constant behavior with increasing compressibility. The SA and SST data overlap at $M_c = 0.8$. The expected behavior for the growth rates is demonstrated with eddy-resolved datapoints at $M_c = 0.2$ and $M_c = 0.8$ for approximately planar shear layers, where a decrease in growth rate of about 50% is expected. Inclusion of the Spalart compressibility modification to the SA calculations and the Sarkar compressibility modification to SST shows slightly more satisfactory trend with increasing M_c. However, the decrease in growth rate according to the models is not as dramatic as that predicted by eddy resolved calculations.

The compressibility correction for the SST calculations scale with M_t^2. Fig. 5.7 compares the values of M_t^2 predicted by RANS and predicted by the eddy-resolving calculations (labelled as 'LES' although no subgrid scale model was used). The values of M_t match well between the calculations from *PadeOps* and OVERFLOW, plotted with black markers. The standard SST model (plotted in blue) over-predicts the turbulent Mach number values once compressibility effects become prominent, while application SST with compressibility modification (plotted in orange) reduces the M_t values to match those of the eddy-resolving calculations. The agreement with M_t values and the disagreement in growth rates appears contradictory. However, this discrepancy can be explained because the compressibility modifications are formulated to incorporate dilatational effects on the shear layer's turbulent growth. The SST-CC modification increases dilatational dissipation and the pressure dilatation in the standard evolution equation of TKE, but present knowledge suggests that dilatational effects are not a substantial contributor to growth rate reductions.

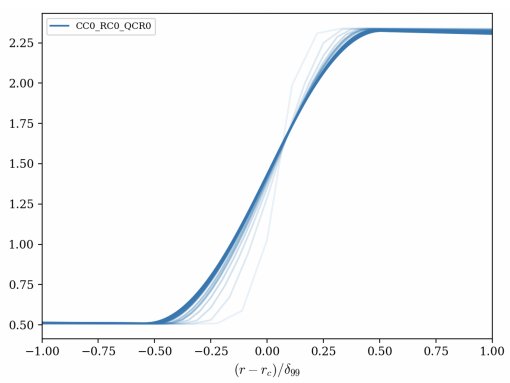

(a) Collapse of $\tilde{u}$ profiles computed with standard SA

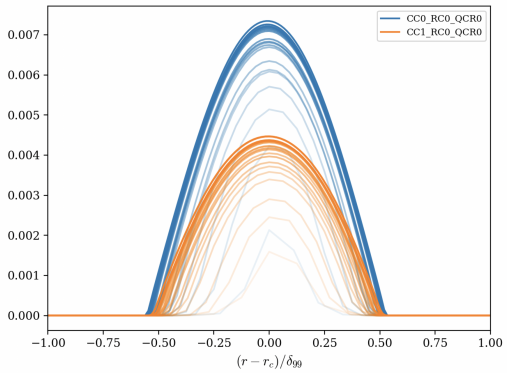

(b) Eddy viscosity profiles $\nu_t/(\delta_{99}\Delta u)$ computed with standard (blue) and compressibility-modified (orange) SA

Figure 5.5: Collapse of mean profiles using SA model at $\delta_0/r_c = 0.001$ and $M_c = 0.8$.

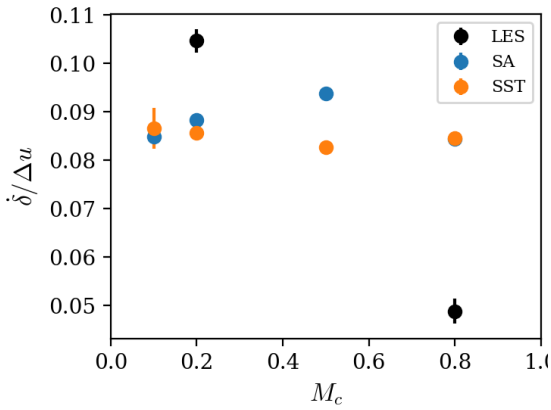

(a) Standard SA and SST

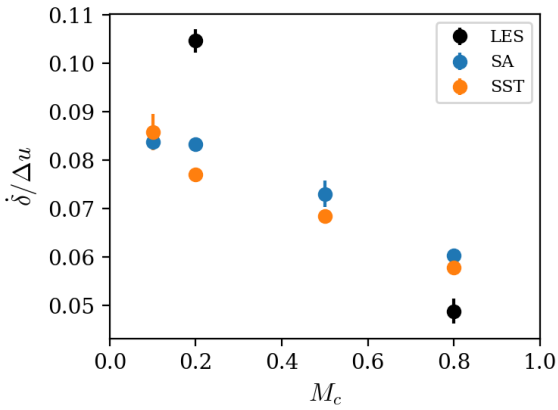

(b) SA and SST with compressibility corrections

Figure 5.6: Effect of compressibility corrections on growth rates compared to eddy-resolved data (labelled 'LES') for $\delta_0/r_c = 0.001$ and $\rho_2/\rho_1 = 1$.

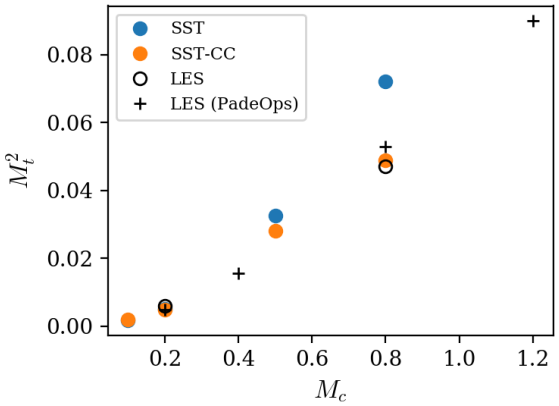

Figure 5.7: Peak turbulent Mach number values with increasing M_c.

Chapter 6

Conclusions

In Chapter 2, the scales governing the turbulent structures in mixing layers with notable compressibility effects were examined. Reduction of growth rates, turbulent normal and shear stresses, and TKE budget terms are confirmed to be consistent with previous experimental and numerical results. Anisotropy invariant maps indicate consistency with previously observed trends of increased streamwise anisotropy with increasing compressibility levels. The contributions of dilatational effects in the form of pressure dilatation and dilatational components of kinematic stresses are demonstrated to be small. As M_c increases, turbulence length scales including the transverse length scale reduce significantly as a fraction of the overall shear layer thickness. These length scales appear to be limited by acoustic communication; turbulence-associated Mach number(s) show saturation at higher levels of compressibility. The internal regulation adapts the spatial and temporal scales of shear layer turbulence inferred from two-point correlations. It reduces the effective velocity scale, suppresses pressure fluctuations and lowers mixing layer growth rates.

In Chapter 3, the effect of the mean density variation in the flow, independent from the effect of compressibility, is demonstrated. Present data comparing thickness growth rates and shear layer decorrelation scales suggests that compressibility and variable density effects cannot be completely decoupled. At $s_\rho = 7$, growth rates decrease with increasing M_c in a similar manner to $s_\rho = 1$ growth rates, though the decrease from $M_c = 0.2$ to $M_c = 2.0$ is not as dramatic at $s_\rho = 7$. Furthermore, the shift in mean velocity profile compared to the mean density profile is also documented to occur consistently at all studied compressibility levels. This offset between the location of turbulent mixing and the location of mean density gradient reduces the momentum mixing efficiency, as seen by turbulent stress profiles which become biased towards the lighter fluid region. Two definitions of the shear layer centerline are compared; the centerline defined by the streamwise velocity profile moves into the lighter freestream region and indicates approximately similar contributions to shear layer growth rates from both sides of the mixing layer. The centerline as defined by mean density gradually moves into the denser fluid region; this definition of the mixing layer centerline implies that the lighter fluid is responsible for most of the mixing layer growth in the turbulent regime. This work also demonstrated that the centerline definition should be considered in the selection of characteristic turbulent scales. Decorrelation length scales are found to be asymmetric about the shear layer centerline, with larger decorrelation scales occurring in the lighter fluid. Internal regulation also occurs at $s_\rho = 7$, which allows for the scaling of TKE production, dissipation and pressure strain to be collapsed when normalized by the 'effective' eddy scales when centered about the velocity-defined centerline. A comparison of density variances associated with compositional, adiabatic, and isobaric effects were examined. Across the M_c range, density fluctuations associated with multi-species mixing were significantly larger than those associated with adiabatic effects. Lastly, aerodynamic heating was observed at both variable and unity density ratios and the corresponding temperature excess scales quadratically with compressibility.

In Chapter 4, the effects of streamwise curvature on turbulent shear layers was examined via eddy-resolved simulations of temporally developing mixing layers at two compressibility levels, three curvature levels and three density ratios. Cases which are approximately planar show good agreement with expected turbulent stress and growth rate trends. Stresses at low curvature, low speed and unity density ratio conditions agree well with previously published literature. Budgets of turbulent kinetic energy and shear stress indicate that baropycnal work and mass flux coupling terms, which depend on the mean pressure gradient inherent in these curved flows, remain small in comparison to stress production and turbulent transport at both unity and variable density conditions. For unity density ratio flows, the centrifugal stability of the flow is determined by the velocity ratio. Increasing the curvature intensity in the unity density ratio cases enhances growth rates and turbulent stresses for centrifugally unstable cases, and vice versa for centrifugally stable cases. Differences in turbulent structure and stress anisotropy were not observed with increasing curvature for unity density ratio cases, at both low and high compressibility cases. Comparison of turbulent growth rates for unity density ratio cases indicates that compressibility and curvature effects for the investigated parameter space are comparable. While criteria developed for linear stability analysis of curved shear layers correctly identify which mixing layers exhibit the slowest or fastest turbulent growth, the corresponding criteria parameters are not necessarily representative of the turbulent growth rates themselves. Lastly, present data demonstrates the combined effects of curvature and variable density effects result in growth rate behavior which is difficult to predict. For example, the present low speed configuration with a denser but slower inner freestream and a reciprocal case with a lighter but faster inner freestream exhibit similar amounts of spanwise baroclinic torque. For comparable velocity ratios, observed growth rates and differences in instantaneous vortical structures are observed with increasing density ratio. Expanding the parameter space beyond the density, velocity, and curvature ratios presented in this chapter would advance the present understanding of these complex interactions between compressibility, variable density and streamwise curvature effects, and is an avenue for future research.

In Chapter 5, TKE levels for shear layers under weak and strong curvature and compressibility levels of $M_c = 0.8$ were compared between various RANS calculations. At weak curvature levels, the standard SST model over-predicts the TKE levels compared to eddy-resolved calculations, but application of the Sarkar compressibility correction resulted in surprisingly good agreement. For both the unity and variable density cases, the introduction of streamwise curvature reduces model predictions of TKE, even with the inclusion of compressibility and curvature modifications. The decrease in growth rate according to the models is not as dramatic as the high-fidelity predictions, although agreement with M_t values was achieved. This discrepancy occurs because the compressibility correction applied to the standard SST model was focused on dilatation effects on

the turbulent growth rates, while present knowledge suggests that dilatational effects are not a substantial contributor to growth rate reductions.

The extensions of this research into future work are plentiful. Both further post-processing of the present data and new simulations in an augmented parameter space would bolster the characterizations presented in this thesis. Additional cases run at higher resolution to fully capture viscous scales would be ideal to verify the observed results. Improved density fluctuation decomposition and similarity analysis of the planar shear layer with consideration of a viscous heating time scale are also avenue of future work. In the analysis of curvature effects on turbulent mixing, a parameter which encompasses centrifugal stability with compressibility effects would compliment the present datasets. Another variation of this curved shear layer configuration with counter-flowing, rather than co-flowing velocities, would also supplement the present work nicely. Lastly, further comparison with RANS model corrections beyond those presented in Chapter 5 and some incorporation of acoustic limitations of turbulent time and length scales in present models would also greatly improve the RANS model contributions of this work.

(To Table of Contents)

Appendix A

Temporal shear layer windowing

For supersonic configurations, a tapered cosine ('Tukey') window was applied in the transverse direction to remove Mach waves from the free-stream region prior to applying a spectral filter. This window w has the form:

$$
\begin{aligned}
w(n) &= \frac{1}{2}\left[1 - cos\left(\frac{2\pi n}{\alpha N}\right)\right], && 0 \leq n < \frac{\alpha N}{2} \\
w(n) &= 1, && \frac{\alpha N}{2} \leq n < \frac{N}{2} \\
w(N-n) &= w(n), && 0 \leq n \leq \frac{N}{2}
\end{aligned}
$$

Where $\alpha = 0.5$ and N is the total number of points spanning the δ_{99} shear layer thickness with a buffer of $0.15\delta_{99}$ above and below the δ_{99} boundaries. On the windowed field, spectral methods can be applied in all spatial directions. The spectrum of TKE is computed and the 90% cutoff wavenumbers k_x, k_y and k_z are calculated. Each velocity field is then transformed to Fourier space, zero-padded for all wavenumbers greater than the cutoff wavenumbers, and transformed back to physical space for each coordinate direction. Figure A.1 shows the effect of windowing and filtering on an instantaneous v velocity field, and Fig. A.2 demonstrates the effect of filtering on velocity, pressure and density variances across the shear layer. The main changes in profiles are due to windowing effects.

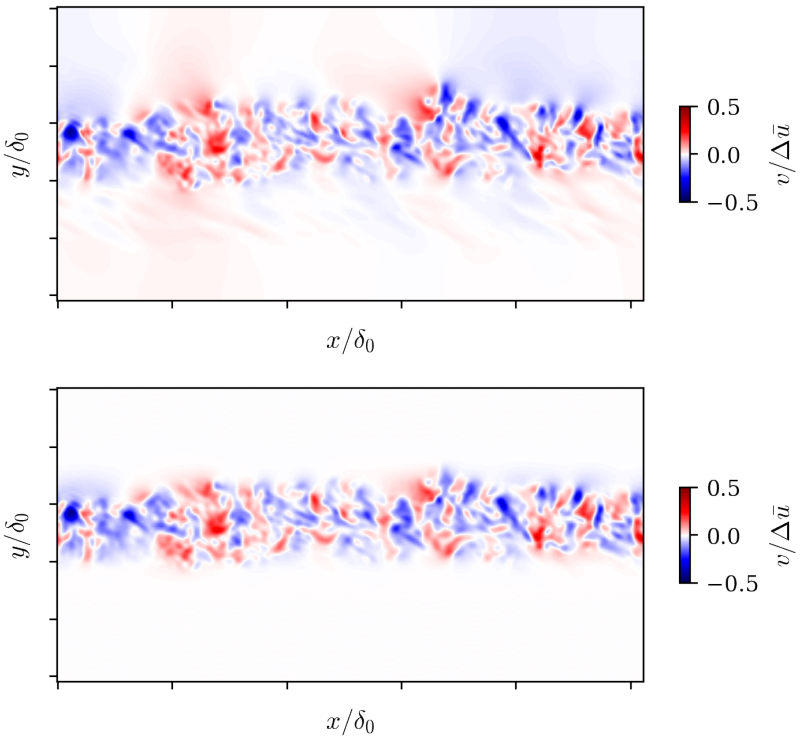

Figure A.1: Transverse velocity field before (top) and after (bottom) windowing and filtering for $M_c = 0.8, s_\rho = 7$

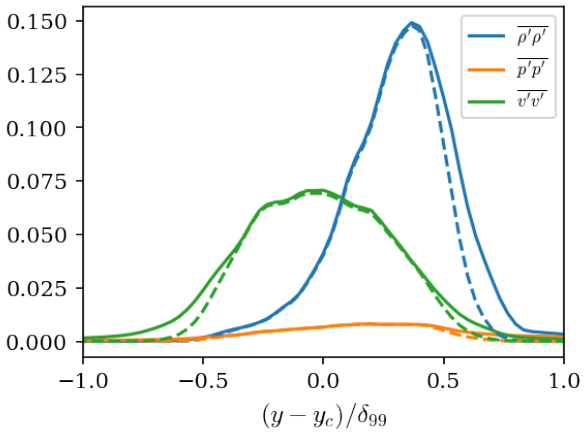

Figure A.2: Instantaneous variances of transverse velocity, pressure and density before and after windowing and filtering for $M_c = 0.8, s_\rho = 7$

Appendix B

Curved shear layer profiles

Mixing layer growth

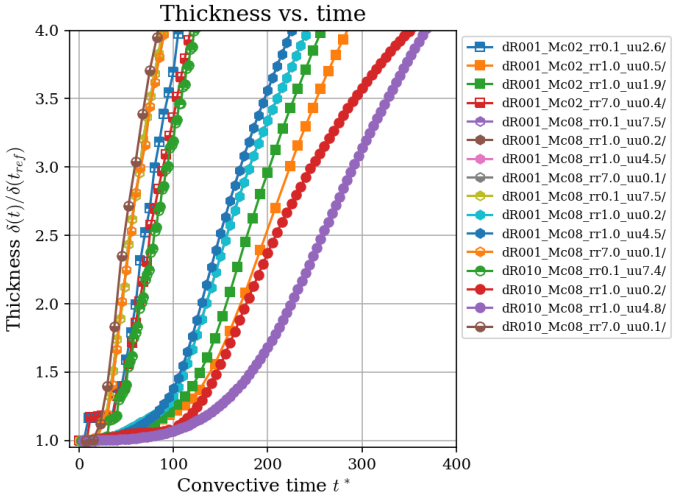

(a) Evolution of δ_Γ

Streamwise contours of radial velocity

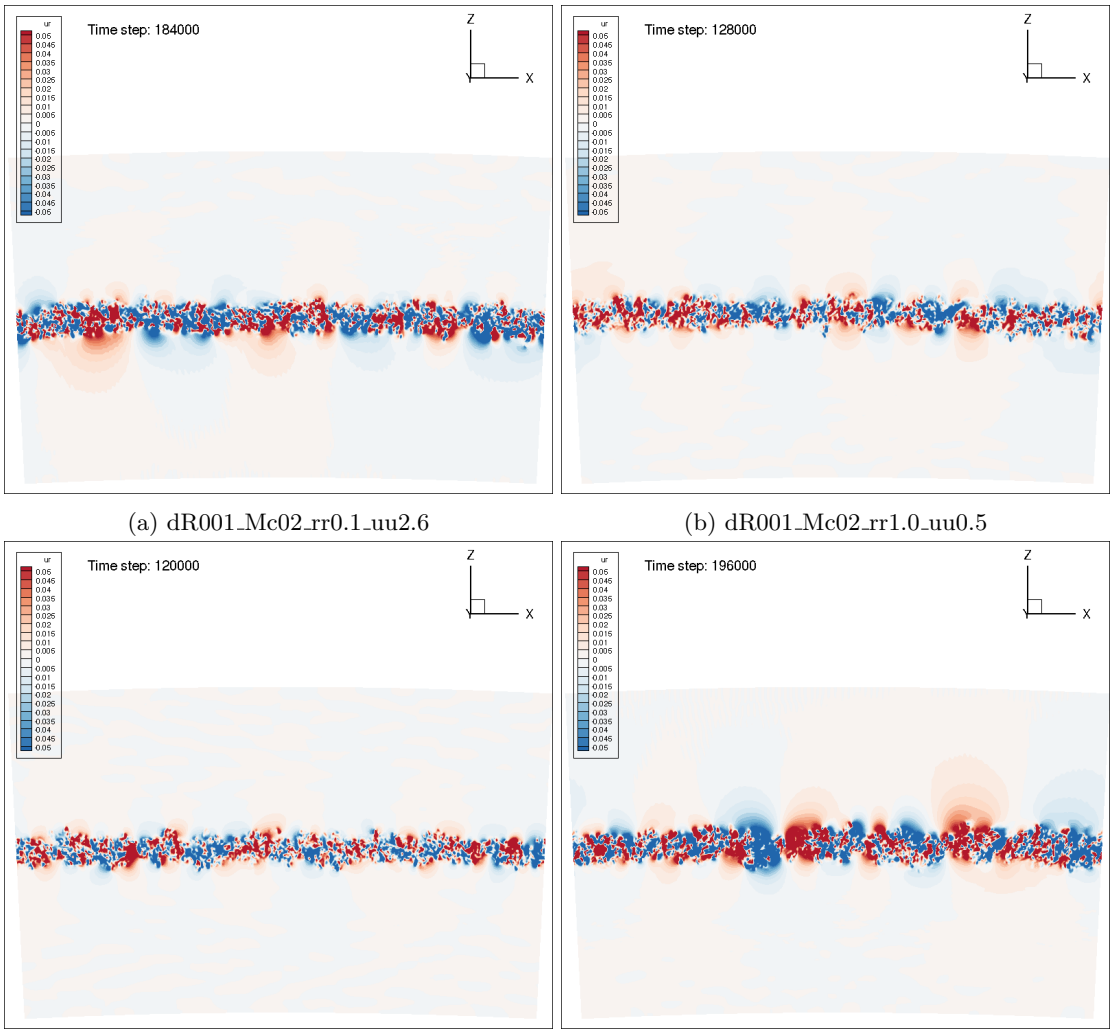

(a) dR001_Mc02_rr0.1_uu2.6

(b) dR001_Mc02_rr1.0_uu0.5

(c) dR001_Mc02_rr1.0_uu1.9

(d) dR001_Mc02_rr7.0_uu0.4

Figure B.2: Slices of u_r at $\delta/\delta_0 = 2.5$ and $\delta_0/R_0 = 0.001, M_c = 0.2$

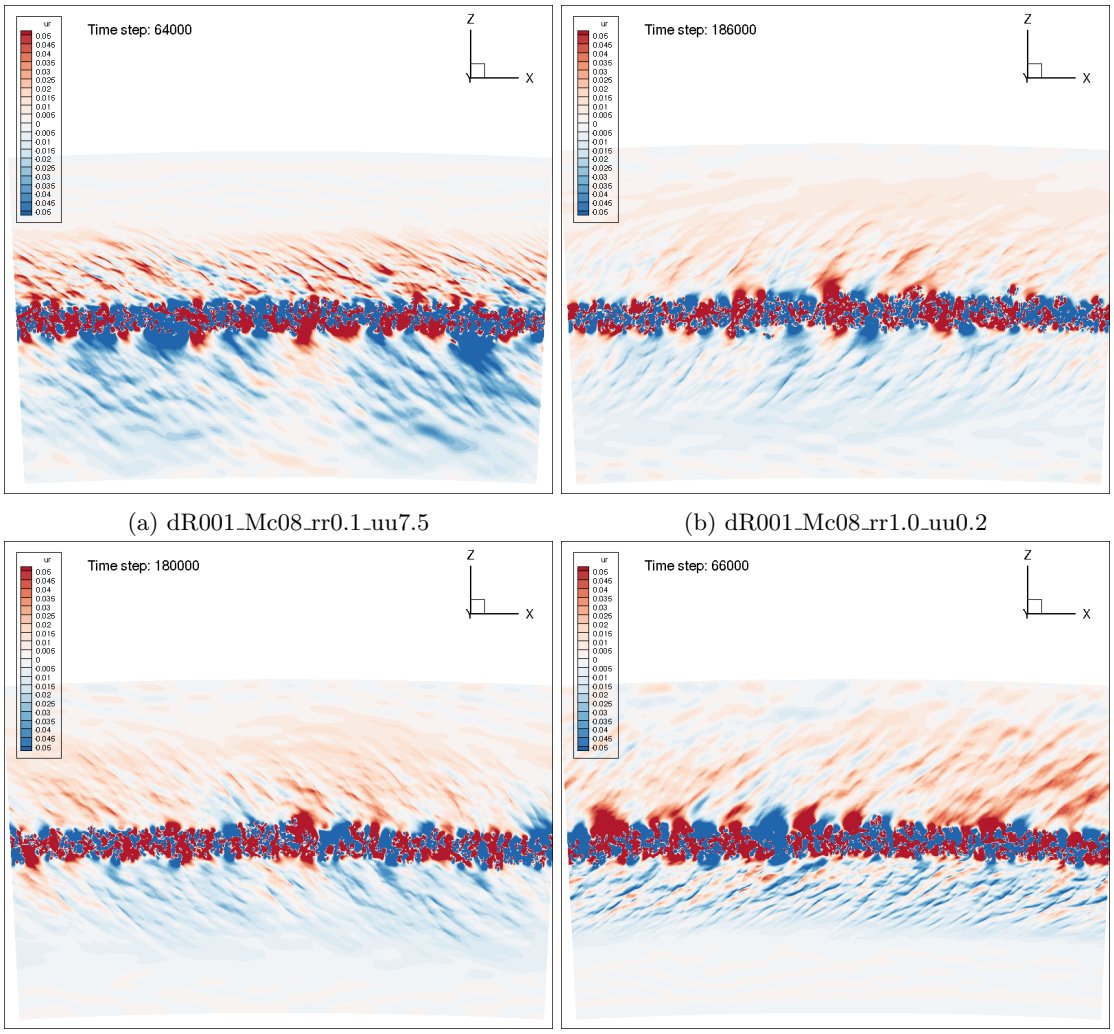

(a) dR001_Mc08_rr0.1_uu7.5

(b) dR001_Mc08_rr1.0_uu0.2

(c) dR001_Mc08_rr1.0_uu4.5

(d) dR001_Mc08_rr7.0_uu0.1

Figure B.3: Slices of u_r at $\delta/\delta_0 = 2.5$ and $\delta_0/R_0 = 0.001, M_c = 0.8$

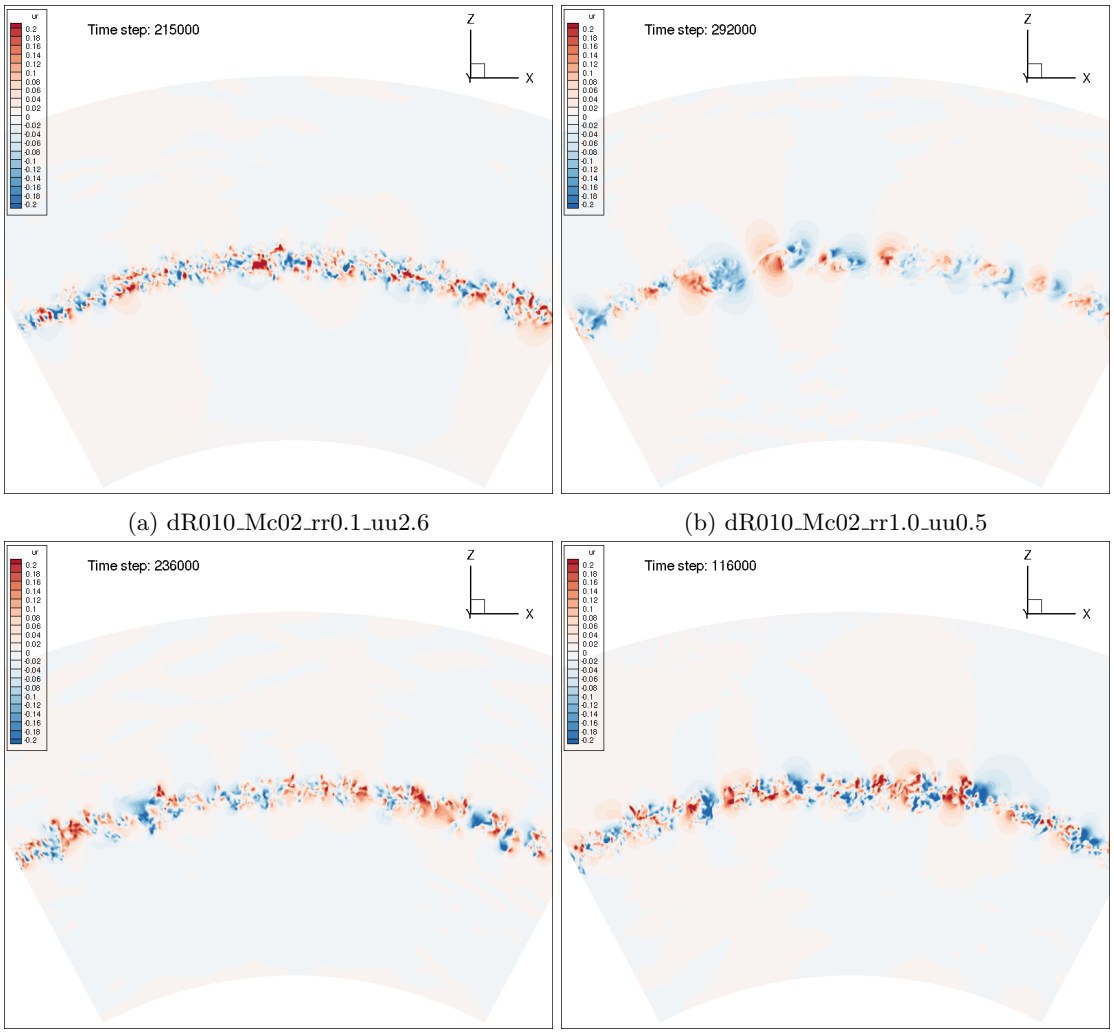

(a) dR010_Mc02_rr0.1_uu2.6

(b) dR010_Mc02_rr1.0_uu0.5

(c) dR010_Mc02_rr1.0_uu1.9

(d) dR010_Mc02_rr7.0_uu0.4

Figure B.4: Slices of u_r at $\delta/\delta_0 = 2.5$ and $\delta_0/R_0 = 0.010, M_c = 0.2$

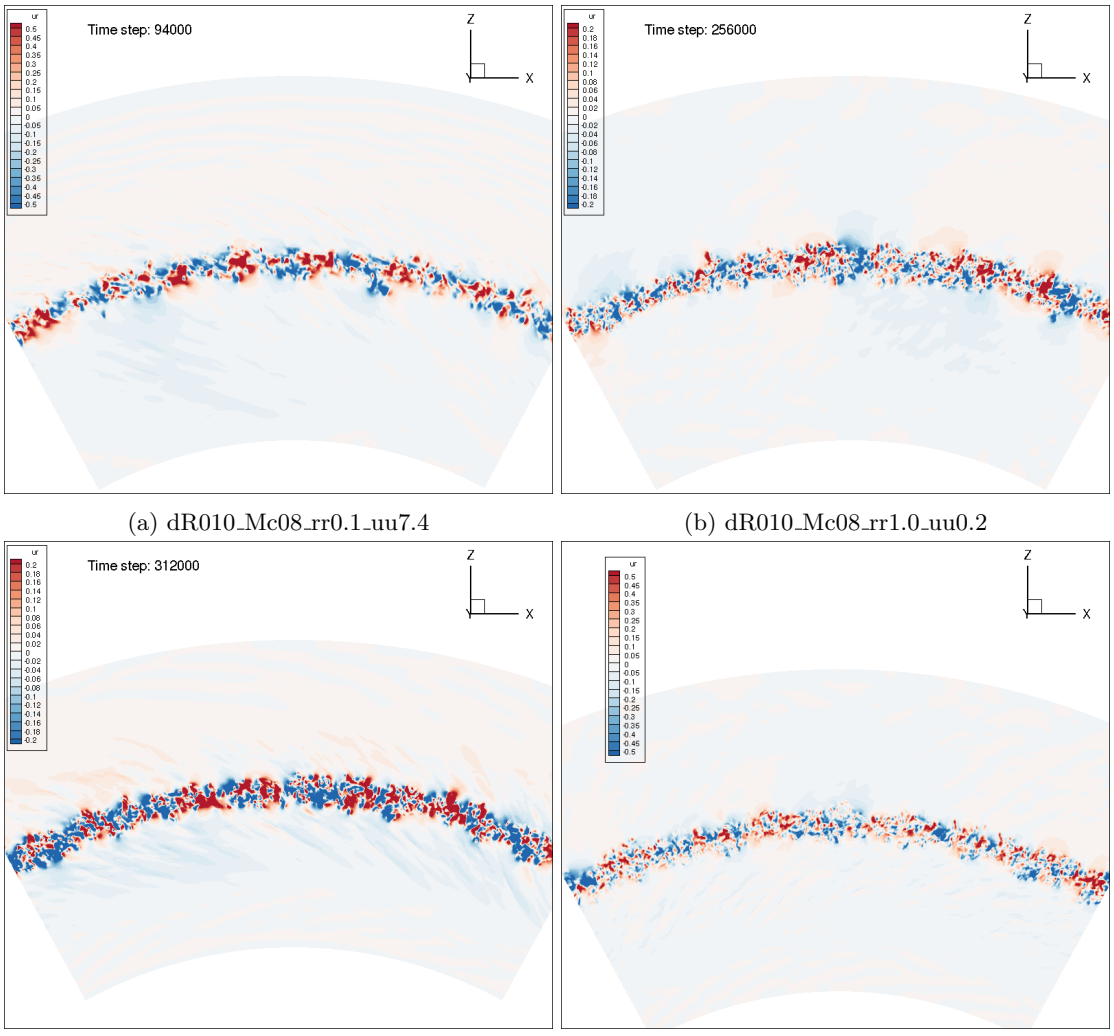

(a) dR010_Mc08_rr0.1_uu7.4

(b) dR010_Mc08_rr1.0_uu0.2

(c) dR010_Mc08_rr1.0_uu4.8

(d) dR010_Mc08_rr7.0_uu0.1

Figure B.5: Slices of u_r at $\delta/\delta_0 = 2.5$ and $\delta_0/R_0 = 0.010, M_c = 0.8$

Mean profiles

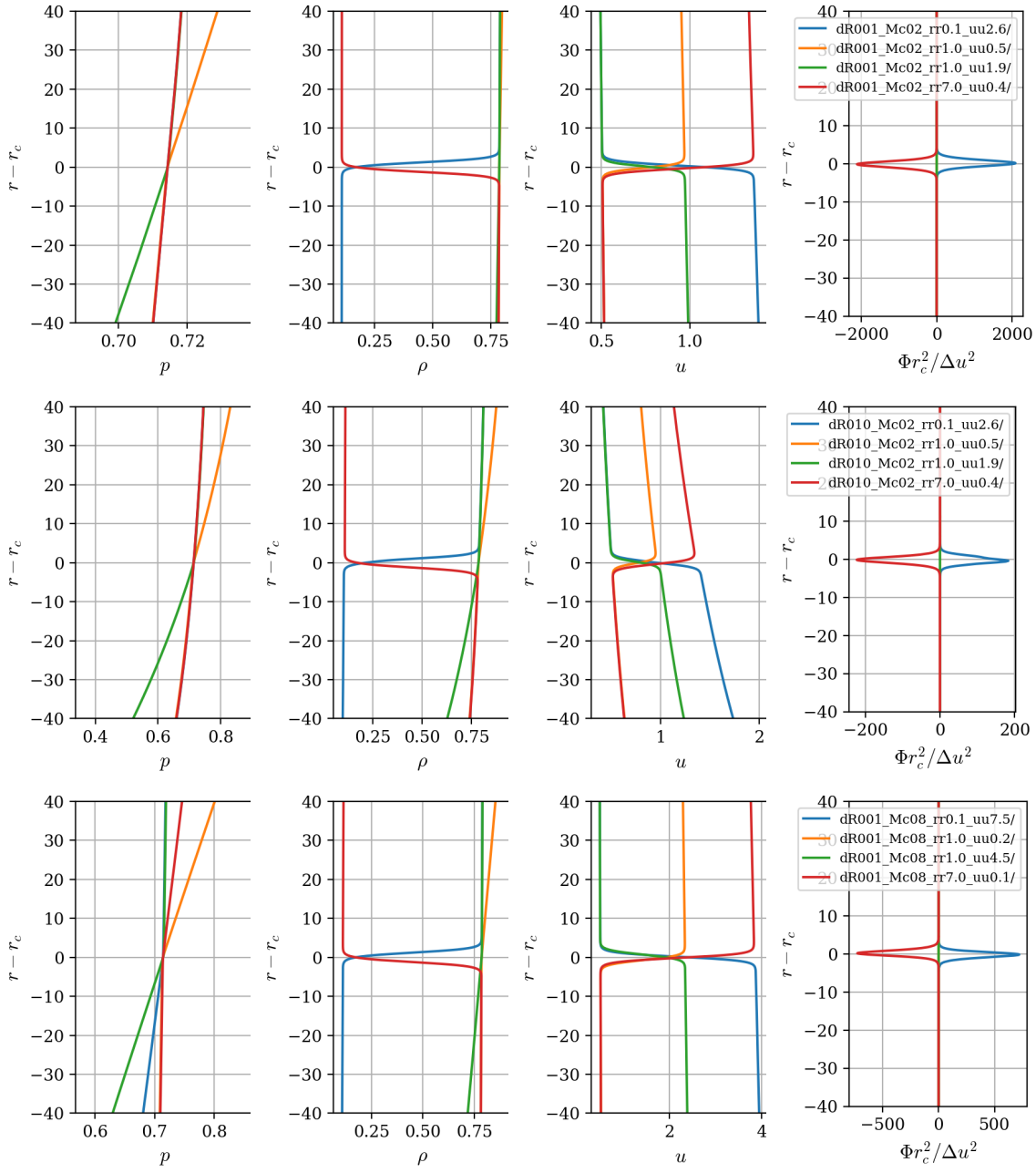

Figure B.6: Initial profiles of pressure, density, streamwise velocity, and normalized Eckhoff criterion for cases at (top row) $\delta_0/r_c = 0.001$ and $M_c = 0.2$; (middle row) $\delta_0/r_c = 0.010$ and $M_c = 0.2$; (bottom row) $\delta_0/r_c = 0.001$ and $M_c = 0.8$.

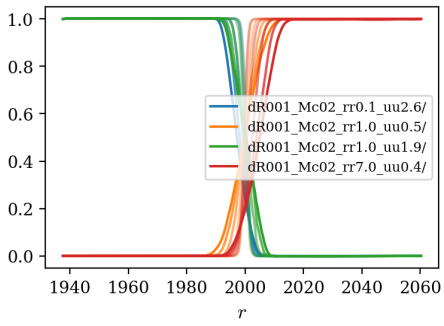

(a) $\delta_0/r_c = 0.001$ and $M_c = 0.2$

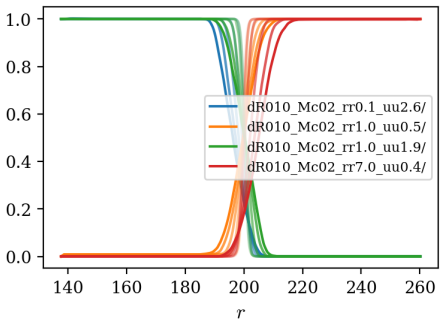

(b) $\delta_0/r_c = 0.010$ and $M_c = 0.2$

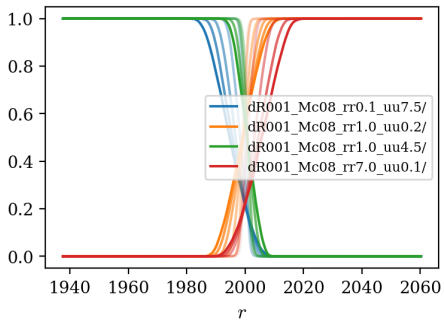

(c) $\delta_0/r_c = 0.001$ and $M_c = 0.8$

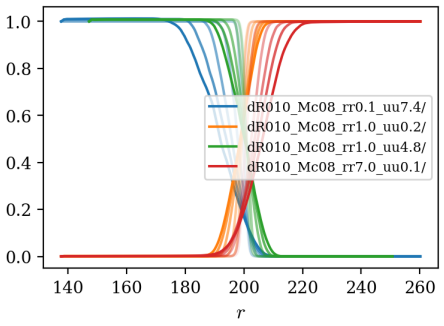

(d) $\delta_0/r_c = 0.010$ and $M_c = 0.8$

Figure B.7: Normalized mean circulation profiles $(\tilde{\Gamma} - \Gamma_{min})/(\Gamma_{max} - \Gamma_{min})$

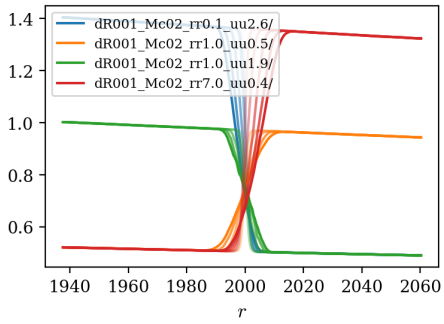

(a) $\delta_0/r_c = 0.001$ and $M_c = 0.2$

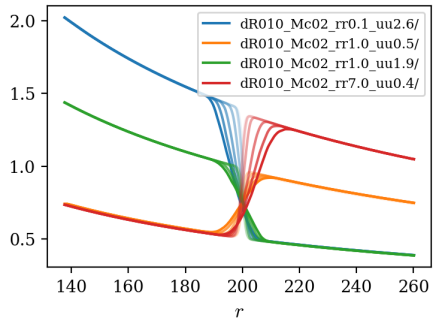

(b) $\delta_0/r_c = 0.010$ and $M_c = 0.2$

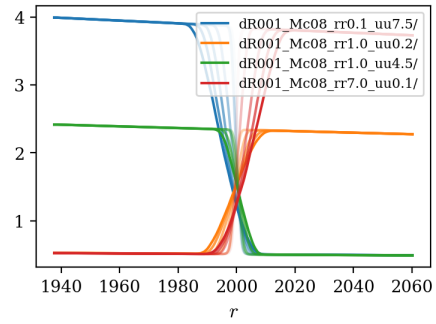

(c) $\delta_0/r_c = 0.001$ and $M_c = 0.8$

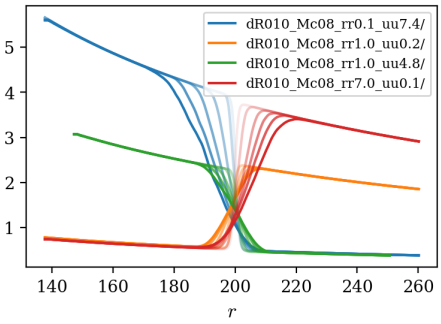

(d) $\delta_0/r_c = 0.010$ and $M_c = 0.8$

Figure B.8: Mean streamwise velocity $\tilde{u}_\theta$

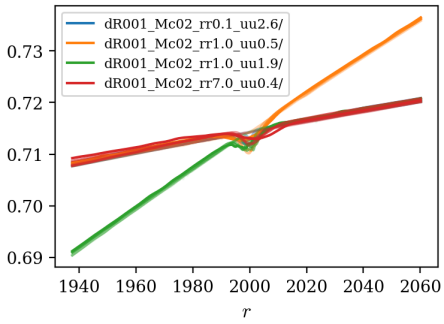

(a) $\delta_0/r_c = 0.001$ and $M_c = 0.2$

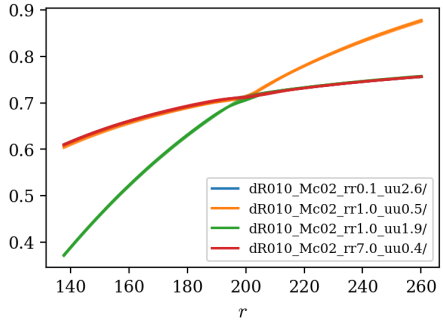

(b) $\delta_0/r_c = 0.010$ and $M_c = 0.2$

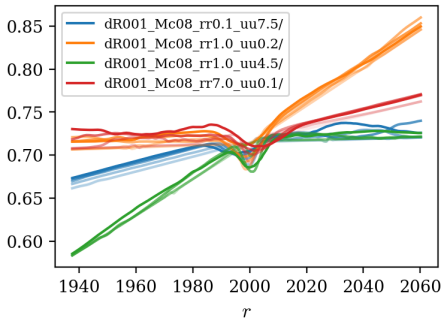

(c) $\delta_0/r_c = 0.001$ and $M_c = 0.8$

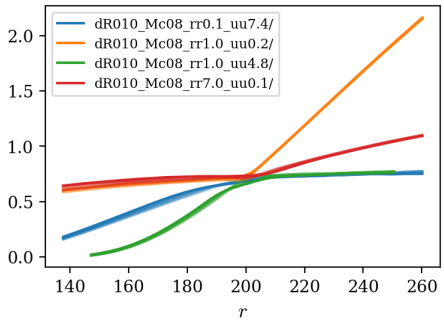

(d) $\delta_0/r_c = 0.010$ and $M_c = 0.8$

Figure B.9: Mean pressure $\bar{p}$

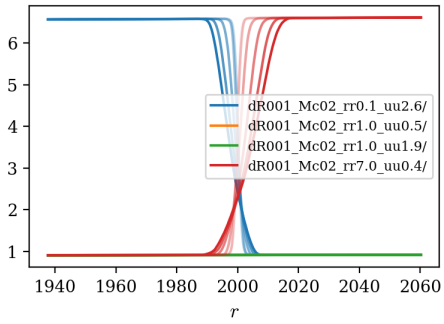

(a) $\delta_0/r_c = 0.001$ and $M_c = 0.2$

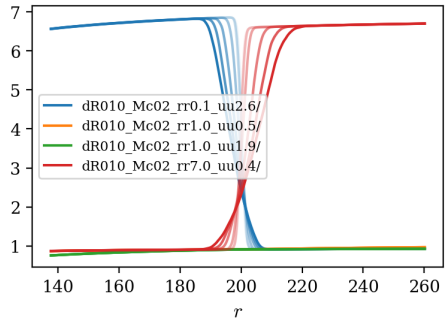

(b) $\delta_0/r_c = 0.010$ and $M_c = 0.2$

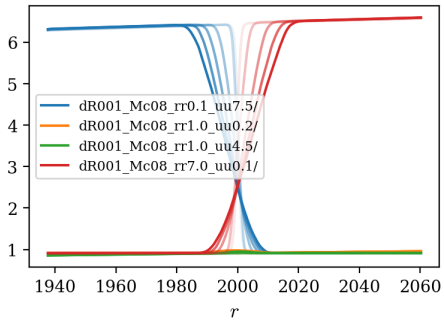

(c) $\delta_0/r_c = 0.001$ and $M_c = 0.8$

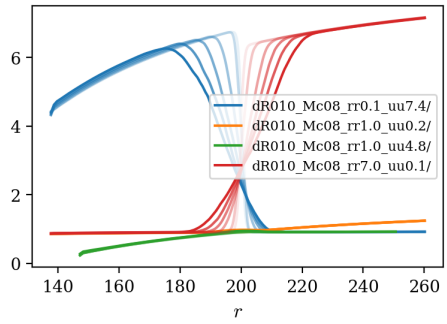

(d) $\delta_0/r_c = 0.010$ and $M_c = 0.8$

Figure B.10: Mean temperature $\bar{T}$

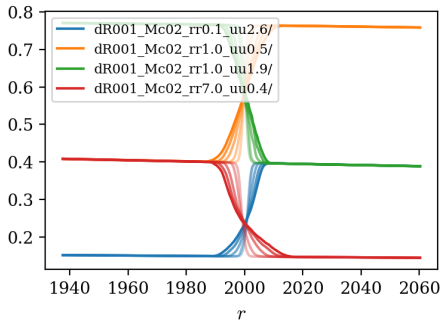

(a) $\delta_0/r_c = 0.001$ and $M_c = 0.2$

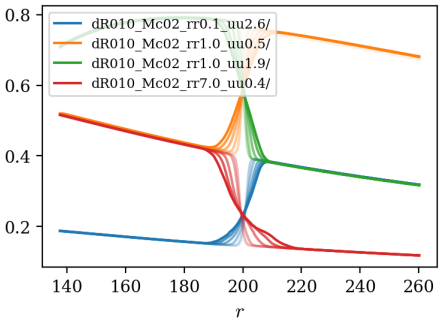

(b) $\delta_0/r_c = 0.010$ and $M_c = 0.2$

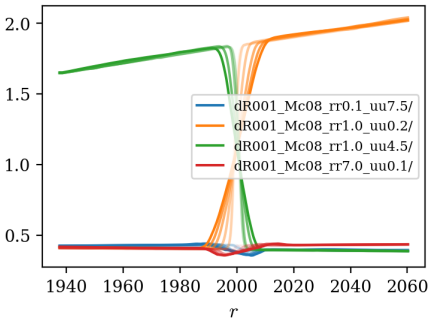

(c) $\delta_0/r_c = 0.001$ and $M_c = 0.8$

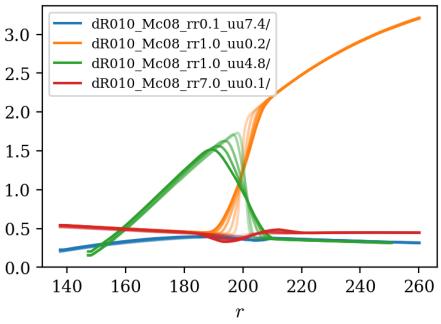

(d) $\delta_0/r_c = 0.010$ and $M_c = 0.8$

Figure B.11: Mean momentum $\bar{\rho}\tilde{u}_\theta$

Turbulent stresses, anisotropy and mass fluxes

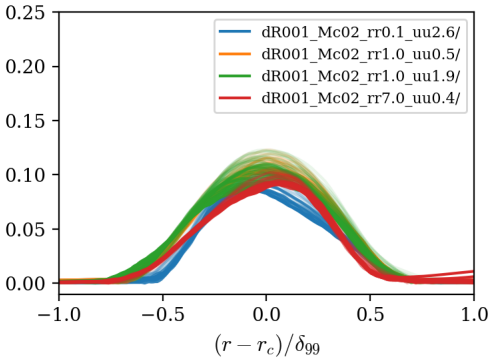

(a) $\delta_0/r_c = 0.001$ and $M_c = 0.2$

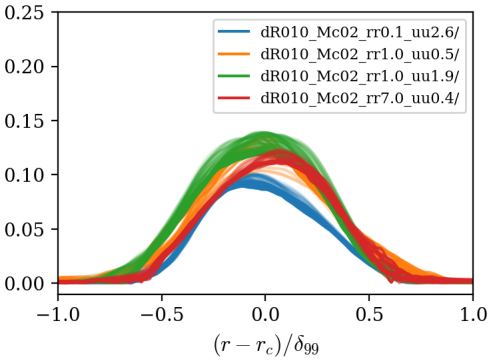

(b) $\delta_0/r_c = 0.010$ and $M_c = 0.2$

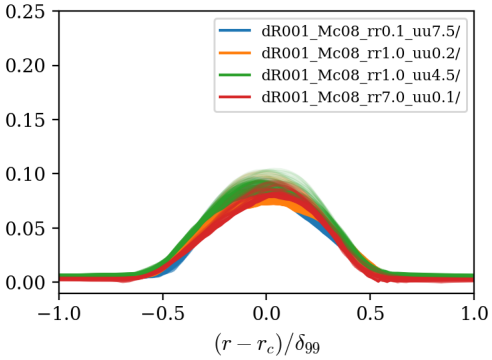

(c) $\delta_0/r_c = 0.001$ and $M_c = 0.8$

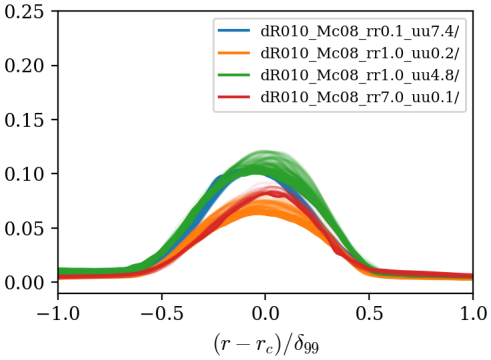

(d) $\delta_0/r_c = 0.010$ and $M_c = 0.8$

Figure B.12: Normalized magnitude of R_{12}: $|\sqrt{\overline{\rho u''_\theta u''_r}/\bar{\rho}\Delta\bar{u}^2}|$

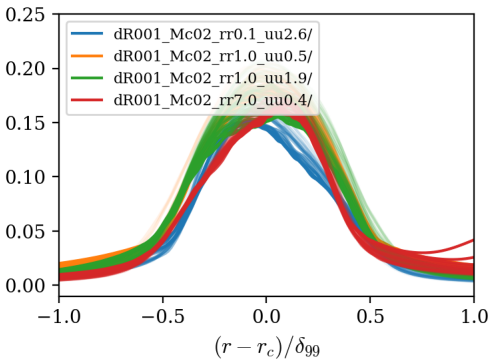

(a) $\delta_0/r_c = 0.001$ and $M_c = 0.2$

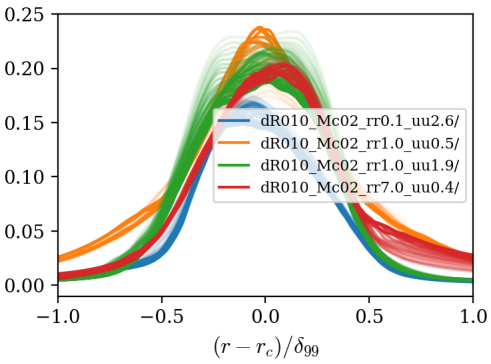

(b) $\delta_0/r_c = 0.010$ and $M_c = 0.2$

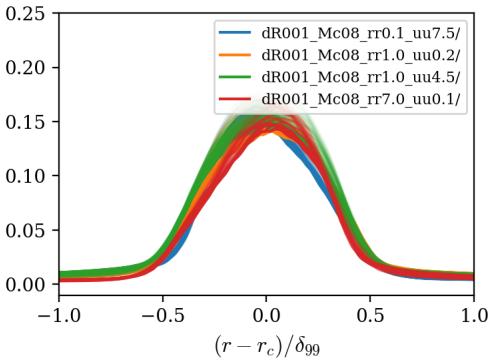

(c) $\delta_0/r_c = 0.001$ and $M_c = 0.8$

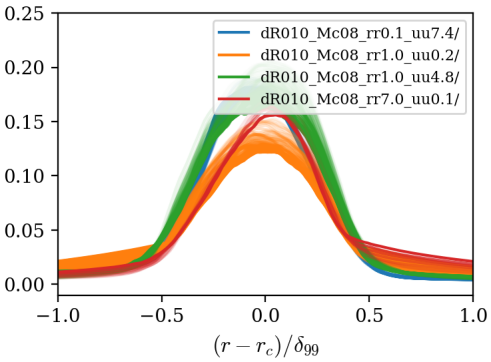

(d) $\delta_0/r_c = 0.010$ and $M_c = 0.8$

Figure B.13: Normalized magnitude of R_{11}: $|\sqrt{\overline{\rho u_\theta'' u_\theta''}/\bar{\rho}\Delta\bar{u}^2}|$

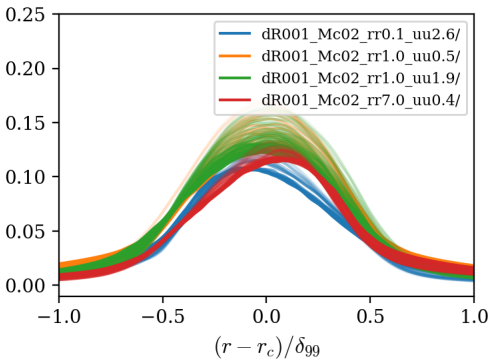

(a) $\delta_0/r_c = 0.001$ and $M_c = 0.2$

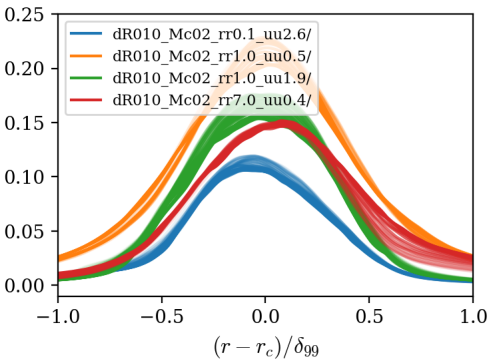

(b) $\delta_0/r_c = 0.010$ and $M_c = 0.2$

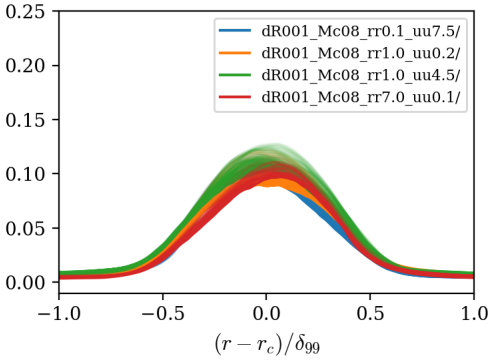

(c) $\delta_0/r_c = 0.001$ and $M_c = 0.8$

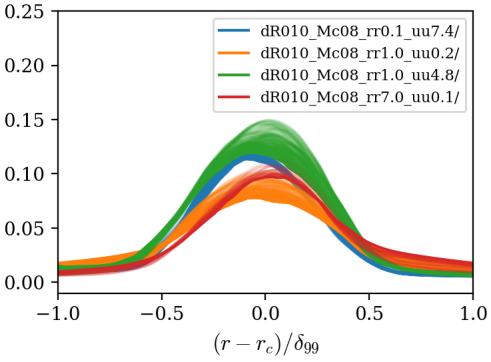

(d) $\delta_0/r_c = 0.010$ and $M_c = 0.8$

Figure B.14: Normalized magnitude of R_{22}: $|\sqrt{\rho u_r'' u_r''}/\bar{\rho}\Delta\bar{u}^2|$

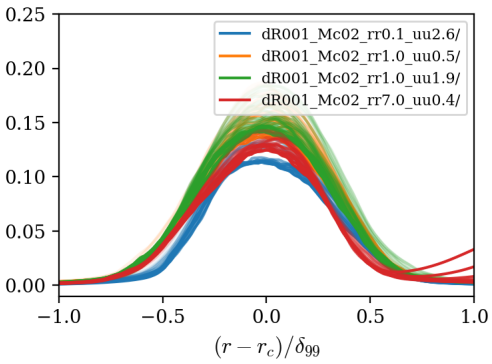

(a) $\delta_0/r_c = 0.001$ and $M_c = 0.2$

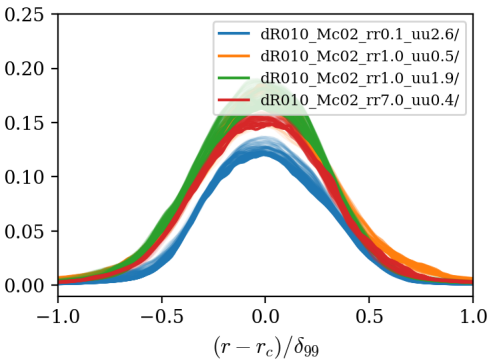

(b) $\delta_0/r_c = 0.010$ and $M_c = 0.2$

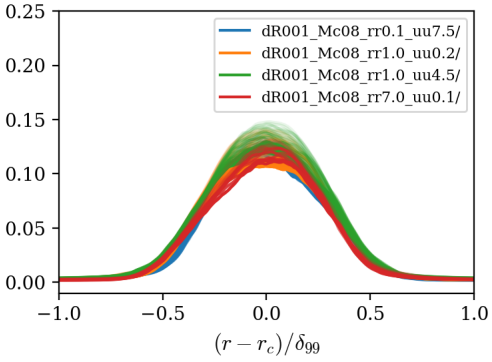

(c) $\delta_0/r_c = 0.001$ and $M_c = 0.8$

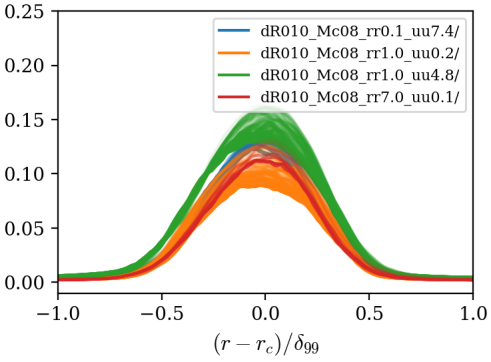

(d) $\delta_0/r_c = 0.010$ and $M_c = 0.8$

Figure B.15: Normalized magnitude of R_{33}: $|\sqrt{\rho u_z'' u_z''}/\bar{\rho}\Delta\bar{u}^2|$

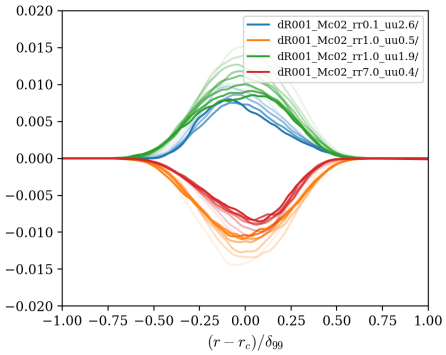

(a) $\delta_0/r_c = 0.001$ and $M_c = 0.2$

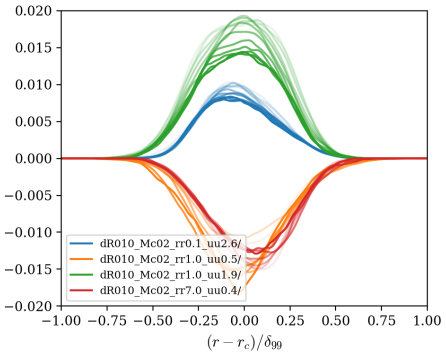

(b) $\delta_0/r_c = 0.010$ and $M_c = 0.2$

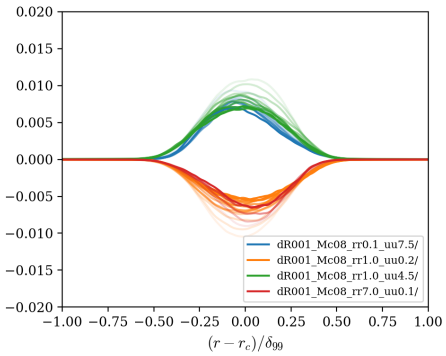

(c) $\delta_0/r_c = 0.001$ and $M_c = 0.8$

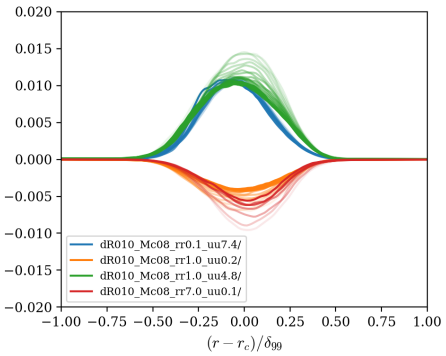

(d) $\delta_0/r_c = 0.010$ and $M_c = 0.8$

Figure B.16: Normalized turbulent shear stress profiles: $R_{12}/(\Delta\bar{u}^2) = \overline{\rho u_\theta'' u_r''}/(\bar{\rho}\Delta\bar{u}^2)$

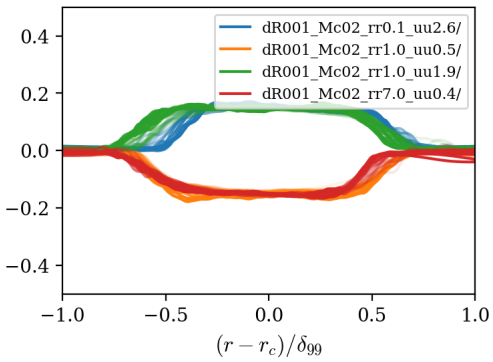

(a) $\delta_0/r_c = 0.001$ and $M_c = 0.2$

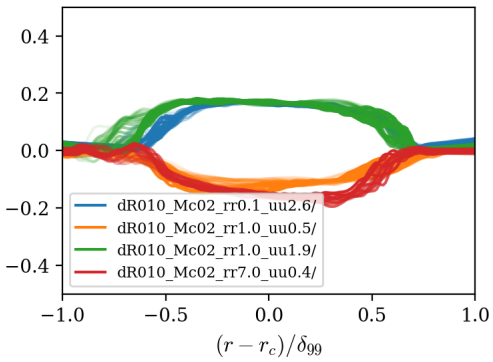

(b) $\delta_0/r_c = 0.010$ and $M_c = 0.2$

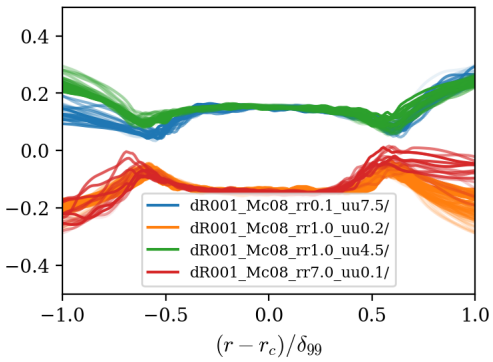

(c) $\delta_0/r_c = 0.001$ and $M_c = 0.8$

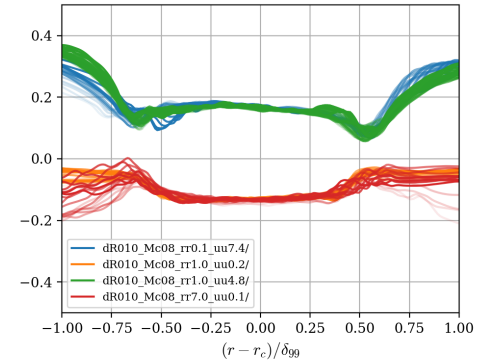

(d) $\delta_0/r_c = 0.010$ and $M_c = 0.8$

Figure B.17: Anisotropy component b_{12}

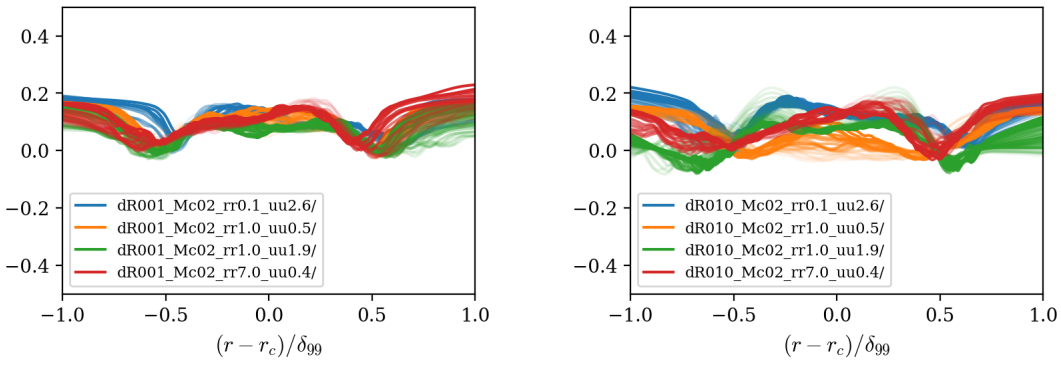

(a) $\delta_0/r_c = 0.001$ and $M_c = 0.2$

(b) $\delta_0/r_c = 0.010$ and $M_c = 0.2$

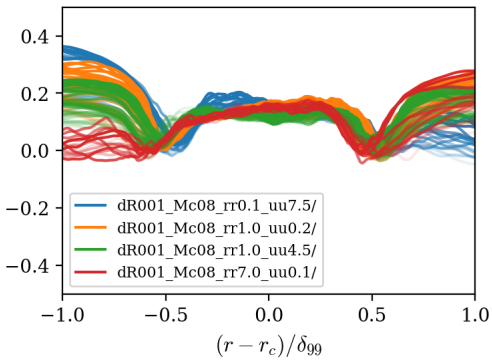

(c) $\delta_0/r_c = 0.001$ and $M_c = 0.8$

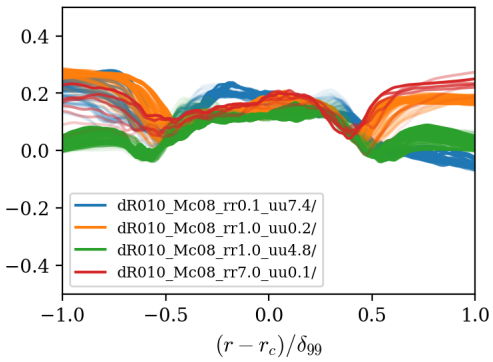

(d) $\delta_0/r_c = 0.010$ and $M_c = 0.8$

Figure B.18: Anisotropy component b_{11}

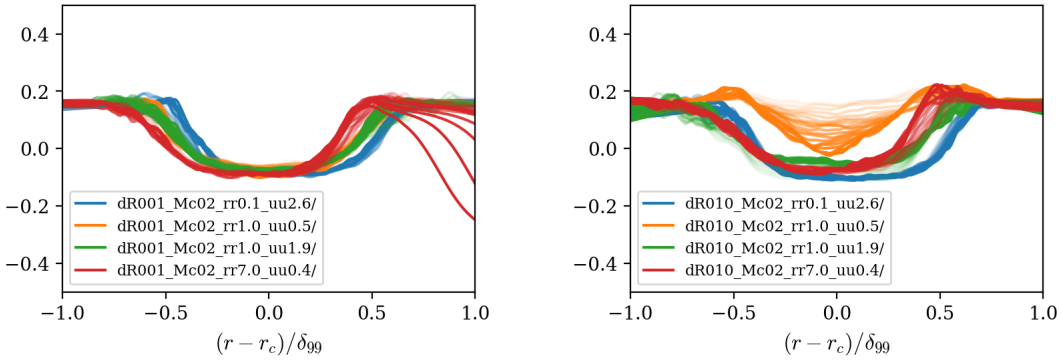

(a) $\delta_0/r_c = 0.001$ and $M_c = 0.2$

(b) $\delta_0/r_c = 0.010$ and $M_c = 0.2$

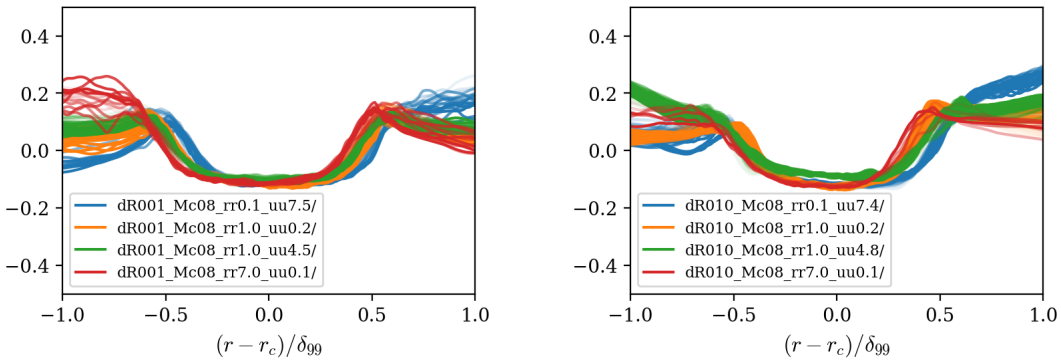

(c) $\delta_0/r_c = 0.001$ and $M_c = 0.8$

(d) $\delta_0/r_c = 0.010$ and $M_c = 0.8$

Figure B.19: Anisotropy component b_{22}

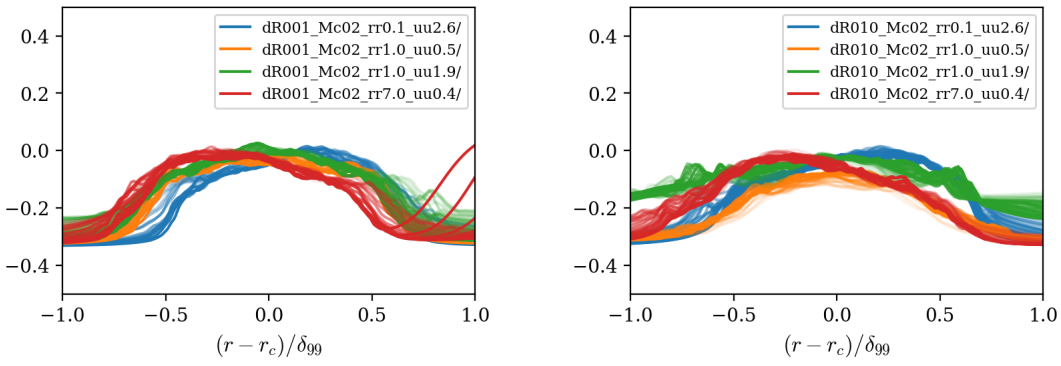

(a) $\delta_0/r_c = 0.001$ and $M_c = 0.2$

(b) $\delta_0/r_c = 0.010$ and $M_c = 0.2$

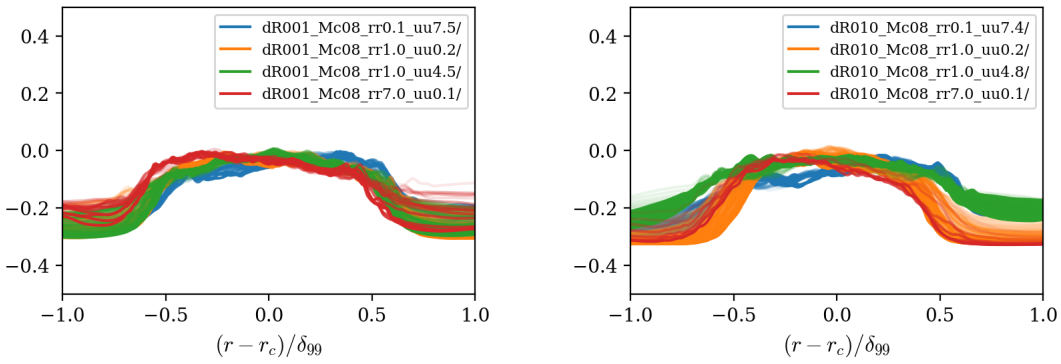

(c) $\delta_0/r_c = 0.001$ and $M_c = 0.8$

(d) $\delta_0/r_c = 0.010$ and $M_c = 0.8$

Figure B.20: Anisotropy component b_{33}

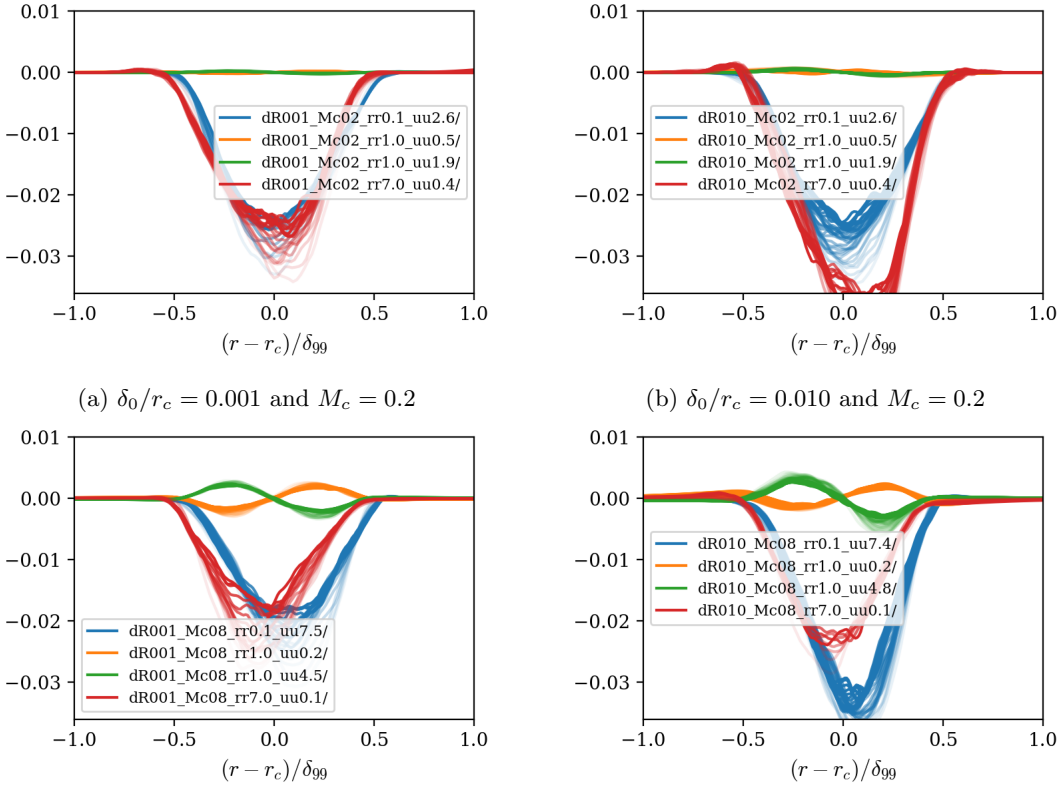

(a) $\delta_0/r_c = 0.001$ and $M_c = 0.2$

(b) $\delta_0/r_c = 0.010$ and $M_c = 0.2$

(c) $\delta_0/r_c = 0.001$ and $M_c = 0.8$

(d) $\delta_0/r_c = 0.010$ and $M_c = 0.8$

Figure B.21: Normalized streamwise turbulent mass flux $\overline{\rho' u'_\theta}/(\bar{\rho}\Delta\bar{u})$

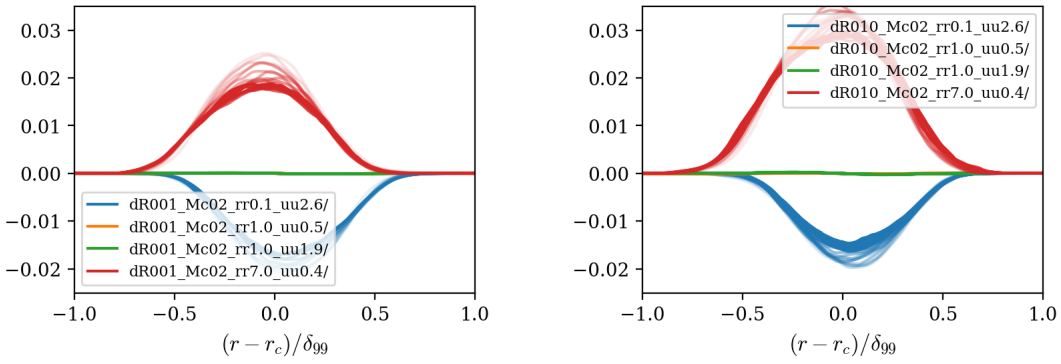

(a) $\delta_0/r_c = 0.001$ and $M_c = 0.2$

(b) $\delta_0/r_c = 0.010$ and $M_c = 0.2$

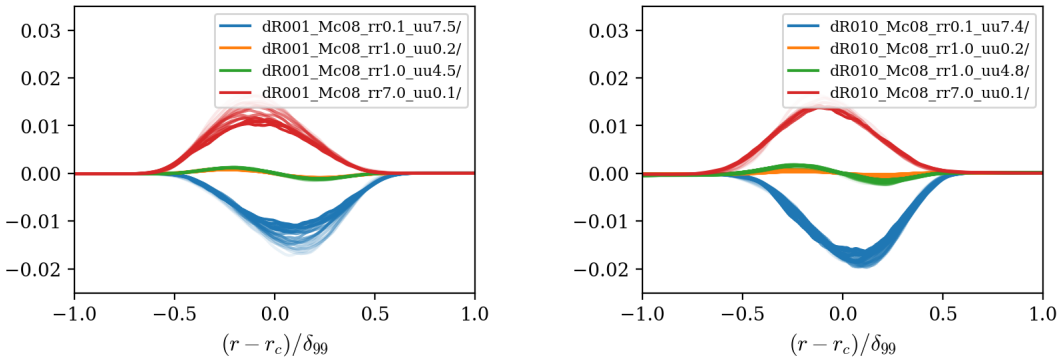

(c) $\delta_0/r_c = 0.001$ and $M_c = 0.8$

(d) $\delta_0/r_c = 0.010$ and $M_c = 0.8$

Figure B.22: Normalized radial turbulent mass flux $\overline{\rho' u_r'}/(\bar{\rho}\Delta\bar{u})$

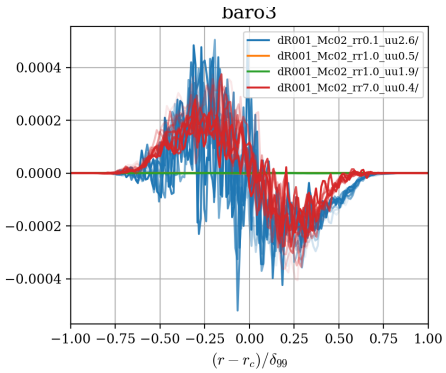

(a) $\delta_0/r_c = 0.001$ and $M_c = 0.2$

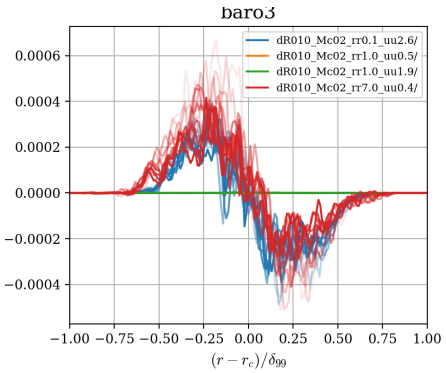

(b) $\delta_0/r_c = 0.010$ and $M_c = 0.2$

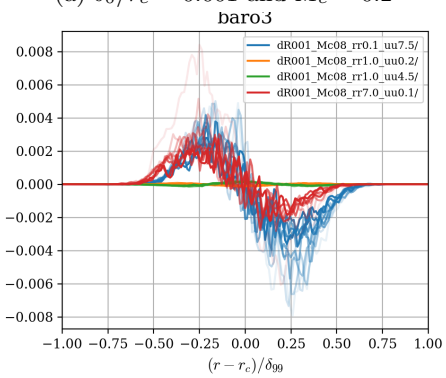

(c) $\delta_0/r_c = 0.001$ and $M_c = 0.8$

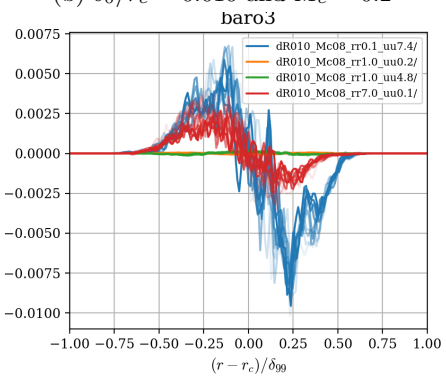

(d) $\delta_0/r_c = 0.010$ and $M_c = 0.8$

Figure B.23: Baroclinic torque acting on spanwise vorticity

Appendix C

Miscellaneous evolution equations

Governing equations in cartesian coordinates and nondimensionalization

The evolution equations in conservative form for mass, momentum and total energy are:

$$\frac{\partial \rho}{\partial t} + \frac{\partial}{\partial x_j}(\rho u_j) = 0 \tag{C.1}$$

$$\frac{\partial}{\partial t}(\rho u_j) + \frac{\partial}{\partial x_j}(\rho u_i u_j) = -\frac{\partial p}{\partial x_i} + \frac{\partial \tau_{ij}}{\partial x_j} \tag{C.2}$$

$$\frac{\partial}{\partial t}(\rho E) + \frac{\partial}{\partial x_j}(\rho u_j H) = \frac{\partial}{\partial x_j}(\tau_i j u_i) - \frac{\partial q_j}{\partial x_j} \tag{C.3}$$

$$\tag{C.4}$$

With

$$
\begin{aligned}
e &= \frac{p}{\rho(\gamma-1)} = c_v T \\
E &= e + \frac{1}{2}u_i u_i & \rho E &= \frac{p}{\gamma-1} + \frac{1}{2}\rho u_i u_i \\
H &= E + \frac{p}{\rho} & \rho H &= \frac{p\gamma}{\gamma-1} + \frac{1}{2}\rho u_i u_i \\
q_j &= -\kappa \frac{\partial T}{\partial x_j} \\
\tau_{ij} &= 2\mu\left(S_{ij} - \frac{1}{3}\frac{\partial u_k}{\partial x_k}\delta_{ij}\right)
\end{aligned}
$$

The following dimensionless variables are introduced:

$$x = x^* x_0 \qquad u_i = u_i^* u_0 \qquad t = t^* x_0/u_0 \qquad \rho = \rho^* \rho_0 \qquad T = T^* T_0$$

$$p = p^* \rho_0 R T_0 \qquad c_0^2 = \gamma R T_0 = \gamma p_0/\rho_0 M_0 = u_0/c_0 \qquad Pr = c_p\mu/\kappa \qquad Re = \rho_0 u_0 x_0/\mu_0$$

Dropping the * notation, the dimensionless evolution equations become:

$$\frac{\partial \rho}{\partial t} + \frac{\partial}{\partial x_j}(\rho u_j) = 0 \tag{C.5}$$

$$\frac{\partial}{\partial t}(\rho u_j) + \frac{\partial}{\partial x_j}(\rho u_i u_j) = -\frac{1}{\gamma M_0^2}\frac{\partial p}{\partial x_i} + \frac{1}{Re}\frac{\partial \tau_{ij}}{\partial x_j} \tag{C.6}$$

$$\frac{\partial}{\partial t}\left[p\frac{1}{\gamma(\gamma-1)M_0^2} + \frac{1}{2}\rho u_i u_i\right] + \frac{\partial}{\partial x_j}\left[u_j(p\frac{\gamma}{\gamma-1}M_0^2 + \frac{1}{2}\rho u_i u_i)\right] = \frac{1}{Re}\frac{\partial}{\partial x_j}(\tau_{ij}u_i) + \frac{1}{PrReM_0^2(\gamma-1)}\frac{\partial^2 T}{\partial x_j x_j} \tag{C.7}$$

Other evolution equations in cylindrical coordinates

- Instantaneous vorticity budget

$$\omega_i = \left[\frac{\partial u_r}{\partial z} - \frac{\partial u_z}{\partial r} \quad \frac{1}{r}\frac{\partial u_z}{\partial \theta} - \frac{\partial u_\theta}{\partial z} \quad \frac{1}{r}\left[\frac{\partial}{\partial r}(r u_\theta) - \frac{\partial u_r}{\partial \theta}\right]\right]$$

$$\frac{\partial \omega_i}{\partial t} + \frac{\partial}{\partial x_i}(u_j\omega_i) = \underbrace{-\omega_i\frac{\partial u_j}{\partial x_j}}_{\text{Dilatation}} + \underbrace{\frac{1}{\rho^2}\epsilon_{ijk}\frac{\partial \rho}{\partial x_j}\frac{\partial p}{\partial x_k}}_{\text{Baroclinic torque}} + \underbrace{\omega_j\frac{\partial u_i}{\partial x_j}}_{\text{Vortex stretching}} + \underbrace{\nu\frac{\partial^2 \omega_i}{\partial x_j x_j}}_{\text{Diffusion}}$$

$$\frac{\partial \bar{\omega}_i}{\partial t} + \frac{\partial}{\partial x_i}(\bar{u}_j \bar{\omega}_i) = - \underbrace{\frac{\partial}{\partial x_j}(\overline{u_j' \omega_i'})}_{\text{Turb. transport}} - \underbrace{\left(\bar{\omega}_i \frac{\partial \bar{u}_j}{\partial x_j} + \overline{\omega_i' \frac{\partial u_j'}{\partial x_j}} \right)}_{\text{Dilatation prod}} + \underbrace{\frac{1}{\rho^2} \epsilon_{ijk} \left(\frac{\partial \bar{\rho}}{\partial x_j} \frac{\partial \bar{p}}{\partial x_k} + \overline{\frac{\partial \rho'}{\partial x_j} \frac{\partial p'}{\partial x_k}} \right)}_{\text{Baroclinic torque}}$$
$$+ \underbrace{\left(\bar{\omega}_j \frac{\partial \bar{u}_i}{\partial x_j} + \overline{\omega_j' \frac{\partial u_i'}{\partial x_j}} \right)}_{\text{Vortex stretching}} + \underbrace{\nu \frac{\partial^2 \bar{\omega}_i}{\partial x_j x_j}}_{\text{Diffusion}}$$

The baroclinic torque term, explicitly:

$$\frac{1}{\rho^2}(\bigtriangledown p \times \bigtriangledown \rho) = \frac{1}{\rho^2} \begin{bmatrix} \frac{\partial p}{\partial z}\frac{\partial \rho}{\partial z} - \frac{\partial p}{\partial r}\frac{\partial \rho}{\partial z} \\ \frac{1}{r}\frac{\partial p}{\partial \theta}\frac{\partial \rho}{\partial z} - \frac{\partial p}{\partial z}\frac{1}{r}\frac{\partial \rho}{\partial \theta} \\ \frac{\partial p}{\partial r}\frac{1}{r}\frac{\partial \rho}{\partial \theta} - \frac{1}{r}\frac{\partial p}{\partial \theta}\frac{\partial \rho}{\partial r} \end{bmatrix}$$

- MKE $K = \frac{1}{2}\tilde{u}_i \tilde{u}_i$ budget equation

$$\frac{\partial}{\partial t}(\bar{\rho} K) + \frac{\partial}{\partial x_j}(\bar{\rho} \tilde{u}_j K) = -\frac{\partial}{\partial x_j}(\bar{\rho} \tilde{u}_i R_{ij}) + R_{ij}\frac{\partial \tilde{u}_i}{\partial x_j} - \tilde{u}_i \frac{\partial \bar{p}}{\partial x_i} + \tilde{u}_i \frac{\partial \bar{\tau}_{ij}}{\partial x_j} \tag{C.8}$$

- TKE $k = \frac{1}{2}\widetilde{u_i'' u_i''}$ budget equation

$$\frac{\partial}{\partial t}(\bar{\rho} k) + \frac{\partial}{\partial x_j}(\bar{\rho} \tilde{u}_j k) = \underbrace{-\bar{\rho} R_{ij} \frac{\partial \tilde{u}_i}{\partial x_j}}_{\text{Production } P} - \underbrace{\overline{\tau_{ij}' \frac{\partial u_i''}{\partial x_j}}}_{\text{Dissipation } D} - \frac{\partial}{\partial x_j} \underbrace{\left(\frac{1}{2}\overline{\rho u_j'' u_i'' u_i''} + \overline{u_j'' p'} - \overline{\tau_{ij}' u_i''} \right)}_{\text{Turbulent transport } T}$$
$$- \underbrace{\overline{u_i''} \frac{\partial \bar{p}}{\partial x_i}}_{\text{Baropycnal work } B} + \underbrace{\overline{p' \frac{\partial u_i''}{\partial x_i}}}_{\text{Pressure dilatation } \Pi} \tag{C.9}$$

- $R_{ij} = \widetilde{u_i'' u_j''}$ budget equation

$$\frac{\partial}{\partial t}(\bar{\rho}R_{ij})+\frac{\partial}{\partial x_k}(\bar{\rho}\tilde{u}_k R_{ij}) = \underbrace{-\bar{\rho}\left(R_{ik}\frac{\partial \tilde{u}_j}{\partial x_k}+R_{jk}\frac{\partial \tilde{u}_i}{\partial x_k}\right)}_{\text{Production } P_{ij}} \underbrace{-\left(\overline{\tau'_{jk}\frac{\partial u''_i}{\partial x_k}+\tau'_{ik}\frac{\partial u''_j}{\partial x_k}}\right)}_{\text{Dissipation } D_{ij}} \underbrace{+\overline{p'\left(\frac{\partial u''_i}{\partial x_j}+\frac{\partial u''_j}{\partial x_i}\right)}}_{\text{Pressure strain } \Pi_{ij}}$$
$$\underbrace{-\frac{\partial}{\partial x_k}\left(\overline{\rho u''_i u''_j u''_k}+\overline{p'u''_i}\delta_{jk}+\overline{p'u''_j}\delta_{ik}-\overline{\tau'_{jk}u''_i}-\overline{\tau'_{ik}u''_j}\right)}_{\text{Turbulent transport } T_{ijk}} \underbrace{+\overline{u''_i}\left(\frac{\partial \bar{\tau}_{jk}}{\partial x_k}-\frac{\partial \bar{p}}{\partial x_j}\right)+\overline{u''_j}\left(\frac{\partial \bar{\tau}_{ik}}{\partial x_k}-\frac{\partial \bar{p}}{\partial x_i}\right)}_{\text{Mass flux coupling } \Sigma_{ij}} \tag{C.10}$$

Bibliography

[1] V. Adumitroaie, J. Ristorcelli, and D. Taulbee. Progress in Favre–Reynolds stress closures for compressible flows. *Physics of Fluids*, 11(9):2696–2719, 1999.

[2] A. Almagro, M. García-Villalba, and O. Flores. A numerical study of a variable-density low-speed turbulent mixing layer. *Journal of Fluid Mechanics*, 830:569–601, 2017.

[3] S. Arun, A. Sameen, and B. Srinivasan. Structure of vorticity field in compressible turbulent mixing layers. *Physica Scripta*, 2019.

[4] B Aupoix. Modelling of compressibility effects in mixing layers. *Journal of Turbulence*, 5(7): 1–17, 2004.

[5] S. Bagheri, P. Schlatter, P. Schmid, and D. Henningson. Global stability of a jet in crossflow. *Journal of Fluid Mechanics*, 624(9):33–44, 2009.

[6] J. Baltzer and D. Livescu. Variable-density effects in incompressible non-buoyant shear-driven turbulent mixing layers. *Journal of Fluid Mechanics*, 900:A16, 2020. doi: 10.1017/jfm.2020.466.

[7] M. Barone, W. Oberkampf, and F. Blottner. Validation case study: prediction of compressible turbulent mixing layer growth rate. *AIAA journal*, 44(7):1488–1497, 2006.

[8] S. Barre and J. Bonnet. Detailed experimental study of a highly compressible supersonic turbulent plane mixing layer and comparison with most recent DNS results. *International Journal of Heat and Fluid Flow*, 51:324–334, 2015.

[9] P. Batten, N. Clarke, C. Lambert, and D. Causon. On the choice of wavespeeds for the hllc riemann solver. *SIAM Journal on Scientific Computing*, 18(6):1553–1570, 1997.

[10] D. Besnard, F. Harlow, R. Rauenzahn, and C. Zemach. Turbulence transport equations for variable-density turbulence and their relationship to two-field models. Technical report, Los Alamos National Lab., NM (United States), 1992.

[11] G. Borghesi, A. Krisman, T. Lu, and J. Chen. Direct numerical simulation of a temporally evolving air/n-dodecane jet at low-temperature diesel-relevant conditions. *Combustion and Flame*, 195:183–202, 2018.

[12] P. Bradshaw. The analogy between streamline curvature and buoyancy in turbulent shear flow. *Journal of Fluid Mechanics*, 36(1):177–191, 1969.

[13] P. Bradshaw. The effect of streamline curvature on turbulent flow. In *ADARGDograph 169*, 1973.

[14] P. Bradshaw. Compressible turbulent shear layers. *Annual Review of Fluid Mechanics*, 9(1): 33–52, 1977.

[15] R. Breidenthal. Sonic eddy-a model for compressible turbulence. *AIAA journal*, 30(1):101–104, 1992.

[16] L Bretonnet, J. Cazalbou, P. Chassaing, and M. Braza. Deflection, drift, and advective growth in variable-density, laminar mixing layers. *Physics of Fluids*, 19(10):103601, 2007.

[17] J. Bridges and M. Wernet. Establishing consensus turbulence statistics for hot subsonic jets. In *16th AIAA/CEAS Aeroacoustics Conference*, page 3751, 2010.

[18] J. Bridges and M. Wernet. Validating large-eddy simulation for jet aeroacoustics. *Journal of Propulsion and Power*, 28(2):226–235, 2012.

[19] G. Brown and A. Roshko. On density effects and large structure in turbulent mixing layers. *Journal of Fluid Mechanics*, 64(4):775–816, 1974.

[20] D. Buchta and J. Freund. The near-field pressure radiated by planar high-speed free-shear-flow turbulence. *Journal of Fluid Mechanics*, 832:383–408, 2017.

[21] D. Buchta, A. Anderson, and J. Freund. Near-field shocks radiated by high-speed free-shear-flow turbulence. In *20th AIAA/CEAS Aeroacoustics Conference*, page 3201, 2014-3201.

[22] P Buning. Nasa overflow cfd code. https://overflow.larc.nasa.gov/users-manual-for-overflow-2-3/, 2021.

[23] P. Buning, D. Jespersen, T. Pulliam, W. Chan, Je. Slotnick, S. Krist, and K. Renze. Overflow user's manual. *NASA Langley Research Center, Hampton, VA*, 2002.

[24] I. Castro and P. Bradshaw. The turbulence structure of a highly curved mixing layer. *Journal of Fluid Mechanics*, 73(2):265–304, 1976.

[25] S. Catris and B. Aupoix. Density corrections for turbulence models. *Aerospace Science and Technology*, 4(1):1–11, 2000.

[26] P. Chassaing. The modeling of variable density turbulent flows. a review of first-order closure schemes. *Flow, Turbulence and Combustion*, 66(4):293–332, 2001.

[27] R. Childs, J. Garcia, J. Melton, S. Rogers, A. Shestopolov, and D. Vicker. Overflow simulation guidelines for orion launch abort vehicle aerodynamic analyses. In *29th AIAA Applied Aerodynamics Conference*, page 3163, 2011.

[28] N. Chinzei, G. Masuya, T. Komuro, A. Murakami, and K. Kudou. Spreading of two-stream supersonic turbulent mixing layers. *The Physics of Fluids*, 29(5):1345–1347, 1986.

[29] K. Choi and J. Lumley. The return to isotropy of homogeneous turbulence. *Journal of Fluid Mechanics*, 436:59–84, 2001.

[30] N. Clemens and M. Mungal. Large-scale structure and entrainment in the supersonic mixing layer. *Journal of Fluid Mechanics*, 284:171–216, 1995.

[31] R. Corral and J. Jimenez. Fourier/chebyshev methods for the incompressible navier-stokes equations in infinite domains. *Journal of Computational Physics*, 121(2):261–270, 1995.

[32] J. Dacles-Mariani, G. Zilliac, J. Chow, and P. Bradshaw. Numerical/experimental study of a wingtip vortex in the near field. *AIAA journal*, 33(9):1561–1568, 1995.

[33] M. Day, W. Reynolds, and N. Mansour. The structure of the compressible reacting mixing layer: Insights from linear stability analysis. *Physics of Fluids*, 10(4):993–1007, 1998.

[34] J. Debisschop and J. Bonnet. Mean and fluctuating velocity measurements in supersonic mixing layers. In *Engineering Turbulence Modelling and Experiments*, pages 467–478. Elsevier, 1993.

[35] G. Dimonte and R. Tipton. K-l turbulence model for the self-similar growth of the Rayleigh-Taylor and Richtmyer-Meshkov instabilities. *Physics of Fluids*, 18(8):085101, 2006.

[36] P. Dimotakis. Two-dimensional shear-layer entrainment. *AIAA journal*, 24(11):1791–1796, 1986.

[37] F. Ducros, V. Ferrand, F. Nicoud, C. Weber, D. Darracq, C. Gacherieu, and T. Poinsot. Large-eddy simulation of the shock/turbulence interaction. *Journal of Computational Physics*, 152 (2):517–549, 1999.

[38] K. Duraisamy and S. K. Lele. Evolution of isolated turbulent trailing vortices. *Physics of Fluids*, 20(3):035102, 2008.

[39] J. Dussauge and C. Quine. A second-order closure for supersonic turbulent flows application to the supersonic mixing. Technical report, 1992.

[40] K. Eckhoff. A note on the instability of columnar vortices. *Journal of Fluid Mechanics*, 145: 417–421, 1984.

[41] K. Eckhoff and L. Storesletten. A note on the stability of steady inviscid helical gas flows. *Journal of Fluid Mechanics*, 89(3):401–411, 1978.

[42] A. El Baz and B. Launder. Second-moment modelling of compressible mixing layers. In *Engineering Turbulence Modelling and Experiments*, pages 63–72. Elsevier, 1993.

[43] G. Elliott and M. Samimy. Compressibility effects in free shear layers. *Physics of Fluids A: Fluid Dynamics*, 2(7):1231–1240, 1990.

[44] A. Favre. Statistical equations of turbulent gases. *Problems of hydrodynamics and continuum mechanics*, pages 231–266, 1969.

[45] M. Ferrer, G. Lehnasch, and A. Mura. Compressibility and heat release effects in high-speed reactive mixing layers i: Growth rates and turbulence characteristics. *Combustion and Flame*, 180:284–303, 2017.

[46] V. Fortuné, É. Lamballais, and Y. Gervais. Noise radiated by a non-isothermal, temporal mixing layer. part i: Direct computation and prediction using compressible DNS. *Theoretical and Computational Fluid Dynamics*, 18(1):61–81, 2004.

[47] J. Freund, S. K. Lele, and P. Moin. Compressibility effects in a turbulent annular mixing layer. part 1. turbulence and growth rate. *Journal of Fluid Mechanics*, 421:229–267, 2000.

[48] H. Fujiwara, Y. Matsuo, and C. Arakawa. A turbulence model for the pressure–strain correlation term accounting for compressibility effects. *International Journal of Heat and Fluid Flow*, 21(3):354–358, 2000.

[49] S. Goebel and C. Dutton. Experimental study of compressible turbulent mixing layers. *AIAA Journal*, 29(4):538–546, 1991.

[50] C. Gomez and S. Girimaji. Toward second-moment closure modelling of compressible shear flows. *Journal of Fluid Mechanics*, 733:325–369, 2013.

[51] C. Gomez and S. Girimaji. Explicit algebraic Reynolds stress model (EARSM) for compressible shear flows. *Theoretical and Computational Fluid Dynamics*, 28(2):171–196, 2014.

[52] J. Hall, P. Dimotakis, and H. Rosemann. Experiments in nonreacting compressible shear layers. *AIAA Journal*, 31(12):2247–2254, 1993.

[53] L. Howard. On the stability of compressible swirling flow. *Studies in Applied Mathematics*, 52(1):39–43, 1973.

[54] F. Hu, S. Otto, and T. Jackson. On the stability of a curved mixing layer. In *Transition, Turbulence and Combustion*, pages 107–116. Springer, 1994.

[55] P. Huang, G. Coleman, and P. Bradshaw. Compressible turbulent channel flows: DNS results and modelling. *Journal of Fluid Mechanics*, 305:185–218, 1995.

[56] P. Iyer and K. Mahesh. A numerical study of shear layer characteristics of low-speed transverse jets. *Journal of Fluid Mechanics*, 790:275–307, 2016.

[57] S. Jagannathan. *Reynolds and Mach Number Scaling in Stationary Compressible Turbulence Using Massively Parallel High Resolution Direct Numerical Simulations*. PhD thesis, Texas A&M University, 2014.

[58] R. Jahanbakhshi and C. Madnia. Entrainment in a compressible turbulent shear layer. *Journal of Fluid Mechanics*, 797:564–603, 2016.

[59] A. Jeans and J. Johnston. The effects of streamwise concave curvature on turbulent boundary layer structure. Technical report, Massachusetts Institute of Tech., Cambridge, 1982.

[60] L. Joly, J. Fontane, and P. Chassaing. The Rayleigh–Taylor instability of two-dimensional high-density vortices. *Journal of Fluid Mechanics*, 537:415–431, 2005.

[61] Y. Kamotani and I. Greber. Experiments on a turbulent jet in a cross flow. *AIAA journal*, 10(11):1425–1429, 1972.

[62] P. Karasso and M. Mungal. Mixing and reaction in curved liquid shear layers. *Journal of Fluid Mechanics*, 334:381–409, 1997.

[63] S. Kawai and S. K. Lele. Large-eddy simulation of jet mixing in supersonic crossflows. *AIAA Journal*, 48(9):2063–2083, 2010.

[64] C. Kennedy and T. Gatski. Self-similar supersonic variable-density shear layers in binary systems. *Physics of Fluids*, 6(2):662–673, 1994.

[65] K. Kim, G. Elliott, and C. Dutton. Three-dimensional experimental study of compressibility effects on turbulent free shear layers. *AIAA Journal*, 58(1):133–147, 2020.

[66] W. Kleb, D. Schauerhamer, K. Trumble, E. Sozer, M. Barnhardt, J. Carlson, and K. Edquist. Toward supersonic retropropulsion CFD validation. In *42nd AIAA Thermophysics Conference*, page 3490, 2011.

[67] R. Kleinman and J. Freund. The sound from mixing layers simulated with different ranges of turbulence scales. *Physics of Fluids*, 20(10):101503, 2008.

[68] H. Klifi and T. Lili. A compressibility correction of the pressure strain correlation model in turbulent flow. *Comptes Rendus Mécanique*, 341(7):567–580, 2013.

[69] A. Kourta and R. Sauvage. Computation of supersonic mixing layers. *Physics of Fluids*, 14 (11):3790–3797, 2002.

[70] B. Launder, G. Reece, and W. Rodi. Progress in the development of a Reynolds-stress turbulence closure. *Journal of Fluid Mechanics*, 68(3):537–566, 1975.

[71] J. Lei, X. Wang, G. Xie, and G. Lorenzini. Turbulent flow field analysis of a jet in cross flow by DNS. *Journal of Engineering Thermophysics*, 24(3):259–269, 2015.

[72] S. Leibovich. Stability of density stratified rotating flows. *AIAA Journal*, 7(1):177–178, 1969.

[73] S. Leibovich and K. Stewartson. A sufficient condition for the instability of columnar vortices. *Journal of Fluid Mechanics*, 126:335–356, 1983.

[74] S. K. Lele. Direct numerical simulation of compressible free shear flows. In *27th Aerospace Sciences Meeting*, page 374, 1989-25317.

[75] S. K. Lele. Compact finite difference schemes with spectral-like resolution. *Journal of Computational Physics*, 103(1):16–42, 1992.

[76] D. Li, A. Peyvan, Z. Ghiasi, J. Komperda, and F. Mashayek. Compressibility effects on energy exchange mechanisms in a spatially developing plane free shear layer. *Journal of Fluid Mechanics*, 910, 2021.

[77] D. Li, J. Komperda, A. Peyvan, Z. Ghiasi, and F. Mashayek. Assessment of turbulence models using DNS data of compressible plane free shear layer flow. *Journal of Fluid Mechanics*, 931, 2022.

[78] W. Liou. Linear instability of curved free shear layers. *Physics of Fluids*, 6(2):541–549, 1994.

[79] D. Livescu. Turbulence with large thermal and compositional density variations. *Annual Review of Fluid Mechanics*, 52:309–341, 2020.

[80] R. Lock. The velocity distribution in the laminar boundary layer between parallel streams. *The Quarterly Journal of Mechanics and Applied Mathematics*, 4(1):42–63, 1951.

[81] A. Lopez-Zazueta, J. Fontane, and L. Joly. Optimal perturbations in time-dependent variable-density Kelvin–Helmholtz billows. *Journal of Fluid Mechanics*, 803:466–501, 2016.

[82] C. Lui and S. K. Lele. Direct numerical simulation of spatially developing, compressible, turbulent mixing layers. In *39th Aerospace Sciences Meeting and Exhibit*, page 291, 2001.

[83] D. Margolis and J. Lumley. Curved turbulent mixing layer. *The Physics of Fluids*, 8(10): 1775–1784, 1965.

[84] K. Matsuno and S. K. Lele. Compressibility effects in high speed turbulent shear layers–revisited. In *AIAA SciTech 2020 Forum*, page 0573, 2020.

[85] K. Matsuno and S. K. Lele. Internal regulation in compressible turbulent shear layers. *Journal of Fluid Mechanics*, 907, 2021.

[86] K. Matsuno and S. K. Lele. Variable density mixing in compressible turbulent shear layers. In *AIAA Aviation 2021 FORUM*, 2021-2912.

[87] K. Matsuno, R. Childs, T. Pulliam, P. Stremel, and J. Garcia. OVERFLOW analysis of supersonic retropropulsion testing on the CobraMRV mars entry vehicle concept. In *AIAA SciTech 2022 Forum*, 2022.

[88] F. Menter. Two-equation eddy-viscosity turbulence models for engineering applications. *AIAA journal*, 32(8):1598–1605, 1994.

[89] R. Mittal and P. Moin. Suitability of upwind-biased finite difference schemes for large-eddy simulation of turbulent flows. *AIAA journal*, 35(8):1415–1417, 1997.

[90] B. Morgan. Scalar mixing in a Kelvin-Helmholtz shear layer and implications for Reynolds-averaged Navier-Stokes modeling of mixing layers. *Physical Review E*, 103(5):053108, 2021.

[91] B. Morgan and M. Wickett. Three-equation model for the self-similar growth of Rayleigh-Taylor and Richtmyer-Meskov instabilities. *Physical Review E*, 91(4):043002, 2015.

[92] B. Morgan, B. Olson, W. Black, and J. McFarland. Large-eddy simulation and Reynolds-averaged Navier-Stokes modeling of a reacting Rayleigh-Taylor mixing layer in a spherical geometry. *Physical Review E*, 98(3):033111, 2018.

[93] R. Moser and M. Rogers. Coherent structures in a simulated turbulent mixing layer. In *Eddy Structure Identification in Free Turbulent Shear Flows*, pages 415–428. Springer, 1993.

[94] M. Nagata and N. Kasagi. Spatio-temporal evolution of coherent vortices in wall turbulence with streamwise curvature. *Journal of Turbulence*, 5(1):017, 2004.

[95] V. Nair, B. Wilde, B. Emerson, and T. Lieuwen. Shear layer dynamics in a reacting jet in crossflow. *Proceedings of the Combustion Institute*, 37(4):5173–5180, 2019.

[96] J. Naughton, L. Cattafesta, and G. Settles. An experimental study of compressible turbulent mixing enhancement in swirling jets. *Journal of Fluid Mechanics*, 330:271–305, 1997.

[97] R. Nichols. Algorithm and turbulence model requirements for simulating vortical flows. In *46th AIAA Aerospace Sciences Meeting and Exhibit*, page 337, 2008.

[98] R. Nichols, R. Tramel, and P. Buning. Solver and turbulence model upgrades to overflow 2 for unsteady and high-speed applications. In *24th AIAA Applied Aerodynamics Conference*, page 2824, 2006.

[99] N. Okong'o and J. Bellan. Direct numerical simulation of a transitional supercritical binary mixing layer: heptane and nitrogen. *Journal of Fluid Mechanics*, 464:1–34, 2002.

[100] S. Otto, T. Jackson, and F. Hu. On the spatial evolution of centrifugal instabilities within curved incompressible mixing layers. *Journal of Fluid Mechanics*, 315:85–103, 1996.

[101] S. Otto, J. Stott, and J. Denier. On the role of buoyancy in determining the stability of curved mixing layers. *Physics of Fluids*, 11(6):1495–1501, 1999.

[102] S. Pandya, S. Venkateswaran, and T. Pulliam. Implementation of preconditioned dual-time procedures in overflow. In *41st Aerospace Sciences Meeting and Exhibit*, page 72, 2003.

[103] C. Pantano and S. Sarkar. A study of compressibility effects in the high-speed turbulent shear layer using direct simulation. *Journal of Fluid Mechanics*, 451:329–371, 2002.

[104] D. Papamoschou and S. K. Lele. Vortex-induced disturbance field in a compressible shear layer. *Physics of Fluids A: Fluid Dynamics*, 5(6):1412–1419, 1993.

[105] D. Papamoschou and A. Roshko. The compressible turbulent shear layer: an experimental study. *Journal of Fluid Mechanics*, 197:453–477, 1988.

[106] O. Planché and W. Reynolds. Heat release effects on mixing in supersonic reacting free shear-layers. In *30th Aerospace Sciences Meeting and Exhibit*, page 92, 1992.

[107] M. Plesniak, R. Mehta, and J. Johnston. Curved two-stream turbulent mixing layers: Three-dimensional structure and streamwise evolution. *Journal of Fluid Mechanics*, 270:1–50, 1994.

[108] M. Plesniak, R. Mehta, and J. Johnston. Curved two-stream turbulent mixing layers revisited. *Experimental Thermal and Fluid Science*, 13(3):190–205, 1996.

[109] Lord Rayleigh. On the dynamics of revolving fluids. *Proceedings of the Royal Society of London. Series A, Containing Papers of a Mathematical and Physical Character*, 93(648): 148–154, 1917.

[110] M. Regan and K. Mahesh. Global linear stability analysis of jets in cross-flow. *Journal of Fluid Mechanics*, 828:812–836, 2017.

[111] J. Reinaud, L. Joly, and P. Chassaing. The baroclinic secondary instability of the two-dimensional shear layer. *Physics of Fluids*, 12(10):2489–2505, 2000.

[112] M. Rogers and R. Moser. Direct simulation of a self-similar turbulent mixing layer. *Physics of Fluids*, 6(2):903–923, 1994.

[113] T. Rossmann, M. Mungal, and R. Hanson. Evolution and growth of large scale structures in high compressibility mixing layers. *Journal of Turbulence*, 3:N9, 2001.

[114] N. Sandham and W. Reynolds. Three-dimensional simulations of large eddies in the compressible mixing layer. *Journal of Fluid Mechanics*, 224:133–158, 1991.

[115] S. Sarkar. The pressure–dilatation correlation in compressible flows. *Physics of Fluids A: Fluid Dynamics*, 4(12):2674–2682, 1992.

[116] S. Sarkar and B. Lakshmanan. Application of a Reynolds stress turbulence model to the compressible shear layer. *AIAA journal*, 29(5):743–749, 1991.

[117] S. Sarkar, G. Erlebacher, M. Hussaini, and H. Kreiss. The analysis and modelling of dilatational terms in compressible turbulence. *Journal of Fluid Mechanics*, 227:473–493, 1991.

[118] J. Sarkies and S. Otto. Görtler vortices in compressible mixing layers. *Journal of Fluid Mechanics*, 427:359–388, 2001.

[119] D. Sipp, D. Fabre, S. Michelin, and L. Jacquin. Stability of a vortex with a heavy core. *Journal of Fluid Mechanics*, 526:67–76, 2005.

[120] M. Slessor, M. Zhuang, and P. Dimotakis. Turbulent shear-layer mixing: growth-rate compressibility scaling. *Journal of Fluid Mechanics*, 414:35–45, 2000.

[121] P. Smirnov and F. Menter. Sensitization of the sst turbulence model to rotation and curvature by applying the spalart–shur correction term. *Journal of Turbomachinery*, 131(4), 2009.

[122] H. Song, A. Ghate, K. Matsuno, J. West, A. Subramaniam, L. Brown, and S. K. Lele. Robust high-resolution simulations of compressible turbulent flows without filtering. In *AIAA Aviation 2022 FORUM*, 2022.

[123] M. Soteriou and A. Ghoniem. Effects of the free-stream density ratio on free and forced spatially developing shear layers. *Physics of Fluids*, 7(8):2036–2051, 1995.

[124] P. Spalart. Trends in turbulence treatments. In *Fluids 2000 Conference and Exhibit*, page 2306, 2000.

[125] P. Spalart and S. Allmaras. A one-equation turbulence model for aerodynamic flows. In *30th Aerospace Sciences Meeting and Exhibit*, page 439, 1992.

[126] P. Spalart and M. Shur. On the sensitization of turbulence models to rotation and curvature. *Aerospace Science and Technology*, 1(5):297–302, 1997.

[127] C. Speziale, S. Sarkar, and T. Gatski. Modelling the pressure–strain correlation of turbulence: an invariant dynamical systems approach. *Journal of Fluid Mechanics*, 227:245–272, 1991.

[128] A. Stabnikov and A. Garbaruk. Testing of modified curvature-rotation correction for k-ω sst model. In *Journal of Physics: Conference Series*, volume 769, page 012087. IOP Publishing, 2016.

[129] A. Subramaniam. *Simulations of Shock Induced Interfacial Instabilities Including Materials with Strength*. PhD thesis, Stanford University, 2018.

[130] Y. Suzen and K. Hoffmann. Investigation of supersonic jet exhaust flow by one-and two-equation turbulence models. In *36th AIAA Aerospace Sciences Meeting and Exhibit*, page 322, 1998.

[131] J. Synge. The stability of heterogeneous liquids. *Trans. R. Soc. Canada*, 27:1, 1933.

[132] E. Toro, M. Spruce, and W. Speares. Restoration of the contact surface in the hll-riemann solver. *Shock waves*, 4(1):25–34, 1994.

[133] W. Urban and M. Mungal. Planar velocity measurements in compressible mixing layers. *Journal of Fluid Mechanics*, 431:189–222, 2001.

[134] S. Vaghefi and C. Madnia. Local flow topology and velocity gradient invariants in compressible turbulent mixing layer. *Journal of Fluid Mechanics*, 774:67–94, 2015.

[135] A. Vreman, N. Sandham, and K. Luo. Compressible mixing layer growth rate and turbulence characteristics. *Journal of Fluid Mechanics*, 320:235–258, 1996.

[136] C. Wang. *The effects of curvature on turbulent mixing layers*. PhD thesis, California Institute of Technology, 1984.

[137] Q. Wang, Z. Wang, and Y. Zhao. The impact of streamwise convex curvature on the supersonic turbulent boundary layer. *Physics of Fluids*, 29(11):116106, 2017.

[138] D. Wilcox. Dilatation-dissipation corrections for advanced turbulence models. *AIAA Journal*, 30(11):2639–2646, 1992.

[139] D. Wilcox. Formulation of the kw turbulence model revisited. *AIAA journal*, 46(11):2823–2838, 2008.

[140] I. Wygnanski and H. Fiedler. The two-dimensional mixing region. *Journal of Fluid Mechanics*, 41(2):327–361, 1970.

[141] J. Wyngaard, H. Tennekes, J. Lumley, and D. Margolis. Structure of turbulence in a curved mixing layer. *The Physics of Fluids*, 11(6):1251–1253, 1968.

[142] D. Yoder. *Algebraic Reynolds stress modeling of planar mixing layer flows*. University of Cincinnati, 2005.

[143] K. Zarchi, D. Schauerhamer, W. Kleb, J. Carlson, and K. Edquist. Computational fluid dynamics validation and post-test analysis of supersonic retropropulsion in the Ames 9x7 unitary tunnel. In *42nd AIAA Fluid Dynamics Conference and Exhibit*, page 2705, 2012.

[144] O. Zeman. Dilatation dissipation: the concept and application in modeling compressible mixing layers. *Physics of Fluids A: Fluid Dynamics*, 2(2):178–188, 1990.

[145] D. Zhang, J. Tan, L. Lv, and F. Li. Characterization of flow mixing and structural topology in supersonic planar mixing layer. *Acta Astronautica*, 156:33–43, 2019.

[146] Q. Zhou, F. He, and M. Shen. Direct numerical simulation of a spatially developing compressible plane mixing layer: flow structures and mean flow properties. *Journal of Fluid Mechanics*, 711:437–468, 2012.

[147] M. Zhuang. The effects of curvature on wake-dominated incompressible free shear layers. *Physics of Fluids*, 11(10):3106–3115, 1999.